

Crystal and spin structure and their relation to physical properties in some geometrical and spin spiral multiferroics

Von der Fakultät für Mathematik, Informatik und Naturwissenschaften der Rheinisch-Westfälischen Technischen Hochschule Aachen zur Erlangung des akademischen Grades eines Doktors der Naturwissenschaften genehmigte Dissertation

vorgelegt von
Master of Science

Chogondahalli Muniraju Naveen Kumar

aus
Bengaluru, Indien

Berichter: Universitätsprofessor Dr. Thomas Brückel
Universitätsprofessor Dr. Uwe Klemradt

Diese Dissertation ist auf den Internetseiten der Hochschulbibliothek online verfügbar

Contents

1	MULTIFERROIC COMPOUNDS	1
1.1	Introduction	2
1.2	Magnetoelectric multiferroics	3
1.2.1	The origin of multiferroicity	4
1.2.2	Different routes to multiferroicity	6
1.3	Aims of research	11
2	THEORETICAL BACKGROUND AND EXPERIMENTAL METHODS	13
2.1	Synthesis of polycrystalline powders and growth of single crystals	14
2.1.1	Solid state reaction route	14
2.1.2	Crystal growth by optical floating zone technique	15
2.2	Powder X-ray diffraction	17
2.2.1	Theoretical background	17
2.2.2	Experimental technique	22
2.3	Neutron scattering	24
2.3.1	Theoretical background	24
2.3.2	Scattering formulae	25
2.3.3	Experimental techniques	35
3	STRUCTURAL, MAGNETIC AND THERMAL PROPERTIES OF HoCrO_3	41
3.1	Introduction	42
3.2	Experimental	44
3.3	Results	44
3.3.1	Crystal Structure	44
3.3.2	Magnetization	48
3.3.3	Specific heat	49
3.4	Discussion	58
3.5	Conclusions	60

4	MAGNETIC ORDERING AND MAGNETOELASTIC EFFECT IN HoCrO_3	63
4.1	Introduction	64
4.2	Experimental	65
4.3	Results and discussion	66
4.3.1	Magnetic ordering	66
4.3.2	Magnetoelastic effect	79
4.4	Conclusions	82
5	CRYSTAL FIELDS AND MAGNETIC EXCITATIONS IN HoCrO_3	85
5.1	Introduction	86
5.2	Crystal field calculation	86
5.2.1	Crystal field theory versus Ligand field theory	86
5.2.2	Point-charge model	87
5.3	Experimental	91
5.4	Results and discussion	91
5.4.1	Crystal field levels	91
5.4.2	Spin fluctuations	97
5.5	Conclusions	99
6	UNCONVENTIONAL MAGNETIC ORDERING IN HEXAGONAL DyMnO_3	101
6.1	Introduction	102
6.2	Experimental results and discussion	103
6.2.1	Synthesis and growth of single crystals	103
6.2.2	Structural properties	104
6.2.3	Magnetic properties	107
6.2.4	Thermal properties	110
6.2.5	Neutron scattering measurements	114
6.2.6	Single crystal neutron scattering measurements	120
6.3	Conclusions	123
7	INCOMMENSURATE MAGNETIC ORDERING IN $\text{Mn}_{0.9}\text{M}_{0.1}\text{WO}_4$ (M=Co, Cu)	127
7.1	Introduction	128
7.2	Experimental	129
7.2.1	Synthesis	129
7.2.2	Crystal structure	130
7.2.3	Magnetic and thermal properties	130

CONTENTS

7.3	Magnetic ordering	133
7.3.1	Experimental	133
7.3.2	Magnetic structure refinement	134
7.4	Summary and Conclusions	139
8	Summary and outlook	141
8.1	Orthorhombic HoCrO_3	142
8.2	Hexagonal DyMnO_3	144
8.3	Wolframite $\text{Mn}_{0.9}\text{Co}_{0.1}\text{WO}_4$ and $\text{Mn}_{0.9}\text{Cu}_{0.1}\text{WO}_4$	145
Appendices		
A	List of acronyms	149
B	The Rietveld Method	151
C	Crystal and magnetic structure determination of HoCrO_3	157
C.1	Representation analysis of HoCrO_3 with <i>BasIreps</i>	157
C.2	Magnetic structure refinement of HoCrO_3 using <i>FullProf</i>	159
D	Refined structure parameters of HoCrO_3	163
E	Refined structure parameters of $h\text{DyMnO}_3$	165
F	<i>FullProf</i> control (input) files used for the Rietveld refinement of the magnetic structures of $\text{Mn}_{1-x}\text{M}_x\text{WO}_4$	169
	Bibliography	175
	Acknowledgements	

Chapter 1

MULTIFERROIC COMPOUNDS

1.1 Introduction

One of the promising approaches to create novel materials is to combine different physical properties in one material to achieve rich functionality. The early attempts to combine (ferro)magnetic and ferroelectric(FE) properties dates back to 1960s [1–3]. Materials combining these ferroic properties [4] were later on called multiferroics [5]. In general, multiferroics are the compounds in which at least two of the following phenomena are coupled: ferroelectricity, magnetic ordering or ferroelasticity (figure1.1). In recent years with rapid growth of information technology one of the key issues is being the necessity of production of storage media (like hard drives) with higher data density. The discovery of the giant magnetoresistance effect significantly promoted magnetic memory technology and was a revolution in the field of magnetoelectronics or spintronics. Currently either ferroelectric or ferromagnetic materials are used for data storage media. If instead a multiferroic (with both magnetic and ferroelectric ordering) could be used in memory devices, it would add an extra dimension to the field of data storage resulting in an increase of the data density. In addition, the possibility to switch the magnetic state by an electric field pulse in multiferroic devices can lead to a reduced power consumption.

From the physical point of view multiferroics present an extremely interesting class of systems and problems. Such as, what are microscopic conditions, and sometimes constraints which determine the possibility to combine in one system both magnetic and ferroelectric properties. This turned out to be a quite nontrivial question, and usually in ‘conventional’ systems, these two phenomena tend to exclude one another which is the main cause for the scarcity of magnetoelectric multiferroics. The scarcity of ferromagnetic ferroelectric is now well understood to result from the contra-indication between the conventional mechanisms for cation off-centering in ferroelectrics (which requires formally empty d orbitals), and the formation of magnetic moments (which usually results from partially filled d orbitals) [6]. This makes the presence of magnetism and ferroelectricity simultaneously *chemically exclusive*. Despite this fact, more than 100 compounds that exhibit the magnetoelectric effect have been discovered [6–12]. In the present work we have synthesized and studied crystal and magnetic properties of several multiferroic compounds via macroscopic and microscopic measurements. A better knowledge of crystal and magnetic structures is a key to understand the

underlying physics in multiferroics, which could help to design efficient materials for the applications. In present chapter we give a brief introduction to multiferroics, restricting our attention to single-phase multiferroic compounds exhibiting (anti)ferromagnetism and ferroelectricity simultaneously.

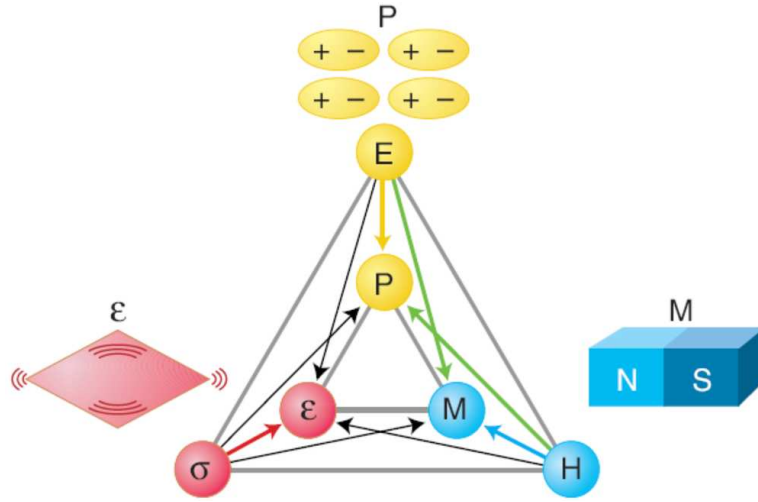


Figure 1.1: Relationship between ferroelectricity (polarization P and electric field E), magnetism (magnetization M and magnetic field H), and ferroelasticity (strain ϵ and stress σ). Multiferroics are the materials in which at least two of these order parameters are coupled and a mutual control is possible (Taken from Spaldin et al [13]).

1.2 Magnetolectric multiferroics

In recent years, there has been a renewed interest in the coexistence and interplay of magnetism and electrical polarization. So called magnetolectric (ME) multiferroics (simply referred as multiferroics here on) are presently attracting considerable attention [6–10, 14]. There exist several different classes of multiferroics [9], a very interesting type being the recently discovered [15–19] systems in which ferroelectricity appears only in certain magnetically ordered states, typically, although not necessarily, spiral ones [10]. Some of them are multiferroic in zero magnetic field, while others develop an electric polarization only if a magnetic field is applied [20–22]. These compounds belong to different crystallographic classes, and although some general rules governing their behavior are already established [10], there is as yet no complete or general understanding

of the origin of multiferroic behavior. Even though their electric polarization P is usually not large, one can easily influence it by comparatively weak magnetic fields or electric switching of magnetization (M). It is this electric ‘switching’ of M which makes multiferroics potentially very useful in device applications. In the present trends in device miniaturization and high-density data storage, an integration of multifunctions into one material system has become highly desirable. Emerging from the extensive applications of magnetic and ferroelectric materials, it is natural to pursue a new generation of memories and sensing/actuating devices tailored by materials that combine magnetism and ferroelectricity in an effective and intrinsic manner as shown in figure 1.2.

One way to enhance the magnetoelectric response in single-phase compounds significantly is to make use of strong internal electromagnetic fields in the components with large dielectric and magnetic susceptibilities. It is well known that ferroelectric/ferromagnetic materials have the largest dielectric/magnetic susceptibility, respectively. Ferroelectrics with ferromagnetism, i.e. ferroelectro-magnets [2], would be prime candidates for an enhanced magnetoelectric effect. Except for the coexistence of ferroelectricity and ferromagnetism, materials with strong coupling between primary ferroelastic and ferromagnetic order parameters, in the class of ferromagnetic martensitic systems, were also studied about 10 years ago [23].

1.2.1 The origin of multiferroicity

The ME effect, meaning magnetic (electric) induction of polarization P (magnetization M), was first confirmed in 1959 – 1960 theoretically by Dzyloshinsky [25] and experimentally by Astrov [26]. Since then several magnetic materials have been demonstrated to show this effect [27]. In general magnetoelectric effect describes the coupling between electric and magnetic fields in matter (i.e. induction of magnetization (M) by an electric field (E) or polarization (P) generated by a magnetic field (H)). Thermodynamically, the ME effect can be understood within the Landau theory framework, approached by the expansion of free energy for a magnetoelectric system, i.e.

$$F(\vec{E}, \vec{H}) = F_0 - P_i^s E_i - M_i^s H_i - \frac{1}{2} \varepsilon_0 \varepsilon_{ij} E_i E_j - \frac{1}{2} \mu_0 \mu_{ij} H_i H_j - \alpha_{ij} E_i H_j - \frac{1}{2} \beta_{ijk} E_i H_j H_k - \frac{1}{2} \gamma_{ijk} H_i E_j E_k - \dots, \quad (1.1)$$

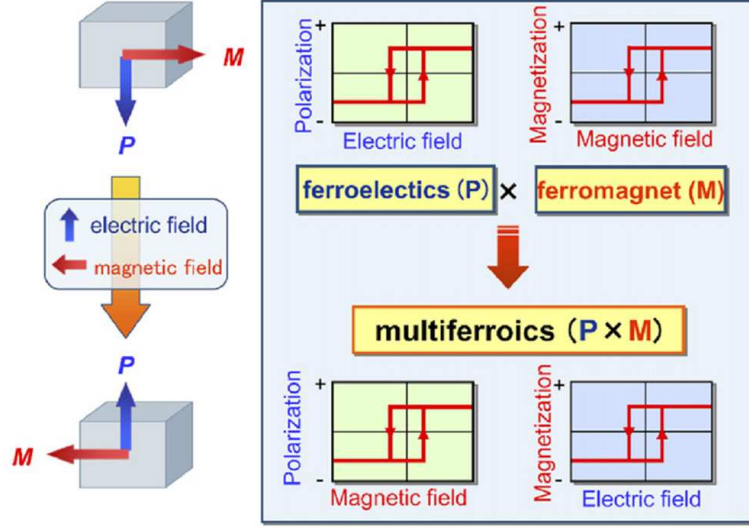


Figure 1.2: A schematic of the ferroelectricity and ferromagnetism integration as well as the mutual control between them in multiferroics. Ideal multiferroics would offer an excellent ferroelectric polarization and ferromagnetic magnetization (polarization-electric field hysteresis and magnetization-magnetic field hysteresis) and also high quality polarization-magnetic field hysteresis and magnetization-electric field hysteresis (Reproduced from Tokura et al [24]).

where F_0 is the ground state free energy and subscripts (i, j, k) refer to the three components of a variable in spatial coordinates. E_i and H_i are the components of the electric field \vec{E} and magnetic field \vec{H} , respectively; P_i^s and M_i^s are the components of the spontaneous polarization \vec{P}^s and magnetization \vec{M}^s ; ϵ_0 and μ_0 are the dielectric and magnetic susceptibilities, β_{ijk} and γ_{ijk} are the third-order tensor coefficients and, most importantly, α_{ij} is the component of tensor $\hat{\alpha}$. The tensor $\hat{\alpha}$ corresponds to induction of polarization by a magnetic field or of magnetization by an electric field which is designated as the linear magnetoelectric effect. The rest of the terms in the preceding equations correspond to the high-order magnetoelectric effects parameterized by tensors β and γ [7]. The differentiation of equation (1.1) leads to the polarization

$$P_i(E, H) = \frac{\partial F}{\partial E_i} = P_i^s + \epsilon_0 \epsilon_{ij} E_j + \alpha_{ij} H_j + \frac{1}{2} \beta_{ijk} H_j H_k + \gamma_{ijk} H_i E_j + \dots, \quad (1.2)$$

and to the magnetization

$$M_i(E, H) = -\frac{\partial F}{\partial H_i} = M_i^s + \mu_0 \mu_{ij} H_j + \alpha_{ij} E_j + \beta_{ijk} H_j E_i + \frac{1}{2} \gamma_{ijk} E_j E_k + \dots, \quad (1.3)$$

1.2.2 Different routes to multiferroicity

Unfortunately, the ME effect in single-phase compounds is usually too small to be practically applicable. A breakthrough in terms of the giant magnetoelectric effect was achieved in composite materials; for example, in the simplest case the multilayer structures composed of a ferromagnetic piezomagnetic layer and a ferroelectric piezoelectric layer [7, 28–30]. Other kinds of magnetoelectric composites including co-sintered granular composites and column-structure composites were also developed [31–33]. In the composites, the ME effect is generated as a product property of the magnetostrictive and piezoelectric effects, which is a macroscopic mechanical transfer process. A linear ME polarization is induced by a weak a.c. magnetic field imposed on to a d.c. bias magnetic field. Meanwhile, a magnetoelectric voltage coefficient up to $100 \text{ Vcm}^{-1}\text{Oe}^{-1}$ in the vicinity of electromechanical resonance was reported [7]. A complete introduction to the magnetoelectric effects in composite materials can be found in articles by Fiebig [7] and Nan *et al* [28]. Despite of apparently bad compatibility of magnetism and ferroelectricity, we now know many systems in which these properties coexist. In the following sections we give a brief overview of few of the possible ways to combine magnetism and ferroelectricity in single-phase materials. A detailed overview of classification of multiferroics based on the mechanism underlying the ME phenomena can be found in references [7, 34, 35].

1.2.2.1 Independent system

One of the simplest approach, conceptually, to combine ferroelectricity and magnetism is to synthesize multiferroics with two structural units functioning separately for the ferroelectricity and magnetism. One of the first and well known examples are borates, such as $\text{GdFe}_3(\text{BO}_3)_4$, which contain ferroelectricity active BO_3 groups and magnetic ions Fe^{3+} [36, 37]. In addition to multiferroicity, these materials exhibit interesting optical properties. Boracites, such as $\text{Ni}_3\text{B}_7\text{O}_{13}\text{I}$, are also in this category [38, 39]. Few other to mention in the same category are $\text{Fe}_3\text{B}_7\text{O}_{13}\text{Cl}$ and $\text{Mn}_3\text{B}_7\text{O}_{13}\text{Cl}$. All the above mentioned compounds are non-perovskite compounds. First attempts to prepare perovskite multiferroics were made by Russian scientists. They proposed to mix both transition metal (TM) ion with d electrons and ferroelectrically active TM ions with d^0 configurations at B-sites. The idea was that the magnetic ions and d^0 -shell TM ions separately favor a magnetic order and a ferroelectric order. The typical compound is

$\text{PbFe}_{0.5}\text{Nb}_{0.5}\text{O}_3$ (PFN) in which Nb^{5+} ions are ferroelectrically active and Fe^{3+} ions are magnetic, respectively. The coupling between magnetic and ferroelectric order in this kind of multiferroic is very weak because these two order parameters originate from different kinds of ions, hence the name independent multiferroic materials. In addition to PFN, other multiferroics falling in this category of $\text{AB}_{1-x}\text{B}'_x\text{O}_3$, such as $\text{PbFe}_{0.5}\text{Ta}_{0.5}\text{O}_3$ [40] and $\text{PbFe}_{0.5}\text{W}_{0.5}\text{O}_3$ [41] which also showed weak magnetoelectric coupling.

1.2.2.2 Ferroelectricity induced by lone-pair electrons

In the magnetic perovskite structure oxides and related materials, multiferroism is most commonly achieved by making use of the stereochemical activity of the lone pair on the large (A-site) cation to provide the ferroelectricity, while keeping the small (B-site) cation magnetic. The ions with lone-pair of electrons, such as Bi^{3+} and Pb^{2+} , always locate at A-site in an ABO_3 perovskite structure. This allows TM ion to locate at B-site so that the incompatibility for TM ions to induce magnetism and ferroelectricity is partially avoided. The typical examples are (and the most widely studied) BiFeO_3 and BiMnO_3 where B-site ions contribute to the magnetism and the A-site ions via the lone pair mechanism lead to the ferroelectricity. In these compounds, Bi^{3+} ions with two electrons in a $6s$ orbit (lone pair) shift away from centrosymmetric positions with respect to the surrounding oxygen ions, favoring the ferroelectricity. BiMnO_3 is unique, in which both M and P are reasonably large and is one of the exceptional multiferroic offering both ferroelectric and ferromagnetic orders [42, 43]. BiMnO_3 is another well-known multiferroic material because it is one of the few multiferroics with both ferroelectricity and magnetism above room temperature. BiFeO_3 is well-known because it is one of the few multiferroics with both ferroelectricity and magnetism above room temperature. The ferroelectric Curie point is $T_C \sim 1103$ K and the antiferromagnetic Néel temperature is $T_N \sim 643$ K, while weak ferromagnetism at room temperature can be observed due to a residual moment in a canted spin structure [44, 45]. The high ferroelectric Curie point usually refers to a large polarization since other typical ferroelectrics with such Curie points have a polarization up to about $100 \mu\text{Ccm}^{-2}$. In recent studies on high quality single crystals of BiFeO_3 polarization of about $60 \mu\text{Ccm}^{-2}$ were obtained [46, 47].

In addition to BiMnO_3 and BiFeO_3 several other multiferroics were studied in same category. For example, PbVO_3 in which multiferroism is facilitated with lone-pair ion, Pb^{2+} [48], which is very similar to conventional ferroelectric material, PbTiO_3 .

Another example, Cu_2OSeO_3 , which is another lone pair containing material, exhibits the coexistence of piezoelectricity and ferrimagnetism but unfortunately no spontaneous polarization was measured. It exhibits significant magnetocapacitance effects below ferromagnetic Curie temperature ~ 60 K [49, 50]. This is because Cu_2OSeO_3 is metrically cubic down to 10 K but the ferrimagnetic ordering reduces the symmetry to rhombohedral which excludes the spontaneous ferroelectric lattice distortion. Similar effects were also observed in SeCuO_3 [51].

1.2.2.3 Geometrically driven ferroelectricity in hexagonal manganites

In the ferroelectrics referred in last two sections, the driving force for the ferroelectricity is structural instability towards the polar state associated with electronic pairing. Such ferroelectrics were coined as ‘proper’ ferroelectrics. In contrast to this class of ferroelectrics, in some other ferroelectrics the polarization develops as the by-product of a complex lattice distortion. This class of materials, together with all other ferroelectrics with their polarization originating from by-product of order configurations, were coined as ‘improper’ ferroelectrics. Hexagonal manganites $R\text{MnO}_3$ with R the rare-earth element (Ho–Lu, or Y), fall into the latter category, and are often cited as typical examples that violate the $d^0 - \text{ness}$ rule.

YMnO_3 is one of the first compounds in this class of multiferroics which is a well-known multiferroic system with a ferroelectric Curie temperature $T_C = 950$ K and an antiferromagnetic Néel temperature $T_N = 77$ K. In YMnO_3 paramagnetic phase (centrosymmetric) to ferroelectric phase (non-centrosymmetric) is characterized by buckling of the layered MnO_5 polyhedra accompanied by displacement of the Y ions which lead to net electric polarization. A schematic of crystal structure of YMnO_3 in paraelectric and ferroelectric phases is presented in figure 1.3. We expect a similar behavior in near FE Curie temperature of recently synthesized metastable hexagonal DyMnO_3 . In addition we also observe magnetoelastic effect which further indicates a strong spin-phonon coupling. We present our findings in chapter-6.

From density functional calculations Van Aken *et al* [52] showed that the polarization mechanism is driven entirely by electrostatic and size effects, in contrast to the usual changes in chemical bonding associated with ferroelectric phase transition in perovskite oxides. As neither Y^{3+} nor Mn^{3+} has a lone pair of electrons, lone pair stereochemical activity can not be the driving force for ferroelectricity in YMnO_3 . Only other possible

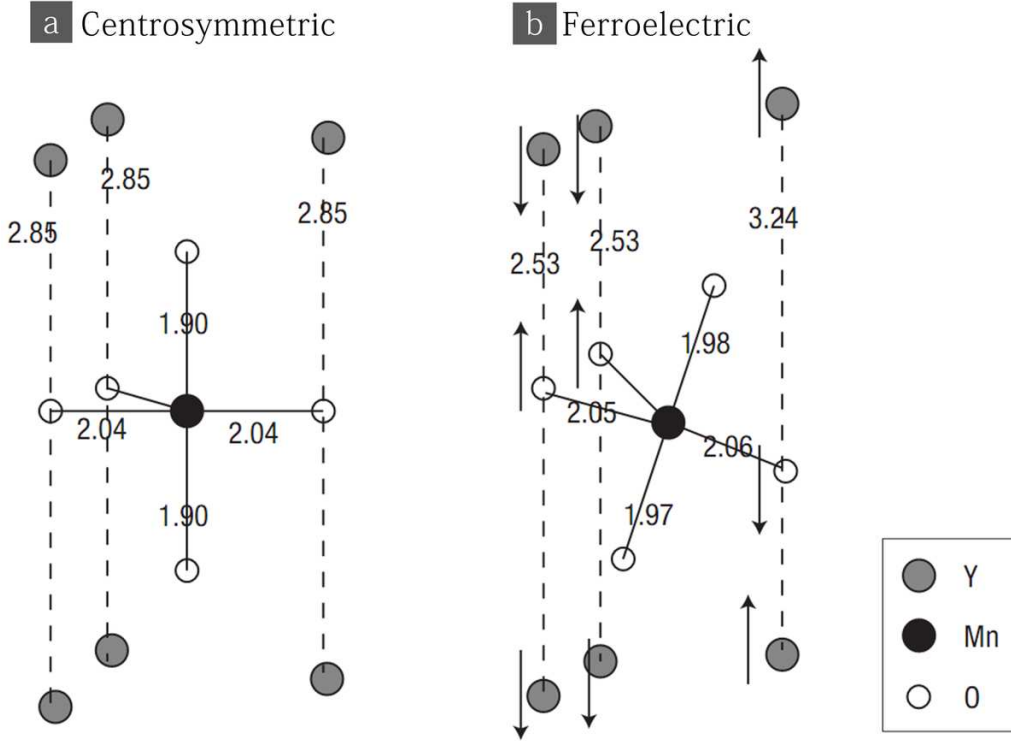


Figure 1.3: Schematic of a MnO_5 polyhedra in (a) Paraelectric and (b) Ferroelectric phases. The number indicate the bond lengths in \AA and the arrows indicate atomic displacements with respect to the centrosymmetric structure. (Taken from [52]).

chemical mechanism is ligand–field hybridization. As one can notice from figure 1.3(b) that Mn ions remain close to the center of their oxygen cages, it is highly unlikely that they re-hybridize with the surrounding oxygen anions during phase transition. Instead, long–range dipole–dipole interactions and oxygen rotations both cooperate to drive the system towards the stable ferroelectric state. Indeed, the Y– O_P (where O_P) off-centre displacements are quite distinct from the small displacements driven by chemical activity found in conventional ferroelectric perovskites, and represent a completely different mechanism for ferroelectric distortion. For $RMnO_3$ such as $HoMnO_3$, in addition to the complex Mn spin structure, usually R^{3+} ions also carry their own spin that is non-collinear with the Mn spins. The FE phase of $HoMnO_3$ appears at the Curie point $T_C = 875$ K and possesses $P6_3cm$ symmetry with polarization $P = 5.6 \mu Ccm^{-2}$ along the hexagonal c -axis [53–56]. One of the most fascinating effects with hexagonal $RMnO_3$ is the magnetic phase control by an electric field, as demonstrated in $HoMnO_3$. Few more candidates in this category are $YbMnO_3$ [57], $InMnO_3$ [58, 59] and $(Lu/Y)CrO_3$ [60–62]. However,

the detailed mechanism of FE in these compounds remains a puzzle. For instance, more recently it was proposed that in YCrO_3 *local non-centrosymmetry* accounts for the small value of polarization observed in spite of the large A-cation off-centering distortion [60, 61]. In chapter 3–4 we present our investigations on one such compound, HoCrO_3 .

1.2.2.4 Ferroelectricity induced by spiral spin-order

In all the above mentioned multiferroics the magnetoelectric coupling is rather weak as the ferroelectricity and magnetism basically originate from different ions or subsystems. There are few exceptional compounds in which ferroelectricity induced directly by the spin order, meaning that an intrinsic magnetoelectric coupling occurs between the ferroelectric and magnetic order parameters. Two mechanisms are being considered to understand such a magnetoelectric effect:

1. *Symmetry consideration*

The inter-exclusion between ferroelectricity and magnetism originates not only from the *d⁰-ness* rule, but also from the symmetry restriction of two types of order. Ferroelectricity needs the broken spatial-inversion symmetry and usually invariant time reverse symmetry. In contrast, the broken time-reversal symmetry is the prerequisite for magnetism. Consequently, a multiferroic system requires the simultaneous breaking of the spatial-inversion and time-reversal symmetries. The ME coupling between polarization and magnetization is derived from this general symmetry argument [25, 63, 64]. In this class of multiferroics, in general, two or more competing magnetic interactions can induce the spin frustration and the spiral (helical) spin symmetries simultaneously, thus establishing the ferroelectric order.

2. *Microscopic mechanism*

In addition to the symmetry argument mentioned above, a microscopic mechanism responsible for ferroelectricity in magnetic spiral systems is required. Till date it remains unclear whether the spiral spin order (spiral SDW) is a prerequisite for generating ferroelectricity. It was predicted that the acentric dislocated SDW may also drive a ferroelectric polarization [64]. Currently, three theories on microscopic aspect of magnetoelectric coupling in magnetic spiral multiferroics have been proposed: the inverse Dzyaloshinskii-Moriya (DM) model [65–67], the spin current model (KNB model) [68], and the electric current cancelation model [68].

Considerable research has been carried out recently on TbMnO_3 and related manganites where spin frustration causes sinusoidal antiferromagnetic ordering. Large magnetocapacitance and ME effects are observed in TbMnO_3 due to the switching of the electric domains by the magnetic field [69]. DyMnO_3 shows similar properties [70]. Wolframite MnWO_4 is another most studied compound in this class of materials [71–74]. This is the first example of the ferroelectric polarization flop induced by magnetic fields in transition-metal oxide systems without rare-earth $4f$ moments. In chapter–7, we present our studies on the effect of doping on the frustrated spin structure of MnWO_4 .

1.3 Aims of research

The general motivation behind the research in this thesis is to understand the crystal and magnetic structures which in turn give a clearer idea for magnetoelectric coupling in several multiferroics. In magneto ferroelectrics there are still aspects of the mechanisms giving rise to ferroelectricity that are not fully understood. In the present work we study the structural and magnetic properties of few magnetoelectric multiferroics.

Chapter 2

THEORETICAL BACKGROUND AND EXPERIMENTAL METHODS

2.1 Synthesis of polycrystalline powders and growth of single crystals

2.1.1 Solid state reaction route

All the samples used in the present work were prepared by conventional solid state synthesis technique. This technique involve heating (not melting !) mixtures of two or more solids to form a desired solid phase product. Unlike gas phase and solution reactions, the limiting factor in solid-solid reactions is usually diffusion. The diffusion process can be described by *Fick's laws* which can be used to solve for the diffusion coefficient, D . To obtain good rates of reaction the diffusion coefficient has to be larger than 10^{-12} cm²/s. The diffusion coefficient increases rapidly with temperature as the melting point is approached. This concept leads to Tamman's rule [75]: *Extensive reaction will not occur until the temperature reaches at least $2/3^d$ of the melting point of one or more of the reactants.*

The rates of solid state reactions are controlled by two factors:

- (1) The area of contact between reaction solids: To maximize this one should use the starting reagents with large surface area, which can be achieved by fine milling of starting reagents (precursors).
- (2) The rate of diffusion: This can be increased by increasing the temperature.

Steps in conventional solid state synthesis:

1. Selection of appropriate starting materials: Fine grain powders should be chosen to maximize surface area. In most of the cases well defined composition is also very crucial. In the present work we used high purity precursors in their oxide forms, for example, to prepare HoCrO₃ (Chapter 3) we used Ho₂O₃(99.99%) and Cr₂O₃(99.999%) as precursors, the values in the brackets indicate the purity.
2. Weigh out and mix starting materials together: Starting materials in appropriate stoichiometric ratio should be weighed very precisely on an electronic balance. Then they are mixed in an agate mortar and pestle or in a ball mill (for large preparations). An organic solvent such as isopropanol can be used optionally to facilitate better mixing

of precursors.

3. Pelletize: Pelletizing the mixed precursors can enhance the intimate contact of reactants and it also minimizes contact with the crucible. An organic binder can be used for a better binding. For some of the preparations we used 10% solution of (by weight, in water) polyvinyl alcohol with chemical formula $(C_2H_4O)_n$.

4. Select sample container: For the selection of containers one should consider the reactivity of the sample container with precursors used for the synthesis, strength, cost and durability. One can choose from a variety of sample containers made of, (a) ceramic refractories such as Al_2O_3 or ZrO_2/Y_2O_3 , (b) Precious metals such as Pt, Au, Ag and Ir and (c) SiO_2 , Mo, W *etc* (mostly as sealed tubes). We used Al_2O_3 and Pt crucibles for the sample preparation during the course of present work.

5. Heat treatment: Factors influencing the choice of temperature include Tamman's rule and potential for volatilization. For example in the case of $HoCrO_3$ the precursors Ho_2O_3 and Cr_2O_3 are having melting temperatures 2360 °C and 2435 °C, respectively. Applying Tamman's rule, precursors should be heated to 1575 °C for a substantial reaction to occur. Keeping in mind the volatile nature of Cr_2O_3 we heated the precursors to only 1200 °C. Though this procedure took longer time for the complete reaction, we could prepare good quality stoichiometric $HoCrO_3$. Precursors were also preheated at 1000 °C before the main sintering process, to prevent volatilization. The atmosphere during the reaction is also critical, one should consider a variety of gaseous atmospheres (air, O_2 , H_2/Ar *etc*) based on whether oxidizing conditions or reduction conditions are required for the preparation of a particular compound.

6. Verification of phase purity (powder diffraction).

7. Improvement: if reaction is incomplete the steps from 4 were repeated until desired phase product is obtained.

2.1.2 Crystal growth by optical floating zone technique

Crystal growth using optical floating zone (OFZ) technique has been extensively used to grow a variety of bulk crystals, particularly single crystals of metal oxides with very high melting temperatures [76, 77]. The group of materials for which OFZ growth technique has been mostly used are those termed as functional oxides, which find applications in lasers, electronic and optical devices, catalysts, solid oxide fuel cells, memory and

magnetic devices and as multiferroic and superconducting materials. The basic idea of OFZ technique is that either ellipsoidal or parabolic mirror(s) (or a combination of both) is used to focus the light from halogen or xenon lamp(s) onto a vertically held rod shaped sample to produce a molten zone, which is then moved along the sample in order to grow a single crystal. The greatest advantage of the OFZ technique is the fact that no crucible is necessary and that both congruently and incongruently melting materials can be grown.

The growth of single crystals by OFZ can be broadly classified in to two stages.

1. Preparation of polycrystalline feed rod: This process starts with the synthesis of the compound, for instance as described in the previous section. Then the polycrystalline material is filled tightly in to a latex tube homogenously with out any voids. Then it was evacuated, sealed (tied) and pressed in a hydrostatic press. Usually the tube is pressed at approximately 2000 kg/cm^2 . We used few drops of polyvinyl alcohol (PVA) binder to avoid breaking of rods. After pressing the rod, the latex tube is cut and removed and the sample rod is heated slowly up to $700 \text{ }^\circ\text{C}$ to remove all the binder and then sintered at $1400 \text{ }^\circ\text{C}$ for about 10 hours to achieve higher density. The final product will be a rod of about $8 - 10 \text{ cm}$ in length with a diameter of $\sim 6 - 8 \text{ mm}$. A small hole of 1 mm was drilled along the diameter at one end of the rod. A thin platinum wire is thread through the hole to make a loop. Another short sample rod is prepared, the same way as feed rod, which can be used as seed for the growth in case there is no single crystal available for the growth to start with.

2. Growth of single crystal: The OFZ furnace used for the growth is shown in figure 2.1(a) (model FZ-T-10000-H-VI-VPO from Crystal System Inc., Japan). It is equipped with four halogen lamps which can deliver a total power of 4kW , situated inside the growth chamber which is shown in the figure 2.1(b) (lamps can be changed to attain powers up to 6 kW). A schematic diagram of the growth chamber is presented in figure 2.1(c), where only two lamps are shown for simplicity. The lamps are situated at one of the foci of the hemi-ellipsoidal mirrors. The feed rod is hung freely from the upper shaft and the seed rod which is tied to a ceramic tube is fixed to the lower shaft in such a way that their tips meet at the second foci of the hemi-ellipsoidal mirrors. Both rods are carefully aligned to lie coaxially at the center of one of the foci of the hemi-ellipsoidal mirrors. A quartz tube is fitted around the seed and feed rods, which enables one to maintain a desired atmosphere by passing a regulated gas (Air, Ar, N_2 etc).

The growth process is started by melting the tips of polycrystalline rods touching them carefully by slowly bringing them closer and establishing a molten zone called *floating zone* between the bottom of the feed rod and top of the seed rod. Once the zone is created it is moved upwards (either by moving the mirrors up or by moving the seed and feed rods simultaneously down). During this process the melt crystallizes on the seed rod by melting the feed forming crystallites which eventually results in a single grain (single crystal). The growth chamber as seen in the CCTV during a growth and a schematic view of seed and feed rods and different stages in the (single) crystal formation are presented in figure 2.1(d). In this figure it can be noted that after touching the feed and seed rods the diameter of the crystallized part is decreased drastically over few millimeter to centimeter length (by carefully tailoring the growth-rate, power of the lamp, seed-feed rotation rates *etc*). This is done to achieve a selective growth of single grain by getting rid of multiple grains which were seeded in the early stages after touching. This technique is called *necking*. It increases the chances of obtaining a single crystal drastically. During the growth the feed and seed rod are rotated in apposite directions. The rate of rotation is important as it is responsible for a pattern of forced convection flows within the zone and – as a result – mixing of the material, for the shape of the crystallization front (solid–liquid interface), and for the defects resulting from it [77]. The crystal growth rate (the rate at which the zone is moved), the rotation rate and the gas flow rate all are optimized experimentally for each material. As grown hexagonal DyMnO₃ single crystal is shown in figure 2.1(e).

2.2 Powder X-ray diffraction

2.2.1 Theoretical background

A precise knowledge of the crystal structure is essential for interpretation of the physical properties. Powder diffraction with x-rays has played a vital role in the structural characterization of materials over the last four decades. We can as well say that powder diffraction techniques have had an impact in most of the major developments in the field of functional materials during recent years: high temperature superconductors, fullerenes, giant magnetoresistance (GMR) materials, multiferroics are a few to mention. Laboratory powder X-ray diffraction (PXRD) is the most widely used X-ray diffraction technique for

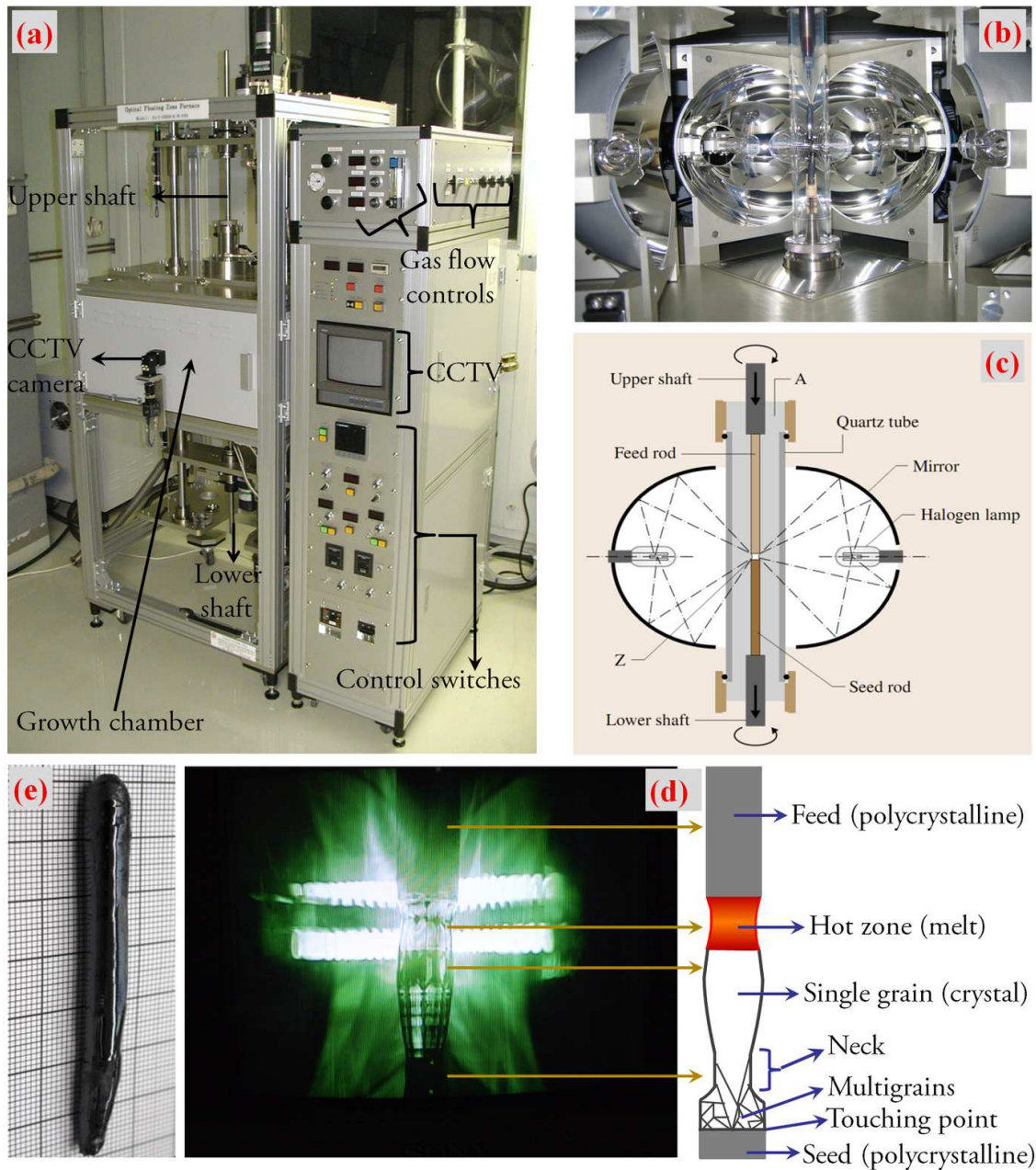


Figure 2.1: (a) The optical floating zone furnace FZ-T-10000-H-VI-VPO, (b) inside view of the growth chamber: at the center two rods can be seen fixed to upper and lower shaft and fixed with a quartz tube. Four halogen lamps and hemi-ellipsoidal mirrors are also seen (two on the back, one on the left and other on the right side). Note that the front mirrors are moved apart for a better view. (c) schematic diagram of the growth chamber (A-atmosphere, Z-floating zone), (d) the growth chamber as seen in CCTV during a growth and a schematic of the growth process and (e) as grown hexagonal DyMnO_3 single crystal.

characterizing materials. As the name suggests, the sample will be taken in the form of powder, consisting of fine grains of single crystals called crystallites. The term *powder* means that the crystallites are randomly oriented in the sample. The diffraction process is described by well known *Bragg's law*, given by:

$$2d_{hkl} \sin \theta = \lambda \quad (2.1)$$

Where d_{hkl} is the distance between the parallel lattice planes with Miller indices (hkl) , θ is the angle between the lattice planes and X-rays (neutrons) of wavelength λ and n is an integer number. From Bragg's law, for a fixed wavelength λ , for all θ and d values satisfying the above equation, *i.e.*, when the product $2d \sin \theta$ is equal to an integral multiple of the incident wavelength λ , an intensity maximum occurs due to constructive interference of the scattered beam. A pictorial illustration of Bragg's law is presented in figure 2.2. Thus when the 2-D diffraction pattern is recorded, it shows concentric rings (Debye–Scherrer lines) of scattered intensities corresponding to various d_{hkl} -spacings in the crystal lattice. The positions and intensities of the peaks are used to identify the underlying structure of the material.

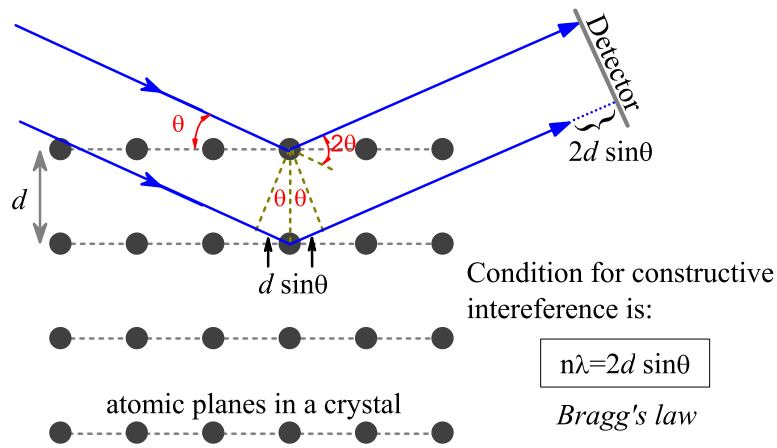


Figure 2.2: Illustration of Bragg's law

To calculate the line intensities in a powder pattern let us consider a diffracting material of volume dV small enough that the absorption can be neglected, composed of a very large number of randomly oriented tiny crystals. A Debye–Scherrer line of indices hkl is produced by reflection on all the crystal planes having the same spacing d_{hkl} . The number of the lattice planes which are equivalent (with equal d -spacing) due to crystal

symmetry is called the multiplicity factor n and depends on the nature of the lattice and on the indices hkl . If a crystal gives rise to a Debye–Scherrer line with indices hkl , the normal to the lattice plane (hkl) must make an angle $(\pi/2) - \alpha$ with the direction (\mathbf{S}_0) of the incident rays, the angle α being within the region of reflection, or very close to the Bragg angle θ . The probability that the normal is within $(\pi/2) - \alpha$ and $(\pi/2) - \alpha + d\alpha$ of \mathbf{S}_0 is $\cos \alpha d\alpha/2$. Since there are n equivalent normal directions, the total volume of the crystal having a normal to a plane hkl in this direction is $(ndV/2) \cos \alpha d\alpha$ or, since α is very close to θ , $(ndV/2) \cos \theta d\alpha$. If $I(\alpha)$ is the energy reflected per second by the plane (hkl) for the angle of incidence α , the total energy diffracted per second by the volume dV in the ring hkl is

$$\Phi = \frac{ndV}{2} \cos \theta \int I(\alpha) d\alpha \quad (2.2)$$

This is the energy which is reflected by the single crystal of volume $ndV/2 \cos \theta$ crossing the reflection position at an angular velocity $\omega = 1$. The expression (2.2) can be rewritten with Q_{hkl} , the reflecting power per unit volume for the hkl reflection, thus

$$\Phi = \frac{ndV}{2} \cos \theta Q_{hkl} I_0 \quad (2.3)$$

For an ideal powder without texture the energy Φ is distributed uniformly over all the Debye-Scherrer ring. At a distance r from the sample, the length of this ring is $2\pi r \sin 2\theta$ and the diffracted energy per second and per unit length of the ring is therefore

$$I = \frac{\Phi}{2\pi r \sin 2\theta} = \frac{I_0 Q_{hkl} ndV}{8\pi r \sin \theta}. \quad (2.4)$$

Where I is the power diffracted per unit length of a Debye-Scherrer line at a distance r from the sample, I_0 is the intensity per unit area of the incident beam, θ is the Bragg angle ($\lambda = 2d_{hkl} \sin \theta$) and the value of Q_{hkl} , the reflecting power per unit volume for the hkl reflection from a small crystal is given by [78]

$$Q_{hkl} = r_e^2 \frac{\lambda^3}{\sin 2\theta} \frac{1 + \cos^2 2\theta}{2} \frac{1}{V_c^2} F_{hkl}^2. \quad (2.5)$$

Where r_e is electron radius, $F_{hkl} = \sum_{i=1}^n f_i \exp[-2\pi i (hx_i + ky_i + lz_i)]$ is the structure factor for the lattice plane (hkl) (in case of cubic crystal) with scattering factor f_i for the i^{th} atom and V_c is unit cell volume of the crystal.

The factor $\lambda^3/\sin 2\theta$ comes from the integration of the intensity over the sharp

peak in the region of a node for given experimental conditions. It is called *Lorentz factor*.

The term $(1 + \cos^2 2\theta)/2$ is the polarization factor. This is valid only if incident beam is unpolarized. For a beam of unspecified polarization the calculation is made by decomposing the beam into two separate beams whose electric vectors are respectively perpendicular and parallel to the plane of the incident and scattered rays, and in the proportions k_{\parallel} and k_{\perp} . This occurs when a crystal monochromator is used for the incident beam. If α is the reflection angle at the monochromator crystal, the two components of the reflected ray which are polarized in the directions parallel and perpendicular to the plane of incidence vary as 1 and $\cos^2 2\alpha$, and their relative intensities are

$$k_{\parallel} = \frac{1}{1 + \cos^2 2\alpha}, \quad k_{\perp} = \frac{\cos^2 2\alpha}{1 + \cos^2 2\alpha}.$$

This modifies equation (2.5) as follows, according to *Thomson formula* [78],

$$Q_{hkl} = r_e^2 F_{hkl}^2 \frac{\lambda^3}{V_e^2 \sin 2\theta} \frac{1 + \cos^2 2\alpha \cos^2 2\theta}{1 + \cos^2 2\alpha}. \quad (2.6)$$

Further more, it should be noted that equation (2.5) was deduced by neglecting thermal agitation. But the atoms vibrates about their theoretical mean positions with an amplitude which increases with temperature. One of the effects of thermal agitation is to reduce the intensity of the selective reflections. We must therefore multiply the reflecting power as given by equation (2.5) by a coefficient D which is less than unity; this is called the *Debye* or *temperature factor*. The value of D decreases with temperature and with $s = (2 \sin \theta / \lambda)$. The effect can be important for larger values of θ , even at room temperature.

Now substituting the value of Q_{hkl} from equation (2.6) in equation (2.4) D we can write the power diffracted per unit length of Debye-Scherrer line at r as:

$$I = I_0 r_e^2 \frac{1 + \cos^2 2\theta}{2} \frac{1}{16\pi r \sin^2 \theta \cos \theta} \lambda^3 F_{hkl}^2 n \frac{1}{V_e^2} D dV. \quad (2.7)$$

The equation (2.7) is valid only if the crystallites in the powder sample are small so that there are no extinction phenomena and if their orientations are perfectly isotropic. If the crystallites are large enough, absorption becomes significant and one must integrate over the volume, taking the absorption into account. The intensity is then given by equation (2.7), where dV is replaced by the *effective volume*. In a transmission camera

with a thin sample of thickness a , the effective volume is

$$\frac{S}{\mu\rho \left[1 - \frac{\cos\alpha}{\cos(2\theta-\alpha)}\right]} \left[\exp\left\{\frac{-\mu\rho a}{\cos(2\theta-\alpha)}\right\} - \exp\left\{\frac{-\mu\rho a}{\cos\alpha}\right\} \right], \quad (2.8)$$

Where S is the cross section of the incident beam, μ is absorption coefficient, ρ is the density of the material and α is the incident angle. This applies to the case where a monochromator is used [79]. When $\alpha = \theta$ the above equation simplifies to

$$\frac{Sa}{\cos\theta} \exp\left(-\frac{\mu\rho a}{\cos\theta}\right). \quad (2.9)$$

The optimum thickness of the sample is $a_m = \cos\theta/\mu\rho$ which reduces the incident intensity by a factor of $1/e$, or about $1/3$.

2.2.2 Experimental technique

Powder diffraction data can be collected using either reflection or transmission geometry. All the PXRD patterns described in this thesis were collected in transmission geometry using a Huber diffractometer operating with $\text{Cu-}K_\alpha$ radiation and equipped with a G670 Guinier camera with integrated imaging plate detector. In contrast to the Guinier cameras with old wet film technique which took measurement times from hours to days, with the new image plate detection method the desired data can be acquired within few minutes. Another advantage of this new diffractometer is the amount of sample required for the measurement of only a few milligrams. A schematic view of powder diffractometer setup with Guinier geometry is presented in figure 2.3.

Finely powdered samples were spread on a thin polythene film (commercially available from Huber) by mixing with a small amount of isopropanol to increase adhesion over an area of about 10×20 mm. Isopropanol also helps to spread the sample powder homogeneously. During the exposure the sample oscillates horizontally in its plane at about 1 Hz and an amplitude of 10 mm to obtain better powder-averaged-data by compensating intensity variations caused by differently oriented crystallites in the powder sample. In addition to imaging plate, the housing of the G670 camera contains the laser recording unit with photomultiplier and pre-amplifier as well as the halogen deleting lamp. After the intensity data is read out from a laser recording unit which outputs digitized 2θ vs. Intensity data. Before the *next* measurement, intensity data on the detector is erased with halogen deleting lamp. A typical 2D diffraction pattern as seen on the detector with

Debye Scherrer line and powder diffraction pattern of the integrated intensities of Debye Scherrer lines is presented in figure 2.4. The profiles of the PXRD data were analyzed by Rietveld method (Appendix B) [80] using the *FullProf* software [81].

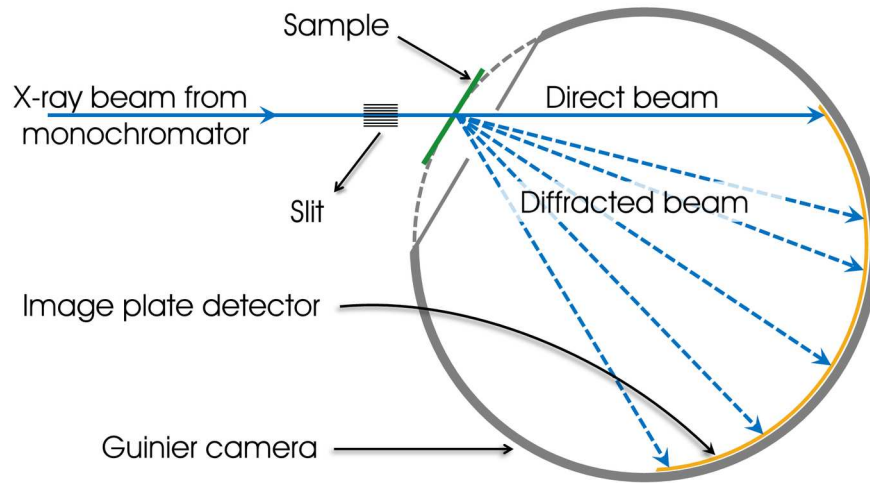


Figure 2.3: A schematic view of the powder diffractometer set up with Guinier geometry

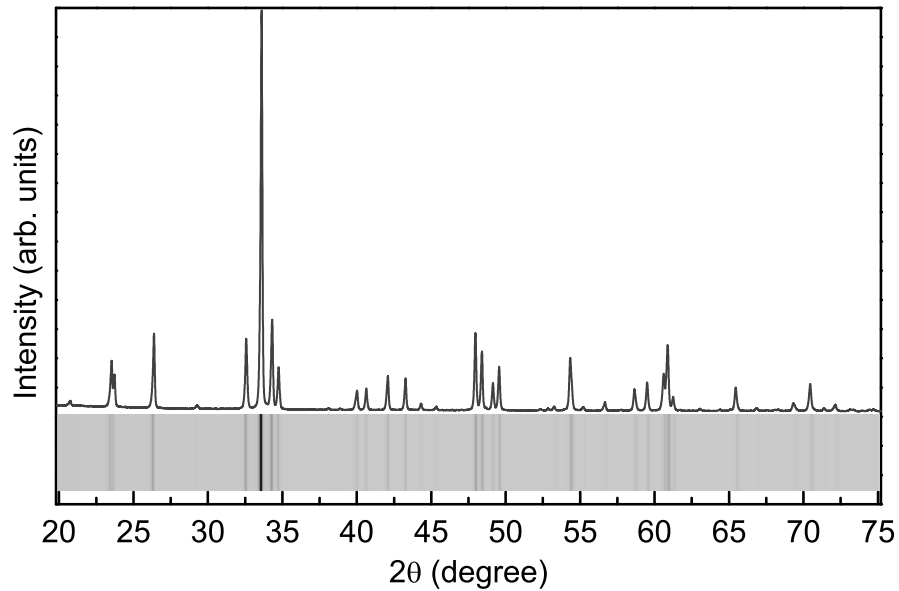


Figure 2.4: A typical powder diffraction pattern (continuous line) obtained by integrating the intensities of Debye-Scherrer lines (bottom strip) along 2θ .

2.3 Neutron scattering

2.3.1 Theoretical background

The fundamental scattering processes underpinning neutron diffraction are different from those in X-ray diffraction and so whilst the two techniques are in many ways analogous, neutron and X-ray diffraction patterns obtained from a given sample differ substantially. In many ways, these differences serve to make the two techniques complementary; however, neutron powder diffraction has many advantages and can provide many types of information not readily obtained in other ways. X-rays interact primarily with electrons. On the other hand, neutrons are non charged subatomic particles having a mass (m) of 1.0087 atomic mass units (1.675×10^{-27} kg), spin 1/2 and a magnetic moment (μ_n) of -1.9132 nuclear magnetons. These properties of the neutrons give rise to two principal modes of interaction which are different from those of X-rays.

Since neutrons have no charge, their nuclear interaction with matter is short ranged. As a result of this small interaction probability, neutrons can penetrate deep into condensed matter. Moreover, the interaction between the neutron and atomic nuclei involve complex nuclear interactions between the nuclear spins and magnetic moments. For this reason, there is no general trend throughout the periodic table of an atom's ability to scatter neutrons. This is quite unlike the X-ray atomic scattering factor which increases with atomic number. In addition, nuclear dependence of neutron scattering allows isotopes of the same element to have considerably different scattering lengths for neutrons, so that isotopic substitution can be employed.

The second mode of interaction is the magnetic dipole interaction between the magnetic moments associated with unpaired electron spins in magnetic samples and the nuclear magnetic moment of the neutron. As a result spin-up and spin-down electrons 'look' different to neutrons. Hence, when a sample becomes magnetic, new peaks can appear in the neutron diffraction pattern. The position and amplitude of the magnetic Bragg peaks can be used as a measure of the direction and strength of the magnetic moments, hence neutron scattering can be used to determine the arrangement of the atomic magnetic moments in a magnetically ordered system. The magnetic neutron scattering technique is the most direct method available for determining the details of the magnetic structure of a sample.

Thermal neutrons for condensed matter research are usually obtained by slowing down

energetic neutrons by means of inelastic collisions in a moderating material containing light atoms. Most of the slow neutrons thus produced will have kinetic energies of the order of $k_B T$ where T is the moderator temperature, typically about 300 K for thermal neutrons, and k_B is Boltzmann's constant. If one considers the wave nature of the neutron, it can be described by a wavelength λ given by

$$\lambda = \frac{h}{\sqrt{2mk_B T}}. \quad (2.10)$$

where h is Planck's constant and m is the mass of the neutron. For the equation (2.10), temperature value of $T \approx 300$ K corresponds to the wavelength $\lambda \approx 2 \text{ \AA}$ (2×10^{-8} cm), a distance comparable to the mean atomic separation in a solid or dense fluid. So called *thermal neutrons* are therefore ideally suited to resolve the atomic structure as well as the magnetic structure of condensed matter.

2.3.2 Scattering formulae

The neutron scattering intensity from magnetic materials is a superposition of both nuclear and magnetic scattering. In order to be able to separate magnetic scattering from nuclear scattering and to extract information about the magnetic structure and spin dynamics, it is important to understand the basic principles of both processes. The theory of neutron scattering has been discussed in detail in several books [82–85]. In the present section we summarize some of the more useful formulae for interpreting experimental measurements on crystalline solids.

Consider a monoenergetic neutron beam described by wave vector \mathbf{k}_i and flux $\Phi(k_i)$, incident on a sample (scatterer). The rate at which they are scattered by a sample is given by the product $\Phi(k_i)\sigma$, where σ is the scattering cross section. In a neutron scattering experiment, we are interested in the rate at which neutrons are scattered into a given solid angle element $d\Omega_f$, in the direction of the wave vector \mathbf{k}_f , with a final energy between E_f and $E_f + dE_f$. This rate is given by the product of $\Phi(k_i)$ and the double-differential cross section, $d^2\sigma/d\Omega_f dE_f$. It is conventional to express the double differential scattering cross section as a sum of coherent and incoherent parts:

$$\frac{d^2\sigma}{d\Omega_f dE_f} = \left. \frac{d^2\sigma}{d\Omega_f dE_f} \right|_{coh} + \left. \frac{d^2\sigma}{d\Omega_f dE_f} \right|_{inc} \quad (2.11)$$

The coherent part provides information about the cooperative effects among different atoms, such as elastic Bragg scattering or inelastic scattering by phonons or magnons and the incoherent part is proportional to the time correlation of an atom with itself and provides information about individual particle motion, such as diffusion.

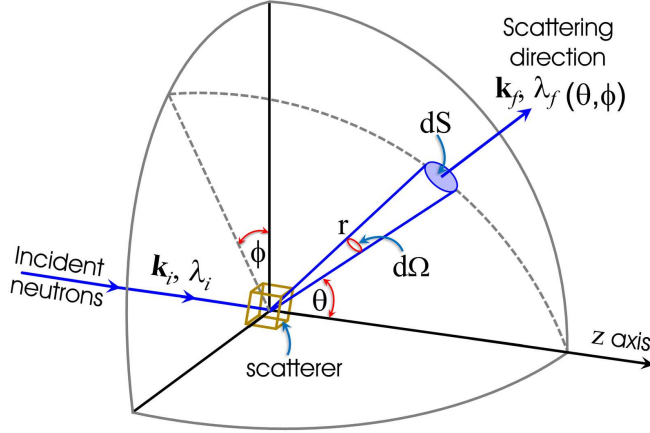


Figure 2.5: Geometry for scattering experiment

2.3.2.1 Fermi's Golden Rule and Born approximation

A neutron acts as a very weak perturbation of the scattering system. When a neutron scatters, it can cause a transition of the sample from one quantum state to another, but it does not modify the nature of the states themselves. As a consequence, the differential scattering cross section can be obtained from Fermi's Golden Rule. Let V represent the interaction operator for the neutron with the sample, then, if the initial and final states are labeled by quantum number λ_i and λ_f , the differential cross section is

$$\left. \frac{d^2\sigma}{d\Omega_f dE_f} \right|_{\lambda_i \rightarrow \lambda_f} = \frac{k_f}{k_i} \left(\frac{m_n}{2\pi\hbar^2} \right)^2 |\langle \mathbf{k}_f \lambda_f | V | \mathbf{k}_i \lambda_i \rangle|^2 \delta(\hbar\omega + E_i - E_f). \quad (2.12)$$

It should be noted that, in the derivation of equation (2.12) the spin states of sample and neutrons are not considered. Because the effective interaction is weak, the interaction matrix element can be evaluated using the Born approximation, treating the incident and outgoing neutrons as plane waves:

$$\langle \mathbf{k}_f \lambda_f | V | \mathbf{k}_i \lambda_i \rangle = V(\mathbf{Q}) \left\langle \lambda_f \left| \sum_l e^{i\mathbf{Q} \cdot \mathbf{r}_l} \right| \lambda_i \right\rangle, \quad (2.13)$$

where scattering $\mathbf{Q} = \mathbf{k}_f - \mathbf{k}_i$ is the scattering vector, \mathbf{r}_l are the coordinates of the scattering centers (assumed here to be identical) and

$$V(\mathbf{Q}) = \int d\mathbf{r} V(\mathbf{r}) e^{i\mathbf{Q}\cdot\mathbf{r}}. \quad (2.14)$$

For nuclear scattering, the nuclear potential is essentially a delta function in \mathbf{r} , so

$$V(\mathbf{Q}) = \frac{2\pi\hbar^2}{m_n} b, \quad (2.15)$$

where b is the nuclear scattering length.

In a scattering experiment, one generally averages over initial states and sums over all final states. If $P(\lambda_i)$ is the statistical weight factor for initial state $|\lambda_i\rangle$, then

$$\frac{d^2\sigma}{d\Omega_f dE_f} = \frac{k_f}{k_i} \sum_{\lambda_i, \lambda_f} P(\lambda_i) \left| \left\langle \lambda_f \left| \sum_l e^{i\mathbf{Q}\cdot\mathbf{r}_l} \right| \lambda_i \right\rangle \right|^2 \delta(\hbar\omega + E_i - E_f). \quad (2.16)$$

By assuming scattering from a sample with only one type of atom and one isotope with scattering length b , Van Hove [86] showed that the equation (2.16) can also be expressed as,

$$\frac{d^2\sigma}{d\Omega_f dE_f} = N \frac{k_f}{k_i} b^2 S(\mathbf{Q}, \omega), \quad (2.17)$$

where

$$S(\mathbf{Q}, \omega) = \frac{1}{2\pi\hbar N} \sum_{ll'} \int_{-\infty}^{\infty} dt \langle e^{-i\mathbf{Q}\cdot\mathbf{r}_{l'}(0)} e^{i\mathbf{Q}\cdot\mathbf{r}_{l'}(t)} \rangle e^{-i\omega t}, \quad (2.18)$$

N is the number of nuclei, t is time, the angle brackets $\langle \dots \rangle$, denote the average over initial states. The scattering function depends on the momentum and energy transferred from neutron to the sample, and not on absolute values of \mathbf{k}_i and \mathbf{k}_f . It contains information on both the positions and motions of the atoms comprising the sample. The goal of most neutron scattering experiments is to measure $S(\mathbf{Q}, \omega)$ and thereby determine the microscopic properties of the system under investigation.

2.3.2.2 Coherent vs. incoherent scattering

Consider a monatomic sample containing isotopic nuclei with different scattering lengths. The isotopes of the same element have different scattering lengths. Furthermore, for an isotope with a nuclear spin, the scattering length varies depending on whether the neutron and nuclear spins are parallel or antiparallel. Let us suppose that r th distinct

isotope or nuclear spin state has scattering length b_r and occurs with frequency c_r . If there are no correlations between nuclear positions and scattering length, then scattering which depends on the relative positions of the atoms will depend only on the average (or coherent) scattering length, given by,

$$\bar{b} = \sum_r c_r b_r. \quad (2.19)$$

The average coherent cross section per atom is then

$$\sigma_{coh} = 4\pi(\bar{b})^2. \quad (2.20)$$

The random fluctuations in scattering lengths of different sites will not contribute to collective scattering, but only to incoherent scattering. The total scattering cross section is given by,

$$\sigma_{scat} = 4\pi \sum_r c_r b_r^2 = 4\pi\overline{b^2}, \quad (2.21)$$

so, using $\sigma_{inc} = \sigma_{scat} - \sigma_{coh}$, the incoherent cross section per atom is given by

$$\sigma_{scat} = 4\pi(\overline{b^2} - \bar{b}^2) = 4\pi\overline{(b - \bar{b})^2}. \quad (2.22)$$

Most elements have significant coherent cross sections, but there are few examples, such as hydrogen and vanadium, for which the incoherent scattering is large and dominant. The incoherent cross section is zero only for single isotopes with zero nuclear spin.

2.3.2.3 Coherent nuclear scattering

The differential cross section associated with only coherent scattering can be written as,

$$\left. \frac{d^2\sigma}{d\Omega_f dE_f} \right|_{coh} = N \frac{k_f}{k_i} \frac{\sigma_{coh}}{4\pi} S(\mathbf{Q}, \omega). \quad (2.23)$$

The above formula applies when the sample consists of a single element. More generally, one must include the site-dependent scattering lengths in the scattering function $S(\mathbf{Q}, \omega)$. The scattering function was expressed in a more plausible way by Van Hove [86] using the definition of the atomic density operator:

$$\rho_{\mathbf{Q}}(t) = \sum_l e^{i\mathbf{Q}\cdot\mathbf{r}_l}. \quad (2.24)$$

Using the above expression we can rewrite equation (2.18) as

$$S(\mathbf{Q}, \omega) = \frac{1}{2\pi\hbar N} \int_{-\infty}^{\infty} dt e^{-i\omega t} \langle \rho_{\mathbf{Q}}(0) - \rho_{\mathbf{Q}}(t) \rangle. \quad (2.25)$$

It is clear from the above equation that the scattering function is the Fourier transform of the time-dependent pair-correlation function.

2.3.2.4 Elastic nuclear scattering (Bragg diffraction)

For coherent, elastic nuclear scattering, we consider the time average of the density operator, so that

$$S(\mathbf{Q}, \omega) = \delta(\hbar\omega) \frac{1}{N} \left\langle \sum_{ij} e^{i\mathbf{Q} \cdot (\mathbf{r}_i - \mathbf{r}_j)} \right\rangle. \quad (2.26)$$

In case of an infinite Bravais lattice, this becomes

$$S(\mathbf{Q}, \omega) = \delta(\hbar\omega) \frac{(2\pi)^3}{v_0} \sum_{\mathbf{G}} \delta(\mathbf{Q} - \mathbf{G}). \quad (2.27)$$

where v_0 is the unit-cell volume and the vector \mathbf{G} are reciprocal-lattice vectors. The coherent, elastic cross section is then

$$\left. \frac{d\sigma}{d\Omega} \right|_{coh}^{el} = N \frac{(2\pi)^3}{v_0} (\bar{b})^2 \sum_{\mathbf{G}} \delta(\mathbf{Q} - \mathbf{G}). \quad (2.28)$$

The above equation describes the scattering from a perfectly rigid lattice. In reality, the fluctuations of the atoms about their equilibrium positions cause some reduction of the Bragg intensities. Let \mathbf{u} be the instantaneous displacement of an atom from its mean position \mathbf{r} . Averaging of the phase factor $\exp(-i\mathbf{Q} \cdot \mathbf{r})$ in equation (2.26) results in an extra factor in equation (2.28) equal to $\exp(-2W)$, known as the *Debye-Waller factor*, where for small displacements,

$$W = \frac{1}{2} \langle (\mathbf{Q} \cdot \mathbf{u})^2 \rangle. \quad (2.29)$$

Since there are three degrees of freedom for the atomic displacement in a crystal (along three crystallographic directions) for a cubic crystal

$$\langle u_x^2 \rangle = \langle u_y^2 \rangle = \langle u_z^2 \rangle = \frac{1}{3} \langle u^2 \rangle, \quad (2.30)$$

so that

$$W = \frac{1}{6} Q^2 \langle u^2 \rangle. \quad (2.31)$$

The above equation (2.31) can be expressed in more convenient notation in terms of scattering angle and incident wavelength as

$$W = B \sin^2 \theta / \lambda, \quad (2.32)$$

with B typically assumed to be isotropic. It follows that

$$B = \frac{8\pi^2}{3} \langle u^2 \rangle. \quad (2.33)$$

So far our calculations were limited to the case of Bravais lattice. Now, let us consider a lattice with more than one atom per unit cell. If the j th atom within the unit cell occupies the position \mathbf{d}_j , then the coherent elastic differential cross section generalized to

$$\left. \frac{d\sigma}{d\Omega} \right|_{coh}^{el} = N \frac{(2\pi)^3}{v_0} \sum_{\mathbf{G}} \delta(\mathbf{Q} - \mathbf{G}) |F_N(\mathbf{G})|^2, \quad (2.34)$$

where,

$$F_N(\mathbf{G}) = \sum_j \bar{b}_j e^{i\mathbf{G} \cdot \mathbf{d}_j} e^{-W_j} \quad (2.35)$$

The static nuclear structure factor $F_N(\mathbf{G}) = F_N(hkl)$ contains information on the atomic positions \mathbf{d}_j within a unit cell and the mean-square displacements $\langle u_{jx}^2 \rangle$. In crystallography, the standard approach is to measure structure factors for a large number of reflections and to fit a model for the atomic parameters to the results. The square of the nuclear structure factor can be obtained from a scan through a Bragg peak.

Consider a neutron scattering measurement on a single crystal using a monochromatic incident beam of wavelength λ . For a reflection (hkl) in the scattering plane, with scattering angle θ relative to the diffracting lattice planes, the diffracted beam is deflected by 2θ with respect to the incident beam. If a detector is placed near 2θ , and then measurements are made as the crystal is rotated through the reflection, the area under the peak (integrated intensity) is given by

$$I = A \frac{\lambda^3 |F_N(hkl)|^2}{v_0^2 \sin 2\theta}, \quad (2.36)$$

where A is a constant that depends on the incident flux, the sample volume and the counting time. If these factors are fixed in a series of measurements, then A is simply an overall scale factor. For a large single crystal, the diffracted intensity for strong reflections will eventually saturate, so that the integrated intensity is no longer proportional to $|F_N|^2$. The precise relationship between the intensity and $|F_N|^2$ will depend on the nature and shape of the crystal. A formula that is useful for modeling the measured intensities is

$$I \sin 2\theta = \frac{\alpha_1 |F_N^{\text{calc}}|^2}{1 + \alpha_2 |F_N^{\text{calc}}|^2}, \quad (2.37)$$

Where F_N^{calc} is the calculated structure factor, and α_1 and α_2 are adjustable parameters.

For the case of polycrystalline sample (with randomly oriented grains), the orientation of the sample is irrelevant, and a Bragg peak is measured by rotating the detector or from a fixed array of detectors covering large 2θ range. In this case, the appropriate formula formula for the integrated intensity is

$$I = A \frac{m_{hkl} \lambda^3 |F_N^{\text{calc}}|^2}{v_0^2 \sin \theta \sin 2\theta}, \quad (2.38)$$

Where m_{hkl} is the multiplicity of the reflection (hkl). The multiplicity is the number of equivalent permutations of the indices hkl . For example, the multiplicity of (100) reflection from a cubic crystal is 6 because (100), ($\bar{1}00$), (010), ($0\bar{1}0$), (001) and ($00\bar{1}$) are equivalent reflections in cubic system and all deflected along same 2θ direction adding up 6 times to the intensity of (100).

2.3.2.5 Coherent magnetic scattering

The cross section for the magnetic scattering can be obtained by taking into account the neutron spin state and the magnetic interactions in equation (2.16) [87]. It depends not only on initial and final wave vectors of the neutron, but also on the corresponding neutron spin states, \mathbf{S}_i and \mathbf{S}_f , with $\mathbf{S} = \sigma/2$. Generalizing equation (2.16) with the inclusion of neutron spin state and the magnetic interaction, the differential cross section can be written as

$$\left. \frac{d^2\sigma}{d\Omega_f dE_f} \right|_{s_i s_f} = \frac{k_f}{k_i} \sum_{i,f} P(\lambda_i) \left| \left\langle \lambda_f \left| \sum_l e^{i\mathbf{Q}\cdot\mathbf{r}_l} U_l^{s_i s_f} \right| \lambda_i \right\rangle \right|^2 \delta(\hbar\omega + E_i - E_f). \quad (2.39)$$

The quantity $U_l^{s_i s_f}$ is the atomic scattering amplitude from the spin state s_i to s_f for atomic site l ,

$$U_l^{s_i s_f} = \langle s_f | b_l - p_l \mathbf{S}_{\perp l} \cdot \sigma + B_l \mathbf{I}_l \cdot \sigma | s_i \rangle, \quad (2.40)$$

where b is the nuclear coherent scattering amplitude, B is the spin-dependent nuclear amplitude, and \mathbf{I} is the nuclear spin operator. The quantity \mathbf{S}_{\perp} is the magnetic interaction vector given by [88, 89],

$$\begin{aligned} \mathbf{S}_{\perp} &= \hat{\mathbf{Q}} \times (\mathbf{S} \times \hat{\mathbf{Q}}), \\ &= \mathbf{S} - \hat{\mathbf{Q}} (\hat{\mathbf{Q}} \cdot \mathbf{S}), \end{aligned} \quad (2.41)$$

where $\hat{\mathbf{Q}}$ is a unit vector along \mathbf{Q} . It should be noted that from the above expression, only the component of \mathbf{S} perpendicular to \mathbf{Q} contributes to the scattering amplitude.

2.3.2.6 Magnetic structure determination from neutron scattering

Neutrons scatter from the magnetization density of an atom. The magnetization density comes from the contributions due to spin angular momentum and also from orbital angular momentum. The scattering cross section is obtained from the Fourier transform of the magnetization density. For spin-only moment we have

$$\mathbf{M}(\mathbf{Q})/\mu_B = g\mathbf{S}f(\mathbf{Q}), \quad (2.42)$$

with $g = 2$. Let $\Phi(r)$ is the radial wave function corresponding to the unpaired spin, then

$$f(\mathbf{Q}) = \int_0^{\infty} dr r^2 j_0(\mathbf{Q}r) |\Phi(r)|^2 \equiv \langle j_0 \rangle, \quad (2.43)$$

where $j_0(\mathbf{Q}r)$ is a spherical Bessel function of order 0 ignoring aspherical effects. The orbital moment can be included in a simple form, provided that \mathbf{Q} is much smaller than the inverse of the mean radius of the wave function for the unpaired electrons [90]. In this case,

$$\mathbf{M}(\mathbf{Q})/\mu_B = 2 \langle j_0 \rangle \mathbf{S} + (\langle j_0 \rangle + \langle j_2 \rangle) \mathbf{L}, \quad (2.44)$$

where \mathbf{L} is the angular moment vector.

Some transition-metal ions exhibit small orbital moments, with the consequence that the Landé splitting factor g differs slightly from its spin-only value of 2. In such a case

the form factor as in equation (2.42) is given by

$$f(\mathbf{Q}) = \langle j_0 \rangle + \left(\frac{g-2}{2} \right) \langle j_2 \rangle. \quad (2.45)$$

For the case of rare-earth ions, the orbital moment is generally unquenched. So in this case, we have to consider angular momentum \mathbf{J} resulting from \mathbf{S} and \mathbf{L} . Within the given states of \mathbf{J} , one has

$$2\mathbf{S} = g_S \mathbf{J}, \quad (2.46)$$

$$\mathbf{L} = g_L \mathbf{J}, \quad (2.47)$$

$$\mathbf{L} + 2\mathbf{S} = g\mathbf{J}, \quad (2.48)$$

where

$$g_S = \frac{J(J+1) - L(L+1) + S(S+1)}{J(J+1)}, \quad (2.49)$$

$$g_L = \frac{J(J+1) + L(L+1) - S(S+1)}{2J(J+1)}, \quad (2.50)$$

and $g = g_S + g_L$. Thus in the scattering formula one should replace $g\mathbf{S}$ with $g\mathbf{J}$ and the form factor is given by

$$f(\mathbf{Q}) = \langle j_0 \rangle + \frac{g_L}{g} \langle j_2 \rangle. \quad (2.51)$$

The values of $\langle j_n \rangle$ have been tabulated for magnetic ions by Brown [91]. The coherent elastic differential cross section for magnetic scattering from a magnetically ordered crystal is given by

$$\left. \frac{d\sigma}{d\Omega_f} \right|_{coh}^{el} = N_M \frac{(2\pi)^3}{v_M} \sum_{\mathbf{G}_M} \delta(\mathbf{Q} - \mathbf{G}_M) |\mathbf{F}_M(\mathbf{G}_M)|^2, \quad (2.52)$$

where F_M , the static magnetic structure factor, is given by

$$\mathbf{F}_M(\mathbf{G}_M) = \sum_j p_j \mathbf{S}_j e^{i\mathbf{G}_M \cdot \mathbf{d}_j} e^{W_j}. \quad (2.53)$$

The subscript M indicate that V_M and N_M refer to the volume of the magnetic unit cell and the number of such cells in the sample respectively; the sum in equation (2.53) is over all the sites within the magnetic unit cell. Except for the case of ferromagnetic ordering, the magnetic unit cell is typically larger than the chemical unit cell. This leads to a new

reciprocal-lattice vector \mathbf{G}_M . The relation between the integrated intensity of a magnetic Bragg peak and $|\mathbf{F}_M(hkl)|$ is same as that for nuclear scattering, *i.e.*, by substituting $|\mathbf{F}_M|$ for F_N in equation (2.36) and (2.38).

2.3.2.7 Inelastic magnetic scattering: Crystal field excitations

Inelastic magnetic neutron scattering can originate either from single particle excitations like crystal-field excitations or collective excitations like spin waves. Spin waves occur when strong exchange coupling between nearby spins leads to a collective behavior. In the opposite limit one can consider the case when strong interactions with the electrostatic crystalline field of neighboring ions dominate and lead to energy levels with zero or small dispersion. The electrostatic and spin-orbit interactions lift the degeneracy of the unfilled $4f^n$ configuration of rare-earth ions and give rise to the J -multiplets. Inelastic neutron scattering is a powerful technique to determine the positions of energy levels and the matrix elements of the transitions between them. Transitions between these levels can be observed with inelastic neutron scattering if the symmetry allows magnetic dipole transitions between the states involved. The cross section for such process can be derived as:

$$\begin{aligned} \frac{d^2\sigma}{d\Omega dE} &= \frac{1}{N_m} \left(\frac{k_f}{k_i} \right) (\gamma r_e)^2 \sum_{\alpha\beta} \left(\delta_{\alpha\beta} - \hat{\mathbf{Q}}_\alpha \hat{\mathbf{Q}}_\beta \right) |f(\mathbf{Q})|^2 e^{-2W} \\ &\times \frac{1}{Z} \sum_{\lambda_i \lambda_f} e^{-E_i/k_B T} \langle \lambda_i | \mu_\alpha^+ | \lambda_f \rangle \langle \lambda_i | \mu_\beta | \lambda_f \rangle \delta(E + E_i - E_f), \end{aligned} \quad (2.54)$$

where α and β stand for x , y , z and $\delta_{\alpha\beta}$ is the Kronecker delta. r_e and N_m are the classical electron radius and number of magnetic ions, respectively. Z is the partition function $\sum_{\lambda_i} e^{-E_i/k_B T}$.

For rare-earth compounds, simple models for the crystal field based on charged point ions may give a good description of the results obtained if appropriate values are taken for the ionic charges and the moments of the radial wave functions of the magnetic ions. In inelastic neutron scattering investigations one faces the problem of distinguishing between crystal-field excitation peaks and phonon peaks. In such cases one can check the Q dependence of the intensity of the inelastic peak. The intensity of phonon peak is usually proportional to Q^2 whereas the intensity of the crystal field excitations decreases with Q according to $|f(\mathbf{Q})|^2$.

2.3.3 Experimental techniques

In an elastic neutron scattering experiment, elastically scattered neutrons produce a strong Bragg reflection when the scattering vector is equal to a reciprocal lattice vector. These reflections can be studied in samples by a number experimental methods, including (i) rotating crystal and measuring the scattering from a monochromatic beam, looking for strong reflections, (ii) using a range of incident wavelengths (the Laue method) and (iii) measuring the diffraction of monochromatic neutrons from a powder sample. In this section we briefly describe a neutron powder diffractometer and a single crystal diffractometer and also a time-of-flight spectrometer used for inelastic neutron scattering measurements.

2.3.3.1 Elastic neutron powder diffractometer

All the neutron powder diffraction (NPD) measurements presented in this thesis were carried out with the high resolution neutron powder diffractometer SPODI at research nuclear reactor FRM II, Garching, Germany. The instrument layout of SPODI is similar to that of the powder diffractometer D2B located at Institut Laue-Langevin (ILL), Grenoble, as shown in figure 2.6.

The diffractometer SPODI is equipped with the monochromator consisting of 17 Ge(551) single crystals. The orientation (551) was used to obtain neutrons of wavelength 1.549 Å. The distance between the monochromator and sample position is 5 m and that from sample position to detectors is 1.12m. The detector array consists of 80 ³He position sensitive detector tubes with fixed collimators of 10' horizontal divergence located in front of each detector. The multi-detector of SPODI spans an angular range of $2\Theta = 160^\circ$. As each detector covers 2° the data collection is performed via stepwise positioning of the detector array to obtain a diffraction pattern of desired stepwidth $\Delta(2\Theta)$. For example, a typical step-width of $\Delta(2\Theta) = 0.05^\circ$ requires the number of steps $N = 2^\circ / \Delta(2\Theta) = 40$. The measured diffraction patterns will be smeared Debye-Scherrer rings. A concept based on the combination of Monte Carlo (MC) simulations and empirical approximation methods was used to reverse the smearing [92]. This was done by deconvolution and then summing up along the rings, including the corrections for different arc lengths, resulting in conventional one-dimensional diffraction patterns suitable for Rietveld-refinement programs, which was treated later by using the program *FullProf* to determine the nuclear and magnetic structures of the sample under study.

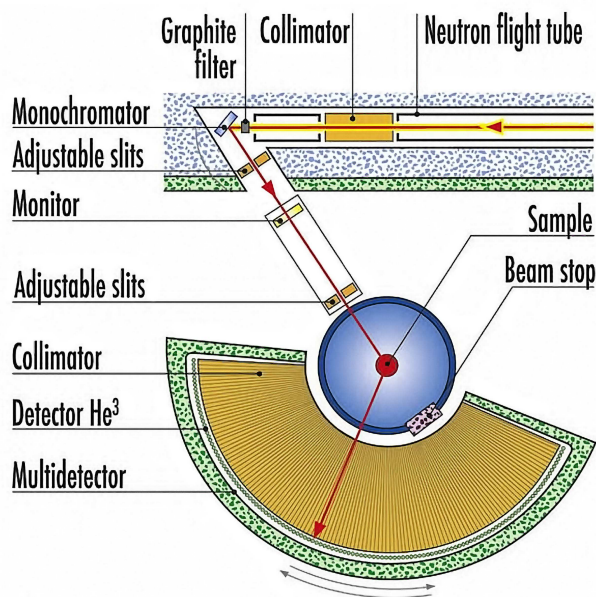


Figure 2.6: Instrument layout of a typical modern neutron powder diffractometer. Taken from [93].

2.3.3.2 Elastic single crystal neutron diffractometer

Single crystal neutron scattering measurements presented in this thesis were carried out on the instruments D9 and D23 at ILL. The diffractometer D9 is a four-circle hot neutron diffractometer with a possible wavelength range $0.35 - 0.85 \text{ \AA}$. The wavelength of neutrons is among the shortest available for diffraction at any reactors in the world. A copper crystal is used as a monochromator in transmission geometry using (220) planes. The instrument is placed on a Tanzboden floor allowing a continuous choice of wave-lengths in the range from $0.35 - 0.85 \text{ \AA}$. In order to suppress $\lambda/2$ contribution several resonance filters are available (0.48 \AA , 0.55 \AA , 0.7 \AA , and 0.84 \AA). In its standard 'four-circle' geometry (figure 2.7) the sample holder is an Eulerian cradle with offset χ -circle. D9 is equipped with a small two-dimensional position sensitive area detector, programs are available on-site for the intensity integration using this system [94]. A displax cryostat with the J-T stage or a 4-circle He-flow cryostat can be used for the temperature dependent measurements down to 2 K.

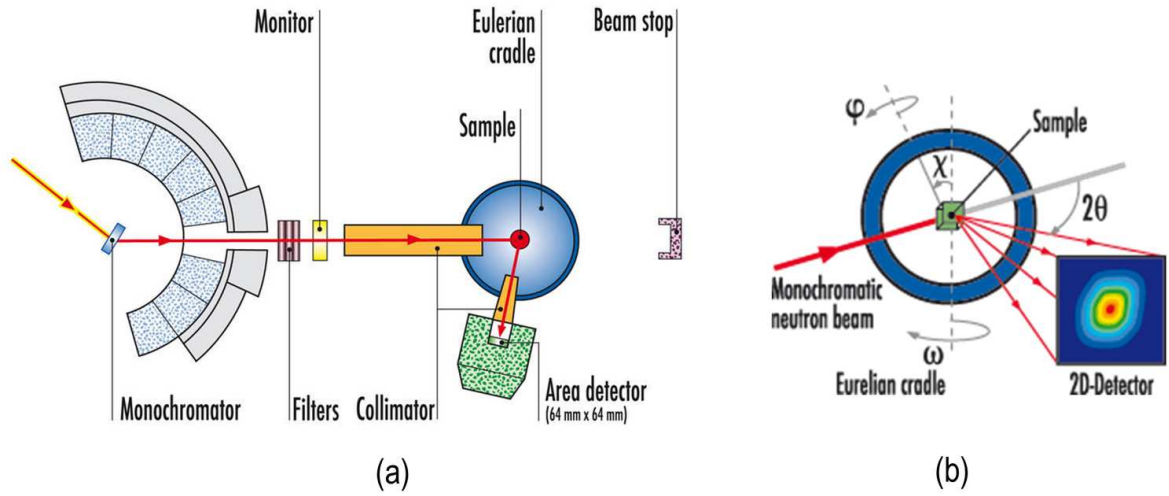


Figure 2.7: (a) Instrument layout of the hot neutron four-circle single crystal diffractometer D9 at ILL, Grenoble, (b) Description of the experimental geometry showing four possible degrees of rotation. Reproduced from [94].

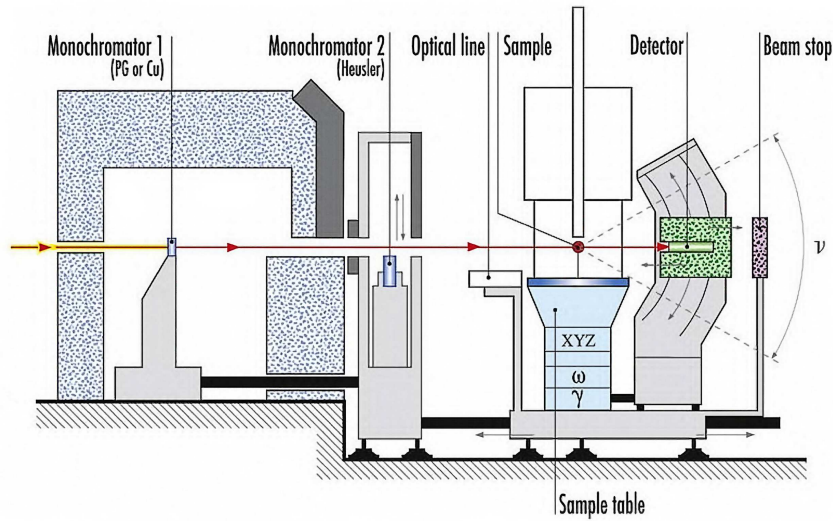


Figure 2.8: Instrument layout of the thermal neutron two-axis single crystal diffractometer D23 at ILL, Grenoble. Reproduced from [95].

The instrument D23 is a double-monochromator thermal neutron two-axis diffractometer for single crystals with a lifting detector mounted in an arc. The incident wavelength range is $1 - 3\text{\AA}$. The instrument layout of D23 is presented in figure 2.8. It can support large sample environments and is characterized by a high flux and low background. It is dedicated for the determination of magnetic structures, magnetic phase diagrams and magnetization density maps. A standard orange cryostat can be used for measurements in the temperature range $1.5 - 300\text{ K}$. There is also possibility to use

vertical or horizontal cryomagnets as per requirement.

2.3.3.3 Inelastic neutron scattering with a time-of-flight (TOF) spectrometer

The inelastic neutron powder scattering presented in this thesis were measured on the time-of-flight instrument FOCUS at the spallation neutron source SINQ, Paul Scherrer Institut (PSI), Villigen. FOCUS is a time-and-space focusing time-of-flight spectrometer for cold neutrons. By means of a vertically converging neutron guide the size of the white beam is reduced and then chopped by a pre-selector (disc) chopper. A horizontally and vertically focusing monochromator (18cm \times 18cm) with variable curvature in both directions focuses the beam through a Fermi-chopper on the sample ($w \times h = 3.5\text{cm} \times 5\text{cm}$). For incident wavelengths larger than 4 \AA a Be-filter is used together with the first chopper to suppress higher order contamination. The disc chopper also acts as anti-overlap chopper. The scattered neutrons pass a 2.5 m flight distance through a radial collimator and an argon filled flight box before being detected in three banks of totally 375 ^3He counter tubes of rectangular shape. The scattering angle covers a range from $+10^\circ$ to $+130^\circ$. The distances neutron-guide to monochromator and monochromator to sample, are both variable such that the spectrometer can be operated either in time focusing (TF) or monochromatic focusing (MF) mode, hence being suited for quasi-elastic or inelastic scattering, respectively. It is also equipped with a 2D-multidetector in the angular range between -5° to -24° . The sample space is reserved for standard cryostats, ovens, pressure cells *etc* [96, 97]. In a time-of-flight spectroscopy experiment, neutron from the reactor or a spallation source strike a crystal monochromator which is oriented at an angle θ_M to the initial beam direction. Those with wave length

$$\lambda_0 = 2d_M \sin \theta_M, \quad (2.55)$$

where d_M is the spacing between reflecting planes in the monochromator, are Bragg reflected in the direction of the sample. The monochromatic beam, characterized by energy E_0 and wave vector k_0 , is then pulsed by a chopper placed at a known distance L_{CS} from the sample. An array of detectors is arranged at a fixed distance L_{SD} from the sample, and scattered neutrons arrive at the detectors at times determined by their scattered energies E . The time of flight from the chopper to one of the detectors is simply

$$t_{CD} = t_{CS} + t_{SD} = \tau_0 L_{CS} + \tau L_{SD}. \quad (2.56)$$

Here t_{CS} and t_{SD} are the times-of-flight of the neutron from chopper to sample and sample to detector, respectively, and τ_0 and τ are the reciprocal velocities of the neutron before and after scattering, respectively. From equation 2.56 one can determine τ , E and the energy transfer

$$\hbar\omega = E_f - E_i, \quad (2.57)$$

may be determined from t_{CD} if λ_0 is known. Given the angle between the incident (k_i) and scattered (k_f) neutron wave-vectors, the wave-vector transfer

$$Q = k_f - k_i \quad (2.58)$$

is readily calculated.

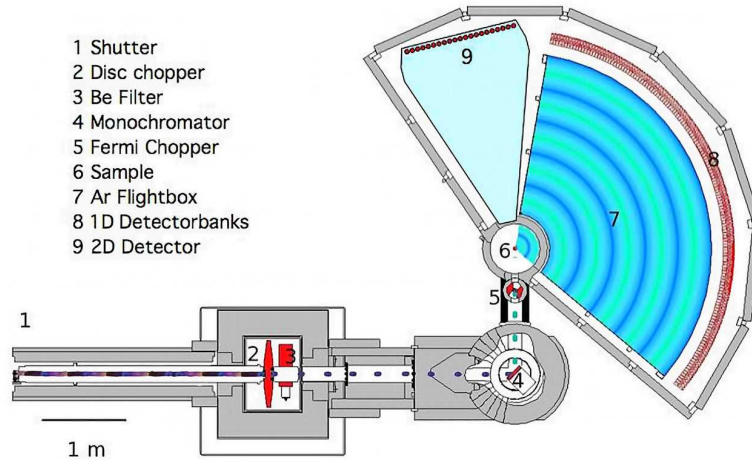


Figure 2.9: Instrument layout of the time-of-flight spectrometer FOCUS at, SINQ, PSI, Villigen. Reproduced from [98].

The basic quantity measured in a TOF experiment is a set of intensities $I(\phi_i, t_j)$ for n_{D} detectors located at scattering angles $\phi_i (i = 1, 2, \dots, n_{\text{D}})$, in n_t time channels centered at times $t_j (j = 1, 2, \dots, n_t)$ relative to an appropriate start time. Typically, measurements are made for the sample of interest and an "empty container", and in some cases additional measurements are performed on empty vanadium can in order to establish calibration constants for the data analysis. The conversion of the raw data to a differential scattering is straight forward, but corrections for instrumental resolution, and for multiple scattering effects must be dealt with carefully. The final result is the scattering function $S(Q, \omega)$ within the region of (Q, ω) phase space accessed in the experiment.

Chapter 3

STRUCTURAL, MAGNETIC AND THERMAL PROPERTIES OF HoCrO_3

3.1 Introduction

The rare earth orthochromites $R\text{CrO}_3$, where R is a rare earth element or yttrium, all crystallize in an orthorhombically distorted perovskite structure with four formula units per unit cell [99–101]. The compound HoCrO_3 (HCO), in conformity with other rare earth orthochromites, crystallizes in an orthorhombically distorted perovskite structure. The exchange coupling between the Cr^{3+} nearest neighbors is predominantly antiferromagnetic and these ions order magnetically at a Néel temperature of $T_N = 140$ K [102]. It has been reported that cooperatively induced ordering of Ho^{3+} spins occurs at 12 K [102, 103]. Later it was confirmed that no cooperative ordering of Ho^{3+} spins takes place down to 1.5 K [104]. Our specific heat measurements also confirm that no cooperatively induced ordering occurs at temperatures as low as 100 mK. The coexistence of ferroelectric and magnetic orders in rare-earth orthochromites was first reported by Subba Rao *et al.* [105]. Based on the dielectric studies it was reported that some of the heavy rare earth chromites $R\text{CrO}_3$ ($R=\text{Ho}, \text{Er}, \text{Yb}, \text{Lu}$) compounds undergo a ferroelectric transition in the temperature range 439–485 K [62]. The polarization-electric field hysteresis loops of these compounds are similar to those of leaky dielectrics and are comparable to the hysteresis loop in YCrO_3 [106]. Heavy rare earth chromites, like YCrO_3 show low values of polarization and therefore are considered to be weakly ferromagnetic.

The coexistence of both electric and magnetic orders will lead to possibility of multiferroic nature of these heavy rare earth chromites of the formula $R\text{CrO}_3$ with $R=\text{Ho}, \text{Er}, \text{Yb}, \text{Lu}$ and Y . A good deal of attention on the possible multiferroic properties of this family of compounds is given only recently [62, 106]. The temperatures associated with transition from paraelectric to ferroelectric state and paramagnetic to canted antiferromagnetic state as a function of rare-earth ionic radii in several heavy rare-earth chromites is presented in figure 3.1 [62].

To study the multiferroic properties it is very important to understand the nature of both magnetic and ferroelectric orders. Based on the theoretical calculation, Sahu *et al.* [62], predicted that the local magnetic ordering can induce local non-centrosymmetry and weak ferroelectric polarization in these materials. Authors have used density functional theory to study the possibility of broken inversion symmetry leading to a small polarization (less than $0.35 \mu\text{C cm}^{-2}$). Their studies showed (a)

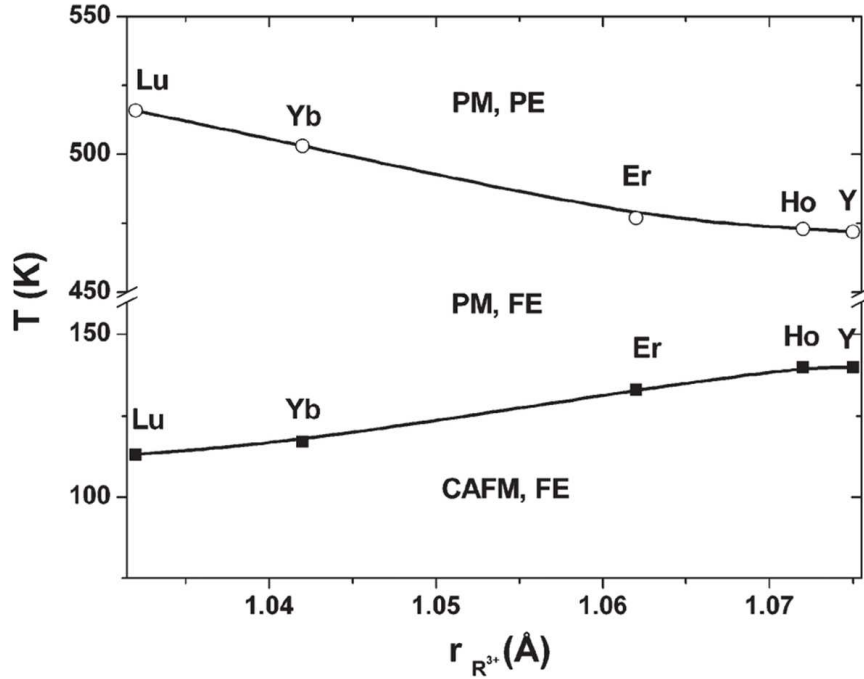


Figure 3.1: Variation of the ferroelectric (FE) transition temperature (open circles) and magnetic transition temperature (closed squares) in the heavy rare-earth chromites. Here PE, PM and CAFM represents paraelectric, paramagnetic and canted antiferromagnetic states, respectively. Taken from [62].

the existence of ferroelectric instability in the cubic structure, (b) its dependence on magnetic ordering, and (c) the small but non-zero values of polarization. It was found that in case of YCrO_3 , Cr atoms are off centered in a disordered manner leading to local non-centrosymmetry, although the the average crystal structure is centrosymmetric [60]. Though the origin of the off-centering displacement of the Cr atoms in YCrO_3 is not clear, the small value of displacement and the local character of the non-centrosymmetry in YCrO_3 could explain the small value of the polarization observed in this material ($2 \mu\text{C cm}^{-2}$ at 300 K). Similar type of local non-centrosymmetry was expected to give rise to ferroelectricity and related phenomena in other materials as well.

Despite of the fact that the magnetic structures of $R\text{CrO}_3$ compounds have been studied for decades during 1960s and 1970s by various macroscopic and microscopic techniques, owing to the complex nature of exchange interactions between two magnetic sublattices, there are several contradicting reports. We took up the compound HoCrO_3 for our study of magnetic ordering in this family of compounds. This chapter is aimed to describe the synthesis and characterization of this compound by means of laboratory PXRD, magnetization and specific heat measurements. These techniques will provide a

good idea of the crystal structure and also the nature of the magnetic structure, which can be better understood eventually with microscopic measurements such as neutron scattering.

3.2 Experimental

Polycrystalline HCO was synthesized by solid state reaction of $\text{Ho}_2\text{O}_3(3\text{N})$ and $\text{Cr}_2\text{O}_3(4\text{N})$ in stoichiometric ratio. The precursors were mixed intimately and subsequently heat treated at $1100\text{ }^\circ\text{C}$ for 48 h. Then, the material was reground and annealed again at $1200\text{ }^\circ\text{C}$ for 24 h. The phase purity of the synthesized powder sample was then confirmed by powder x-ray diffraction with $\text{Cu-}K_\alpha$ ($\lambda = 1.54059\text{ \AA}$) radiation, using a Huber x-ray diffractometer (Huber G670) in transmission Guinier geometry. The PXRD data was collected on finely ground samples. The profiles of the PXRD data were analyzed by Rietveld method (Appendix B) [80] using the *FullProf* software [81] and confirmed the formation of a single phase. The powder is then pressed into pellets and sintered at $1000\text{ }^\circ\text{C}$ for 10 h for further magnetic and thermal characterization. Magnetic measurements were conducted on pressed-sintered pellets in a commercial (Quantum Design) superconducting quantum interference device magnetometer (SQUID) in the temperature range $2 - 300\text{ K}$. Specific heat measurements were performed using a physical property measurement system (Quantum Design) in the temperature range $100\text{ mK}-290\text{ K}$.

3.3 Results

3.3.1 Crystal Structure

The rare-earth chromites crystallize in the perovskite structure of the type ABO_3 . The basic perovskite structure is similar to that of BaTiO_3 , where the Ti^{3+} ion is at the B -site and Ba^{3+} is at the A -site. In the case of chromites, the rare-earth ion occupies the A -site while Cr is at the B -site surrounded by oxygen forming an octahedra. Due to mismatch between the ionic radii of the cations at A and B sites, a structural distortion takes place that results in buckling of the CrO_6 octahedron. As a consequence of the lattice distortions, the symmetry of ideal perovskite structure is lowered. Such a distortion of perovskite structure is governed by Goldschmidt's tolerance factor rule [107]. According

to this rule, the cubic perovskite structure is stable only if the tolerance factor (t_G) defined as,

$$t_G = \frac{\langle r_A \rangle + \langle r_O \rangle}{\sqrt{2}(\langle r_B \rangle + \langle r_O \rangle)} \quad (3.1)$$

is nearly equal to unity. Here, $\langle r_A \rangle$, $\langle r_B \rangle$ and $\langle r_O \rangle$ represent the average ionic radii of respective elements. As t_G decreases, symmetry of the crystal structure also reduces. Limiting values for the tolerance factor have been determined through many experiments. For example, Hines [108] suggested (solely by analysis of the tolerance factor) that the perovskite will be cubic if $0.9 < t_G < 1.0$ (figure 3.2(a)), and orthorhombic if $0.75 < t_G < 0.9$ (figure 3.2(b)). If the value of t_G drops below 0.75 the compound has been seen to adopt an hexagonal ilmanite structure (FeTiO_3) [108].

Using Shannon-radii values for the ions [109] in equation 3.1, the value of t_G for HCO is found to be ~ 0.866 , thus the expected distortion-type is orthorhombic. As expected, the compound HoCrO_3 is an orthorhombically distorted perovskite. It belongs to the space group $D_{2h}^{16} - Pbnm$ and has four formula units per unit cell [99–101]. The Rietveld refinement results of room temperature PXRD data is presented in figure 3.3, and the results are tabulated in table 3.1. The graphical representation of the crystal structure is presented in the inset of figure 3.3.

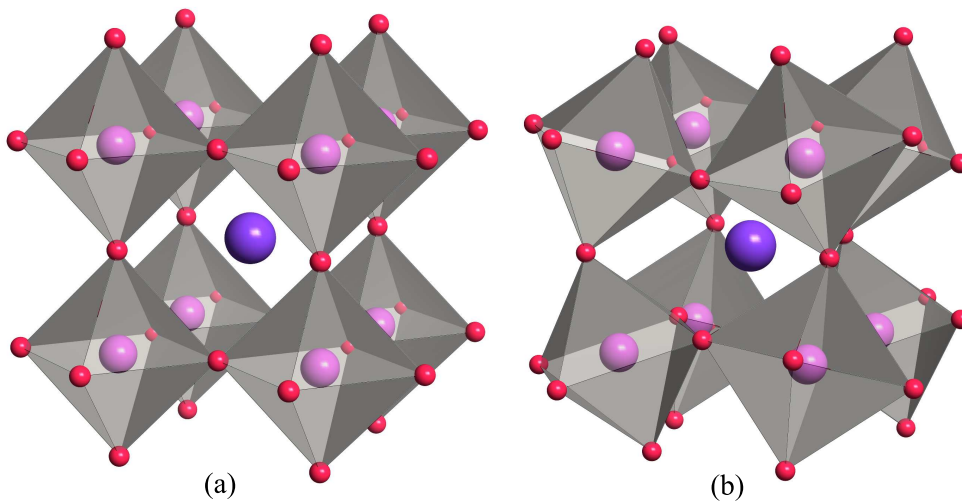


Figure 3.2: Clinographic view of the octahedra in (a) cubic (ideal) and (b) orthorhombic (distorted) perovskite.

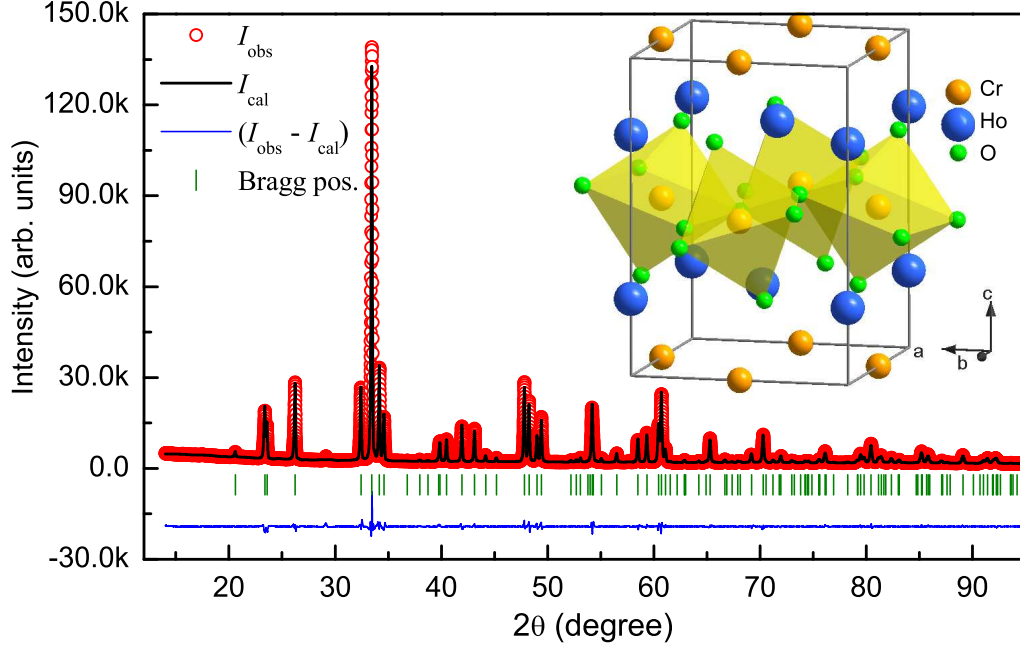


Figure 3.3: PXRD pattern and Rietveld refinement results for HoCrO_3 at 300 K. Red circles mark the data points, black line represents calculated pattern and blue line represents the difference. The bars below the patterns denote the position of Bragg peaks. Inset is the graphical representation of the crystal structure of HoCrO_3 .

Table 3.1: Lattice parameters, atomic positions, and discrepancy factors of HoCrO_3 obtained in the Rietveld refinement of PXRD pattern at 300 K with $\lambda = 1.54059 \text{ \AA}$. The values inside the brackets are the standard deviations.

Atoms	Wyckoff positions	x	y	z
Cr	4b	0.5	0	0
Ho	4c	-0.0168(8)	0.0655(5)	0.25
O1	4c	0.1026(8)	0.4664(8)	0.25
O2	8d	-0.3054(6)	0.3055(6)	0.0497(4)
Unit Cell Dimensions				
$a = 5.2463(1) \text{ \AA}$	$b = 5.5177(8) \text{ \AA}$	$c = 7.5412(8) \text{ \AA}$	$V = 218.276(8) \text{ \AA}^3$	
Discrepancy Factors				
$R_p = 3.98\%$	$R_{wp} = 5.53\%$	$R_{exp} = 3.06\%$	$\chi^2 = 3.27$	

The refined lattice parameters at 300 K are $a = 5.2463(5) \text{ \AA}$, $b = 5.5177(8) \text{ \AA}$ and $c = 7.5412(9) \text{ \AA}$. Previous structural studies on HCO report the orthorhombic structure $D_{2h}^{16} - Pbnm$ with similar values for the lattice parameters [110]. The temperature

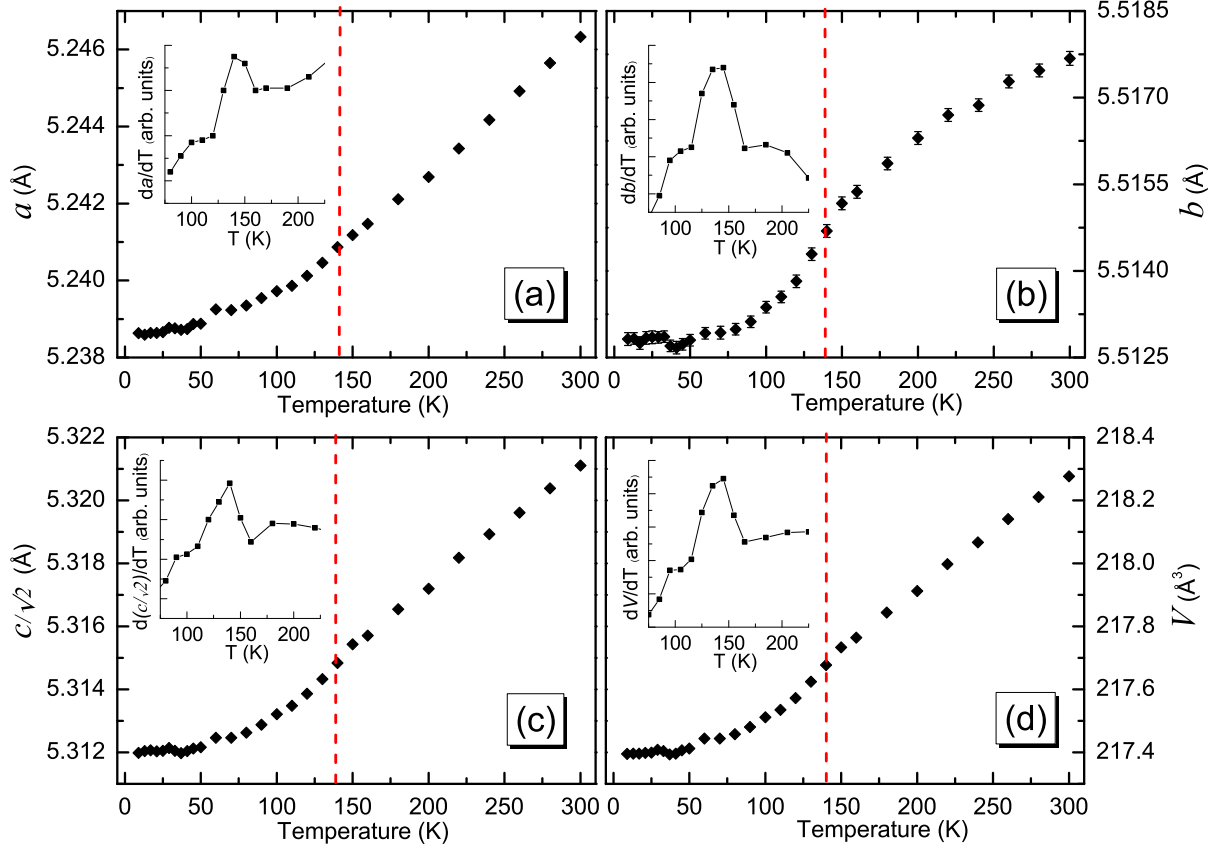


Figure 3.4: The temperature dependence of lattice parameters (a) a , (b) b , (c) $c/\sqrt{2}$ and (d) unit cell volume (V). Vertical dashed line corresponds to the magnetic ordering temperature. Inset in each panel is the first derivative of corresponding lattice parameter.

dependence of lattice parameters was obtained from the analysis of several PXRD patterns obtained in the temperature range 10 – 300 K, the results are presented in figure 3.4. In the temperature range of interest no structural transitions were observed. But, surprisingly, all the cell parameters and unit cell volume showed an anomaly close to magnetic transition temperature ~ 142 K. This can be clearly seen in the first derivative of lattice parameters with respect to temperature, around the transition temperature, shown as insets in figure 3.4. We believe that the anomalous change in lattice parameters and the unit cell volume indicates the presence of magnetoelastic effect in this compound. To the best of our knowledge magnetoelastic effect has not been reported in $R\text{CrO}_3$ family so far and this is the first observation of this phenomenon in HoCrO_3 . Magnetoelastic effects in this compound will be discussed in detail in the next chapter based on neutron powder diffraction measurements.

3.3.2 Magnetization

The field-cooled (FC) and zero field-cooled (ZFC) dc magnetization curves measured with an applied magnetic field of 2 Oe presented in figure 3.5(a) show a bifurcation around 142 K. It is attributed to the magnetic ordering of Cr^{3+} sub-lattice [103, 104]. The thermal evolution of reciprocal susceptibility calculated from the FC magnetization curve (figure 3.5(a)) is presented in figure 3.5(b). The inverse susceptibility follows Curie-Weiss law above the transition temperature and there is a marked deviation below the ordering temperature. From a Curie-Weiss fit of the magnetic susceptibility, the Weiss temperature Θ is found to be $-28.8(6)$ K and the effective moment is found to be $11.15 \pm 0.02 \mu_B$. By considering the theoretical values $3.87 \mu_B$ for Cr^{3+} (for the spin only $S = 3/2$) and $10.63 \mu_B$ for Ho^{3+} ($J = 8$) and assuming that the total effective magnetic moment is given by $\mu_{\text{total}} = [\mu_{\text{eff}}^2(\text{Cr}^{3+}) + \mu_{\text{eff}}^2(\text{Ho}^{3+})]^{1/2}$, we expect a total magnetic moment of $11.31 \mu_B$. Susceptibility was also measured in the high temperature regime (300 – 900 K, figure 3.5(c)) which follows Curie-Weiss law and gives similar values as above for Weiss temperature and effective moment.

Magnetic hysteresis measured at 2 K and 300 K is presented in figure 3.6(a). The hysteretic behavior of HCO below transition temperature indicates the presence of weak ferromagnetism. At 300 K it does not show any hysteresis. In figure 3.6(b) several isothermal magnetization curves are presented, each measured after a zero field-cooled cycle from 200 K, well above the transition temperature (142 K) to remove any remnant magnetization in the sample. Two distinct features can be seen in virgin curves as broad dips, denoted by arrows in figure 3.6(b). A possible origin of these features could be field induced spin reorientation of Cr^{3+} and/or Ho^{3+} magnetic sublattice. By taking the derivative of isothermal magnetization, the two critical-fields associated with field induced phase transition, H_{C1} (lower critical field) and H_{C2} (upper critical field) were obtained at different temperatures as shown in figure 3.6(c). The $H - T$ phase diagram thus obtained is presented in figure 3.6(d). From the $H - T$ phase diagram it is clear that only H_{C2} is temperature dependent and decreases with an increase in temperature from, ~ 1.38 T at 2 K to ~ 1.05 at 50 K, above this temperature H_{C2} is temperature independent. On the other hand in the whole temperature range H_{C1} is found to be constant with a value of ~ 0.7 T. The nature of these field induced phase transitions should be elucidated by single crystal neutron scattering measurements.

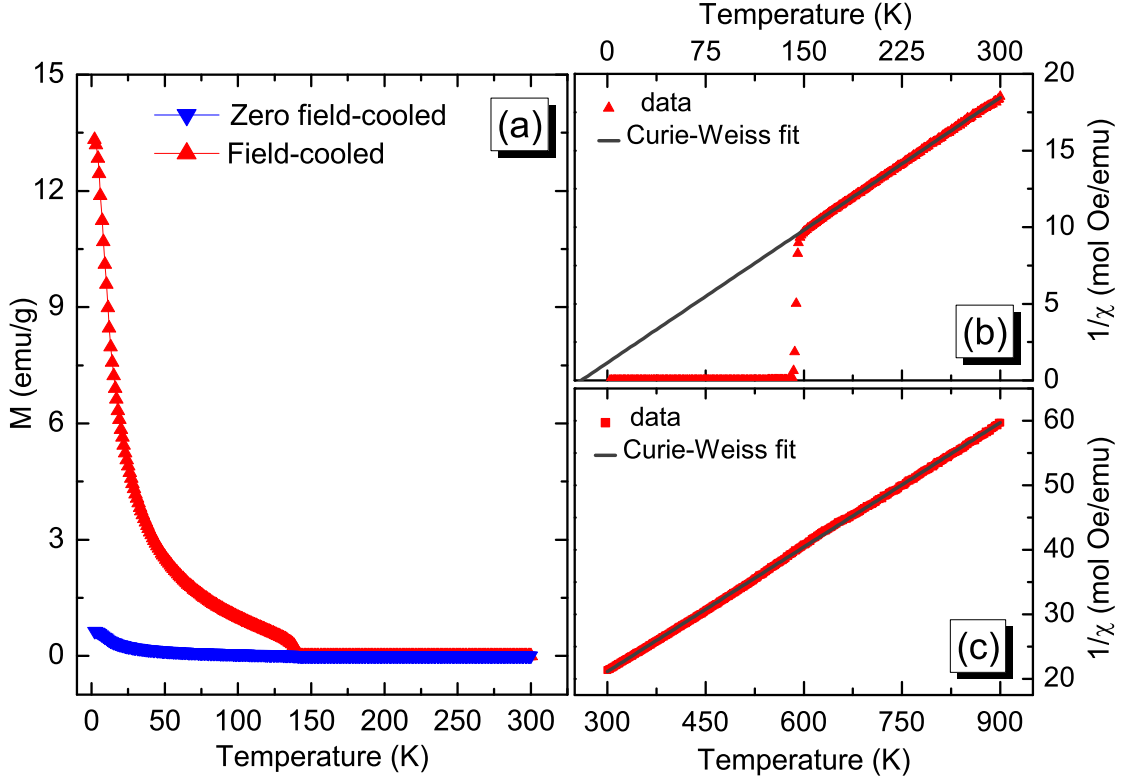


Figure 3.5: (a) DC magnetization of HoCrO_3 at applied field of 2 Oe. (b) A Curie-Weiss law fit to inverse susceptibility measured at 2 Oe deviates significantly below the transition temperature. (c) A Curie-Weiss law fit to the inverse susceptibility data at an applied field of 100 Oe in high temperature region.

3.3.3 Specific heat

The variation of specific heat (C_P) of HoCrO_3 with temperature is presented in figure 3.7. The low temperature part of specific heat can be well appreciated in the log-log plot as shown in the inset of figure 3.7. The direct inspection of specific heat curve evidences the presence of three main contributions or features: (1) A sharp increase in specific heat below 2 K with a maxima at ~ 0.3 K, due to anomalously large hyperfine interaction between the electronic and nuclear spins of $^{165}\text{Ho}^{3+}$ leading to a nuclear-Schottky specific heat (C_N). (2) The electronic Schottky contribution ($C_{Schottky}$) from thermal depopulation of the ground 5I_8 multiplet of Ho^{3+} with a maxima at ~ 7 K. The thermal population of an energy level ε_i which can arise due to removal of orbital or spin degeneracy. It is proportional to the Boltzmann factor $\exp(-\varepsilon_i/k_B T)$, where T is the temperature and k_B is the Boltzmann's constant ($k_B = 1.38 \times 10^{-23}$ J/K). In most crystalline solids one of the main contribution to the low temperature specific heat is from the crystalline electric field (CEF) that lifts the degeneracy in the electronic

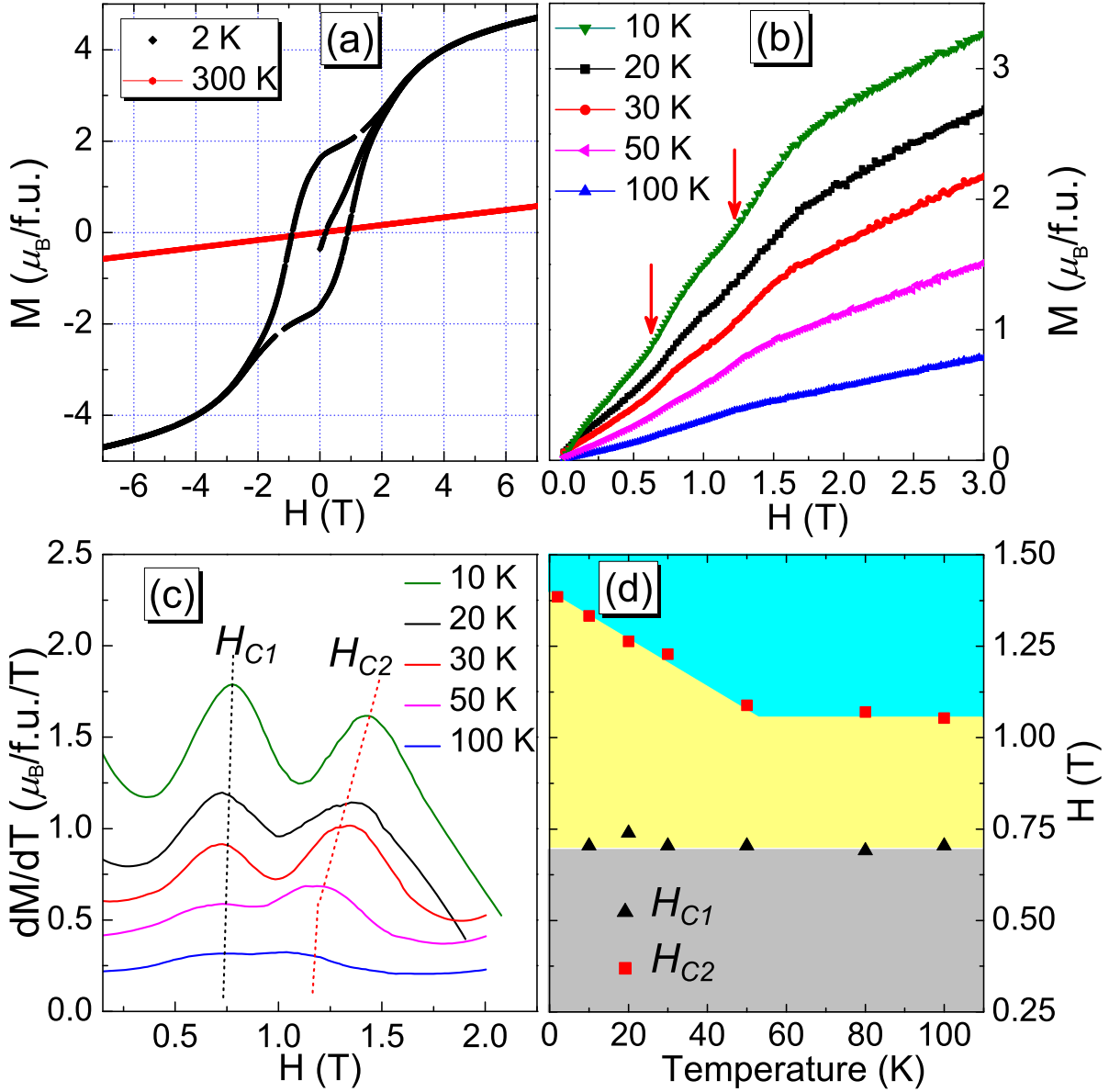


Figure 3.6: (a) Hysteresis curves measured at 2 K and 300 K. Hysteresis behavior below the transition temperature indicates the presence of weak ferromagnetism. (b) Magnetization curves, each measured after a zero field-cooled cycle from temperature above the transition. (c) The derivative plots of the magnetization curves, indicating two anomalies corresponding to H_{C1} and H_{C2} and (d) A tentative $H - T$ phase diagram obtained from the derivative plots in (c).

energy levels (ε_i). From the Boltzmann factor it is clear that the largest contribution to the Schottky heat capacity $C_{Schottky}$ occurs at temperature where $k_B T$ is comparable with ε_i . Quantitative estimates of $C_{Schottky}$ can be made in terms of the Boltzmann factors. (3) The λ like anomaly with a peak at $T \approx 142$ K, due to the magnetic ordering of the Cr^{3+} moments. To find the different possible contributions to C_P a detailed

analysis was performed in two steps. First the C_P was modeled in the temperature range $0.1 \leq T \leq 30$ K as described in the section 3.3.3.1 and then in the temperature range $2 \leq T \leq 290$ K which is described in the section 3.3.3.2.

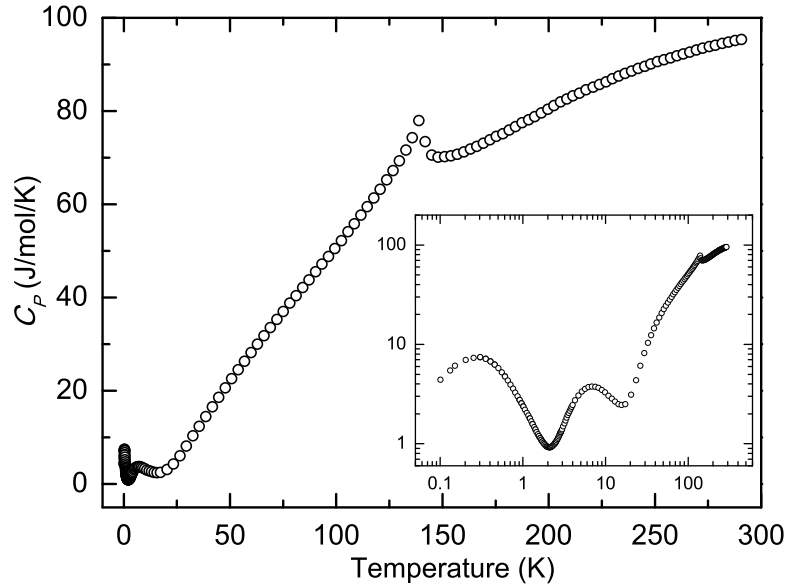


Figure 3.7: Specific heat of HoCrO_3 , C_P measured at zero magnetic field. Inset, C_P in double logarithmic scale, three distinct features in the specific heat are discernible.

3.3.3.1 Hyperfine interactions

The specific heat below ≈ 30 K has two broad features with maxima around ~ 0.3 K and ~ 6.5 K. From the low temperature specific heat measurements of Holmium metal it was found that anomalously large hyperfine interaction between the electronic and nuclear spins for Ho commonly leads to a nuclear specific heat Schottky anomaly with a maxima at ≈ 0.3 K. Hyperfine interactions have been studied for many years by various methods [111]. These techniques for studying hyperfine interactions in magnetic materials, such as Mössbauer effect, nuclear specific heat, nuclear magnetic resonance, angular correlation of γ -rays interaction of polarized neutrons with polarized nuclei, provide improved understanding of the electronic magnetism and also nuclear magnetism. In this section, the study of hyperfine interactions in HoCrO_3 by low temperature specific heat measurements will be presented.

The nuclei in many rare-earth metals find themselves in a strong effective magnetic field, H_{eff} [112, 113] which arises from several sources: (1) The magnetic moments of

other rare-earth ions will produce a field of 1 to 2 T. (2) Polarization of conduction electrons by the $4f$ electrons will cause an effective field which, from the measurement of hyperfine interactions in the $3d$ metals, can be estimated as 20 to 40 T. (3) The orbital angular momenta of the $4f$ electrons produce a large field at the nucleus of the same atom. This field is of several hundred tesla. (4) The spin angular momenta of the $4f$ electrons also cause an effective field at the nucleus. This field is about one tenth of that caused by the orbital angular momenta. (5) Polarization of the inner shell electrons by the spins of the $4f$ electrons may also produce an effective field at the nucleus. The magnitude of this field can be estimated from electron spin resonance experiments; the estimates are about 30 T. The main contribution to H_{eff} in case of Ho thus comes from the orbital angular momenta of $4f$ electrons [114].

In addition to H_{eff} a considerable electric field gradient, parallel to H_{eff} because of strong coupling between the spin and orbital, can also be expected at the nucleus. Bleaney and Hill [115] write the Hamiltonian for hyperfine interactions in the form

$$\frac{\mathcal{H}}{k_B} = a'I_z + P \left[I_z^2 - \frac{1}{3}I(I+1) \right] \quad (3.2)$$

Where a' is magnetic hyperfine constant which is a measure of the strength of the hyperfine interaction, *viz.*, the magnetic moment associated with the $4f$ electrons. P is the quadrupolar coupling constant. The field is applied in the z direction. Since the projection I_z can take $2I + 1$ values i.e., $-I, -I + 1, \dots, I$, the hyperfine specific heat C_N will be a Schottky type specific heat, associated with the $2I + 1$ hyperfine levels.

Due to hyperfine interaction the holmium nucleus with a spin $I = 7/2$ (the only stable isotope of holmium is ¹⁶⁵Ho) will have $2I + 1 = 8$ possible spin orientations relative to effective field H_{eff} . The energies ε_i/k_B of various nuclear spin states, i.e. the eigenvalues of the Hamiltonian in equation (3.2) are

$$\frac{\varepsilon_i}{k_B} = a'i + P \left[i^2 - \frac{1}{3}I(I+1) \right] \quad (3.3)$$

Where $i = -7/2, -5/2, \dots, 5/2, 7/2$. Information about a' and P can be obtained by measuring the heat capacity at sufficiently low temperatures. In case of holmium, the quadrupolar coupling contribution is small and can be neglected [116]. Therefore for $P \approx 0$ the above equation can be written as,

$$\frac{\varepsilon_i}{k_B} \approx a'i \quad (3.4)$$

The specific heat in the temperature range 100 mK-30 K is modeled by taking into consideration the contributions from nuclear specific heat C_N , an electronic Schottky term $C_{Schottky}$ and a lattice term $C_{Lattice}$. Thus at low temperatures the C_P of HCO is given by

$$C_p = C_N + C_{Schottky} + C_{Lattice} \quad (3.5)$$

Where C_N and $C_{Schottky}$ are given by the general expression for an n-level Schottky specific heat term give by [117]:

$$C_{Schottky} = \frac{R}{T^2} \frac{\sum_i \sum_j (\Delta_i^2 - \Delta_i \Delta_j) \exp[-(\Delta_i + \Delta_j)/T]}{\sum_i \sum_j \exp[-(\Delta_i + \Delta_j)/T]} \quad (3.6)$$

In this expression, $\Delta_i = \varepsilon_i/k_B$. To calculate nuclear specific heat C_N a Schottky curve for eight energy levels at $\varepsilon_i/k_B \approx a'i$, where $i = -7/2, -5/2, \dots, 5/2, 7/2$ must be used. To calculate the electronic Schottky specific heat $C_{Schottky}$, a simple two level Schottky term with energy splitting ε_s/k_B is used, as the contribution from higher energy terms is negligible in this temperature range. In this temperature range the lattice contribution is expressed by a single Debye term. At low temperatures, when $T \ll \Theta_D$, the Debye specific heat can be represented by well-known *Debye T^3 - law* as [117],

$$C_{Debye} = R \frac{234r_D T^3}{\Theta_D^3} = \beta_3 T^3 \quad (3.7)$$

Where, r_D is the number atoms per molecule and Θ_D is the Debye temperature.

The fit results are given in figure 3.8 (a). From the fit the values of a' , ε_s/k_B and Θ_D are found to be, 0.2615(6) K, 16.00(5) K and 318(2), respectively. The effective magnetic field at the holmium nuclei can be computed by writing [114],

$$a' = \frac{\mu H_{eff}}{k_B I} \quad (3.8)$$

Where, $\mu = 4.17 \mu_N$ for ^{165}Ho and μ_N is the nuclear Bohr magneton ($\mu_B = 9.274 \times 10^{-24}$ J/T). The H_{eff} is found to be 600(3) T. From equation 3.4 we can calculate the energy difference between two adjacent nuclear levels as $\sim 20.68 \mu\text{eV}$. The entropy, S_N associated with the nuclear specific heat was calculated by the numerical integration of

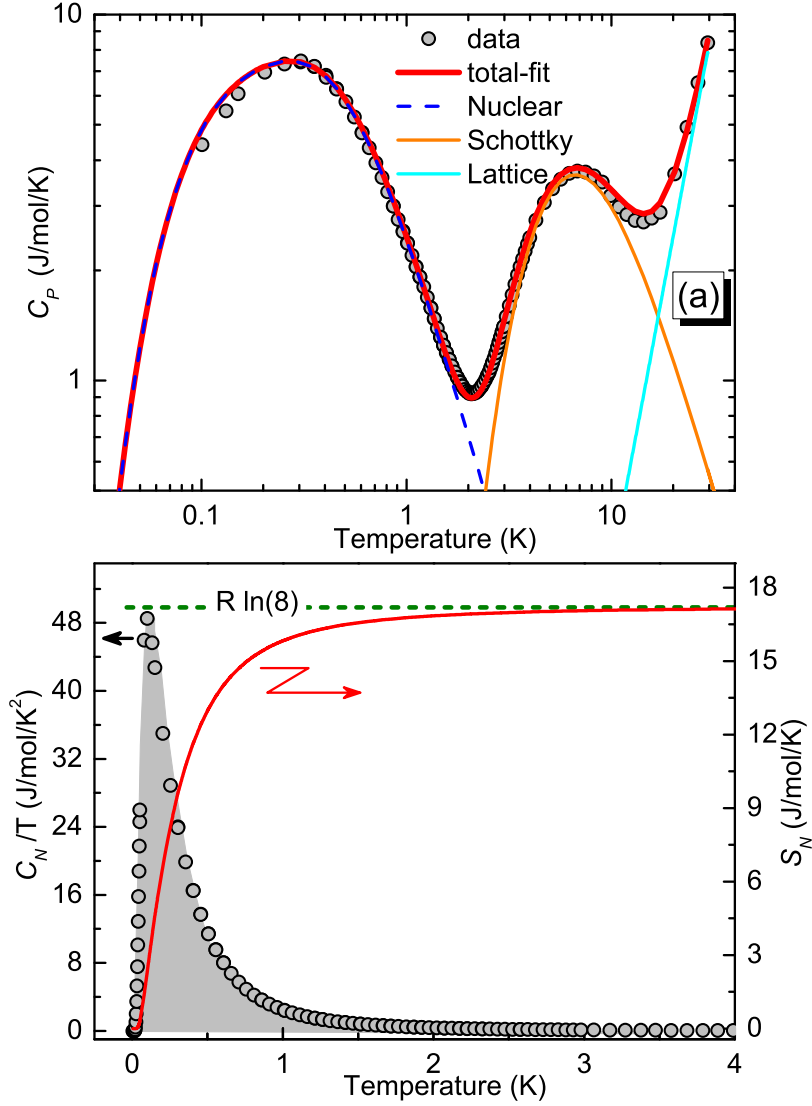


Figure 3.8: (a) Double logarithmic plot of specific heat, C_P measured at zero magnetic field (circles) plotted along with fit results. Different contributions to the total specific heat, C_P are also shown. (b) A plot of C_N/T vs. T and the entropy associated with the nuclear specific heat, S_N obtained by the numerical integration of C_N/T (shaded region). The horizontal dashed-line corresponds to the theoretical value of the entropy.

C_N/T . The S_N is given by the expression,

$$S_N(T) = \int_0^T \left(\frac{C_N}{T'} \right) dT' \quad (3.9)$$

The C_N/T vs. T and the computed S_N are presented in figure 3.8(b). The value of S_N reaches the expected value $\sim 17.2 \text{ Jmol}^{-1}\text{K}^{-1}$ consistent with $R \ln 8 = 16.9 \text{ Jmol}^{-1}\text{K}^{-1}$ at

~ 4 K.

3.3.3.2 High temperature specific heat ($2 \leq T \leq 290$ K)

The total specific heat (C_{total}) in the temperature region 2 – 290 K is fitted assuming the contributions from $C_{Schottky}$, $C_{Lattice}$ and electrons C_{Linear} . A good fit to the experimental data is achieved by considering contributions from a Debye term (C_{Debye}) and an Einstein term ($C_{Einstein}$) to the lattice term ($C_{Lattice}$). The specific heat associated with the magnetic ordering of Cr^{3+} and Ho^{3+} moments, (C_m) resulting in lambda like transition with a maximum at ~ 142 K and tail extending to ~ 60 K. It is obtained by subtracting C_{total} from the experimental data (C_P). The magnetic entropy S_m associated with C_m is obtained by the numerical integration of C_m/T . The C_{total} and C_m in the temperature range 2 – 290 K can be written as [117, 118],

$$\begin{aligned} C_{total} &= C_{Schottky} + C_{Lattice} + C_{Linear} \\ C_{Lattice} &= C_{Debye} + C_{Einstein} \\ C_m &= C_P - C_{total} \end{aligned} \quad (3.10)$$

Where, $C_{Schottky}$ is given by equation 3.6 and,

$$C_{Debye} = 9rR/x_D^3 \int_0^{x_D} x^4 e^x / (e^x - 1)^2 dx \quad (3.11)$$

$$C_{Einstein} = 3rR \sum_i a_i [x_i^2 e^{x_i} / (e^{x_i} - 1)^2] \quad (3.12)$$

$$C_{Linear} = \gamma T \quad (3.13)$$

In these expressions, R is the gas constant, $x_D = \hbar\omega_D/k_B T$, $x_i = \hbar\omega_E/k_B T$, k_B is Boltzmann constant, γ is the coefficient of linear term and r is the number of atoms in unit cell. The linear coefficient is usually attributed to charge carriers, and is proportional to the density of states at the Fermi level. But HCO is insulating, hence the appearance of a linear term in the specific heat must be more carefully interpreted. The fit results are shown in figure 3.9(a). The values of Debye temperature (Θ_D) and two Einstein temperatures ($\Theta_{E1,E2}$) obtained from the fit are 802(27) K, 602(19) K and 171(2) K respectively. The two Einstein terms are related to minimal and maximal phonon energies in the perovskites [119, 120].

Based on optics [121], magnetization and magnetic susceptibility [104], specific

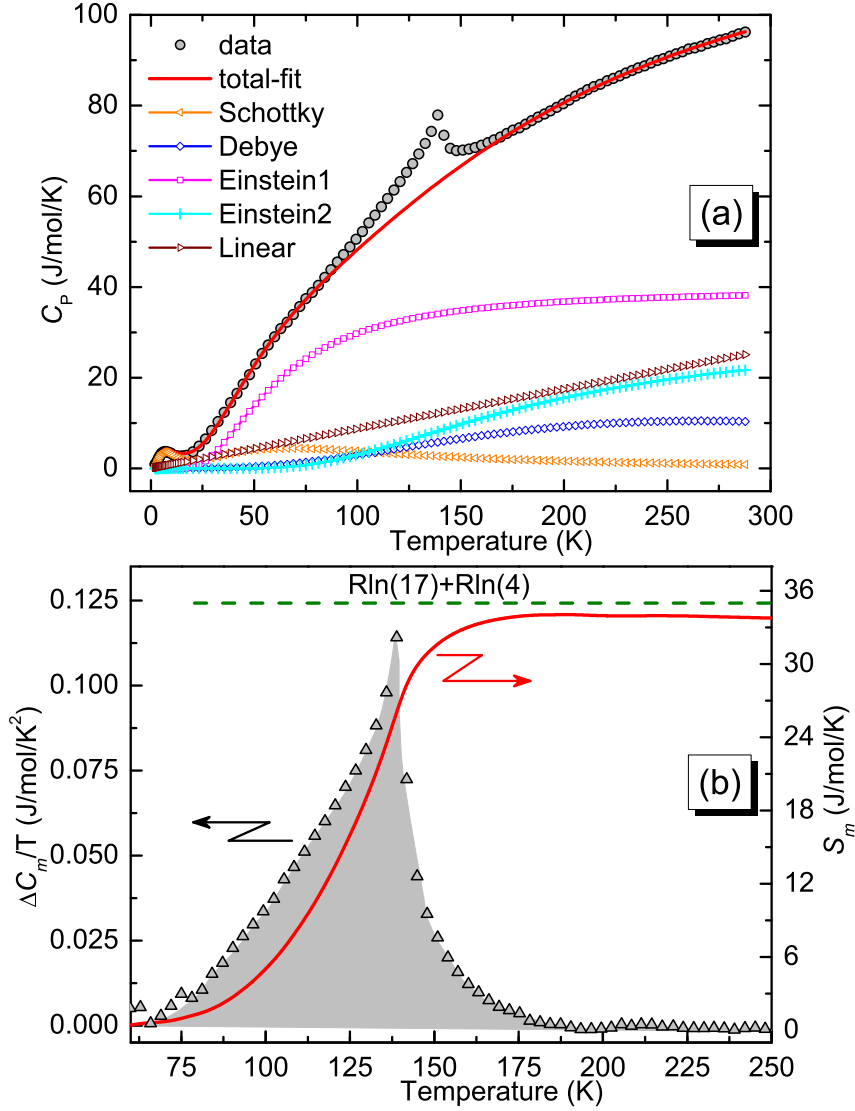


Figure 3.9: (a) Specific heat, C_P measured at zero magnetic field (circles) plotted along with fit results. Different contributions to the total specific heat, C_{total} are also shown. (b) The C_m/T vs. T and the magnetic entropy, S_m obtained by the numerical integration of C_m/T (shaded region). The horizontal dashed-line corresponds to the theoretical value of the entropy.

heat [122], elastic neutron diffraction [123] and inelastic neutron scattering (INS) [124] experiments five electronic Schottky levels were observed with fifth level being at ~ 272 K. To calculate $C_{Schottky}$, a Schottky curve for five energy levels is used which contribute to $C_{Schottky}$ below 300 K. The ground energy level is assumed to be zero i.e., $\varepsilon_1/k_B = 0$. From the low temperature specific heat analysis where a simple two level Schottky model was used to calculate $C_{Schottky}$, the energy splitting was found to be $16.00(5)$ K which we fixed as ε_2/k_B in the present calculations. The higher energy levels are taken from the

inelastic neutron scattering measurements and fixed to be, $\varepsilon_3/k_B = 121$ K, $\varepsilon_4/k_B = 179$ K and $\varepsilon_5/k_B = 272$ K [124]. The value of γ from the fit is $3.9(6)$ mJmol⁻¹K⁻². The value of γ is comparable to $5 - 7$ mJ/mol/K² which is associated with conduction electrons in some doped manganites [125–128]. HCO is an insulator so the linear specific heat is not associated with the conduction electrons, thus the origin of linear term should be interpreted with caution. A similar observation was made in insulator LaMnO_{3+ δ} in which a large value of $\gamma \approx 20$ mJ/mol/K² was found. This was attributed to the thermal excitations of, although localized but closely spaced electron levels [129]. In BaVS₃ it was found that the low temperature specific heat consists of a linear term with $\gamma = 15.7$ mJ/mol/K² in spite of absence of conduction electrons [130]. This was interpreted as due to spin wave excitations for a one-dimensional antiferromagnet, in which the spin ordering in the insulator state is not simple but may be due to frustration effects. Another insulator with large γ value (41.5 mJ/mol/K²) is the layered manganite La_{2.3}YCa_{0.7}Mn₂O₇ [131]. This was attributed to magnetic phase separation in the system. Neutron diffraction studies of manganite samples have shown that many of the hole-doped manganites become mixtures of ferromagnetic and antiferromagnetic (or canted antiferromagnetic) phases. Thus the compound La_{2.3}YCa_{0.7}Mn₂O₇ expected to segregate into a mixture of ferromagnetic and antiferromagnetic phases with unconnected ferromagnetic clusters embedded in an antiferromagnetic matrix. In such situation the bulk heat capacity associated with the sample would include a large electronic contribution to the heat capacity associated with the ferromagnetic clusters which are metallic, but the electrical behavior of the sample would be insulating due to the lack of a percolating conducting path. Most plausible explanation for the large linear term in the heat capacity of HCO is a situation similar to La_{2.3}YCa_{0.7}Mn₂O₇. In later chapter we show that in HCO, Cr orders canted-antiferromagnetically with a small canting angle along crystallographic *c*-direction and Ho orders canted antiferromagnetically within *ab*-plane with a weak ferromagnetic component along *a*-direction. We propose that a competition between antiferromagnetic and ferromagnetic ordering in this compound might lead to a large electronic contribution. It is also noteworthy that a linear variation of the low temperature specific heat is claimed to be a common feature of spin glasses with short range magnetic order [132]. It was found from our neutron scattering experiments (discussed later) that in HCO a short range ordering due to spin fluctuations was observed, which could also be another reason for the presence of linear term in bulk specific heat of HCO. After subtracting the contributions, $C_{Lattice}$ and C_{Linear} from C_P the magnetic

specific heat C_m is obtained which can be seen as the deviation from the total fit in figure 3.9(a) in the temperature range 60 – 180 K. The magnetic entropy, S_m was calculated by the numerical integration of C_m/T using the expression (3.9). The C_m/T versus T and computed S_m is presented in figure 3.9(b).

3.4 Discussion

HCO was synthesized by solid state reaction method and Rietveld analysis of PXRD patterns, using *FullProf* suit confirmed phase purity of the prepared polycrystalline samples. HCO crystallizes in distorted perovskite type structure which is consistent with expected crystal structure based on Goldschmidt's tolerance factor rule. The unit-cell parameters verify the relationship, $a < c/\sqrt{2} < b$ which is a characteristic of *O*-type orthorhombic structure. A buckling of the network of octahedra corresponding to co-operative rotation about a [110]-axis leads to the *O*-type orthorhombic structure. The clinographic view of the CrO_6 octahedra in HoCrO_3 can be seen in the inset of figure 3.3. In case of orthorhombic RMnO_3 ($R = \text{La, Pr, Nd, Sm, Eu, Gd, Tb and Dy}$), in addition to the distortion due to buckling of the MnO_6 octahedron a second distortion also arises because of Jahn-Teller effect. This is because the Mn^{3+} in RMnO_3 with four unpaired electrons in *d*-orbital which will be in high spin state is Jahn-Teller active, on the other hand Cr^{3+} in chromites with three unpaired electrons in *d*-orbital is Jahn-Teller inactive. Following, the contribution due to Jahn-Teller effect to the lattice distortion from the ideal cubic perovskite structure in RCrO_3 is ruled out. The temperature dependence of lattice parameters shows an anomaly at the magnetic transition temperature indicating the existence of magnetoelastic effect in this compound. A qualitative analysis of magneto-elastic effect will be presented in the next chapter.

From the ZFC and FC magnetization measurements the magnetic transition temperature is found to be 142 K is in agreement with the earlier reports [103, 104]. Above this temperature the inverse susceptibility follows the Curie-Weiss law with a Curie temperature, $\Theta = -28.8(6)$ K, the negative sign of Θ indicates the presence of antiferromagnetic exchange interactions. The effective moment is found to be $11.15(2) \mu_B$ this figure is very close to the expected theoretical total effective moment value, $\mu_{\text{total}} = 11.31 \mu_B$, suggesting the ground states of both Cr^{3+} and Ho^{3+} ions are those of the free ions. From the isothermal magnetization curves two field induced phase transitions are found, characterized by H_{C1} and H_{C2} . An $H-T$ phase diagram was constructed as shown

in figure 3.6(c) which shows three magnetic phases defined in terms of applied magnetic field (H) as: (1) $0 \leq H \leq H_{C1}$, (2) $H_{C1} < H < H_{C2}$ and (3) $H_{C2} \leq H$. It was found that in the temperature range 2–50 K, H_{C2} decreases with increase in temperature from, ~ 1.38 T at 2 K to ~ 1.05 at 50 K, above ~ 50 K it is unchanged. On the other hand it was found that H_{C1} is independent of temperature with a constant value, ~ 0.7 T. The observation of field induced phase transitions indicate possible complex magnetic interactions in this compound. Based on optical studies, field induced spin-orientation was reported in case of ErCrO_3 [133, 134]. Detailed magnetization and neutron scattering experiments on single crystals of HoCrO_3 are necessary to shed light on the nature of field induced transitions.

From the analysis of measured specific heat in the temperature range $0.1 \leq T \leq 30$ K, the values of a' , ε_s/k_B and Θ_D are found to be, 0.2615(6) K, 16.00(5) K and 318(2) respectively. The value of $\varepsilon_s/k_B = 16.00(5)$ is consistent with earlier reports based on specific heat measurements [103], optical absorption Zeeman spectroscopy [121]. The value of a' from our analysis is slightly smaller compared to the value found in metallic Ho, $a' \approx 0.31 - 0.32$ [114, 135, 136], in inter-metallic HoCo_2 , $a' \approx 0.31$ [137] and in paramagnetic salts, $a' \approx 0.31$ [135]. Using the value of a' in equation 3.8 the hyperfine field, H_{eff} is found to be 600(3) T. In an early report [103] authors have calculated hyperfine field ~ 700 K, from the heat capacity measurement above 2 K, where one can measure the high temperature tail of the nuclear Schottky specific heat. It should be noted that the authors have used for ^{165}Ho , $\mu = 3.31 \mu_N$ instead of $4.17 \mu_N$. With this right value their results will give a value, $H_{eff} \simeq 550$ T. The observed discrepancy is attributed to the insufficient data used in [103], which rendered an approximate but not an accurate value of hyperfine field. The energy difference between two adjacent nuclear levels due to hyperfine fields is found to be $\sim 20.68 \mu\text{eV}$. From the inelastic neutron scattering measurements it should be possible to observe these energy levels, directly with an inelastic peak around $\sim 20.68 \mu\text{eV}$. Similar observation were made in spin-ice compound $\text{Ho}_2\text{Ti}_2\text{O}_7$ which shows a nuclear Schottky peak around 0.3 K [138] which was later observed in inelastic neutron scattering measurements as a peak at $\sim 26 \mu\text{eV}$ [139]. The nuclear entropy S_N reaches a maximum value of ~ 17.2 J/mol/K at ~ 5 K. The theoretical value of entropy for ^{165}Ho with nuclear spin $I = 7/2$ is calculated as $R \ln(2I + 1) = R \ln(8) \simeq 17.29$ J/mol/K; it is denoted as an horizontal dashed-line in figure 3.8(b). An excellent agreement between the experimental S_N with the theoretical value suggests that only contribution to the low temperature peak in the specific heat is from the nuclear Schottky term due to hyperfine

interactions.

From the analysis of specific heat measured in the temperature range $2 \leq T \leq 290$ K, the values of Debye temperature (Θ_D) and two Einstein temperatures ($\Theta_{E1,E2}$) obtained from the fit are 802(27) K, 602(19) K and 171(2) K, respectively. The value of γ from the fit is 0.0039(6) J/mol/K². The linear coefficient γ is usually attributed to charge carriers, and is proportional to the density of states at the Fermi level. However, transport measurements showed that HoCrO_3 is insulating, so the linear term in the specific heat must be interpreted carefully. The contribution from the linear term is attributed to the presence of canted AFM and FM ordering in this compound [131, 140] or due to magnetic fluctuations [132]. The experimental magnetic entropy value reaches a maximum of ~ 34 J/mol/K. The theoretical value of S_m was calculated by assuming the contributions due to ordering of both Cr^{3+} ($S = 3/2$) and Ho^{3+} ($J = 8$) moments, i.e., $R \ln(17) + R \ln(4) \simeq 35.08$ J/mol/K, denoted as a horizontal dotted line in figure 3.9(b). The experimental S_m is very close ($\sim 97\%$) to the theoretical magnetic entropy. An excellent agreement of experimental and theoretical values of S_m ensures the reliability of analysis of experimental specific heat data to ascertain various contributions to the total specific heat.

3.5 Conclusions

We have prepared high quality polycrystalline HoCrO_3 by solid state reaction method. Polycrystalline HCO is then characterized by means of x-ray powder diffraction, magnetization and heat capacity measurements. From structural analysis we could establish the consistency of observed crystal structure and theoretical predictions based on Goldschmidt's tolerance factor rule. The dc magnetization measurements confirmed the ordering temperature of Cr^{3+} ions and also presence of antiferromagnetic exchange interactions in this compound. Isothermal magnetization measurements indicated presence of two possible field induced phase transitions, based on this observation a tentative $H - T$ phase diagram was constructed which still needs to be scrutinized by detailed single crystal magnetization and neutron scattering measurements. The strength of hyperfine interactions in terms hyperfine field constant (a') and effective field (H_{eff}) were calculated from the low temperature specific heat. We could also calculate the value of hyperfine splitting energy and entropy (S_N) associated with nuclear hyperfine specific heat (C_N), which is in excellent agreement with the theory. From the lattice contribution

to the total specific heat obtained from high temperature specific heat analysis we deduced the energies associated with Debye and Einstein modes. The magnetic entropy (S_m) associated with the magnetic specific heat (C_m) was obtained, which confirmed the ordering of both Cr^{3+} and Ho^{3+} in the temperature range 60 – 142 K. The agreement of experimental value of S_m with the theoretical value established the self consistency of our high temperature specific heat analysis.

Chapter 4

MAGNETIC ORDERING AND MAGNETOELASTIC EFFECT IN HoCrO_3

4.1 Introduction

The magnetic properties of orthoferrites and orthochromites have extensively studied about four decades ago by magnetization, specific heat, optical absorption spectroscopy and neutron scattering methods [102, 141–143]. All kinds of magnetic structures in the orthorhombic perovskites can be well-described in connection with the crystal symmetry under the notation developed by Bertaut [144]. In most cases the collinearly ordered spins are along a or c axis of the $Pbnm$ cell. However, the coupling between the magnetic moment on the rare earth (RE) and the spins on Cr^{3+} is responsible for an easy axis rotation below T_N in some orthochromites [142]. The exchange coupling between the magnetic moments of the Cr^{3+} nearest neighbors is predominantly antiferromagnetic and these compounds order magnetically at Néel temperatures T_N between 100 and 300 K. In many ways the properties of the $R\text{CrO}_3$ compounds are similar to those of the isomorphic $R\text{FeO}_3$ series [145]. However there are several important differences that make the orthochromites better candidates for a study of the effects of rare earth-transition metal couplings in oxides: (1) the transition metal ordering temperatures are a factor of two to six lower in the orthochromites; (2) the magnitude of the rare earth-transition metal coupling is, generally, at least twice as great in the orthochromites as in the orthoferrites; and (3) since $S = \frac{3}{2}$ for Cr^{3+} (whereas $S = \frac{5}{2}$ for Fe^{3+}), to a first (single-ion) approximation, Cr^{3+} spin-systems will not have four-fold anisotropy terms. The first two points noted above indicate that the influence of the rare earth-transition metal coupling should be roughly an order of magnitude greater in the $R\text{CrO}_3$ than in the $R\text{FeO}_3$ series, while the third implies that this coupling plays a decisive role in determining the character of spin reorientation phase transitions in the orthochromites.

Based on neutron powder diffraction (NPD) studies Bertaut *et al.* [102] reported that the spin configuration of Cr^{3+} ions in HoCrO_3 is, in Bertaut notation, $(G_{xz}86^\circ)$ at 80 K and (G_z) at 4.2 K and Ho spin configuration was reported to be $(F_x; C_y)$. This means at 80 K Cr magnetic moments order in a canted antiferromagnetic configuration with main spin direction along c with a weak ferromagnetic component along a . At 4.2 K the moments are bound to c axis without any ferromagnetic component. On the other hand Ho exhibits canted antiferromagnetic ordering with spins in ab -plane. Hornreich *et al.* reported, based on single crystal magnetization studies, the spin configuration of

Cr sublattice in whole temperature range below T_N to be G_z . In another report based on NPD studies, Shamir *et al.* [143] calculated the Cr spin configuration to be $(G_z; -C_y, -F_x)$ in whole temperature range below T_N and ordering of Ho moments was found to be $-C_y, -F_x$; further the authors assume that the canting angles of both Cr and Ho sublattices are constant versus temperature. It should be noted that the NPD studies [102, 143] were limited by the resolution and limited data, and the calculations were performed based on the intensities of limited number of magnetic peaks.

In this chapter we present our investigations on the magnetic structure and magnetoelastic effects of HoCrO_3 . To determine spin configurations of Cr and Ho sublattices and their evolution with temperature in HCO we have performed high resolution NPD measurements in temperature range 3 – 300 K. We found Cr spin configuration to be $(G_z; C_y, F_x)$ and that of Ho to be (C_y, F_x) in the entire temperature range below T_N . We have also found that the canting angles of both Cr and Ho moments are not constant as function of temperature. The temperature dependence of ordered moments of both Cr and Ho ions were treated with mean field theory. We also report for the first time the presence of magnetoelastic or magnetovolume effect in this compound. From our powder x-ray diffraction measurements we have found that lattice parameters and unit cell volume (V) in HCO undergoes an anomalous change around the magnetic ordering temperature T_N . From the analysis of NPD data, we present the qualitative treatment of magnetoelastic effect of V and show that the change in unit cell volume ΔV due to the magnetoelastic effect is proportional to the magnetic moment of the Cr ion.

4.2 Experimental

To determine the magnetic ordering of Ho and Cr ions in HCO, several NPD patterns were acquired in the temperature range 3 – 300 K. About 15 g of polycrystalline powder sample was used in the NPD measurements using the high-resolution powder diffractometer, SPODI at the research reactor FRM II, Garching. The powder sample was held in a vanadium cylinder of diameter 8 mm with helium exchange gas. A vertical focussing monochromator, consisting of 17 Ge(551) crystals was used to achieve neutrons of wavelength 1.549\AA . Both crystal and magnetic structures were refined from the NPD data using *FullProf*.

4.3 Results and discussion

4.3.1 Magnetic ordering

4.3.1.1 Experimental results

The thermal evolution of a part of NPD patterns and integrated intensities of typical Bragg peaks (1 0 0), (0 1 1) and (1 0 1) are shown in figure 4.1(a)-(d). Strong changes occur around $T_N = 142$ K, which corresponds to the magnetic transition. Below this temperature, an intensity of magnetic origin grows at (1 0 0) and (0 1 1) Bragg positions, where the nuclear reflections are forbidden by the $Pbnm$ symmetry, and the intensity of the (1 0 1) peak strongly increases due to an additional magnetic contribution. All peaks can be indexed within the orthorhombic space group $Pbnm$ and propagation vector $\vec{k} = (0\ 0\ 0)$. The temperature dependence of (1 0 0) and (1 0 1) Bragg peaks strongly differ from each other. The (1 0 0) peak remains rather weak down to about 25 K then strongly increases below. In contrast, (1 0 1) peak increases abruptly below 142 K. These variations suggest that (1 0 0) and (1 0 1) peaks are controlled by Ho and Cr ordering, respectively, with the (0 1 1) Bragg peak involving contributions from both orderings. Further the shape of the curve (figure 4.1(b)), the temperature dependence of (1 0 0), mainly the concavity is characteristic of induced ordering owing to the strong Ho-Cr coupling in HCO as expected in most of orthochromites [142].

A temperature induced spin reorientation (SR) transition was observed in several isomorphous RE, orthoferrites [145] and orthochromites [133, 141]. There is, however, a significant difference between orthoferrites and orthochromites. To a first (single-ion) approximation, Fe^{3+} ions, with $S = \frac{5}{2}$, can have single-ion four fold anisotropy term while Cr^{3+} ions, with $S = \frac{3}{2}$, cannot. In the absence of a four fold anisotropy term it is well known [146] that any SR phase transition will be abrupt rather rotational character. That is, as the temperature is varied SR occur by an essentially discontinuous process, wherein the antiferromagnetic axis of the spin system jumps abruptly from one crystallographic axis to another rather than by a continuous and gradual rotation over a finite temperature interval. The temperature dependence of integrated intensities of magnetic Bragg peaks presented in figure 4.1(b-d) is monotonic in the temperature range 3-142 K with no abrupt change in intensity confirming the absence of any temperature induced spin reorientation transitions in HoCrO_3 .

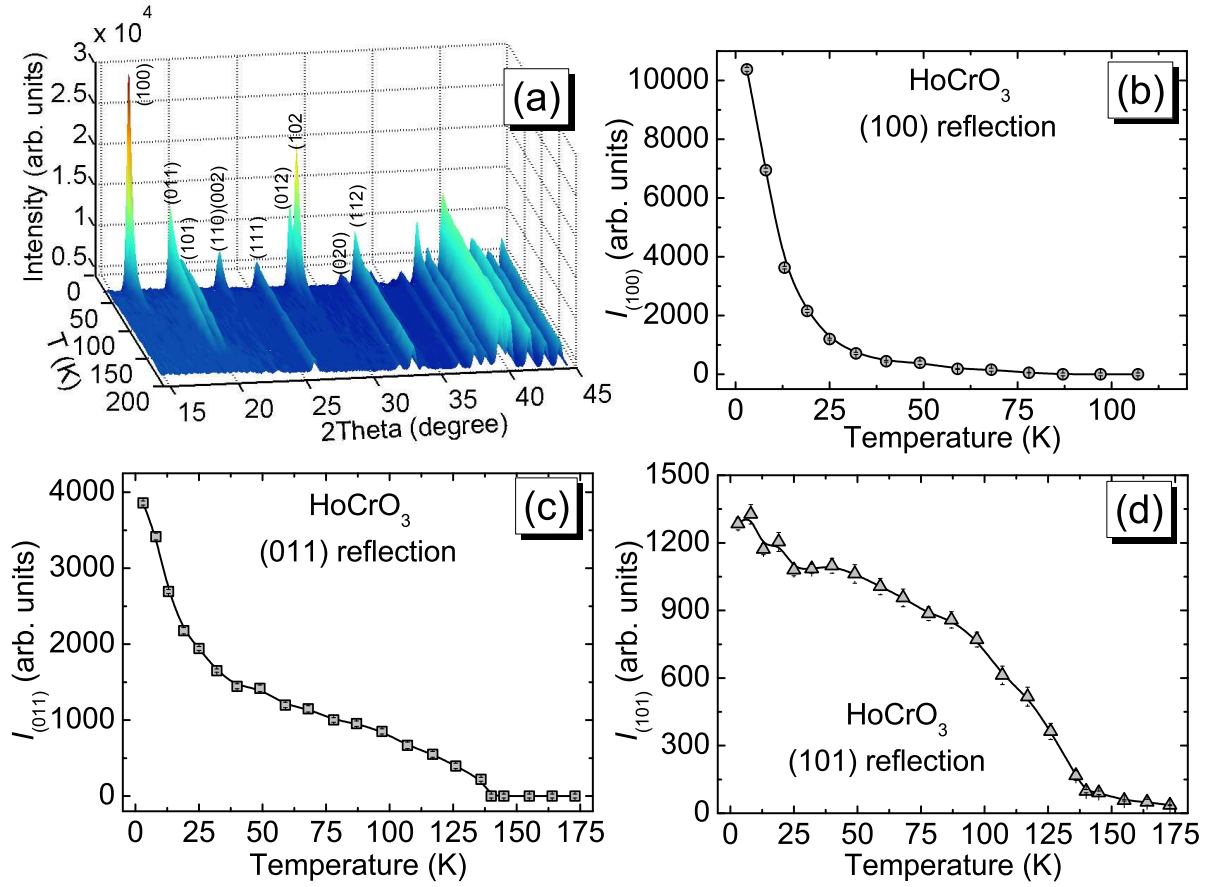


Figure 4.1: (a) Temperature variation of part of the diffraction pattern of HoCrO_3 , few Bragg reflections are indexed. (b)-(d) integrated intensities of the (1 0 0), (0 1 1) and (1 0 1) reflections (lines are guides for the eyes).

4.3.1.2 Symmetry considerations

The possible magnetic configurations with symmetry isomorphic to $D_{2h}^{16} - Pbnm$ *i.e.*, under the assumption that the magnetic and crystalline unit cells are identical, were defined by Wollan and Koehler [147] and by Bertaut [144]. It should be noted that space group $Pbnm$ (*cab*) is different setting of $Pnma$ (*abc*)(#62) [148]. The determination of magnetic structures from NPD data is often carried out by trial and error. A great deal of time is wasted in the examination of structures that are in fact symmetry forbidden. The technique of Representation Analysis (RA) [149–151] based on group theory, reduces the time burden by allowing the determination of all the spin configurations compatible with the crystal symmetry. RA allows determination of the allowed magnetic structures that can result from a second order magnetic phase transition, given the crystal structure before the transition and the propagation vector of the magnetic ordering. To determine the possible magnetic arrangements based on symmetry considerations, it will

be convenient to consider the crystal structure of HCO with Ho and Cr sublattices as shown in figure 4.2, the nonmagnetic oxygen ions having been omitted for simplicity. The Cr ions lie on the undistorted positions relative to the orthorhombic cell and the Ho ions are slightly removed from the special positions by an amount parameterized by the numbers u and v . The coordinates of the Ho and Cr sites, numbered 1 – 4 in figure 4.2, are given in table 4.1. The values of u and v are found to be $-0.0168(8)$ and $0.0655(5)$ respectively in HCO at room temperature (see table 3.1 in previous chapter).

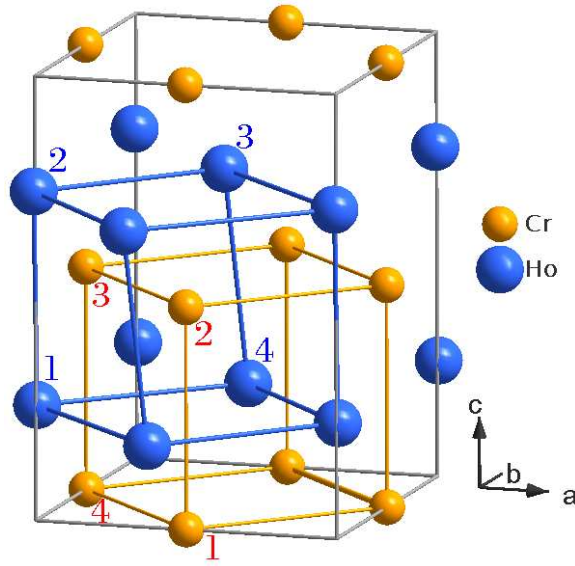


Figure 4.2: Ho and Cr sublattices and crystallographic unit cell of HoCrO_3 .

Table 4.1: Positions of Ho^{3+} and Cr^{3+} ions in the perovskite structure as indicated in figure 4.2.

Ho sites (4c)		Cr sites (4b)	
(1)	$u, v, \frac{1}{4}$	(1)	$\frac{1}{2}, 0, 0$
(2)	$\bar{u}, \bar{v}, \frac{3}{4}$	(2)	$\frac{1}{2}, 0, \frac{1}{2}$
(3)	$\frac{1}{2} + u, \frac{1}{2} - v, \frac{3}{4}$	(3)	$0, \frac{1}{2}, \frac{1}{2}$
(4)	$\frac{1}{2} - u, \frac{1}{2} + v, \frac{1}{4}$	(4)	$0, \frac{1}{2}, 0$

Considering the spin components of four in-plane nearest neighbors as indicated in figure 4.2, four possible ordering patterns can be realized. These patterns are called basis functions (BFs). For these basis functions we use the symbols: $F(++++)$, $G(+--+)$,

$C(++--)$ and $A(+--+)$ corresponding to the well known Bertaut's notations [149]. A schematic view of BFs is presented in figure 4.3.

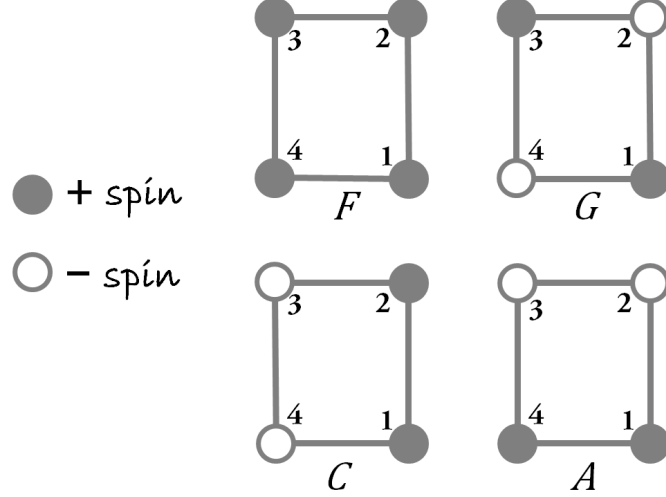


Figure 4.3: Schematic representation of four basis functions, F , G , C and, A (Refs. [147] and [144]). The (+)-spin means moment parallel to a particular direction, (-)-spin means antiparallel to same direction. The numbers corresponds to ionic sites as indicated in figure 4.2

For the present case the symmetry calculations were carried out using the program *BasIreps*. First the magnetic propagation vector was determined by using the program *k-search* which is included in the *FullProf* suit. The propagation vector was found to be $\vec{k} = (0\ 0\ 0)$. The details of the representation analysis using the program *BasIreps* is presented in appendix C.1. The representation analysis leads to four possible spin configurations for Cr at 4b Wyckoff positions and eight spin configurations for Ho at 4c Wyckoff position. RA is based on the Landau thermodynamic theory of a second-order phase transition [152] and involves the systematic decomposition of a magnetic representation (MR) Γ of the little group G_k into irreducible representations (IRs) [153]. The spin configurations of all possible IRs are presented in table 4.2.

When a simultaneous ordering of both the Cr and Ho systems is considered, only ordering modes belonging to the same representation can couple together. It should be noted that this restriction depends on the assumption that the magnetic and crystalline unit cells are identical, and the ordering has not been accompanied by a distortion lowering the symmetry. From PXRD results presented in previous chapter it was found that HCO undergoes only iso-structural distortion at the magnetic ordering temperature. Following the reasons above, it is clear from the table 4.1 that there are only four allowed

Table 4.2: Possible magnetic structures consistent with space group $Pbnm$ and propagation vector $\vec{k} = (0\ 0\ 0)$ for Cr at 4b and Ho at 4c Wyckoff positions. The atomic positions are defined according to $Cr_1 : (0.5, 0, 0)$, $Cr_2 : (-0.5, 0, 0.5)$, $Cr_3 : (1.0, 0.5, 0)$, $Cr_4 : (0, 0.5, 0.5)$, $Ho_1 : (-0.018, 0.0657, 0.25)$, $Ho_2 : (0.018, -0.0657, 0.75)$, $Ho_3 : (0.4821, 0.4343, -0.25)$ and $Ho_4 : (0.5179, 0.5657, 0.25)$. (u, v, w) and (p, q, r) are the (x, y, z) components of magnetic moments of Cr and Ho, respectively.

Atoms at 4b Wyckoff position						
IRs	Cr_1	Cr_2	Cr_3	Cr_4	Spin modes (Bertaut notation)	Magnetic space group
Γ_1	$[u, v, w]$	$[-u, -v, w]$	$[u, -v, -w]$	$[-u, v, -w]$	(A_x, G_y, C_z)	$Pbnm$
Γ_3	$[u, v, w]$	$[-u, -v, w]$	$[-u, v, w]$	$[u, -v, w]$	(G_x, A_y, F_z)	$Pb'n'm$
Γ_5	$[u, v, w]$	$[u, v, -w]$	$[u, -v, -w]$	$[u, -v, w]$	(F_x, C_y, G_z)	$Pbn'm'$
Γ_7	$[u, v, w]$	$[u, v, -w]$	$[-u, v, w]$	$[-u, v, -w]$	(C_x, F_y, A_z)	$Pb'nm'$
Atoms at 4c Wyckoff position						
IRs	Ho_1	Ho_2	Ho_3	Ho_4	Spin modes (Bertaut notation)	Magnetic space group
Γ_1	$[0, 0, r]$	$[0, 0, r]$	$[0, 0, -r]$	$[0, 0, -r]$	$(0, 0, C_z)$	$Pbnm$
Γ_2	$[p, q, 0]$	$[-p, -q, 0]$	$[p, -q, 0]$	$[-p, q, 0]$	$(A_x, G_y, 0)$	$Pbnm'$
Γ_3	$[0, 0, r]$	$[0, 0, r]$	$[0, 0, r]$	$[0, 0, r]$	$(0, 0, F_z)$	$Pb'n'm$
Γ_4	$[p, q, 0]$	$[-p, -q, 0]$	$[-p, q, 0]$	$[p, -q, 0]$	$(G_x, A_y, 0)$	$Pb'n'm'$
Γ_5	$[p, q, 0]$	$[p, q, 0]$	$[p, -q, 0]$	$[p, -q, 0]$	$(F_x, C_y, 0)$	$Pbn'm'$
Γ_6	$[0, 0, r]$	$[0, 0, -r]$	$[0, 0, -r]$	$[0, 0, r]$	$(0, 0, G_z)$	$Pbn'm$
Γ_7	$[p, q, 0]$	$[p, q, 0]$	$[-p, q, 0]$	$[-p, q, 0]$	$(C_x, F_y, 0)$	$Pb'nm'$
Γ_8	$[0, 0, r]$	$[0, 0, -r]$	$[0, 0, r]$	$[0, 0, -r]$	$(0, 0, A_z)$	$Pb'nm$

spin configurations in which both Cr and Ho belong to same MR *viz.*, Γ_1 , Γ_3 , Γ_5 and Γ_7 . Landau theory predicts that only one of the four above mentioned MRs is realized at the phase transition [153]. Further, simulation of neutron powder diffraction patterns was performed using the program *FullProf* for all four allowed spin configurations. The results of the simulations for three important magnetic reflections, $(1\ 0\ 0)$, $(0\ 1\ 0)$ and $(0\ 0\ 1)$ is presented in table 4.3. Simulations show that the magnetic reflection $(0\ 0\ 1)$ is allowed only in MRs Γ_1 and Γ_3 hence will produce a peak with finite intensity. But as NPD data collected at 3 K (figure 4.4) does not show any intensity corresponding to

(0 0 1), Γ_1 and Γ_3 representations can be excluded. Now, out of two remaining possible MRs, Γ_5 and Γ_7 , (0 0 1) is an allowed magnetic reflection only in Γ_5 which can be seen in the experimental data presented in figure 4.4, also (0 1 0) magnetic reflection which has a finite intensity in Γ_7 is not present in the experimental data. Hence from symmetry analysis along with the simulations of diffraction patterns of all four allowed MRs will lead to the conclusion that the MR in HCO is, unambiguously, Γ_5 ($Pbn'm'$). Hence, in the refinement of crystal and magnetic structures we used space group $Pbnm$ and magnetic representation Γ_5 ($Pbn'm'$), respectively.

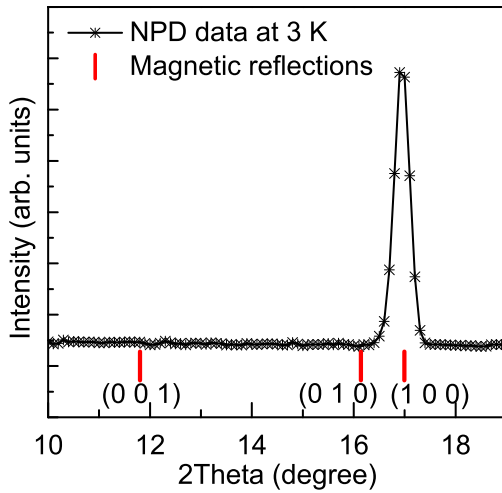


Figure 4.4: NPD data collected at 3 K along with the magnetic peak positions obtained by simulations using FullProf for different IRs.

IRs	Magnetic reflections		
	(0 0 1)	(0 1 0)	(1 0 0)
Γ_1	✓	✓	✓
Γ_3	✓	✓	✓
Γ_5	×	×	✓
Γ_7	×	✓	×

Table 4.3: Simulation results which shows whether the magnetic reflections (0 0 1), (0 1 0) and (1 0 0) are allowed (marked as ✓) or not (marked as ×) in a given irreducible representation allowed by symmetry.

4.3.1.3 Magnetic structure refinement

The Rietveld refinement of the crystal and magnetic structures from the NPD data yielded structural parameters and the ordered magnetic moments of Cr and Ho ions. The NPD patterns and results of Rietveld refinement of the data collected at 300 K, 100 K and 3 K is presented in figure 4.5 and the results are tabulated in table 4.4. An example of an input file used for the refinement of 3 K data using *FullProf* is given in appendix C.2. The lattice parameters obtained from the refinement of 300 K data are in good agreement with the ones obtained from PXRD measurements. From the refinement we found that for Cr spin configuration is (F_x, C_y, G_z) and that of Ho is $(F_x, C_y, 0)$ in

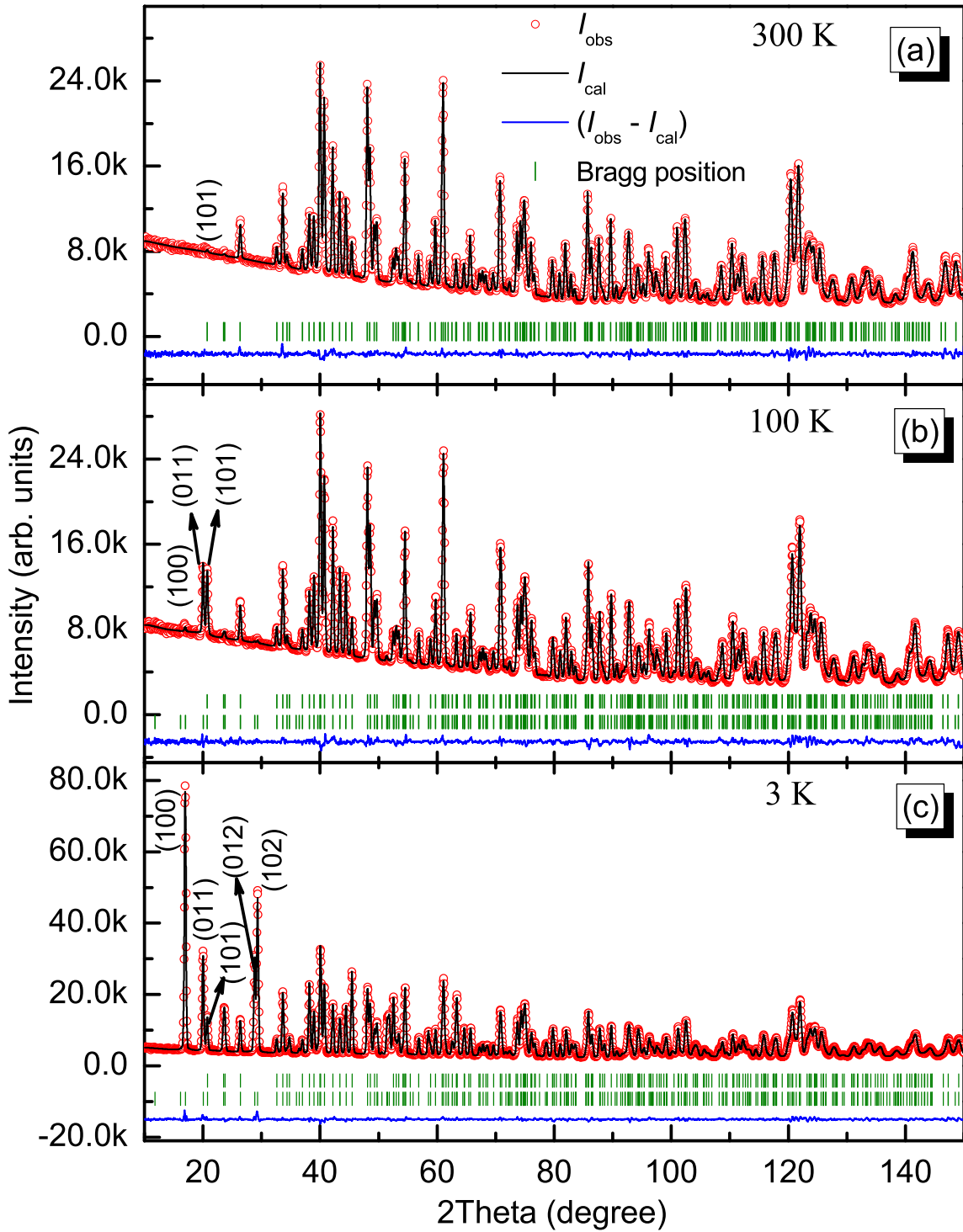


Figure 4.5: NPD data and Rietveld refinement results for HoCrO_3 at (a) 300 K, (b) 100 K and (c) 3 K. Red circles mark the data points, black line represents calculated pattern and blue line represents the difference. The bars below the patterns denote the position of nuclear and magnetic Bragg peaks. Few typical Bragg peaks are indexed.

4.3 Results and discussion

Table 4.4: Structural and magnetic data corresponding to simultaneous crystal and magnetic structure refinement performed at several characteristic temperatures (data presented only for magnetic ions).

		Temperature		
		300 K	100 K	3 K
a (\AA)		5.2472(1)	5.2393(1)	5.2388(1)
b (\AA)		5.5193(1)	5.5137(1)	5.5134(1)
c (\AA)		7.5414(1)	7.5282(2)	7.5270(1)
V (\AA^3)		218.406(8)	217.474(9)	217.406(6)
Atoms				
Cr	B_{iso} (\AA^2)	1.08(5)	0.69(4)	0.70(4)
	m_x, m_y, m_z (μ_B)	–	0.4(2), 0.9(1), 2.18(6)	0.10(4), 0.08(2), 2.61(4)
	m_{Cr} (μ_B)	–	2.40(8)	2.63(4)
	α ($^\circ$)	–	25(5)	7(11)
Ho	B_{iso} (\AA^2)	0.92(1)	0.62(2)	0.69(2)
	m_x, m_y (μ_B)	–	0.6(1), 0.4(1)	3.64(3), 7.01(3)
	m_{Ho} (μ_B)	–	0.7(1)	7.90(3)
	β ($^\circ$)	–	60(8)	27.5(2)
Discrepancy factors				
	χ^2	2.61	3.10	1.95
	R_p (%)	6.88	3.97	4.78
	R_{wp} (%)	5.81	5.93	5.11
	R_{mag} (%)	–	3.97	1.95

the whole temperature range below T_N . This result is in contrast to reported structure by Bertaut *et al.* [102], who predicted spin configuration of Cr at 4.5 K to be (G_z). Our results also contradicts the magnetic structure reported by Hornreich *et al.* [104] who, based on single crystal magnetization studies, predicted the spin configuration of Cr sublattice in whole temperature range below T_N to be G_z . Though our results support the magnetic structure determined by Shamir *et al.* [143], in contrast to their assumption

we have found that the canting angles of both Cr and Ho moments are not constant as function of temperature. The thermal variation of canting angles α of Cr moments and β of Ho moments are presented as insets in figure 4.7(a) and (c), respectively. The canting angles are represented pictorially in figure 4.7(e) and (f). The thermal variation of Cr^{3+} and Ho^{3+} magnetic moments derived from neutron data is shown in figure 4.7(a) and (c). The thermal variation of Ho moment value has an unusual shape, with an upward curvature in a large temperature range. The refined magnetic structure of HCO at 3 K is presented in figure 4.7(d).

The magnetic structure of HCO was also refined with only z -component of Cr magnetic moment. A comparison of magnetic R -factors (R_{mag}) for the refinements with x , y and z components of Cr magnetic moments (m_{Cr}^{xyz}) and with only z -component (m_{Cr}^z) is presented in figure 4.6. At all temperatures R_{mag} for the refinements with m_{Cr}^{xyz} is smaller than that for refinements with m_{Cr}^z . It should also be noted that at higher temperatures the difference between values of R_{mag} corresponding to the refinements with (m_{Cr}^{xyz}) and (m_{Cr}^z) increased. This is because at higher temperatures the canting angle between Cr magnetic moment is increased with temperature which can be seen in the inset of figure 4.7(a).

We applied the molecular field model in order to compute the temperature

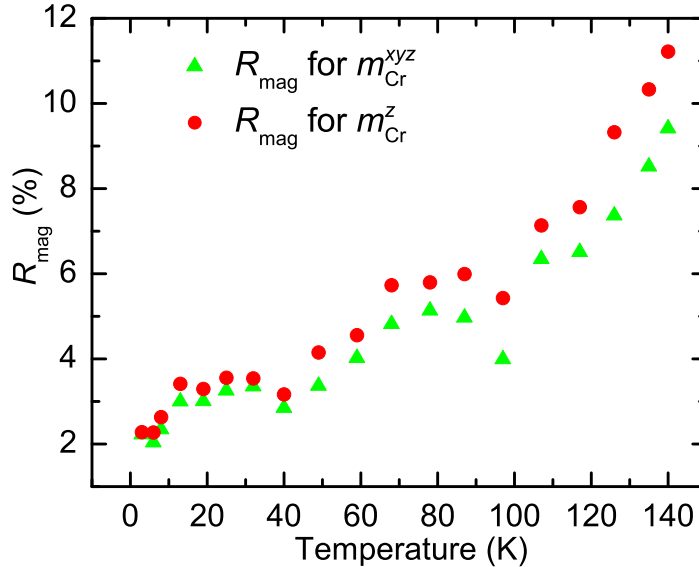


Figure 4.6: Comparison of magnetic R -factors (R_{mag}) obtained from the Rietveld refinement of NPD data. m_{Cr}^{xyz} corresponds to the refinement in which all x , y and z components of Cr magnetic moments are set as free parameters and m_{Cr}^z corresponds to the refinement with Cr moments only along z -axis.

dependence of ordered magnetic moments. We first computed temperature dependence of the Cr^{3+} moment by self-consistent mean-field calculation using the Brillouin function $B_{3/2}$ for $S = 3/2$ and a molecular-field constant λ_0 representing Cr-Cr exchange. The standard formula has to be slightly modified because the saturated Cr moment of $m_{\text{sat}} = 2.62(5) \mu_{\text{B}}$ is lower than the theoretical value, $gS \mu_{\text{B}} = 3 \mu_{\text{B}}$. So we used the following expression [154]:

$$m_{\text{Cr}}(T) = m_{\text{sat}} B_{3/2} \left[\frac{g\mu_{\text{B}}S\lambda_0 m_{\text{Cr}}(T)}{k_{\text{B}}T} \right] \quad (4.1)$$

Where $B_{3/2}$ is Brillouin function for spin only value $S = 3/2$ and λ_0 is molecular-field constant. In general, for an angular momentum J , the Brillouin function given by,

$$B_J(T) = \frac{2J+1}{2J} \coth \left(\frac{2J+1}{2J} T \right) - \frac{1}{2J} \coth \left(\frac{T}{2J} \right) \quad (4.2)$$

For Cr^{3+} , due to quenching of orbital angular moment, we have $J = S = 3/2$. Both m_{sat} and λ_0 were varied as free parameters in the least square fitting procedure. A good fit of the experimental data is obtained with $m_{\text{sat}} = 2.62(5) \mu_{\text{B}}$ and $\lambda_0 = 37.1(7) \text{ T}/\mu_{\text{B}}$. The result of fitting is shown as a solid line in the figure 4.7(a). The observed saturated magnetic moment per Cr^{3+} ion value $m_{\text{sat}} \approx 2.62(5)\mu_{\text{B}}$ at $T = 60 \text{ K}$ is lower than the expected value of $3 \mu_{\text{B}}$ indicating the presence of spin fluctuations down to temperatures as low as 3 K.

As mentioned before, the temperature dependence of order parameter for the Ho moment is quite unusual. The concave curvature of the order parameter may be explained with ground state quasi-doublet crystal field levels, split by an exchange field [155, 156] exerted by Cr sublattice ordering. The non-Kramer's Ho^{3+} ions in HCO are at the positions of local point symmetry m (Schoenflies symbol, C_{1h}) which typically leads to singlet ground-state. Thus the ground multiplet of Ho^{3+} ion, 5I_8 , split into 17 singlets by the crystalline field via $3d - 4f$ exchange interactions. From the reported neutron scattering results [157] and our specific heat studies presented in section (3.3.3), it should be noted that the first crystal electric-field (CEF) level ($\sim 16 \text{ K}$) is well separated from the next level (121 K). When two singlets are close enough and sufficiently isolated from other level they may be treated as *pseudo* or *accidental* doublet [158, 159]. At low temperatures only the ground-state doublet is appreciably populated because the energy difference between first CEF level and next CEF level is large. Taking into account only

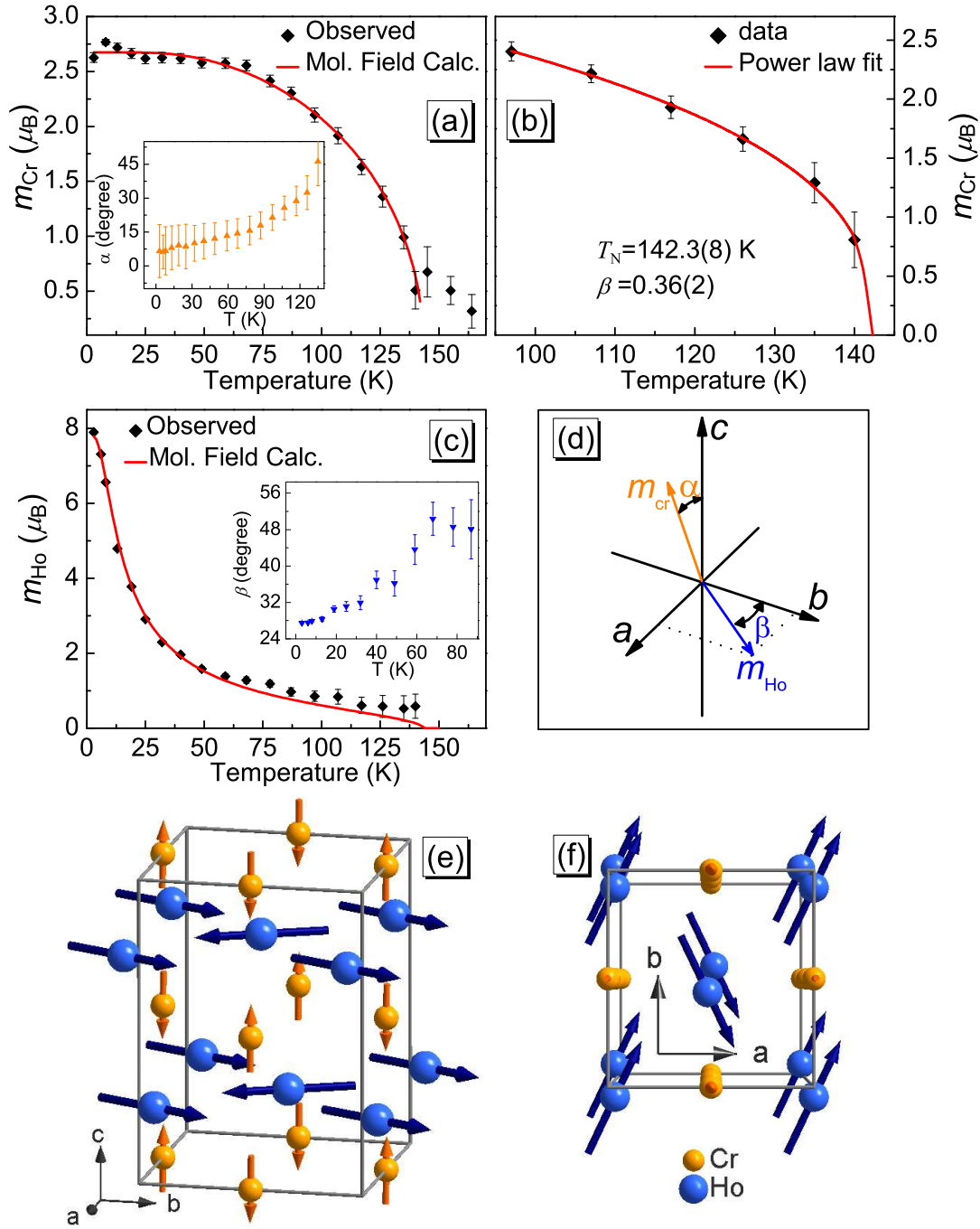


Figure 4.7: (a) The observed moment of Cr^{3+} (dots) and the molecular-field calculation (solid line). (b) A power-law fit to the temperature dependence of Cr ordered moment (c) Observed moment of Ho^{3+} and molecular-field calculation (solid line). Inset of (a) and (c) shows the temperature variation of canting angle of Cr^{3+} ordered moment about crystallographic c -direction (α) and the temperature dependence of canting angle of Ho^{3+} ordered moment about crystallographic b -direction (β), respectively. (d) Graphical representation of the canting angles α and β about crystallographic axes. (e)-(f) Graphical representation of the magnetic structure of HoCrO_3 at 3 K. The non-magnetic oxygen ions were excluded for clarity.

the ground-state doublet (accidental doublet), in case of HCO, and a splitting $\Delta(T)$. we can write [155, 156]:

$$m_{\text{Ho}}(T) = \frac{g_J \mu_B}{2} \tanh \left[\frac{\Delta(T)}{2k_B T} \right] \quad (4.3)$$

where, $\Delta(T) = g_J \mu_B B_{\text{Cr}}^{\text{eff}}(T)$ is the splitting of the ground state doublet by the effective field ($B_{\text{Cr}}^{\text{eff}}$) produced by the Cr sublattice. g_J is the Landé g factor of the free Ho^{3+} and μ_B is the Bohr magneton. The effective field should be proportional to the ordered magnetic moment of Cr, and can be written as: $B_{\text{Cr}}^{\text{eff}}(T) = B_0[(T_N - T)/T_N]^\beta$. The values of T_N and β were obtained by fitting the order parameter, the ordered moment (m_{Cr}) of Cr sublattice using power law fit:

$$m_{\text{cr}}(T) = m_0 \left[\frac{T_N - T}{T_N} \right]^\beta. \quad (4.4)$$

The least-square fit gave $m_0 = 3.63(9) \mu_B$, $T_N = 142.3(8)$ K and $\beta = 0.36(2)$. The results of the fitting are presented in figure 4.7(b).

We fitted the temperature dependence of Ho magnetic moments using the equation (4.3) by writing $\Delta(T)$ in terms of $B_{\text{Cr}}^{\text{eff}}(T)$ along with the values, $T_N = 142.3(8)$ K and $\beta = 0.36(2)$. The fit result is shown as a solid line in figure 4.7(c). From the fitting we obtained the value of $B_0 = 25(2)$ T and the corresponding $\Delta(T = 0) = 1.8(3)$ meV. The value of $\Delta = 1.8(3)$ meV is comparable to the ground state splitting of Ho crystal field levels in HCO, measured using inelastic neutron scattering (INS), 1.65 meV [157] and the value obtained from our specific heat measurements, 1.379(4) meV. We calculated molecular-field constant λ_1 associated with Cr-Ho exchange interactions, using the expression $B_{\text{eff}}(T) = \lambda m_{\text{Cr}}(T)$ [155]. Using the value of saturated magnetic moment $m_{\text{sat}} \approx 2.62 \mu_B$ the value of $B_0 \approx 25$ we get $\lambda_1 \approx 9.5$ T/ μ_B .

The unusual upward curvature comes from the tanh function with a small argument, with the molecular-field constant $\lambda_{\text{Cr-Ho}} (= \lambda_1)$ being much smaller than $\lambda_{\text{Cr-Cr}} (= \lambda_0)$. With this model, a small ordered Ho moment should persist up to $T_N = 142$ K. From this analysis it can be concluded that the Ho ions orient in a non-vanishing net molecular field through Ho-Cr exchange and also Cr-Cr exchange interactions are much higher than the Ho-Cr exchange in this compound. In large number of intermetallic compounds it was found that $4f - 4f$ exchange interactions are negligible. The non-interaction of RE moments should be understood as relative weakness of the RE-RE exchange interaction in such compounds [160]. Thus, a peculiar hierarchy of

exchange interactions takes place in $3d - 4f$ magnetic material, which can schematically expressed as $(3d - 3d) \gg (3d - 4f) \gg (4f - 4f) \approx 0$. This fact enables us to regard the $3d$ subsystem (Cr) that orders due to its internal forces, as something external with respect to the RE (Ho). Then from the view point of the $4f$ electrons the $3d - 4f$ exchange can be presented as the action of an exchange field produced by the ordered $3d$ subsystem. Following the above discussion in HCO, Ho-Ho exchange interactions could be neglected compared to strong, Cr-Cr and Ho-Cr exchange interactions.

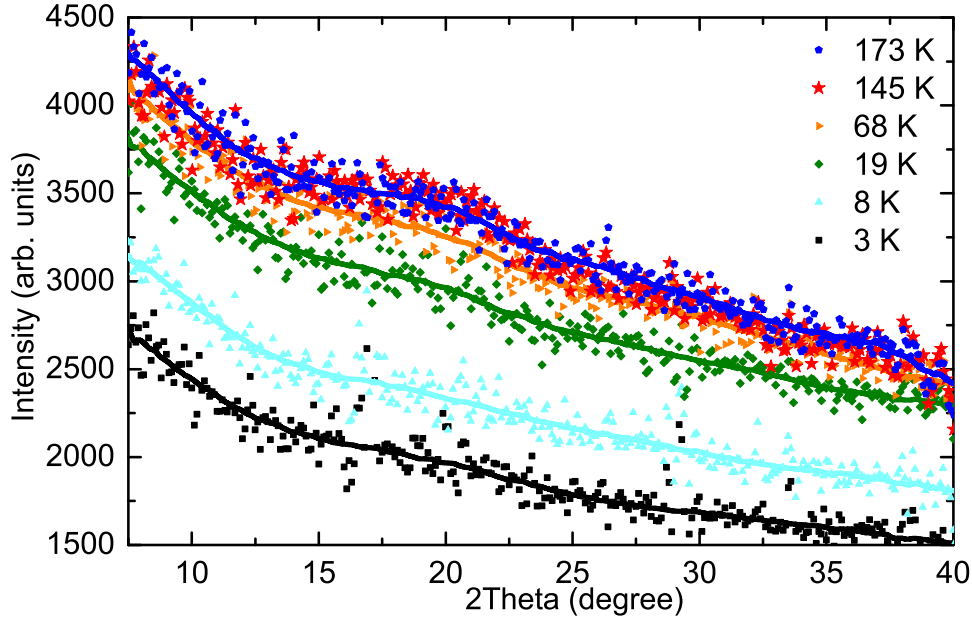


Figure 4.8: The variation in background with temperature, showing the overall decrease in low-angle paramagnetic scattering with decreasing temperature (see text). The solid lines are guides to eyes.

As discussed earlier, to check the existence of possible spin fluctuations in the form of short range ordering we carefully analyzed the low-angle region of NPD pattern. The low-angle paramagnetic scattering decreases significantly from 300 to 3 K (figure 4.8). The plots in figure 4.8 were obtained by subtracting the calculated (Rietveld refined) pattern, with out a background correction, from the observed data at each temperature. A weak broad peak centered near a d -spacing of $\sim 4.4 \text{ \AA}$ ($2\theta \approx 20^\circ$ and $Q \approx 1.41 \text{ \AA}^{-1}$) indicating the presence of short range order, the presence of this peak even at 19 K indicates that short-range correlations persist into the long-range-ordered regime. Furthermore, position of the broad peak coincides with the magnetic reflection (1 0 1) which corresponds to

the ordering of Cr ions (4.1). This indicates that the the origin of short range ordering is being the spin fluctuations in the Cr sublattice, which can also be understood as the reason for the significantly smaller saturated moment value of Cr ions determined from the refinement. The temperature dependence of the peak and the overall background gives a clear idea of their origin. The overall background changes slightly with decrease in temperature from 173 to 19 K, on the other hand, the broad peak diminishes significantly below 60 K where the Cr magnetic moments reach saturation value, though a broad feature is perceivable down to 3 K. A quantitative analysis of short range ordering is not possible from the present data due to high noise level. Single crystal neutron diffraction measurements can shed light on this phenomena.

4.3.2 Magnetoelastic effect

Figure 4.9 shows the temperature variation of the lattice parameters and the unit cell volume determined from the Rietveld refinement of NPD data. As the temperature decreases, all three lattice parameters decrease and show an abrupt change at $T_N \approx 142$ K. Changes in lattice parameters a and c around magnetic ordering temperature are smaller compared to b and unit cell volume (V). The unit cell volume therefore also decrease abruptly at T_N . The anomalous behavior of the temperature variation of lattice parameters and unit cell volume is due to the magneto-elastic effect associated with the antiferromagnetic transition at the Néel temperature. In order to study the spontaneous magnetostriction it is necessary to determine the temperature variation of the lattice parameters and the unit cell volume in the absence of magnetism. One way to determine the background temperature variation of the lattice parameter and unit cell volume is to extrapolate the paramagnetic high temperature data to low temperature by fitting with a polynomial function [161]. This method works approximately in some cases but in general involves some uncertainty. Alternatively, one can use the Grüneisen approximation for the zero pressure equation of state, in which the effects of thermal expansion are considered to be equivalent to elastic strain [162]. Thus, the temperature dependence of the volume can be described by $V(T) = \gamma U(T)/B_0 + V_0$, where γ is a Grüneisen parameter, B_0 is the bulk modulus and V_0 is the volume at $T = 0$ K in the absence of magnetoelastic effect. By adopting the Grüneisen approximation, the internal

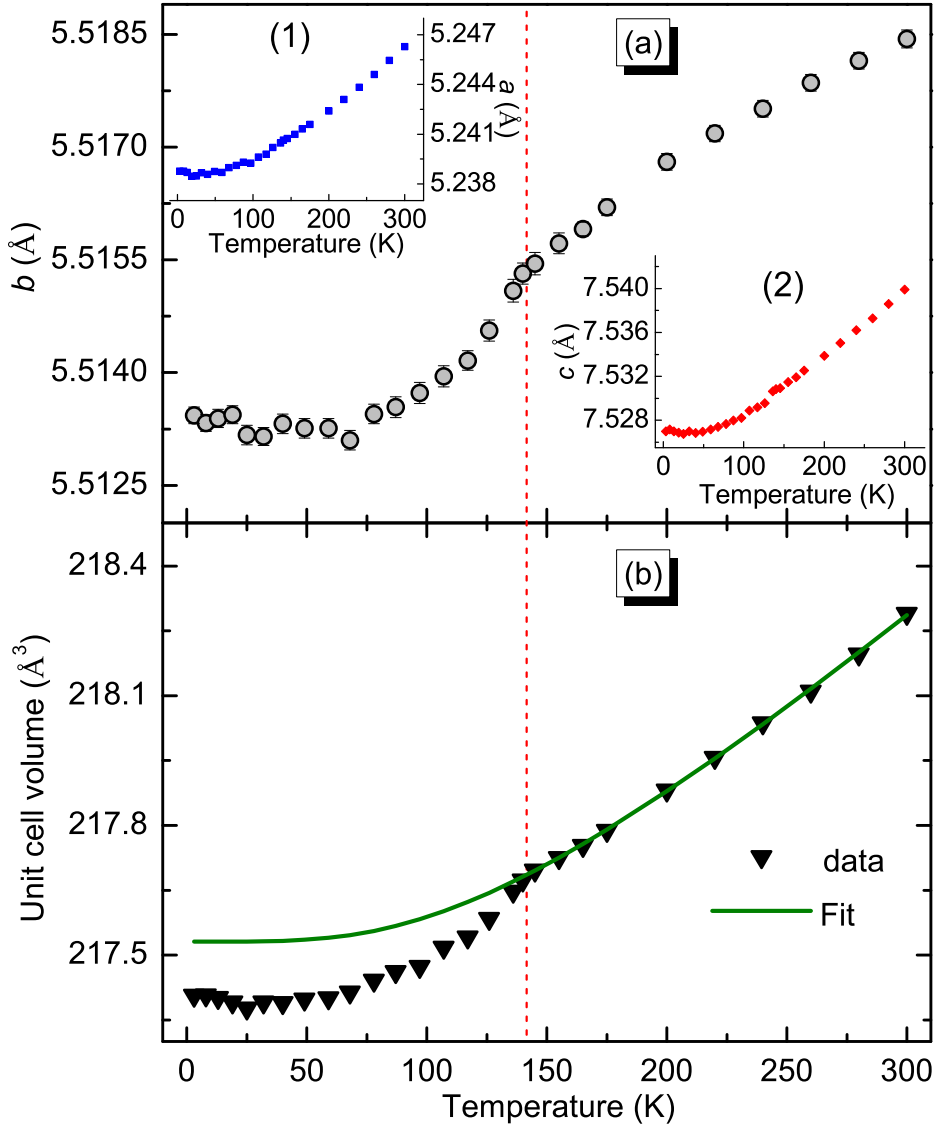


Figure 4.9: (a) The temperature dependence of lattice parameter b , inset (1) and (2) shows the temperature dependence of lattice parameters a and c respectively. (b) The temperature dependence of unit cell volume. The solid line is the fit of the Debye model as described in the text. The vertical dashed line corresponds to T_N .

energy $U(T)$ is given by

$$U(T) = 9Nk_{\text{B}}T \left(\frac{T}{\theta_{\text{D}}} \right)^3 \int_0^{\theta_{\text{D}}/T} \frac{x^3}{e^x - 1} dx \quad (4.5)$$

where N is the number of atoms in the unit cell, k_{B} is Boltzmann's constant and θ_{D} is the Debye temperature. By fitting the unit cell volume of HCO in the paramagnetic state we can get the physical parameters θ_{D} and V_0 . From the present fitting procedure it was not possible to determine γ and B_0 but the ratio of γ/B_0 was set as variable and was found to be 0.500(2) GPa. The result of the fit is shown as a solid line in figure 4.9(b). The value of θ_{D} obtained from the fit was 507(38) K and $V_0 = 217.53(1) \text{ \AA}^3$. Note that the fit line (figure 4.9(b)) deviates from the data at ~ 142 K where the lattice constants and the volume also reflects a marked change. This is inferred as a clear indication of magnetoelastic or magnetovolume effects present in this system.

The excess change in the unit cell volume $|\Delta V|$ due to magnetoelastic effect (exchange striction) is plotted in the temperature range 60–140 K in figure 4.10(a). The inset shows the temperature dependence of $|\Delta V|$ in the temperature range 3–173 K. The ΔV value can be considered as the secondary order parameter. The solid line in figure 4.10(a) is a result of the least-square power-law fit to the temperature variation of ΔV given by the equation,

$$\Delta V = \Delta V_0 \left[\frac{T_{\text{N}} - T}{T} \right]^{\beta'} \quad (4.6)$$

From the least-squares fit we determined $T_{\text{N}} = 141.2(6)$ K and $\beta' = 0.50(5)$. The critical temperature obtained by this fit is about the same, within the error limits, as the Néel temperature determined by fitting the ordered magnetic moment of Cr. We do not trust the critical exponent thus determined due to the uncertainty in the determination of the background, and also due to limited number of measurement points near the transition temperature.

In order to check how the lattice strain ΔV couple to the order parameter it is plotted against the ordered moment per Cr ion in the temperature range 19–135 K as shown in figure 4.10(b). One expects the lattice strain ΔV due to the magnetoelastic effect (exchange striction) to be proportional to the order parameter or ordered magnetic moment [163]. It is clear from the figure 4.10(b), despite the large error bars the linear relationship is fulfilled.

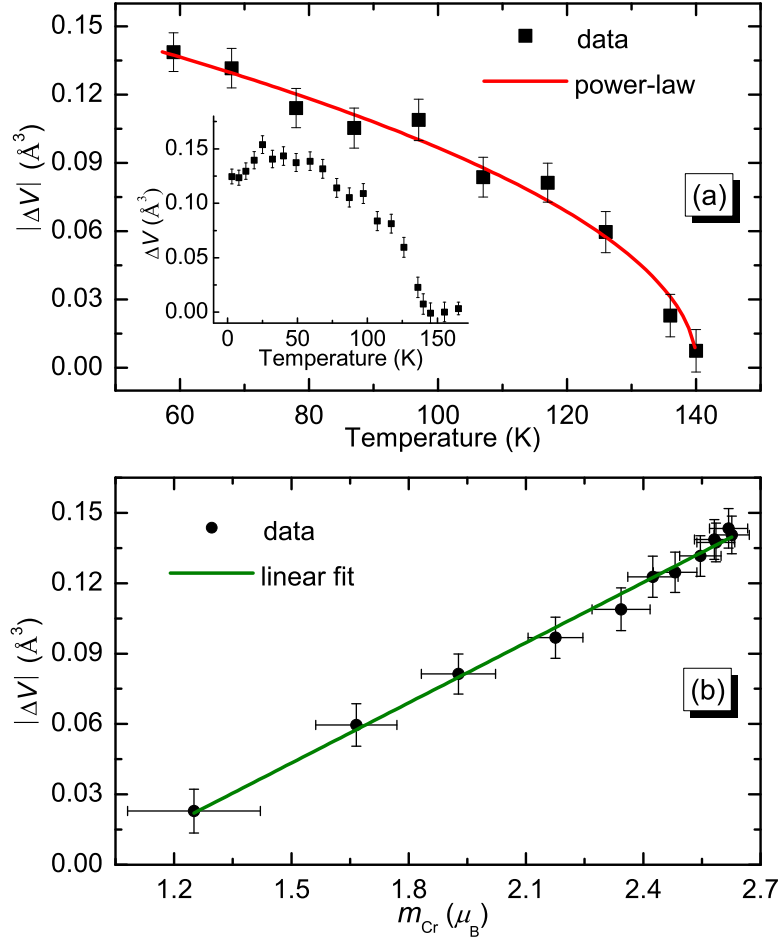


Figure 4.10: (a) Temperature variation of $|\Delta V|$, which is obtained from the unit cell volume V by subtracting the background by the method explained in the text. Solid line is the power-law fit. The inset shows the ΔV in the temperature range 3 – 170 K. (b) ΔV versus Cr-ordered moment in the temperature region 25 – 135 K.

4.4 Conclusions

Neutron powder diffraction measurements were performed on polycrystalline HoCrO_3 samples in the temperature range 3 – 300 K. From the Rietveld refinement of the data we deduced the crystal and magnetic structures. The crystal and magnetic structures are refined in the space groups $Pbnm$ and $Pbn'm'$ respectively. Thermal variation of magnetic moments confirms that spin configuration of Cr ion is (F_x, C_y, G_z) in the whole temperature range. Despite the large error bars, the canting angle α was found to be temperature dependent. The thermal variation of Ho ordered moment indicates the induced type of magnetic ordering. The ordered moment of Cr increases abruptly below the Néel temperature of 142 K and reaches a saturated value of $2.62(5)\mu_{\text{B}}$ at around 60 K. The ordered moment of Ho ion on the other hand remains rather small down to

25 K, below which it increases sharply. The thermal variation of the ordered moments of both, Cr and Ho ions, can be modeled using mean field theory. The results of the least squares fit of ordered moments using mean field theory gave the molecular field constants, $\lambda_0 \approx 37.1 \text{ T}/\mu_B$ and $\lambda_1 \approx 9.5 \text{ T}/\mu_B$, which confirms rather strong Cr-Cr exchange significantly weak Ho-Cr exchange in this compound. From the fitting crystal field splitting of the ground state *accidental* doublet by the effective field produced by the Cr sublattice is, $\Delta = 1.8(3) \text{ meV}$. This value is in agreement with reported values. The small saturated moment, $2.67(1)\mu_B$ per Cr ion hints to possible spin fluctuations. This was confirmed by the observation of a short range ordering resulting in a broad peak centering at the magnetic peak associated with Cr ordering. This observation still needs to be scrutinized, with the help of single crystal neutron scattering experiments.

We also investigated the thermal variation of the lattice constants and unit cell volume of HoCrO_3 . The results of the present investigation show that all lattice parameters and unit cell volume exhibit an anomalous change near $T_N = 142 \text{ K}$ due to magnetoelastic or magnetovolume effect. From a qualitative analysis of the extra change in unit cell volume ΔV due to magnetoelastic effect, we established a linear relationship between ΔV and magnetic moment of the Cr ion.

Chapter 5

CRYSTAL FIELDS AND MAGNETIC EXCITATIONS IN HoCrO_3

5.1 Introduction

The concept of crystal field was first developed by Bethe in 1929 to study the effect of surrounding ions on the electron distribution of a single magnetic ion on a lattice. The ion and its surrounding ions were modeled as uniform spheres, their charges located at a point in the center, with no overlapping of the charge distributions. The crystal field was then defined as the effect of those charges on the central ion, calculated solely from the coulomb interaction between the central and surrounding ions. Crystal field theory (CFT) is the method of calculating the effect of crystal fields on physical properties of the system. The crystal field interactions in rare-earth compounds are responsible for a great variety of magnetic phenomena. In such compounds, magnetism is partially due to the incompletely filled $4f$ shells.

A variety of experimental techniques were employed to study CF interactions. Most commonly used techniques are heat capacity measurements, optical spectroscopy and Inelastic Neutron Scattering (INS). INS has become the key tool to measure crystal-field transitions. INS is by far the most unique and perhaps direct experimental method for the determination of the CF interactions in RE compounds. CF interactions in HoCrO_3 was studied by optics [121], magnetization and magnetic susceptibility [104], specific heat [122], elastic neutron diffraction [123] and inelastic neutron scattering (INS) [124]. Based on these measurements five CF levels have been found at 1.65 meV (19.2 K), 10.4 meV (121 K), 15.5 meV (179 K), and 23.5 meV (272 K) lowest level being at 0 meV. In the present chapter we present our investigations of HCO from INS. Our aim is to study the lowest lying CF levels and also to investigate the presence of spin fluctuations as indicated by our elastic neutron scattering measurements on HCO.

5.2 Crystal field calculation

5.2.1 Crystal field theory versus Ligand field theory

Crystal field theory is one of several chemical bonding models and one that is applicable exclusively to the transition metal and lanthanide elements. CFT describes the origin and consequences of interactions of the surroundings on the orbital energy levels of a transition metal or lanthanide element. If the crystalline electric field effects are taken as a perturbation on the appropriate free-ion wave functions and energy levels, the problem becomes that of finding the perturbing Hamiltonian and its matrix elements. The energy

levels in the crystal field can then be found from standard perturbation theory. Many effects are neglected in this simple theory. A more general model of the field due to the surrounding ions might include covalency effects, spatial distribution of charge allowing for charge distribution overlap, and ligand bond strengths. The term *ligand field theory* has been coined to describe the manner in which the physical properties of an ion in a compound are influenced by all effects of the surrounding ions. CFT is then a limiting case of ligand field theory which considers only electrostatic interactions.

5.2.2 Point-charge model

It has been found that many results of ligand field theory depend largely on the symmetry of the distribution of the ligand surrounding the central ions, and far less on the details of the model. Therefore useful information can be obtained from simple point-charge model using crystal field theory which includes all the information on symmetry of the surrounding ligand. Consider a rare-earth (RE) ion in a solid. The $4f$ electrons experience an electrostatic field potential $V_{\text{CF}}(\vec{r})$ which is set up by the surrounding charge distribution $\rho(\vec{R}_i)$. The potential reflects the point symmetry of the RE ion. The crystal field (CF) at RE ion is based on the electrostatic potential defined by

$$V_{\text{CF}}(\vec{r}) = \sum_j \frac{\rho(\vec{R}_j)}{|\vec{r} - \vec{R}_j|} \quad (5.1)$$

where $\rho(\vec{R}_j)$ denote the charge at the site \vec{R}_j of the i th ligand ion. The CF Hamiltonian *i. e.* the potential energy of all the $4f$ electrons of a RE ion in the crystalline electric field (no external field) is then given by [164],

$$H_{\text{CF}} = e \sum_i V_{\text{CF}}(\vec{r}_i) \quad (5.2)$$

The index i goes over the $4f$ shell. Usually for RE ions the spin-orbit energy is much larger than the CEF energy. Therefore it is sufficient to consider the lowest J multiplets of the $4f$ shell only. Limiting to the lowest multiplet results in drastic simplifications. According to the *Stevens operator equivalents* H_{CF} can be expressed in terms of polynomials in J_α ($\alpha = x, y, z$) operators [165]. They act on the $4f$ shell as a whole and not on individual $4f$ electrons as do the polynomials in x_i, y_i, z_i which appears in $V_{\text{CF}}(\vec{r}_i)$.

The following rules hold for transforming an expression of the form $f(x_i, y_i, z_i)$ into an equivalent one expressed in J operators. Replacing any polynomial in x, y, z by the corresponding product of J_x, J_y, J_z can be written in a symmetrized form. The constants of proportionality depend on the degree l of the polynomial and on L, S and J . They include average $\langle r^l \rangle$ over the $4f$ wave functions. For example [166],

$$\begin{aligned} \sum_i (x_i^2 - y_i^2) &\equiv \alpha_J \langle r^2 \rangle [J_x^2 - J_y^2] \\ &= \alpha_J \langle r^2 \rangle O_2^2. \end{aligned} \quad (5.3)$$

$$\begin{aligned} \sum_i \frac{1}{2} \{ (x_i + iy_i)^4 + (x_i - iy_i)^4 \} &\equiv \beta_J \langle r^4 \rangle \frac{1}{2} [J_+^4 - J_-^4] \\ &= \beta_J \langle r^4 \rangle O_4^2. \end{aligned} \quad (5.4)$$

For Ho^{3+} we have listed S, L, J and the $\alpha_J, \beta_J, \gamma_J$ as well as $\langle r^l \rangle (l = 2, 4, 6)$ in tables (5.1) and (5.2), respectively. The resulting form for H_{CF} is conventionally written as

$$H_{\text{CF}} = \sum_{l,m} B_l^m O_l^m \quad (5.5)$$

where B_l^m and O_l^m are, respectively, CF parameters and Stevens operator equivalents [167]. Equation (5.5) gives rise to a decomposition of the $(2J+1)$ -fold degenerate ground-state multiplet into a series of crystal field states Γ_i with energies E_i . A complete list of the Stevens operators O_l^m was presented by Hutchings [166].

Table 5.1: Quantum numbers for $\text{spin}(S)$, $\text{orbital}(L)$ and total angular momentum (J) and the Landé g -factor (g_J) of the ground state multiplet of Ho^{3+} ion.

Number of 4f electrons	S	L	J	g_J
10	2	6	8	5/4

Few of the matrix elements of $O_2^0 = 3J_z^2 - j(j+1)$ for Ho^{3+} with $J = 8$ were calculated as below:

$$\begin{aligned} [\langle -8 | J_z^2 | -8 \rangle] - 8(8+1) &= 120 \\ [\langle -7 | J_z^2 | -7 \rangle] - 7(7+1) &= 75 \text{ and so on...} \end{aligned}$$

5.2 Crystal field calculation

Table 5.2: List of $\langle r^n \rangle$ for $n = 2, 4, 6$, Stevens factors α_j , β_J , and γ_J for Ho^{3+} ion.

$\langle r^2 \rangle (\text{\AA}^2)$	$\langle r^4 \rangle (\text{\AA}^4)$	$\langle r^6 \rangle (\text{\AA}^6)$	$\alpha_J \times 10^2$	$\beta_J \times 10^4$	$\gamma_J \times 10^6$
0.2085	0.1081	0.1181	-0.222	-0.333	-1.30

The resulting matrix of O_2^0 will be of the form,

$$\begin{pmatrix}
 120 & 0 & 0 & 0 & 0 & 0 & 0 & 0 & 0 & 0 & 0 & 0 & 0 & 0 & 0 & 0 & 0 & 0 \\
 0 & 75 & 0 & 0 & 0 & 0 & 0 & 0 & 0 & 0 & 0 & 0 & 0 & 0 & 0 & 0 & 0 & 0 \\
 0 & 0 & 36 & 0 & 0 & 0 & 0 & 0 & 0 & 0 & 0 & 0 & 0 & 0 & 0 & 0 & 0 & 0 \\
 0 & 0 & 0 & 3 & 0 & 0 & 0 & 0 & 0 & 0 & 0 & 0 & 0 & 0 & 0 & 0 & 0 & 0 \\
 0 & 0 & 0 & 0 & -24 & 0 & 0 & 0 & 0 & 0 & 0 & 0 & 0 & 0 & 0 & 0 & 0 & 0 \\
 0 & 0 & 0 & 0 & 0 & -45 & 0 & 0 & 0 & 0 & 0 & 0 & 0 & 0 & 0 & 0 & 0 & 0 \\
 0 & 0 & 0 & 0 & 0 & 0 & -60 & 0 & 0 & 0 & 0 & 0 & 0 & 0 & 0 & 0 & 0 & 0 \\
 0 & 0 & 0 & 0 & 0 & 0 & 0 & -69 & 0 & 0 & 0 & 0 & 0 & 0 & 0 & 0 & 0 & 0 \\
 0 & 0 & 0 & 0 & 0 & 0 & 0 & 0 & -72 & 0 & 0 & 0 & 0 & 0 & 0 & 0 & 0 & 0 \\
 0 & 0 & 0 & 0 & 0 & 0 & 0 & 0 & 0 & -72 & 0 & 0 & 0 & 0 & 0 & 0 & 0 & 0 \\
 0 & 0 & 0 & 0 & 0 & 0 & 0 & 0 & 0 & 0 & -69 & 0 & 0 & 0 & 0 & 0 & 0 & 0 \\
 0 & 0 & 0 & 0 & 0 & 0 & 0 & 0 & 0 & 0 & 0 & -60 & 0 & 0 & 0 & 0 & 0 & 0 \\
 0 & 0 & 0 & 0 & 0 & 0 & 0 & 0 & 0 & 0 & 0 & 0 & -45 & 0 & 0 & 0 & 0 & 0 \\
 0 & 0 & 0 & 0 & 0 & 0 & 0 & 0 & 0 & 0 & 0 & 0 & 0 & -24 & 0 & 0 & 0 & 0 \\
 0 & 0 & 0 & 0 & 0 & 0 & 0 & 0 & 0 & 0 & 0 & 0 & 0 & 0 & 3 & 0 & 0 & 0 \\
 0 & 0 & 0 & 0 & 0 & 0 & 0 & 0 & 0 & 0 & 0 & 0 & 0 & 0 & 0 & 36 & 0 & 0 \\
 0 & 0 & 0 & 0 & 0 & 0 & 0 & 0 & 0 & 0 & 0 & 0 & 0 & 0 & 0 & 0 & 75 & 0 \\
 0 & 0 & 0 & 0 & 0 & 0 & 0 & 0 & 0 & 0 & 0 & 0 & 0 & 0 & 0 & 0 & 0 & 120
 \end{pmatrix}$$

The crystal field calculations using point charge model were carried out using the software package McPhase [168]. The non-Kramer's Ho³⁺ ions in HCO are at the positions of local point symmetry m (C_{1h}) which typically leads to singlet ground-state. Thus the ground multiplet of Ho³⁺ ion, 5I_8 , split into $2J + 1 = 17$ singlets by the crystalline field via $3d - 4f$ exchange interactions. The 15 non zero crystal field parameters (B_l^m) for the point symmetry m are presented in table 5.3 [169].

Table 5.3: Non zero crystal field parameters corresponding to point symmetry m (C_{1h}).

B_2^0	$B_2^{\pm 2}$	B_4^0	$B_4^{\pm 2}$	$B_4^{\pm 4}$	B_6^0	$B_6^{\pm 2}$	$B_6^{\pm 4}$	$B_6^{\pm 6}$
+	\pm	+	\pm	\pm	+	\pm	\pm	\pm

In a polycrystalline sample, neutron-scattering cross section for a CF transition $i \rightarrow i'$ (in units of b/sr/meV) at a temperature T is expressed in dipole approximation as [170]

$$\begin{aligned}
 \frac{d^2\sigma(i \rightarrow i')}{d\Omega dE'} &= \frac{k'}{k} S(Q, \omega) \\
 &= N \frac{k'}{k} \left(\frac{\hbar\gamma e^2}{mc^2} \right) e^{-2W} \left| \frac{1}{2} g_j F(Q) \right|^2 \frac{\exp(-E_i/k_B T)}{\sum_j \exp(-E_j/k_B T)} \\
 &\quad \times \sum_{\alpha=x,y,z} \frac{2}{3} |\langle i | J^\alpha | i' \rangle|^2 \delta(E_i - E_{i'} - \hbar\omega). \tag{5.6}
 \end{aligned}$$

Here k'/k is the ratio of the momenta of the scattered and the incident neutrons, $4\pi(\hbar\gamma e^2/mc^2)$ is the total magnetic cross section ($= 3.65$ barns), $\gamma = g_n/2\hbar$ ($g_n = 1.913$) is the gyromagnetic ratio of the neutron, and $e^2/mc^2 = 2.82$ fm is the classical electron radius. Furthermore, $z [= \sum_j \exp(-E_j/k_B T)]$ is the single ion partition function, $\sum_{\alpha=x,y,z} |\langle i | J^\alpha | i' \rangle|^2$ is the sum of squares of the transition matrix elements of the angular momentum operator, and $\mathbf{F}(\mathbf{Q})$ is the magnetic form factor of Ho³⁺ ion. In order to compare the cross section given in equation (5.6) to the experimental data, it was convoluted for each transition $i \rightarrow i'$ by a Gaussian with an energy dependent linewidth.

5.3 Experimental

Inelastic neutron scattering experiments were carried out with high-resolution time-of-flight spectrometer FOCUS at the spallation neutron source SINQ at PSI Villigen. The measurements were performed in the temperature range 1.5–200 K using three different incident energies of 19.61, 10.245 and 3.45 meV. The scattered neutrons were detected by an array of ^3He counters covering a large range of scattering angles $10 \leq \Phi \leq 130$. The polycrystalline sample was enclosed in an aluminium cylinder (12 mm diameter, ~ 45 mm height) and placed into a He cryostat, several spectra were collected in the temperature range $1.5 \leq T \leq 200$ K. Additional experiments were performed for the empty container as well as for vanadium to allow the correction of the raw data with respect to background, detector efficiency, absorption, and detailed balance according to standard procedures.

5.4 Results and discussion

5.4.1 Crystal field levels

Few typical INS spectra measured with incident neutron energies $E_i = 19.61$ meV and $E_i = 10.245$ meV are presented in figure 5.2 and figure 5.3, respectively. For the present results we corrected Q resolved raw-experimental data (left panels in figures 5.2 and 5.3) for background scattering, detector efficiency, absorption and self-shielding and transformed to intensity profiles ($S(Q, \omega)$) on energy scale (right panels in figures 5.2 and 5.3) using the software package DAVE (Data Analysis and Visualization Environment) developed at the NIST Center for Neutron Research (NCNR) [171]. In neutron spectroscopy if a spherical target is used, element sensitivities will be directly proportional to those obtained by irradiation in an isotropic neutron field, *i. e.*, one in which the effects of scattering are negligible. The results obtained from any other target shape needs to be corrected for self-shielding and absorption. Absorption and self-shielding corrections compensate for absorption of neutrons by the sample and neutrons that scatter more than once. The correction for background scattering and detector efficiency were accounted by the measurements on empty sample holder (aluminium cylinder) and an empty vanadium can. The self shielding corrections were applied for the cylindrical shaped sample with the help of self-shielding factors calculated

from the tools included in the software package DAVE.

INS spectra taken at 1.5 K exhibit three well-resolved inelastic peaks at energies 1.41(1), 10.10(2) and 15.50(2) meV which are presented in figure 5.1.

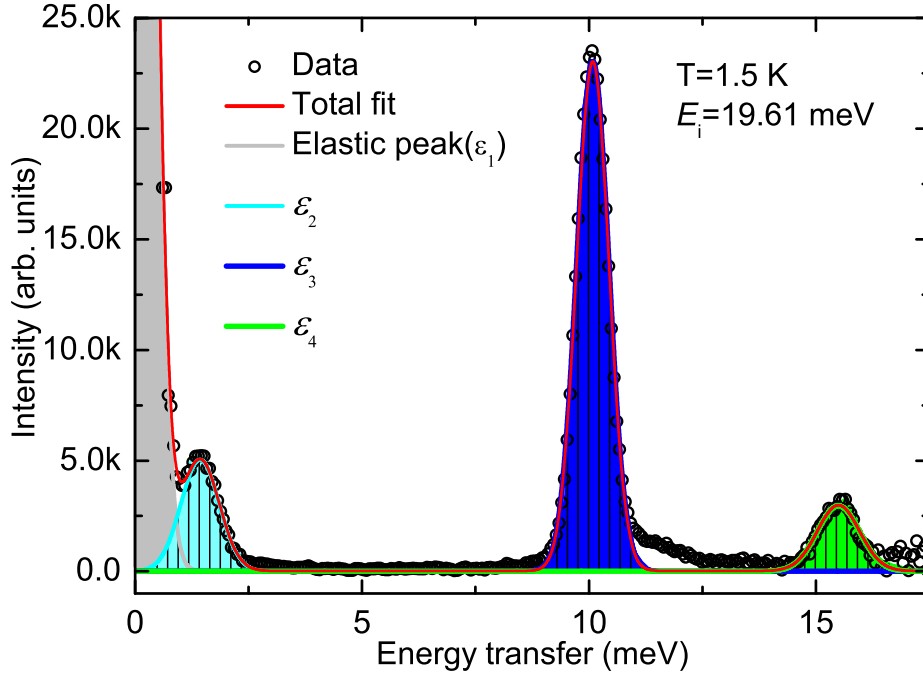


Figure 5.1: INS spectra measured at 1.5 K with neutrons of incident energy $E_i = 19.61$ meV. Three well resolved peaks at ε_2 , ε_3 and ε_4 are fitted using a gaussian peak function (shaded regions).

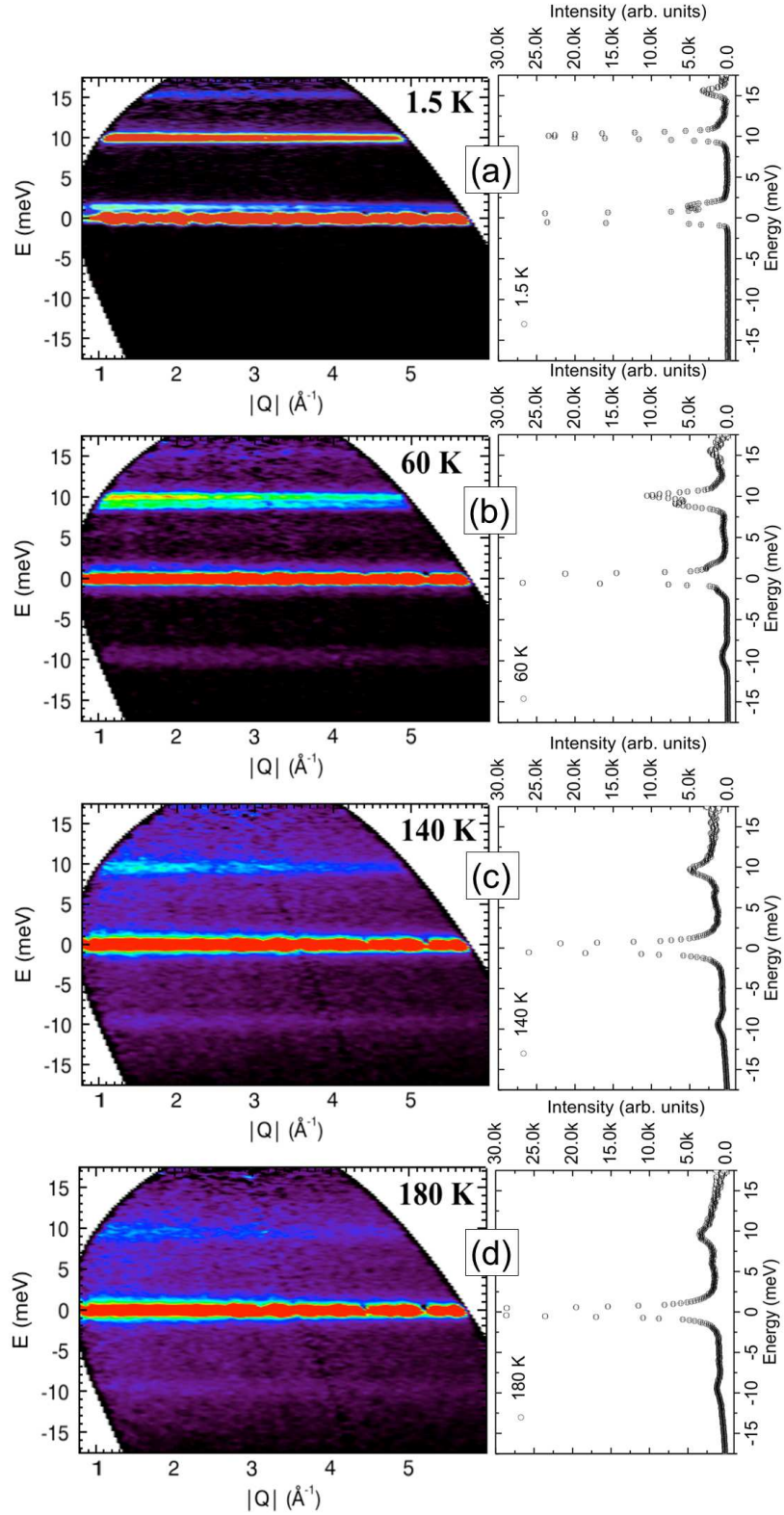


Figure 5.2: Typical INS spectra (left panels) measured with incident energy $E_i = 19.61$ meV at (a) 1.5 K, (b) 60 K, (c) 140 K, and (d) 180 K. Right panels are the intensity profiles obtained by summing the intensities over whole Q range.

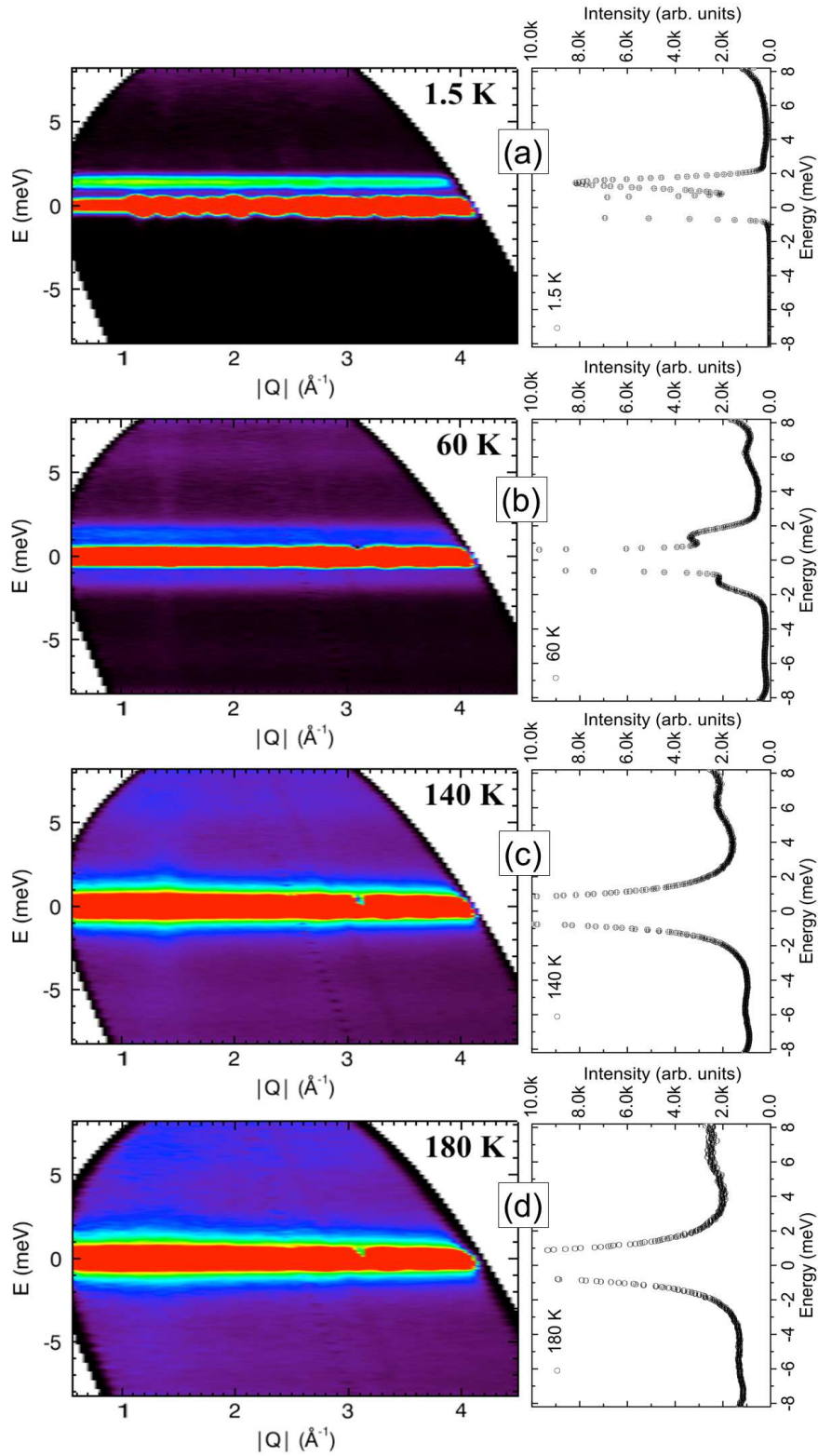


Figure 5.3: Typical INS spectra (left panels) measured with incident energy $E_i = 10.245$ meV at (a) 1.5 K, (b) 60 K, (c) 140 K, and (d) 180 K. Right panels are the intensity profiles obtained by summing the intensities over whole Q range. A careful inspection of the data reveal a intensity surge around $Q = 1.4 \text{ \AA}^{-1}$ in (b), (c) and (d).

First we calculated CF parameters using point charge model by considering 8 nearest neighbor Cr ions and 12 oxygen ions as shown in figure 5.4. The energy level diagram obtained from crystal field calculations using the point charge model and energy eigenvalues are presented in figure 5.5. CF parameters thus obtained were used for the least square fitting of INS spectra collected at 1.5 K ($E_i = 19.61$ meV) using the software McPhase. The results of least squares fit are presented in figure 5.6. The program McPhase is not able to calculate the smallest energy eigenvalue ($\varepsilon_2 = 1.41$ meV) which is shifted to zero because of the calibration freedom. From the reported neutron scattering results [157] and our specific heat studies presented in section (3.3.3), it should be noted that the first CEF level at ~ 1.45 meV (~ 16 K) is well separated from the next level 10 meV (110 K). When two singlets are close enough and sufficiently isolated from other level they may be treated as *pseudo* or *accidental* doublet [158, 159]. Further more due to low point symmetry of Ho^{3+} which results in 17 CF levels, the maximum energy range covered in our measurements (~ 18 meV), is very small. This leads the computation of CF levels by Rietveld least squares fitting of INS spectra using point charge model cumbersome.

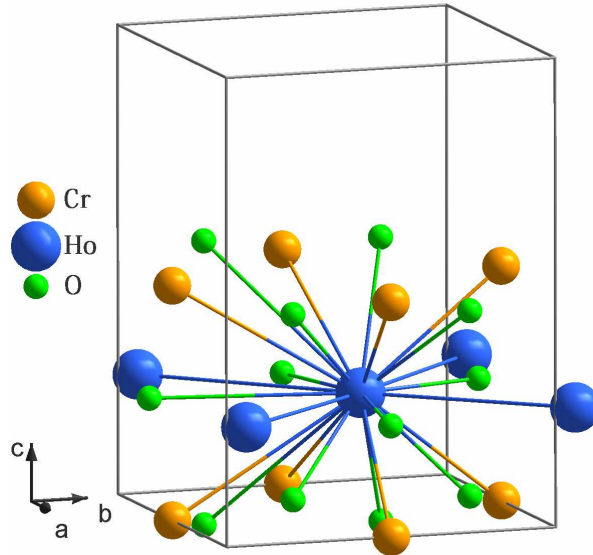


Figure 5.4: The coordination of Ho^{3+} ion with nearest neighbors considered for CF calculations using point-charge-model.

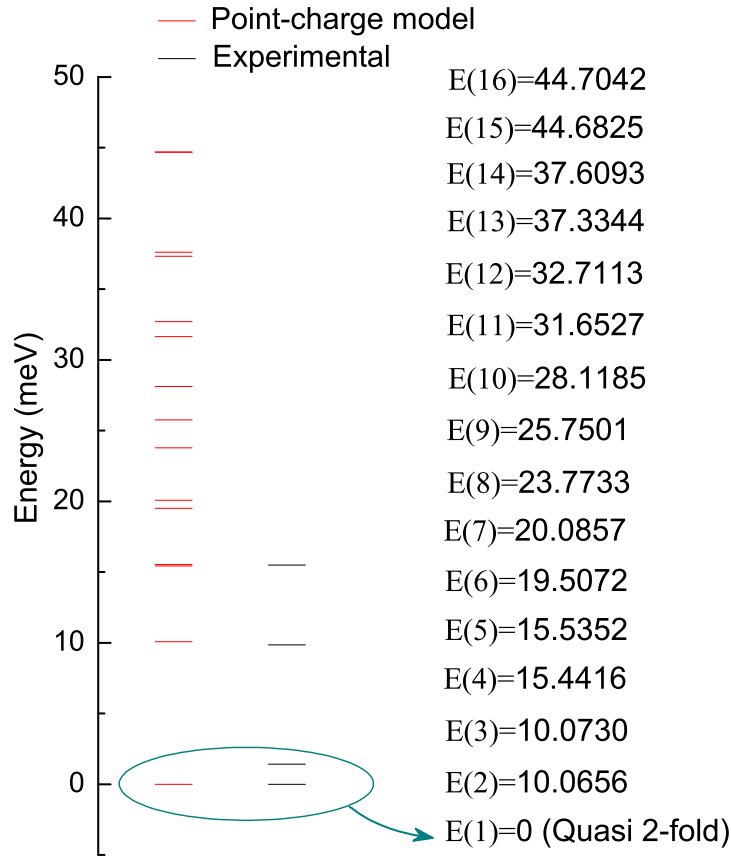


Figure 5.5: The calculated energy levels obtained using the point charge model and experimentally observed levels (see figure 5.1). The energy eigenvalues $E(1)$ – $E(16)$ expressed in meV, are the results obtained from the point-charge model.

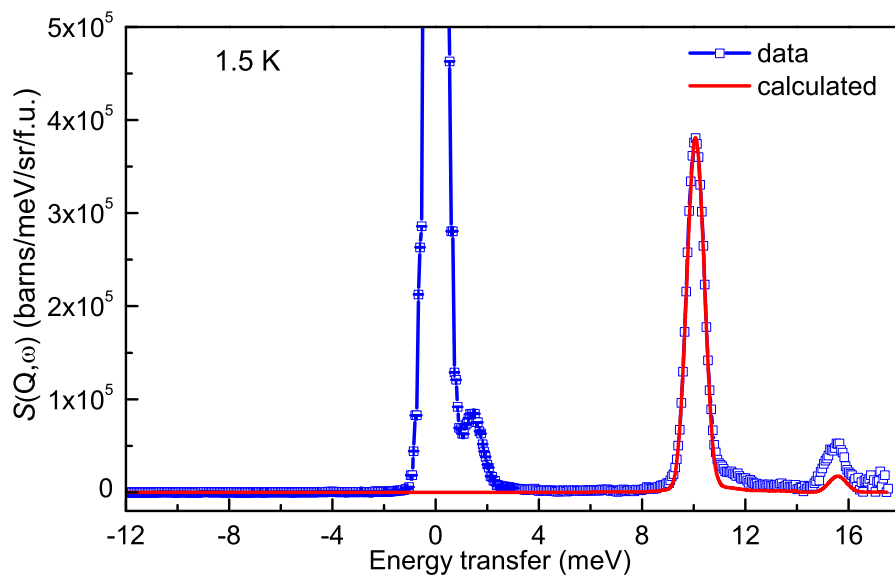


Figure 5.6: INS spectra of HoCrO_3 measured with incident energy $E_i = 19.61$ meV at 1.5 K. The thick line indicate the results of CEF calculations.

The first three CF levels calculated using point charge model and the experimentally observed values, ~ 1.41 meV (≈ 17 K), ~ 10.1 meV (117 K) and ~ 15.5 meV (180 K) are consistent with our heat capacity measurements and earlier reports [103, 121, 123, 124] (see table 5.4). With increase in temperature additional inelastic peaks appeared which are due to transitions between higher CF levels. A summary of all the inelastic peaks observed and associated transition schemes are presented in figure 5.7. Though we could reproduce the experimental data at 1.5 K fairly well, the simulation of high temperature data was not possible. This we attribute to the low symmetry of Ho^{3+} and limited energy range leading to inappropriate solutions during CF calculations.

Table 5.4: First three crystal field levels (CFL) obtained from our heat capacity, neutron powder diffraction (NPD), and inelastic neutron scattering (INS) measurements along with the reported values (in meV).

CFL	Specific heat	NPD	INS	Reported
ε_2	1.38(4)	1.8(3)	1.41	1.65 [104, 121, 122, 124]
ε_3	10.42	–	10.1	10.4 [124]
ε_4	15.42	–	15.5	15.5 [124]

5.4.2 Spin fluctuations

Our elastic NPD measurements indicated the presence of spin fluctuations well below magnetic ordering temperature, with a broad hump like feature centered around magnetic Bragg reflection (1 0 1) with $Q \approx 1.46 \text{ \AA}^{-1}$. The temperature evolution of integrated intensities clearly indicates that major contribution to (1 0 1) magnetic reflection is due to ordering of Cr magnetic moments (see figure 4.1). This suggests that the hump like feature in elastic NPD is due to Cr spin fluctuations. A careful inspection of INS spectra measured with incident energy $E_i = 10.245$ meV showed an increase in intensity around $Q \approx 1.4 \text{ \AA}^{-1}$, above 20 K, confirming the presence of spin fluctuations (5.8(a)). The temperature evolution of this peak was determined by summing all the intensities along Q over the energy range 2.5 – 4.5 meV. The temperature evolution of this peak is presented in figure 5.8(b). The integrated intensity of the peak decreases sharply also the peak-center changes sharply around magnetic ordering temperature as shown in figure 5.8(c). Further, the intensity decreases with temperature even below ordering temperature till down 20 K. This is in agreement with our elastic neutron scattering

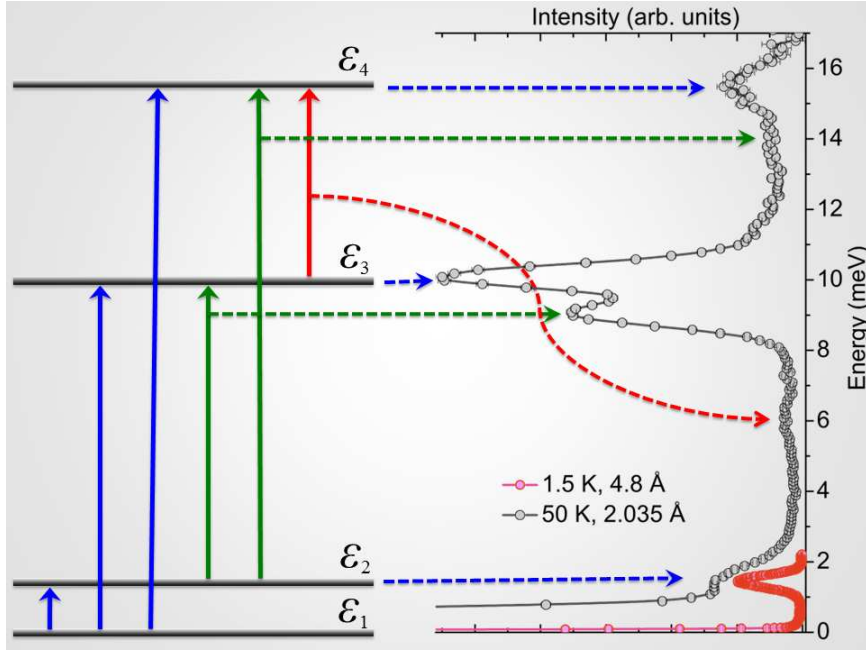


Figure 5.7: Typical INS spectra of HCO at 1.5 K (black circles) and 50 K (red circles) measured with incident wavelengths $E_i = 3.55$ meV and $E_i = 19.61$ meV, respectively. Various transitions are graphically represented on the left-hand side of the figure (blue arrows indicate the transitions from ground state to one of the excited states, green and red arrows indicate the transitions from one excited level to another higher level).

measurements in which we observed short range ordering well below the magnetic ordering temperatures. Using Selyakov-Sherrer formula [172],

$$\xi \approx \frac{\lambda}{\Delta(2\theta) \cos \theta} \quad (5.7)$$

where $\lambda = 2.826 \text{ \AA}$ is the incident wavelength ($E_i = 10.245$ meV). By rewriting equation (5.7) with θ in terms of Q as $\theta = \sin^{-1}(\lambda Q/4\pi)$ and $\Delta\theta = \sin^{-1}(\lambda\Delta Q/4\pi)$, where Q and ΔQ are, respectively, peak center and full width half maximum (FWHM) of the peak, we calculated the correlation length of the fluctuations (ξ). The temperature dependence of FWHM and ξ are presented in figure 5.8(d). Temperature evolution of ξ closely resembles the ordered moment of Cr sublattice, which clearly demonstrates the existence of fluctuations in Cr sublattice magnetic moments. Above magnetic ordering temperature the value of ξ was found to be constant, $\approx 9(1) \text{ \AA}$ which is the next-nearest-neighbor distance. Below magnetic ordering temperature the correlation length increase sharply and reaches a value of $\approx 50 \text{ \AA}$ close to 50 K. Where ordered magnetic moments of Cr reached saturation (see figure 4.7(a)). Below 20 K further increase in ξ was observed which is also the case of Cr ordered moments, but it is difficult

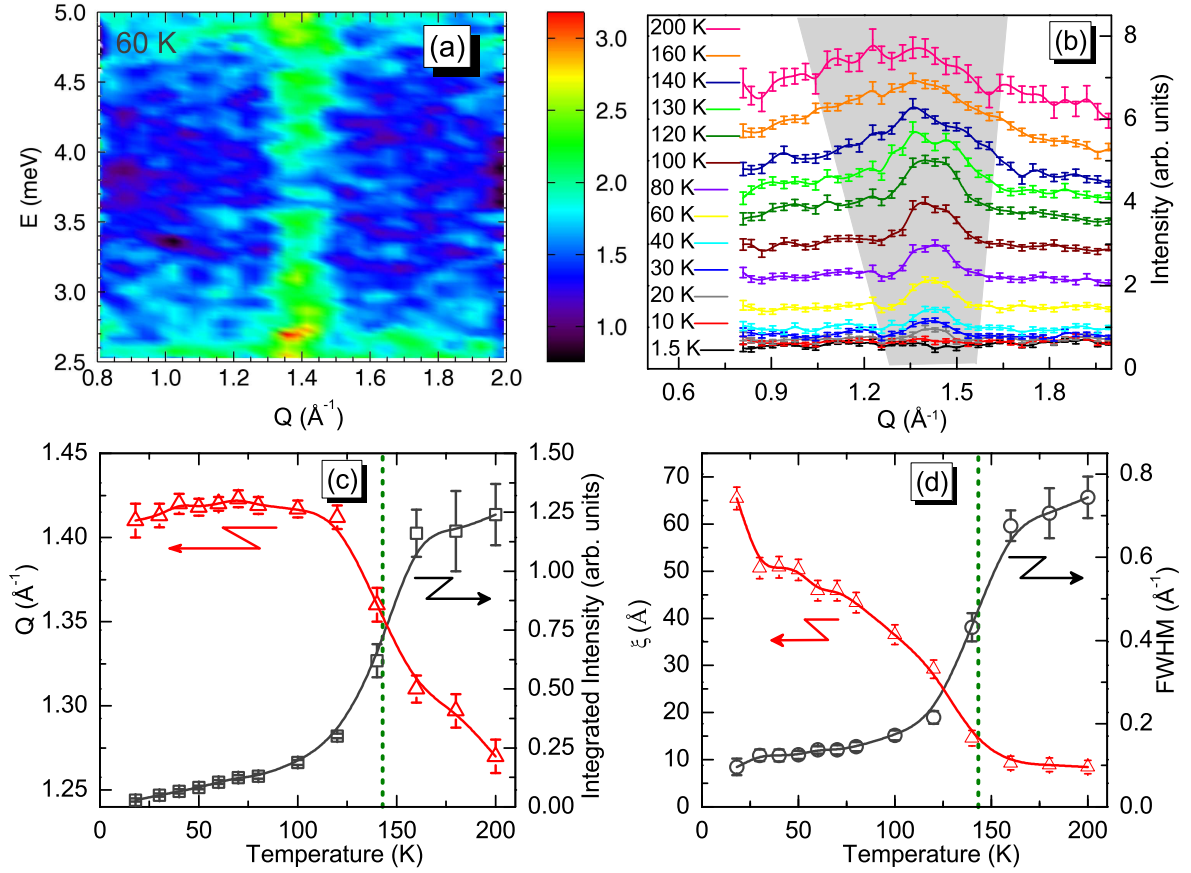


Figure 5.8: (a) A part of inelastic neutron scattering measured at 60 K showing a intensity maxima around $\sim 1.4 \text{ \AA}^{-1}$. (b) The temperature dependence of the peak aforementioned obtained by summing the intensities over the energy range 2.5 – 4.5 meV. (c) The temperature dependence of integrated intensity and peak position and (d) the temperature dependence of full width half-maxima (FWHM) and correlation-length ξ . Continuous lines are guides to the eyes and vertical dotted line corresponds to the magnetic ordering temperature.

to discuss this due to insufficient data points.

5.5 Conclusions

Using point charge model we calculated CF level scheme for Ho^{3+} in HoCrO_3 . Three energy levels observed in the data collected at 1.5 K were modeled from the CF parameters obtained from point charge model. The observed energy levels are in good agreement with those obtained from our specific measurements and also reported values [124]. Due to lower symmetry of Ho^{3+} and limited data range we could not reproduce the high temperature INS data using point charge model. Further we confirmed the presence of magnetic fluctuations in HCO down to 20 K. A broad peak observed around $Q \approx 1.4 \text{ \AA}^{-1}$. We calculated correlation length from FWHM using Selyakov-Scherrer formula.

The temperature dependence of correlation lengths followed the Cr ordered moments confirming Cr as the source of the short-range spin correlations.

Chapter 6

UNCONVENTIONAL MAGNETIC ORDERING IN HEXAGONAL DyMnO₃

6.1 Introduction

Perovskite $RMnO_3$, where $R = Gd, Tb, Dy$, have been identified as multiferroic materials which exhibit coexistence of ferroelectricity and magnetism rendering them one of the favorites of academic as well as technological research [173–175]. Among the compounds mentioned above, $DyMnO_3$ (DMO) is proved to be interesting because of the critical ionic radius of Dy^{3+} and the small difference in Gibb’s free energy between orthorhombic and hexagonal phases. DMO can be crystallized in orthorhombic as well as hexagonal crystal symmetries, through tailored synthesis conditions [176], with orthorhombic structure being the most favorable form under normal synthesis conditions. In the hexagonal $P6_3cm$ symmetry, Mn ions occupy $6c$ Wyckoff position and they are located in the ab plane forming MnO_5 bipyramidal polyhedra with oxygen ions at the corners of the polyhedra. These polyhedra are separated along c axis by layers of R . The Mn^{3+} ions in the basal plane of hexagonal structure form a frustrated magnetic lattice in the $z = 0$ and $z = 1/2$ planes that are stacked $ABAB$ along z axis. A 120° spin structure results below the Néel temperature from inherent frustration of the lattice. Low-dimensionality of the Mn moments and the frustration leads to complex magnetic phenomena in $RMnO_3$ ($hRMnO_3$). In the case of $hYMnO_3$, neutron diffraction studies [177, 178] have evidenced the presence of strong spin fluctuations even above $T_N^{Mn} = 75 K$. The rare earth ions in the hexagonal lattice have a complicated two-sublattice magnetic structure, which can interact with the Mn^{3+} magnetic moment. The complex multi-sublattice effects and their coupling leading to different magnetic phases in hexagonal multiferroics have been reported [179]. $hDMO$ is the only member in this family where manganese and rare earth lattices are reported to order according to different magnetic symmetry representations [180]. Specific heat studies have been judiciously employed to establish a $H - T$ phase diagram, signifying a tetracritical point, the cross-coupling between various orders and different magnetic phases, of $HoMnO_3$ [181]. In addition to the complex magnetic ordering phenomena, some of the hexagonal manganites are reported to exhibit giant magnetoelastic effect [182].

Most of the hexagonal manganites show only one high temperature transition associated with 120° antiferromagnetic ordering of Mn moments in the ab plane. The Mn ordering induces the rare earth sublattice to order in the same magnetic symmetry

due to strong interaction between the sublattices [154]. Strikingly different from most of the hexagonal manganites, our specific heat measurements reveal two high temperature phase transitions in *h*DMO. Through second harmonic generation (SHG) studies on *h*DMO it was found that Mn moments order with $P6_3c'm$ symmetry at high temperature and below ~ 5 K a phase transition to $P6_3c'm'$ occurs [180]. Based on x-ray resonant magnetic spectroscopy (XRMS) the high temperature magnetic symmetry of Dy moments is reported to be $P6_3cm'$ which is antiferromagnetic (AFM) and undergoes a phase transition to ferrimagnetic (FIM), $P6_3c'm'$ below 8 K [183].

The (*h*RMnO₃) are ferroelectric (FE) below $T_c \approx 900$ K [184] and antiferromagnetic (AFM) below $T_N \approx 80$ K. (*h*RMnO₃), which is classified as *geometric multiferroic*, is a system where ferroelectric polarization arises from structural distortions [185]. A recent study on YMnO₃ revealed a giant magneto-elastic coupling below magnetic ordering temperature in this compound associated with giant atomic displacements for every atom in the unit cell [182]. The origin of multiferroic phenomenon was attributed to large magneto-elastic coupling observed in this material. The *h*DMO exhibits ferroelectricity at room temperature [186]. Similar to YMnO₃ we expect *h*DMO to exhibit magneto-elastic coupling below magnetic ordering temperature enhancing the ferroelectric polarization. In this chapter we present our crystal and magnetic structural investigations on *h*DMO through PXRD, magnetization, specific heat and neutron scattering studies.

6.2 Experimental results and discussion

6.2.1 Synthesis and growth of single crystals

For the growth of *h*DMO we used polycrystalline orthorhombic DyMnO₃ (*o*DMO) powder prepared by conventional solid state route. Stoichiometric amount of precursors, Dy₂O₃(99.9) and MnO₂(99.9) was ball-milled about one hour, transferred into an alumina crucible and then sintered in a furnace at 1100 °C for 12 hours. The mixture was mixed once again in a ball-mill, pressed into pellets and sintered at 1200 °C for 48 hours. The resulting compound was characterized by powder X-ray diffraction (PXRD) and found to be *o*DMO, and the structure was refined with space group $Pnma$. The measured PXRD pattern and Rietveld refinement results and the crystal structure are presented in figure 6.2(a) and (b), respectively. The powder is then filled into a latex tube fitted between two halves of a cylindrical steel tube (cut along diameter). Maximum care was

taken to avoid any voids while filling, further the tube was evacuated, sealed and pressed in a hydrostatic press. Then latex tube was carefully separated compact sample rod was sintered at $1350\text{ }^\circ\text{C}$. Single crystals of $h\text{DMO}$ were grown by optical floating-zone method in an infrared furnace (FZ-T-10000-H-VI-VP). The growth is performed in argon ambience with the pressure of 0.3 MPa and the growth rate is $\sim 5\text{ mm/h}$. It should be noted again that the starting material for the growth was $o\text{DMO}$, the growth in the presence of oxygen-rich ambience lead to pure $o\text{DMO}$ single crystals, whereas inert atmospheres (N_2 or Ar) lead to pure $h\text{DMO}$. As grown single crystals were cylindrical in shape with dimensions $50\text{mm} \times 5\text{mm}$. The single crystals were oriented by X-ray Laue method and cut into pieces of desired size for the further measurements.

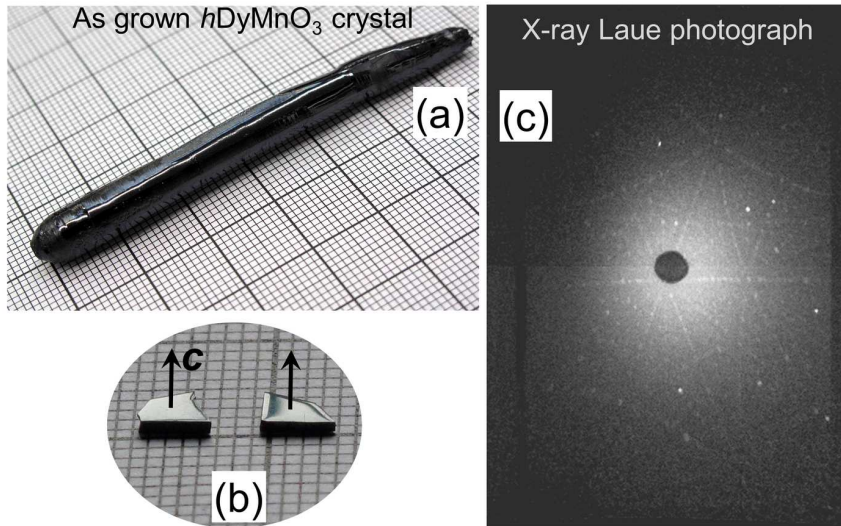


Figure 6.1: (a) As grown $h\text{DMO}$ crystal. (b) Typical oriented single crystals, arrows indicate crystallographic c -axis. (c) X-ray Laue photograph taken in reflection mode during the crystal orientation.

6.2.2 Structural properties

The PXRD patterns of pulverized crystals were performed with $\text{Cu K}\alpha$ radiation ($\lambda = 1.54059\text{ \AA}$) using the Huber X-ray diffractometer (Huber G670) with Guinier geometry. Crystal structure refinement was performed by Rietveld method using the *FullProf*. We succeeded to obtain a pure $h\text{DMO}$ phase by the application of pressure and using oxygen deficient ambience. The PXRD pattern obtained at room temperature along with the Rietveld refinement result is presented in figure 6.2(c). The crystal structure was refined in $P6_3cm$ space group (#185) and the refined lattice parameters are $a = 6.185(1)\text{ \AA}$

and $c = 11.469(4) \text{ \AA}$ and the unit cell volume, $V = 379.58(4) \text{ \AA}^3$. The crystal structure is presented in figure 6.2(d), h DMO is build from MnO_5 bipyramids consisting of five Mn–O bonds: Mn–O1 and Mn–O2 oriented along the crystallographic c -axis while Mn–O3 and a pair of Mn–O4 bonds lie within ab plane. From the previous studies on similar hexagonal manganites it was reported that the main exchange path is the Mn–O–Mn network on the ab plane [187, 188]. The O3 and O4 atoms are located close to the centers of triangles formed by Mn atoms and the Mn–O3–Mn and Mn–O4–Mn bonds have nearly 120° in-plane antiferromagnetic super-exchange. Due to the difference in values of Mn–O3 and Mn–O4 bond lengths and Mn–O3–Mn and Mn–O4–Mn bond angles, the strength of these interactions is slightly different from each other, and geometrical frustration effects are partially lifted, leading to the appearance of the various triangular ordered AFM arrangements in $h\text{RMnO}_3$.

6.2.2.1 Magneto-elastic effect

To study the temperature evolution of crystal structure we collected PXRD patterns in the temperature range 10 – 300 K. The temperature variation of lattice parameters is shown in figure 6.3. Throughout the temperature range studied, DMO does not undergo any structural phase transition, but shows clear anomaly in lattice parameter and unit cell volume around ~ 70 K. We later see that this temperature corresponds to a magnetic ordering temperature, which indicates the presence of magneto-elastic effect in this compound. A similar observation of giant magneto elastic effect was reported in multiferroic hexagonal $(\text{Y}_{1-x}\text{Lu}_x)\text{MnO}_3$, which shows giant atomic displacements and variation in the lattice parameters below magnetic ordering temperature of Mn [182]. It was argued that in hexagonal manganites it is the large magneto-elastic coupling, the primary origin of multiferroic phenomenon. We modeled thermal variation of unit cell volume using Grüneisen approximation for the zero pressure equation of state, in which the effects of thermal expansion are considered to be equivalent to elastic strain [162]. Thus, the temperature dependence of the volume can be described by $V(T) = \gamma U(T)/B_0 + V_0$, where γ is a Grüneisen parameter, B_0 is the bulk modulus and V_0 is the volume at $T = 0$ K in the absence of magnetoelastic effect. By fitting the unit cell volume of DMO in the paramagnetic state we can get the physical parameters θ_D and V_0 . The result of the fit is shown as a solid line in figure 6.3(b). The value of θ_D obtained from the fit was $269(15)$ K and $V_0 = 377.39(6)(1) \text{ \AA}^3$. Note that the fitted curve deviates from the data at ~ 70 K where the lattice parameters show anomalous changes.

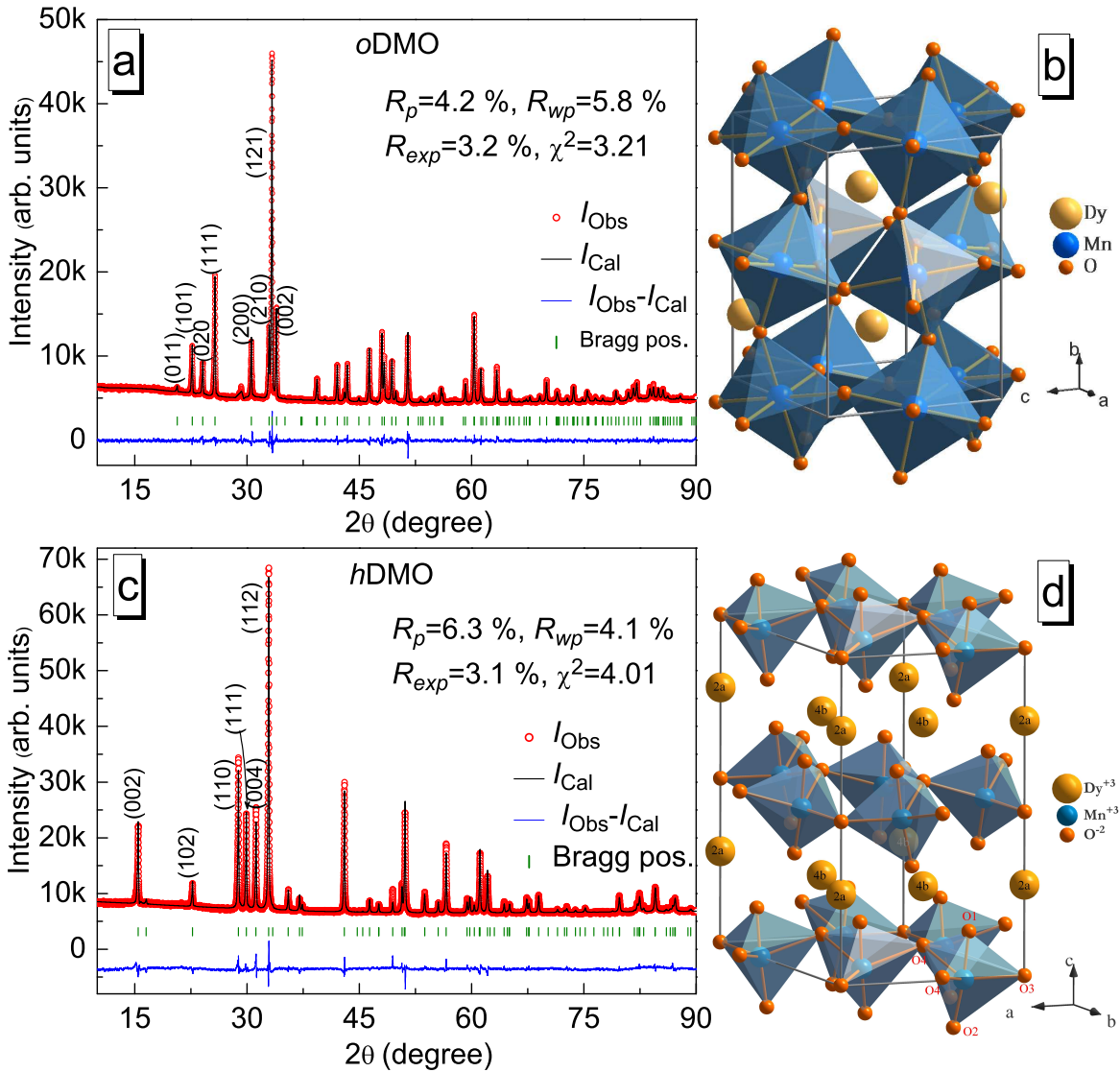


Figure 6.2: (a) PXR patterns collected at room temperature and Rietveld refinement results for *oDMO*, the discrepancy factors of refinement and indices of few Bragg peaks at lower angle are also indicated. Red circles mark the data points, black line represents calculated pattern and blue line represents the difference. The bars below the patterns denote the position of Bragg peaks. (b) A clinographic view of refined orthorhombic crystal structure ($Pnma$). (c) Observed PXR pattern of *hDMO* at room temperature and the results of Rietveld refinement showing octahedral MnO_6 polyhedra. (d) A clinographic view of refined hexagonal crystal structure ($P63cm$) indicating two different Wyckoff positions of Dy ion and also four different positions of oxygen forming MnO_5 bipyramids.

This is inferred as a clear indication of magnetoelastic or magnetovolume effects present in this system.

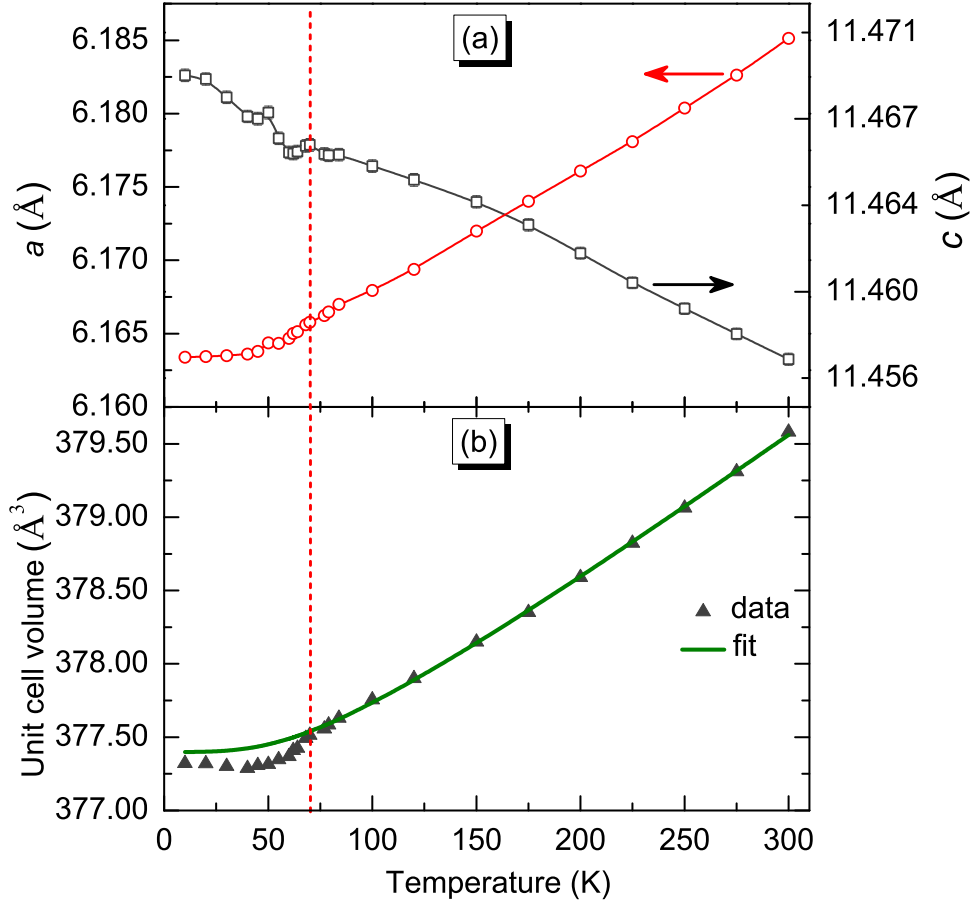


Figure 6.3: (a) The temperature dependence of lattice parameters a and c ; the lines are guide to eyes and (b) the temperature dependence unit cell volume (filled triangles). Solid line is the fit of the Debye model as described in the text, vertical dashed line corresponds to T_N . If not shown, size of the error bars is comparable to the data markers.

6.2.3 Magnetic properties

Oriented single crystals of dimension $\sim 1 \times 1 \times 0.5 \text{ mm}^3$ were used for magnetization measurements. Magnetization versus temperature measurements under very small magnetic fields were carried out in SQUID magnetometer. For ultra-low-field measurements it is necessary to make sure that the remnant magnetization of magnet of the SQUID magnetometer is negligibly small ($< 0.05 \text{ Oe}$). This was achieved by the Ultra Low Field option for the SQUID VSM which employs a fluxgate magnetometer and modulation coil in the magnet to compensate trapped flux from the magnet.

The field-cooled (FC) dc magnetization curves measured with an applied magnetic field of 2 Oe along crystallographic c direction presented in figure 6.4(a) show three anomalies at, $\sim 65 \text{ K}$, $\sim 8.3 \text{ K}$ and $\sim 5 \text{ K}$. The high temperature anomaly was attributed to ordering of Mn sublattice. Due to large paramagnetic moment of Dy the transition

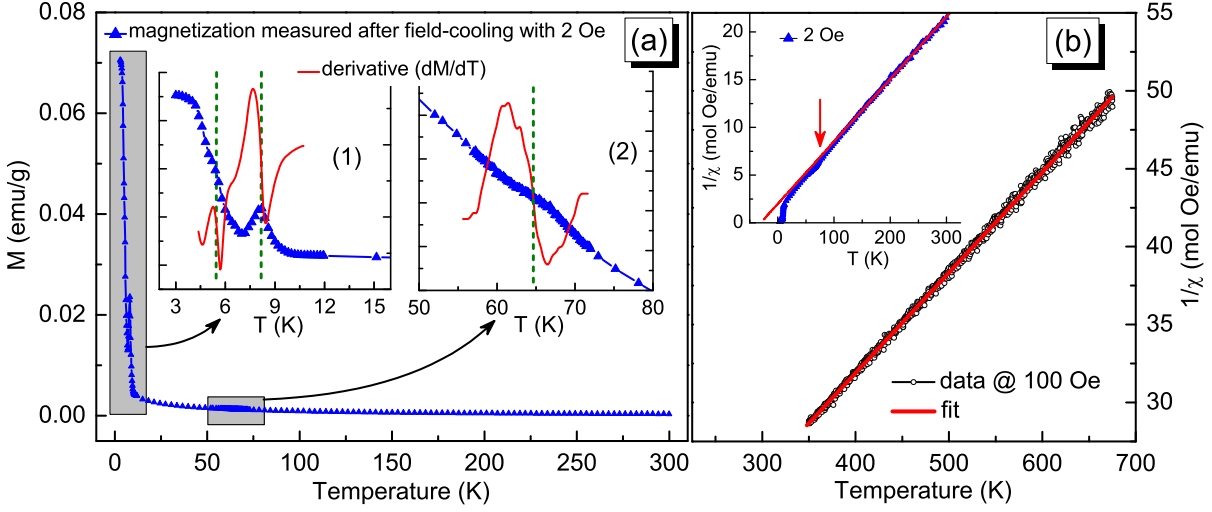


Figure 6.4: (a) Field-cooled dc magnetization of $h\text{DyMnO}_3$ at applied field of 2 Oe. Magnified view of magnetization curves presented in (1) and (2) show two low temperature transitions centered at 5 and 8.3 K and a broad anomaly centered at 64.6 K, respectively. (b) Curie-Weiss law fit to inverse susceptibility measured with 100 Oe field in the high temperature region. Inset of (b) is the temperature dependence of inverse susceptibility calculated from magnetization data presented in (a), which shows a deviation from the Curie-Weiss law below T_N , indicated by red arrow.

is masked and can be seen as small change in the slope of magnetization. The low temperature transitions at ~ 8.2 K and ~ 5 K were attributed to the low temperature ordering of Dy and Mn, as reported by Nandi *et al.* [183] and Wehrenfennig *et al.* [180], based on XRMS and SHG measurements, respectively. The thermal evolution of reciprocal susceptibility calculated from the FC magnetization curve (figure 6.4(a)) is presented in figure 6.4(b) as an inset. The inverse susceptibility follows Curie-Weiss law above transition temperature and there is a marked deviation below the ordering temperature. In the main panel of figure 6.4(a), the inverse susceptibility obtained from the dc magnetization measured in the temperature range 325 – 675 K with an applied field 100 Oe is presented. From Curie-Weiss fit of high temperature magnetic susceptibility the Curie-Weiss temperature, Θ is found to be $-95(3)$ K and the effective moment is found to be $11.14 \pm 0.2 \mu_B$. By considering the theoretical values $4.9 \mu_B$ for Mn^{3+} (for the spin only $S = 2$) and $10.63 \mu_B$ for Dy^{3+} ($J = 15/2$) and assuming that the total effective magnetic moment is given by $\mu_{\text{total}} = [\mu_{\text{eff}}^2(\text{Mn}^{3+}) + \mu_{\text{eff}}^2(\text{Dy}^{3+})]^{1/2}$, we expect a total magnetic moment of $11.67 \mu_B$. This figure is very close to the experimental value, suggesting that the ground states for both ions are those of the free ion. The negative paramagnetic temperature implies the presence of antiferromagnetic (AFM)

exchange interactions. Because of the intrinsically frustrated nature of the triangular lattice with antiferromagnetic interaction, the Mn $S = 2$ moments cannot order until well below their Curie-Weiss temperatures. Therefore, the triangular lattice of the Mn atoms exhibits geometrical frustration effects with so called frustration parameter, $f = |\Theta_{\text{CW}}| / T_{\text{N}}$, which is 65 K for *h*DMO.

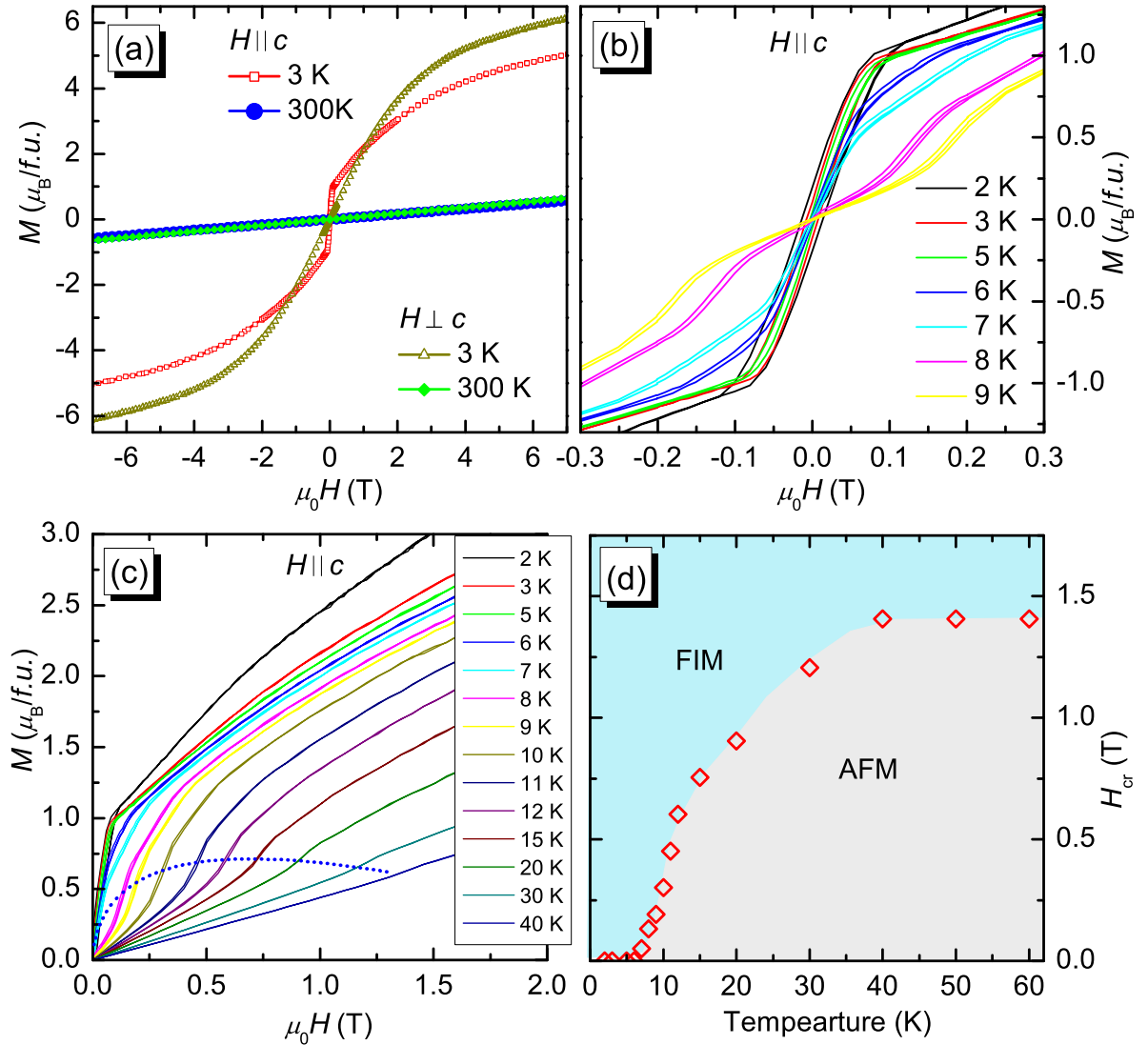


Figure 6.5: (a) Isothermal magnetization curves measured with field parallel (closed symbols) and perpendicular (open symbols) to crystallographic c direction. (b) Magnified view of several isothermal magnetization curves showing hysteresis. (c) The positive field cycle of hysteresis curves of several isotherms showing the temperature dependence of the center of the hysteresis loop which is indicated by dashed line. (d) M - T magnetic phase diagram obtained from the magnetic isotherms (see text for details). Here FIM denotes ferrimagnetic and AFM denotes antiferromagnetic ordering.

Isothermal magnetization curves measured parallel and perpendicular to crystallographic c direction are presented in figure 6.5(a). The hysteresis curves show spontaneous magnetic moment along c direction at low temperatures which is absent perpendicular to c direction. Hysteresis curves perpendicular to c deflection are characterized by that of an antiferromagnet. The isothermal magnetization curve measured with field along c axis at 2 K, shows hysteresis with the center at 0 T, indicating the existence of a state with a spontaneous magnetic moment of $\sim 1 \mu_B/f.u.$, indicating the ferrimagnetic (FIM) type ordering of Dy moments (figure 6.5(b)). With the increase in temperature above 7 K the center of the hysteresis loop is shifted to higher field values indicating the field induced phase transition from AFM to FIM phase. The critical field corresponding to the center of the hysteresis loop as indicated by a dashed line in figure 6.5(c) was computed by taking derivative of the magnetization curve. From the critical field values we have constructed a tentative H-T magnetic phase diagram including the AFM–FIM transition of Dy which is presented in figure 6.5(d). It should be noted from figure 6.5(c) that the field induced transition become more and more dispersive with increase in field. This makes it very difficult to observe these field induced transitions in specific heat measurements under applied magnetic fields, which are discussed later. The critical fields obtained from our measurements are slightly larger than the values reported by Ivano *et al.* [189].

6.2.4 Thermal properties

The specific heat, C_p , of $hDMO$ in zero field is presented in figure 6.6(a). The data reveal four phase transitions: (i) two high temperature transitions at ~ 70 K and ~ 64 K and (ii) two low temperature transitions at ~ 9.5 K and ~ 5.3 K. For clarity, C_p around low temperature and high temperature anomalies is plotted along with its derivative in figure 6.6(b) and (c), respectively. First, we focus on the high temperature transitions.

In order to analyze the specific heat of $hDMO$, we employ a model where the total specific heat consists of contributions from lattice that can be split into Debye and Einstein terms, a linear term and a two-level Schottky term for rare earth ion. Thus:

$$\begin{aligned}
 C_{tot} &= C_{Debye} + C_{Einstein} + C_{Schottky} + C_{linear} \\
 C_{Debye} &= 9rR/x_D^3 \int_0^{x_D} x^4 e^x / (e^x - 1)^2 dx
 \end{aligned} \tag{6.1}$$

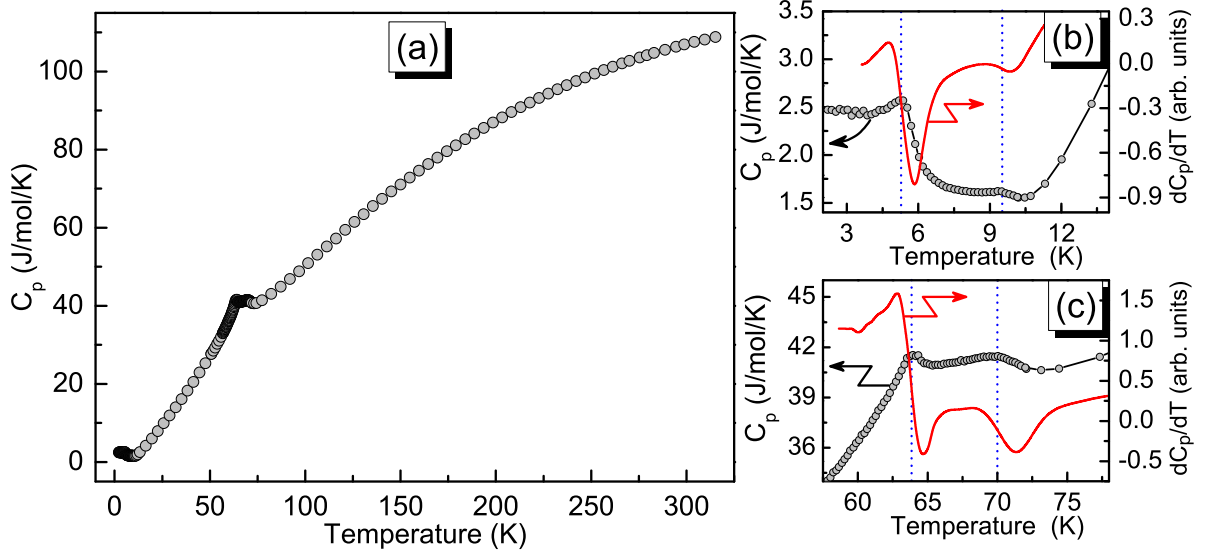


Figure 6.6: (a) The observed specific heat C_p of hDMO. A magnified view of C_p along with its derivative around low and high temperature anomalies is presented in (b) and (c), respectively. From (b) and (c) two low temperature transitions at ~ 5.3 and ~ 9.5 K and two high temperature transitions at ~ 64 and ~ 70 K are discernible (indicated by dashed lines).

$$C_{Einstein} = 3rR \sum_i a_i [x_i^2 e_i^x / (e_i^x - 1)^2] \quad (6.2)$$

$$C_{Schottky} = R \sum_i w_i \frac{(\frac{\Delta_i}{k_B T})^2 \exp(\frac{\Delta_i}{k_B T})}{[1 + \exp(\frac{\Delta_i}{k_B T})]^2} \quad (6.3)$$

$$C_{linear} = \gamma T \quad (6.4)$$

where $x_D = h\nu_D/k_B T$, $x_i = h\nu_E/k_B T_i$, Δ_i is the Schottky energy, γ is the coefficient of linear term and R is the universal gas constant.

The range of data for the fit was $10 \leq T \leq 55$ and $T > 130$ K thereby excluding the magnetic transitions. The results of the fit are presented in figure 6.7(a). The analysis resulted in Debye temperature of $\Theta_D \cong 840(25)$ K, Einstein temperatures $\Theta_{E1} \cong 154(1)$ K, $\Theta_{E2} \cong 622(18)$ K and Schottky energy $\Delta = 55(1)$ K. A linear term in the total C_p was essential for the faithful reproduction of low temperature part of the specific heat. From the fit we obtained a large value of γ as $41(1)$ mJ/mol/K². In an earlier report, a significant linear term in specific heat of hYMnO₃ was attributed to the presence of spin-glass or unconventional magnetic excitations [190]. Later, Tachibana *et al*, [191] suggested that there is no intrinsic linear term in the specific heat study of YMnO₃. Similar behavior was reported in insulating BaVS₃ with large linear contribution to the

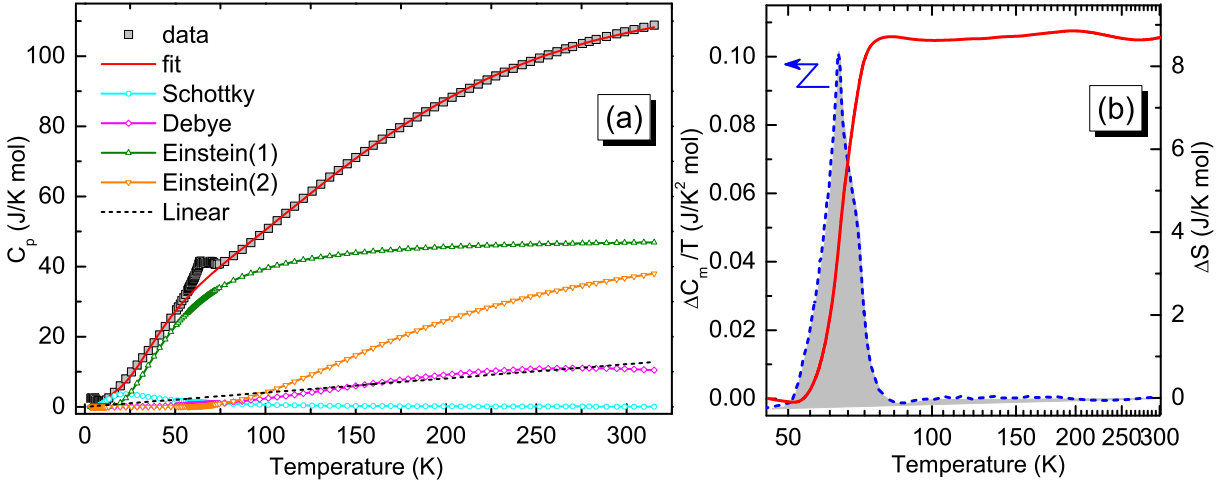


Figure 6.7: (a) The fit to observed C_p assuming the model described in the text. The combination of a Schottky, Debye, two Einstein and linear terms is found to reproduce the experimental data faithfully. (b) Plot of $\Delta C_m/T$ vs T and the entropy obtained by numerical integration (shaded region)

specific heat, in which the spin ordering in the insulator state is not simple but may be due to frustration effects [130]. In $hDMO$, however, a linear term was essential to obtain a best fit, which could be attributed to possible spin-glass like ordering of frustrated triangular Mn lattice as in the case of $YMnO_3$. The value of γ is strikingly close to the value found in insulator layered manganite $La_{2.3}YCa_{0.7}Mn_2O_7$ with large γ value (41.5 mJ/mol/K^2) [131]. Thus in case of $hDMO$ the large value of γ could also be due to competition between magnetic ordering of Dy and Mn magnetic sublattices. The linear contribution in the case of $hDy_{0.5}Y_{0.5}MnO_3$ is slightly larger than (56 mJ/mol/K) $hDMO$ [192]. In $hDy_{0.5}Y_{0.5}MnO_3$ the linear contribution was attributed to the high degeneracy of disordered rare earth spins [129, 140]. The excess entropy (ΔS) calculated from the magnetic specific heat (ΔC_p) of $hDMO$ is presented in figure 6.7(b); the experimentally estimated entropy is $\approx 8.6 \text{ J/mol/K}$. This value of entropy is diminished in magnitude compared to the value expected for Mn^{3+} ion which is $\Delta S = R \ln(2S + 1) = 13.38 \text{ J/mol/K}$.

The low temperature specific heat of $hDMO$ was analyzed by considering contributions from the lattice term and a two-level Schottky term. The harmonic-lattice approximation $C_{\text{Lattice}} = B_3 T^3 + B_5 T^5 + B_7 T^7 + \dots$ is used to evaluate the lattice specific heat [117, 193]. At low temperatures first two terms suffice to account for lattice specific heat. Thus the low temperature specific heat can be modeled as,

$$C_{lowT} = C_{Schottky} + \alpha T^3 + \beta T^5 \quad (6.5)$$

The results of the analysis of C_p at applied fields of 0 and 2 T are presented, respectively, in figures 6.8 (a) and (b). The relevant physical parameters from the fit are tabulated in Table 6.1. The Kramer's Dy^{3+} ions in $h\text{DMO}$ are at the trigonal symmetry and, therefore, must have a doublet ground-state [194, 195]. At low temperatures only the ground-state doublet is appreciably populated because the energy difference between the ground-state and the next crystal-field levels, in general, is large [195]. From XRMS studies [183] it was shown that an exchange field produced by the ordering of Mn^{3+} sublattice causes a doublet splitting $\Delta(T)$ of Dy crystal levels. As a starting value for the estimate of Δ , we used the result from X-ray resonant magnetic scattering (XRMS) experiments on $h\text{DMO}$ ($\Delta = 5.8(8) \text{ meV} \approx 67(9) \text{ K}$) [183]. With the error limits our experimental Δ is in good agreement with the reported value [183]. In case of $h\text{Dy}_{0.5}\text{Y}_{0.5}\text{MnO}_3$ a similar value for Δ (60(5) K) was reported [192]. The θ_D obtained from the low-temperature analysis is in excellent agreement with the value obtained by fitting thermal variation of unit cell volume of $h\text{DMO}$ using Grüneisen approximation (269(15) K).

Table 6.1: Fit parameters derived from the analysis of low temperature specific heat of $h\text{DMO}$ at 0 and 2 T.

H(T)	α (J/mol K ⁴)	β (J/mol K ⁶)	Θ_D (K)	Δ (K)
0	$4.3(1) \times 10^{-4}$	$-10.3(9) \times 10^{-6}$	283(3)	58(1)
2	$5.0(3) \times 10^{-4}$	$-16(3) \times 10^{-6}$	268(6)	62(4)

The presence of two high temperature anomalies in specific heat measurement of $h\text{DMO}$ suggests independent ordering of Mn and Dy sublattice. This is in contrast to most of other candidates of $h\text{RMnO}_3$ family which show induced ordering of the rare earth ion under the molecular field of Mn sublattice. This observation suggests that in $h\text{DMO}$, Mn and Dy sublattice are weakly or not coupled which renders the possibility for the different sublattices to order in different magnetic symmetries. Further, one can notice in figure 6.8 that the low temperature anomalies attributed to low temperature ordering of Dy and Mn are suppressed with the application of 2 T magnetic field. This can be understood from the magnetic $H - T$ phase diagram obtained from the isothermal magnetization measurements (figure 6.5(d)). From the magnetic phase diagram it is clear that above ~ 1.4 T Dy will be in FIM phase at higher temperatures itself. The absence

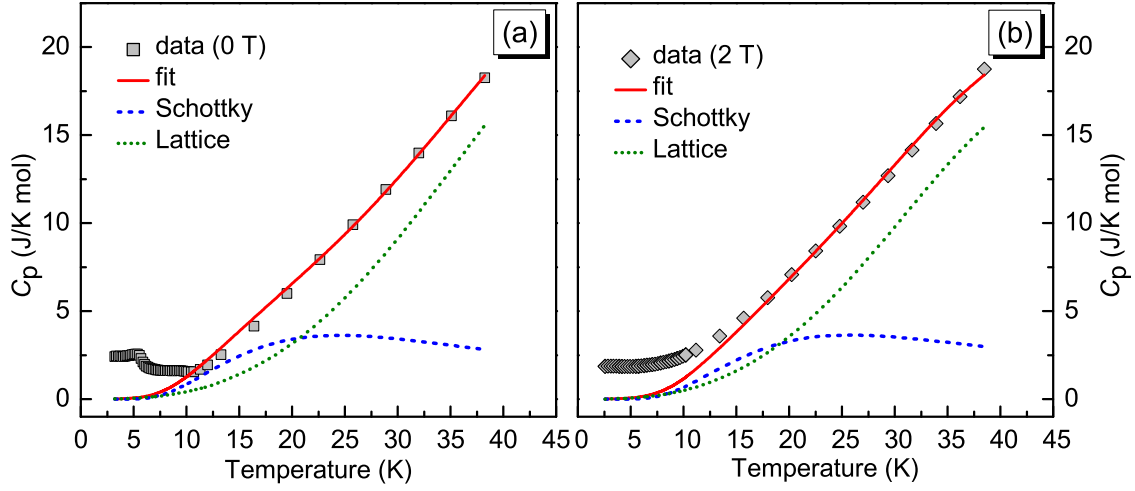


Figure 6.8: The fit to low temperature specific heat of $hDMO$ at (a) 0 T and (b) 2 T. The contributions from Schottky and lattice terms are also shown in both cases.

of another low temperature transition corresponding to re-ordering of Mn sublattice implicates that the Mn sublattice too undergoes a field induced magnetic reordering transition at elevated temperatures. This is consistent with reported results of SHG experiments under magnetic field [180]. Since the reordering of 120° Mn spins will not affect the magnitude of the magnetization, this transition was not observed in our bulk magnetization measurements of $hDMO$, also it is not discernible in specific heat measurements due to dispersive nature of the transition at high temperatures and large contribution from lattice heat capacity.

6.2.5 Neutron scattering measurements

6.2.5.1 Symmetry considerations

All the symmetry allowed magnetic structures of rare-earth and Mn ions in hexagonal manganites were computed by the theory of group representational analysis described by Bertaut [144]. With the propagation vector $\mathbf{k} = 0$, the little group $G_{\mathbf{k}}$ coincides with the space group $P6_3cm$. According to Kovalev [196], $G_{\mathbf{k}}$ has six irreducible representations, four, Γ_1 , Γ_2 , Γ_3 and Γ_4 are unidimensional and two, Γ_5 and Γ_6 are bidimensional. The calculations were carried out using the program *SARAh-Representation Analysis* [197]. They involve first the determination of the space group symmetry elements g that leave the propagation vector \mathbf{k} invariant; these form the little group $G_{\mathbf{k}}$. The magnetic

representation of a crystallographic site can then be decomposed in terms of the irreducible representations (IRs) of G_k :

$$\Gamma_{Mag} = \sum_{\nu} n_{\nu} \Gamma_{\nu}^{\mu} \quad (6.6)$$

where n_{ν} is the number of times that the IR, Γ_{ν} of order μ appears in the magnetic representation, Γ_{Mag} for the chosen crystallographic site.

In our case, the decomposition of Γ in terms of irreducible representations of G_k are: for the Mn atoms,

$$\Gamma = \Gamma_1 + 2\Gamma_2 + 2\Gamma_3 + \Gamma_4 + 3\Gamma_5 + 3\Gamma_6 \quad (6.7)$$

for the Dy(1) atoms (at site 2a),

$$\Gamma = \Gamma_2 + \Gamma_3 + \Gamma_5 + \Gamma_6 \quad (6.8)$$

for the Dy(2) atoms (at site 4b),

$$\Gamma = \Gamma_1 + \Gamma_2 + \Gamma_3 + \Gamma_4 + 2\Gamma_5 + 2\Gamma_6 \quad (6.9)$$

The IRs and basis vectors (BVs) corresponding to the Dy and Mn atoms are presented in tables 6.2 and 6.3, respectively.

From table 6.2, IRs Γ_1 , Γ_2 , Γ_3 and Γ_4 are all having Dy moments aligned along c direction, except, in Γ_1 and Γ_4 Dy(2a) has no ordered moment. According to magnetic representation Γ_5 and Γ_6 the Dy moments are aligned in ab plane. Further, Γ_2 and Γ_5 correspond to ferromagnetic moments along the c direction and in ab plane, respectively.

All the IRs of Mn atoms presented in table 6.3 form 120° spin configurations within ab plane were graphically demonstrated by Brown *et al.* [198] as in figure 6.9 reproduced here. It can be easily conceived from figure 6.9 that in IRs Γ_1 , Γ_2 and Γ_5 Mn of two adjacent planes along z ($z = 0$ and $z = \frac{1}{2}$) are antiferromagnetically coupled, while in Γ_3 , Γ_4 and Γ_6 the coupling is ferromagnetic.

Table 6.2: Irreducible representations (IRs) and basis vectors (BVs) of Dy(1) and Dy(2) atoms which occupy 2a and 4b sites, respectively. The directions are denoted by $[e_x e_y e_z]$, where e_x and e_y are in basal ab plane forming an angle 120° between them and e_z is parallel to the 6-fold axis.

		Dy(1) (2a)		Dy(2) (4b)			
IRs	BVs	Dy1	Dy2	Dy3	Dy4	Dy5	Dy6
		$\begin{pmatrix} 0 \\ 0 \\ z \end{pmatrix}$	$\begin{pmatrix} 0 \\ 0 \\ z + \frac{1}{2} \end{pmatrix}$	$\begin{pmatrix} \frac{1}{3} \\ \frac{2}{3} \\ z \end{pmatrix}$	$\begin{pmatrix} \frac{2}{3} \\ \frac{1}{3} \\ z \end{pmatrix}$	$\begin{pmatrix} \frac{1}{3} \\ \frac{2}{3} \\ z + \frac{1}{2} \end{pmatrix}$	$\begin{pmatrix} \frac{2}{3} \\ \frac{1}{3} \\ z + \frac{1}{2} \end{pmatrix}$
Moments in c direction							
$\Gamma_1(P6_3cm)$	ψ_1^1	–	–	$[0\ 0\ 1]$	$[0\ 0\ \bar{1}]$	$[0\ 0\ \bar{1}]$	$[0\ 0\ 1]$
$\Gamma_2(P6_3c'm')$	ψ_1^2	$[0\ 0\ 1]$	$[0\ 0\ 1]$	$[0\ 0\ 1]$	$[0\ 0\ 1]$	$[0\ 0\ 1]$	$[0\ 0\ 1]$
$\Gamma_3(P6_3c'm')$	ψ_1^3	$[0\ 0\ 1]$	$[0\ 0\ \bar{1}]$	$[0\ 0\ 1]$	$[0\ 0\ 1]$	$[0\ 0\ \bar{1}]$	$[0\ 0\ \bar{1}]$
$\Gamma_4(P6_3c'm)$	ψ_1^4	–	–	$[0\ 0\ 1]$	$[0\ 0\ \bar{1}]$	$[0\ 0\ 1]$	$[0\ 0\ \bar{1}]$
Moments in ab plane							
$\Gamma_5(P6_3')$	ψ_1^5	$[u\ v\ 0]$	$[u\ v\ 0]$	$[p\ \bar{q}\ 0]$	$[r\ \bar{s}\ 0]$	$[r\ \bar{s}\ 0]$	$[p\ q\ 0]$
$\Gamma_6(P6_3)$	ψ_1^6	$[u\ v\ 0]$	$[\bar{u}\ \bar{v}\ 0]$	$[p\ q\ 0]$	$[r\ s\ 0]$	$[\bar{r}\ \bar{s}\ 0]$	$[\bar{p}\ \bar{q}\ 0]$

6.2 Experimental results and discussion

Table 6.3: Irreducible representations (IRs) and basis vectors (BVs) of Mn atoms that occupies 6c site. The directions are denoted by $[e_x e_y e_z]$, where e_x and e_y are in basal ab plane forming an angle 120° between them and e_z is parallel to the 6-fold axis, $\omega = e^{i\pi/3}$.

IRs	BVs	Mn1 ($x, 0, 0$)	Mn2 ($0, x, 0$)	Mn3 ($-x, -x, 0$)	Mn4 ($-x, 0, \frac{1}{2}$)	Mn5 ($0, x, \frac{1}{2}$)	Mn6 ($x, x, \frac{1}{2}$)	
Γ_1	ψ_1^1	[1 2 0]	$[\bar{2} \bar{1} 0]$	[1 $\bar{1}$ 0]	$[\bar{1} \bar{2} 0]$	[2 1 0]	$[\bar{1} \bar{1} 0]$	
Γ_2	ψ_1^2	[1 0 0]	[0 1 0]	$[\bar{1} \bar{1} 0]$	$[\bar{1} 0 0]$	[0 $\bar{1}$ 0]	[1 1 0]	
	ψ_2^2	[0 0 1]	[0 0 1]	[0 0 1]	[0 0 1]	[0 0 1]	[0 0 1]	
Γ_3	ψ_1^3	[1 0 0]	[0 1 0]	$[\bar{1} \bar{1} 0]$	[1 0 0]	[0 1 0]	$[\bar{1} \bar{1} 0]$	
	ψ_2^3	[0 0 1]	[0 0 1]	[0 0 1]	[0 0 $\bar{1}$]	[0 0 $\bar{1}$]	[0 0 $\bar{1}$]	
Γ_4	ψ_1^4	[1 2 0]	$[\bar{2} \bar{1} 0]$	[1 $\bar{1}$ 0]	[1 2 0]	$[\bar{2} \bar{1} 0]$	[1 $\bar{1}$ 0]	
Γ_5	ψ_1^5	[1 0 0]	$\omega[0 \bar{1} 0]$	$\omega^*[1 1 0]$	[1 0 0]	$\omega[0 \bar{1} 0]$	$\omega^*[1 1 0]$	
		$\omega^*[\bar{1} 1 0]$	$\omega[0 \bar{1} 0]$	$[\bar{1} \bar{1} 0]$	$\omega^*[\bar{1} 0 0]$	$\omega[0 \bar{1} 0]$	$[\bar{1} \bar{1} 0]$	
	ψ_2^5	[0 1 0]	$\omega[1 1 0]$	$\omega^*[\bar{1} 0 0]$	[0 1 0]	$\omega[1 1 0]$	$\omega^*[\bar{1} 0 0]$	
		$\omega^*[1 1 0]$	$\omega[\bar{1} 1 0]$	[0 1 0]	$\omega^*[1 1 0]$	$\omega[\bar{1} 1 0]$	[0 1 0]	
	ψ_3^5	[0 0 1]	$\omega[0 0 \bar{1}]$	$\omega^*[0 0 \bar{1}]$	[0 0 $\bar{1}$]	[0 0 $\bar{1}$]	$\omega[0 0 1]$	$\omega^*[0 0 1]$
		$\omega^*[0 0 1]$	$\omega[0 0 \bar{1}]$	[0 0 1]	$\omega^*[0 0 1]$	$\omega[0 0 1]$	[0 0 $\bar{1}$]	[0 0 $\bar{1}$]
Γ_6	ψ_1^6	[1 0 0]	$\omega[0 \bar{1} 0]$	$\omega^*[1 1 0]$	$[\bar{1} 0 0]$	$\omega[0 1 0]$	$\omega^*[\bar{1} \bar{1} 0]$	
		$\omega^*[1 0 0]$	$\omega[0 1 0]$	[1 1 0]	$\omega^*[\bar{1} 0 0]$	$\omega[0 \bar{1} 0]$	$[\bar{1} \bar{1} 0]$	
	ψ_2^6	[0 1 0]	$\omega[1 1 0]$	$\omega^*[\bar{1} 0 0]$	[0 $\bar{1}$ 0]	$\omega[\bar{1} \bar{1} 0]$	$\omega^*[1 0 0]$	
		$\omega^*[\bar{1} \bar{1} 0]$	$\omega[1 1 0]$	[0 $\bar{1}$ 0]	$\omega^*[1 1 0]$	$\omega[\bar{1} 0 0]$	[0 1 0]	
	ψ_3^6	[0 0 1]	$\omega[0 0 \bar{1}]$	$\omega^*[0 0 \bar{1}]$	[0 0 1]	[0 0 1]	$\omega[0 0 \bar{1}]$	$\omega^*[0 0 \bar{1}]$
		$\omega^*[0 0 1]$	$\omega[0 0 \bar{1}]$	[0 0 1]	$\omega^*[0 0 1]$	$\omega[0 0 1]$	[0 0 $\bar{1}$]	[0 0 $\bar{1}$]

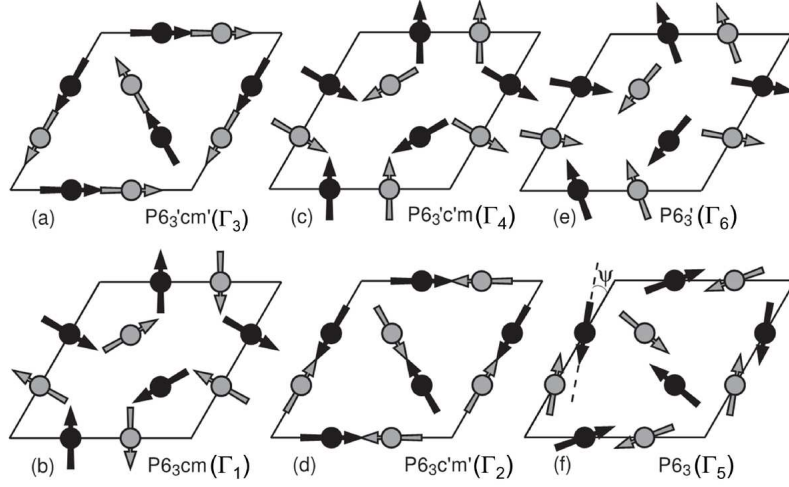


Figure 6.9: Different possible magnetic arrangements of Mn spins in the hexagonal rare-earth manganites as tabulated in table 6.3. Grey and black circles corresponds to $z = 0$ and $z = \frac{1}{2}$ layers, respectively. Taken from [198].

6.2.5.2 Neutron powder diffraction

Neutron powder diffraction (NPD) patterns were collected on pulverized crystals at high resolution neutron powder diffractometer SPODI, FRM II, Garching. Neutrons of wavelength 1.5481 \AA were used for the measurements of the powder samples filled in to a vanadium can of diameter $\sim 5 \text{ mm}$. NPD patterns of three typical temperature are shown in figure 6.10(a)-(c). It can be noted from the difference of diffraction patterns collected at 3 K and 300 K , no acknowledgeable changes in intensity is observed below magnetic ordering temperature expected due to magnetic ordering. This is due to strong neutron absorption cross section of Dy, which is about $856 \times 10^{-24} \text{ cm}^2$ for neutron wavelength 1.548 \AA , also it has significantly large incoherent scattering cross section ($54.4 \times 10^{-24} \text{ cm}^2$).

The NPD data collected at 300 K along with Rietveld refinement results is presented in figure 6.11. Refined structural parameters and discrepancy factors of the refinement are tabulated in the table 6.4. The lattice parameters are similar to those obtained from our PXRD measurements. Few spurious peaks are indicated by arrows are from the aluminium sample environment during the neutron scattering experiment. Due to very weak magnetic reflections no additional information on magnetic structure was obtained from the refinement of low temperature NPD patterns.

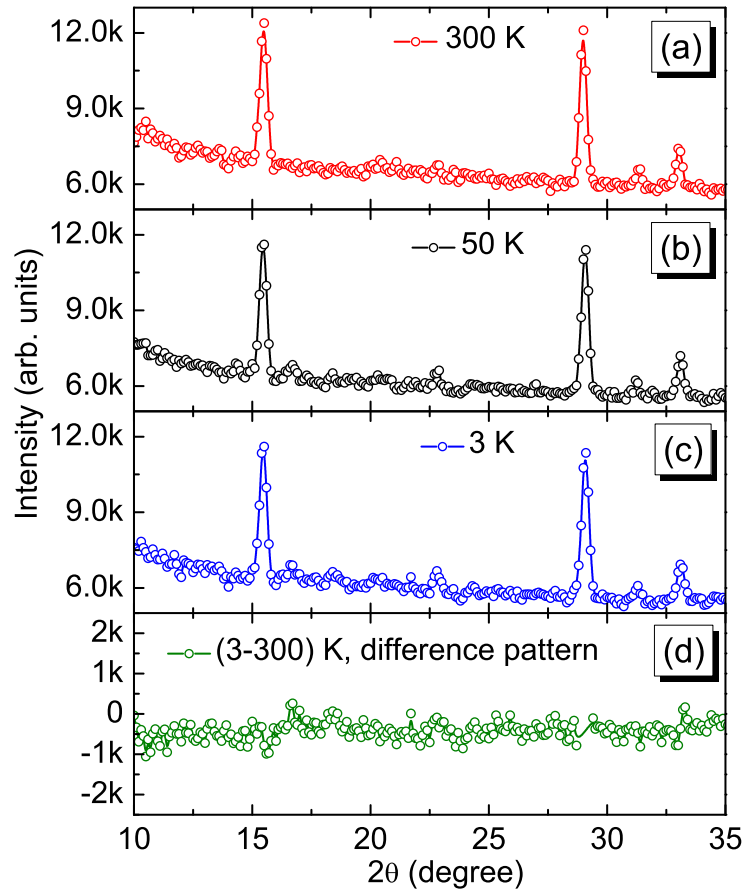


Figure 6.10: Low angle part of the neutron powder diffraction patterns collected at (a) 3 K, (b) 50 K and (c) 300 K. (D) The difference of diffraction patterns collected at 3 K and 300 K does not show acknowledgeable changes in intensity.

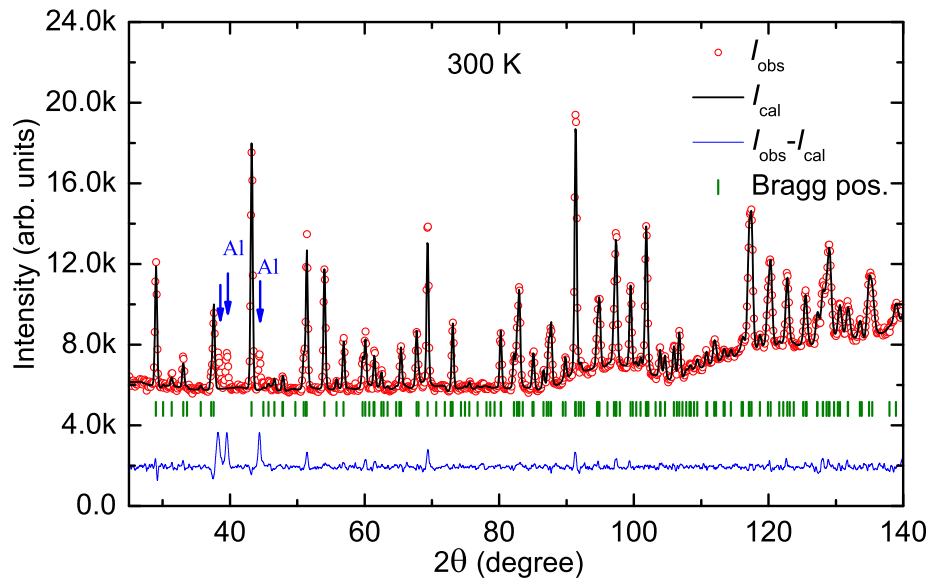


Figure 6.11: NPD data collected at 300 K and Rietveld refinement results. Arrows indicate peaks from Al sample environment during the measurement, this region in the pattern is excluded during the refinement.

Table 6.4: Structural parameters obtained from the Rietveld refinement of 300 K NPD data.

Atoms	Wyckoff positions	x	y	z
Dy1	2a	0	0	0.2789(5)
Dy2	4b	0.3333	0.6666	0.2398(3)
Mn	6c	0.3363(3)	0	0
O1	6c	0.2920(6)	0	0.1415(7)
O2	6c	0.6245(9)	0	0.3452(2)
O1	2a	0	0	0.5011(9)
O2	4b	0.3333	0.6666	0.0601(3)
Unit Cell Dimensions				
$a = 6.1849(3) \text{ \AA}$		$c = 11.4571(8) \text{ \AA}$		$V = 379.562(6) \text{ \AA}^3$
Discrepancy Factors				
$R_p = 12.91\%$	$R_{wp} = 9.35\%$	$R_{exp} = 7.06\%$		$\chi^2 = 5.27$

6.2.6 Single crystal neutron scattering measurements

Single crystal neutron scattering measurements were carried out in four circle hot neutron diffractometer D9 and thermal neutron two-axis diffractometer D23 situated at ILL, Grenoble. We scanned several crystal and magnetic Bragg reflections, as a function of temperature. To reduce the absorption of neutrons we used a small sample of dimensions $\sim 2 \times 2 \times 4 \text{ mm}^3$. Same sample was used for the measurements on both D9 and D23 instruments.

6.2.6.1 High temperature magnetic phases

From heat capacity measurements we had observed two high temperature anomalies at, $\sim 70 \text{ K}$ and $\sim 64 \text{ K}$ and from XRMS measurements it was reported that Dy orders with Γ_3 symmetry at $\sim 68 \text{ K}$ [183]. Also from SHG measurements the high temperature magnetic ordering of Mn was reported to be Γ_4 which takes place at $\sim 65 \text{ K}$. From the magnetic phase diagram (figure 6.5) obtained from isothermal magnetization measurements with field along c direction, a FIM phase was observed below 7 K , where a spontaneous magnetization is present. This directional dependence confirms that this

magnetic phase corresponds to FIM or ferromagnetic (FM) ordering of Dy moments along c , as the easy plane anisotropy of Mn spins restricts the moments strictly on the ab plane [184, 199], which are thus dominated by the strong in-plane antiferromagnetic superexchange interactions. This also means that IR Γ_5 for Dy, with FM ordering perpendicular to c doesn't exist in any temperature region. Further the presence of spontaneous magnetization only below ~ 7 K indicates that above this temperature Dy ordering is not FM or FIM. This rules out the possibility of IR Γ_2 at high temperature range. So the possible high temperature magnetic symmetries for Dy are Γ_1 , Γ_3 , Γ_4 and Γ_6 .

The temperature dependence of (101) integrated intensity of magnetic reflection is presented in figure 6.12. The integrated intensity was fitted employing a power law as,

$$I = I_0 \times \left(\frac{T_N - T}{T_N} \right)^\beta. \quad (6.10)$$

Where I_0 is the intensity at 0 K. The fit results are presented in the inset of figure 6.12. The values of T_N and β obtained from the fit are 66.3(4) K and 0.8(1) respectively. The ordering temperature thus found is close to one of the high temperature anomalies observed in our specific heat measurement (64 K) and to the of value reported from the SHG measurement (65 K), which is associated to the ordering of Mn sublattice in Γ_4

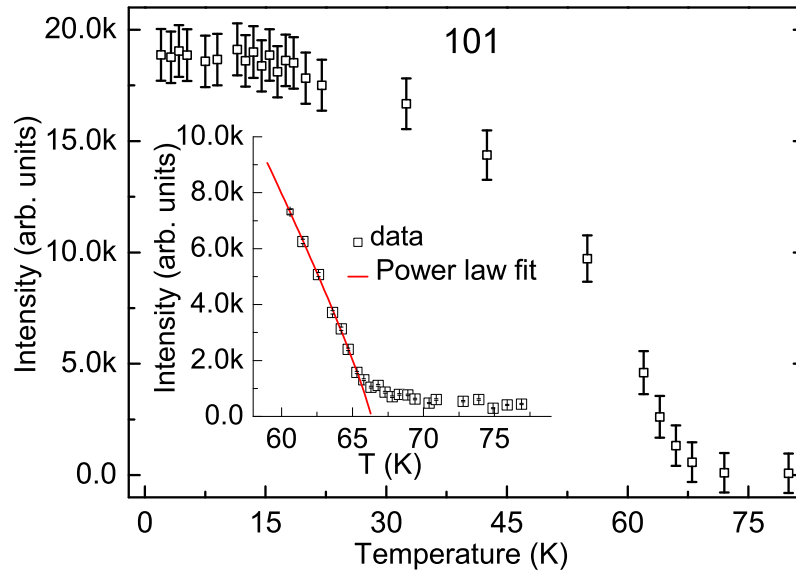


Figure 6.12: Temperature dependence of integrated intensity of magnetic reflections (101) measured at D23. Inset is the integrated intensity of magnetic reflections (101) measured at the instrument D9 (error bars are smaller than data markers), red curve is the result of power law fit near the ordering temperature.

symmetry [180]. But our specific heat data indicate another higher temperature anomaly at ~ 70 K. This we attribute to the ordering of Dy sublattice with Γ_3 symmetry as reported from XRMS studies [183]. This is the most unconventional ordering observed only in $hDMO$ in the family of $hRMnO_3$ compounds usually, in which Mn orders first and then induces rare-earth ordering with same magnetic symmetry, indicating strong $4f$ - $3d$ coupling. Our findings of weak or non-existent coupling between Dy and Mn sublattices can be the answer to the question, *why high temperature magnetic symmetries of Dy and Mn are different in $hDMO$?* That said, we still need to understand the origin of such a magnetic ordering.

6.2.6.2 Low temperature magnetic phases

From our discussions in previous section, possible IRs of Dy at low temperature are Γ_1 , Γ_2 , Γ_4 and Γ_6 . As already discussed in section 6.2.3 isothermal magnetization measurements indicate FIM type of Dy ordering below ~ 7 K with magnetic moments along c -direction. To confirm this we measured thermal evolution of the magnetic reflections (100) and (112) which shows a sharp increase in intensity below ~ 7 K (figure 6.13(a)-(b)). From the magnetic structure factor calculations based on all possible IRs show that only Γ_2 representation for Dy will have a finite magnetic intensity for the (112) reflection. This confirms that low temperature magnetic phase of Dy is Γ_2

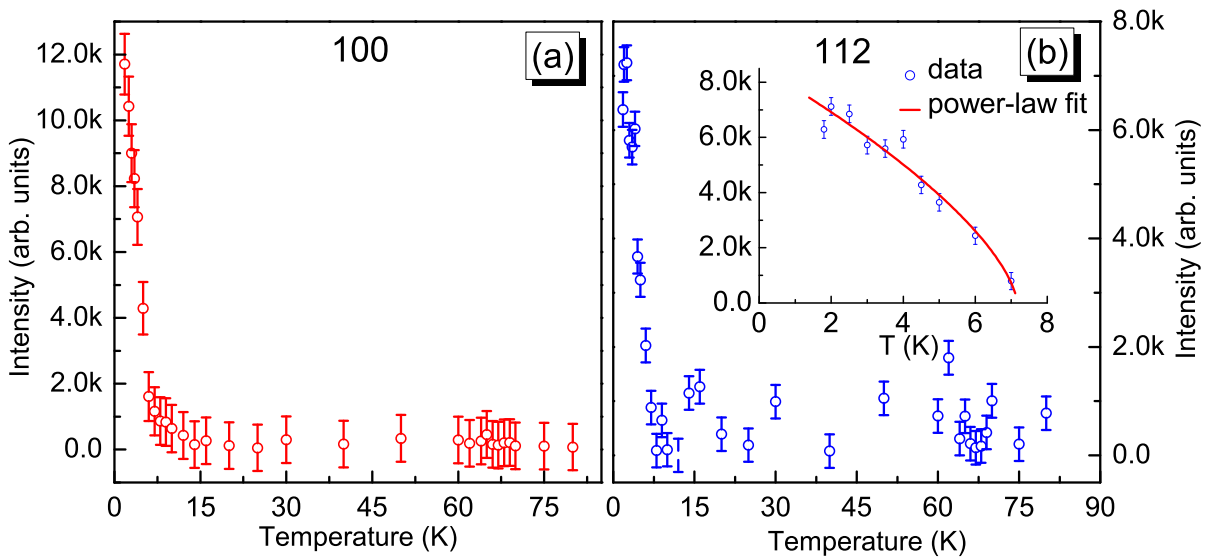


Figure 6.13: Temperature dependence of integrated intensity of magnetic reflections (a) (100) and (b) (112). Both are measured at D23. The inset shows a power-law fit to the integrated intensity of (112) reflection.

(FIM). From a power-law fit of temperature dependence of the magnetic reflection (112) using equation (6.10) we obtained ordering temperature 7.2(5) K, the fit is presented as inset of figure 6.13(b). This value is close to the anomaly observed in our magnetization measurement, ~ 8.3 K (figure 6.4(a)) and low temperature heat capacity measurements, ~ 9.5 K (figure 6.6). Since the magnetic propagation vector is $k = 0$, it is difficult to separate the magnetic contribution of Mn and Dy sublattices at low temperatures. For the low temperature ordering of Mn, we sought to the reported SHG measurements results which confirmed that Mn orders below 5 K with magnetic symmetry Γ_2 . This is in good agreement with the anomalies observed in our heat capacity (~ 5.3 K) and magnetization (~ 5 K) measurements.

6.3 Conclusions

Single crystals of *h*DMO were grown by optical floating zone technique starting from orthorhombic polycrystalline material synthesized by solid state route. This was achieved by tailoring the growth process in an oxygen deficient condition. Dc magnetization measurements showed a high temperature transition (~ 65 K) and two low temperature transitions (~ 8.3 K and ~ 5 K). The crystal structure of the grown crystals was determined from PXRD measurements. The thermal evolution of lattice parameters showed anomalous changes below magnetic ordering temperature and we modeled thermal variation of unit cell volume using Grüneisen approximation which confirmed presence of giant magneto-elastic effect through spin-lattice coupling, which is thought to be the origin of multiferroicity in these geometrically frustrated compounds. From the Curie–Weiss fit of high temperature susceptibility, the calculated Curie–Weiss temperature, Θ was found to be negative ($-95(3)$ K) which implies antiferromagnetic exchange interactions. Isothermal magnetization measurements indicate the presence of a ferrimagnetic phase below ~ 7 K under zero magnetic field with moments align *c*-direction. A magnetic H–T phase diagram was constructed from the isothermal magnetization curves measured at several temperatures. This indicates that, above the critical ~ 1.4 T field, applied along crystallographic *c* direction, FIM phase is stabilized in whole magnetically ordered temperature range. Our specific heat measurements show two high temperature (~ 70 K and ~ 64 K) and two low temperature anomalies (~ 9.5 K and ~ 5.3 K). The observation of two independent high temperature anomalies confirms

the independent ordering of Dy and Mn sublattices indicating a weak $4f-3d$ coupling in h DMO. The low temperature anomalies observed in specific heat measurements are in good agreement with those observed in magnetization measurements. We have modeled the total specific heat by assuming the contributions from a Schottky term, a linear term and lattice term comprising Debye and Einstein terms and the lattice specific heat. The absence of both low temperature anomalies in the specific heat under the applied magnetic field indicate that Mn also undergoes a field induced transition similar to Dy, which is also supported by reported SHG results. From the single crystal neutron scattering measurements the ordering temperature of high temperature phase of Mn was determined (66.3(4) K), also the low temperature magnetic symmetry of Dy was confirmed to be Γ_2 with an ordering temperature of $\sim 7.2(5)$ K. This is in very good agreement with our magnetization and specific heat measurements and also the reported XRMS results. The ordering temperatures of Dy and Mn sublattices in DMO observed from different measurements can be summarized as follows:

Dy ordering:

- Specific heat \Rightarrow Anomalies at ~ 70 K and ~ 9.5 K are attributed to high (Γ_3) and low (Γ_2) temperature magnetic ordering of Dy, respectively (present work).
- Magnetization $\Rightarrow 8.3$ K (present work).
- XRMS \Rightarrow Dy orders with IR Γ_3 at ~ 68 K and remains the same down to 8 K [200].
- Elastic neutron scattering \Rightarrow Orders with IR Γ_2 below ~ 7 K (present work).

Mn ordering:

- Specific heat \Rightarrow Anomalies at ~ 64 K and ~ 5.3 K are attributed to high (Γ_4) and low (Γ_2) temperature magnetic ordering of Mn, respectively (present work).
- Magnetization \Rightarrow Anomaly at 5 K is attributed to Mn ordering with IR Γ_2 (present work).
- Second harmonic generation \Rightarrow Mn orders with IR Γ_4 at ~ 65 K and a transition to IR Γ_2 occurs below 5 K [180].
- Elastic neutron scattering \Rightarrow Orders at ~ 66 K (present work).

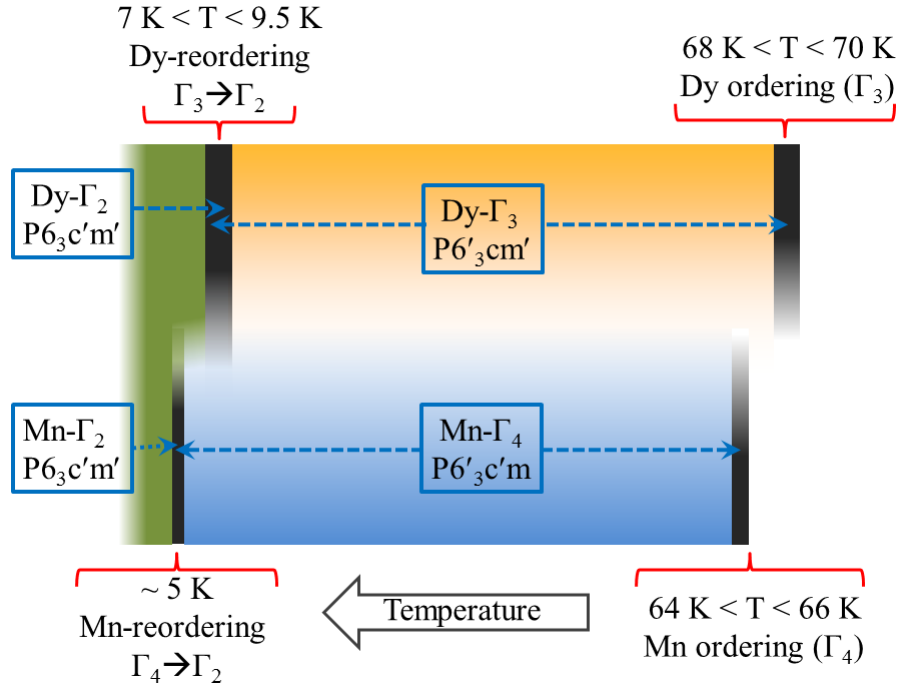


Figure 6.14: Summary of magnetic phase transitions in *hDMO* under zero magnetic field.

Magnetic phase transitions summarized above are graphically represented in figure 6.14.

From our PXR, specific heat, magnetization and neutron scattering measurements along with reported data based on SHG and XRMS, we systematically established the nature of both high and low temperature ordering of Dy and Mn sublattices in *hDMO*. We report an unconventional high temperature ordering of Dy ion which is unique among *hRMnO₃* family. We propose that the ordering of Dy at higher temperature than Mn could explain the observation of weak $4f$ - $3d$ coupling leading to the different magnetic symmetries of two sublattices in this compound.

Chapter 7

INCOMMENSURATE MAGNETIC ORDERING IN $\text{Mn}_{0.9}\text{M}_{0.1}\text{WO}_4$ (M=Co, Cu)

7.1 Introduction

A typical feature of multiferroic materials undergoing a transition to a elliptic spiral ferroelectric phase, is the existence of spectacular magnetoelectric effects, such as the polarization flops observed in $TbMnO_3$ [201] and orthorhombic $DyMnO_3$ [202] or the sign reversal of P_y disclosed under magnetic field in $TbMn_2O_5$ [16]. The orientation of the applied magnetic field with respect to the magnetic spins influence the stability range of the spiral phase and the polarization-flop process. This property was recently illustrated by remarkable magnetic field induced effects observed in ferroelectric phase of manganese tungstate $MnWO_4$ (MWO) in which applied field [71–73] induces a high-field polarization flop transition [74]. In the present chapter we discuss the influence of chemical doping on the elliptic spiral order of MWO.

MWO is made up of MnO_6 octahedra with high-spin Mn^{2+} (d_5) ions and WO_6 octahedra with diamagnetic W^{6+} (d_0) ions. Recently it was found that MWO exhibits multiferroicity in which magnetism causes ferroelectricity, implying a strong coupling between the two [18, 72, 203]. $MnWO_4$ is one of the prototypical multiferroic material exhibiting spin-current ferroelectricity [72]. It possesses a complex phase diagram with 3 antiferromagnetic phases below 14 K namely AF1, AF2 and AF3 at zero magnetic field. AF2 is a ferroelectric (FE) phase, in which net polarization is along b axis which can be flipped to a axis with the application of external magnetic field. This is the first example of the ferroelectric polarization flop induced by magnetic fields in transition-metal oxide systems without rare-earth $4f$ moments. Taniguchi *et al.* showed that the stability of the magnetoelectric domain walls in a canted magnetic field plays a key role in the directional control of the electric polarization flop phenomenon [74]. From polarized neutron scattering measurements Sagayama *et al.* showed that an inverse effect of Dzyloshinskii-Moriya interaction is the origin of the spontaneous electric polarization in the spiral phase of $MnWO_4$ [73].

Very recently it was found that the ferroelectric phase is completely suppressed in MWO by doping 10% iron on Mn site, which can be again restored with the application of a magnetic field. The absence of ferroelectricity (at zero field) in $Mn_{0.9}Fe_{0.1}WO_4$ is explained by the increase of uniaxial spin anisotropy K [204]. Evidence for the increase of K with Fe substitution was also derived from the results of neutron scattering experiments [205]. It was observed in $Mn_{1-x}M_xWO_4$ ($M=Mg, Zn$ and $x \leq 0.3$), substitution of the nonmagnetic ions Mg^{2+} and Zn^{2+} for the magnetic ions Mn^{2+} result in

very similar effects on the magnetic and dielectric properties of MWO. These substitutions destabilized the non-polar magnetic structure AF1 of MWO but the AF3-to-AF2 magnetoelectric phase transition was not affected. This indicated that the nonmagnetic dopants destroy neither the three-dimensional nature of magnetic interactions, nor the spin frustration within each $\parallel c$ -chain and between $\parallel c$ -chains along the a -direction.

In most of the recently discovered multiferroics, the ferroelectric polarization can be explained by the inverse Dzyaloshinski-Moriya effect [63, 206, 207], where the induced electric polarization of a single pair of spins \vec{S}_i, \vec{S}_j separated by a distance vector $\vec{r}_{i,j}$ is given by [206]

$$\vec{P}_{FE} \propto \vec{r}_{ij} \times (\vec{S}_i \times \vec{S}_j). \quad (7.1)$$

The required noncollinear magnetic structure may arise from strong frustration. Since in addition the interaction, equation 7.1, is only a second order effect, the ferroelectric polarization is rather small in these materials. In the REMnO₃ [201, 208] series and in MWO [18, 72, 203] the electric polarization is about two to three orders of magnitude smaller than in a classical ferroelectric perovskite such as BaTiO₃, hindering the observation of electric-field-induced effects in the magnetic structure. Despite, it was shown that it is possible in these chiral multiferroics to switch the magnetic order by the application of an electric field at constant temperature. In the present chapter we present our investigations on the effect of Co and Cu doping on the magnetic ordering of MnWO₄.

7.2 Experimental

7.2.1 Synthesis

Polycrystalline powders of Mn_{0.9}Co_{0.1}WO₄(MCoW) and Mn_{0.9}Cu_{0.1}WO₄(MCuW) were prepared by conventional solid state route. Stoichiometric amount of precursors, W₂O₃(99.9), MnO₂(99.9) and CuO(99.99) or Co₃O₄(99.99) were ground well with a mortar and pestle, pressed into pellets and sintered in a furnace at 900 °C for 12 hours in the presence of atmospheric air. The pellets were ground again, pressed into pellets and sintered at 900 °C for 48 hours. The powder samples were characterized by powder X-ray diffraction (PXRD) and no impurity phases were found [209].

7.2.2 Crystal structure

Both compounds were found to crystallize in monoclinic structure and PXRD patterns were refined with space group $P2/c$ using *FullProf*. The measured PXRD pattern and Rietveld refinement results are presented in figure 7.1(a) & (b). The refined crystal structure presented in figure 7.1(c) shows the clinographic view of the edge sharing Mn(Co/Cu)-O6 bipyramidal polyhedra along c direction. The refined structure parameters and discrepancy parameters are presented in table 7.1. The lattice constants of both the compounds are comparable to that of parent compound $MnWO_4$ [71], with the exception that MCuW has significantly larger monoclinic distortion.

Table 7.1: Structural parameters obtained from the Rietveld refinement of room temperature PXRD.

Atoms	$Mn_{0.9}Co_{0.1}WO_4$			$Mn_{0.9}Cu_{0.1}WO_4$		
	x/a	y/b	z/c	x/a	y/b	z/c
Mn,(Co/Cu)	$\frac{1}{2}$	0.6849(1)	$\frac{1}{4}$	$\frac{1}{2}$	0.6870(2)	$\frac{1}{4}$
W	0	0.18035(6)	$\frac{1}{4}$	0	0.18085(8)	$\frac{1}{4}$
O1	0.2133(5)	0.0980(4)	0.9499(6)	0.2095(5)	0.0895(5)	0.9518(7)
O2	$\frac{1}{4}$	0.3743(4)	0.3968(6)	$\frac{1}{4}$	0.3822(5)	0.3926(8)
Unit Cell Dimensions						
$a = 4.81475(1) \text{ \AA}, b = 5.75124(3) \text{ \AA}$			$a = 4.81065(4) \text{ \AA}, b = 5.76265(5) \text{ \AA}$			
$c = 4.99123(4) \text{ \AA}, V = 138.187(3) \text{ \AA}^3$			$c = 4.98194(5) \text{ \AA}, V = 138.070(2) \text{ \AA}^3$			
$\gamma = 91.0654(4)^\circ$			$\gamma = 91.3731(5)^\circ$			
Discrepancy Factors						
$R_p = 9.17 \%, R_{wp} = 9.3 \%$			$R_p = 11.1 \%, R_{wp} = 11.2 \%$			
$R_{exp} = 3.25 \%, \chi^2 = 4.17$			$R_{exp} = 3.05 \%, \chi^2 = 5.57$			

7.2.3 Magnetic and thermal properties

The field-cooled (FC) and zero field-cooled (ZFC) dc magnetization curves measured with an applied magnetic field of 1 kOe presented in figure 7.2(a) and (b) corresponds to MCoW and MCuW, respectively. The thermal evolution of reciprocal susceptibility calculated from the FC magnetization curves are presented figure 7.2(c) and (d). For

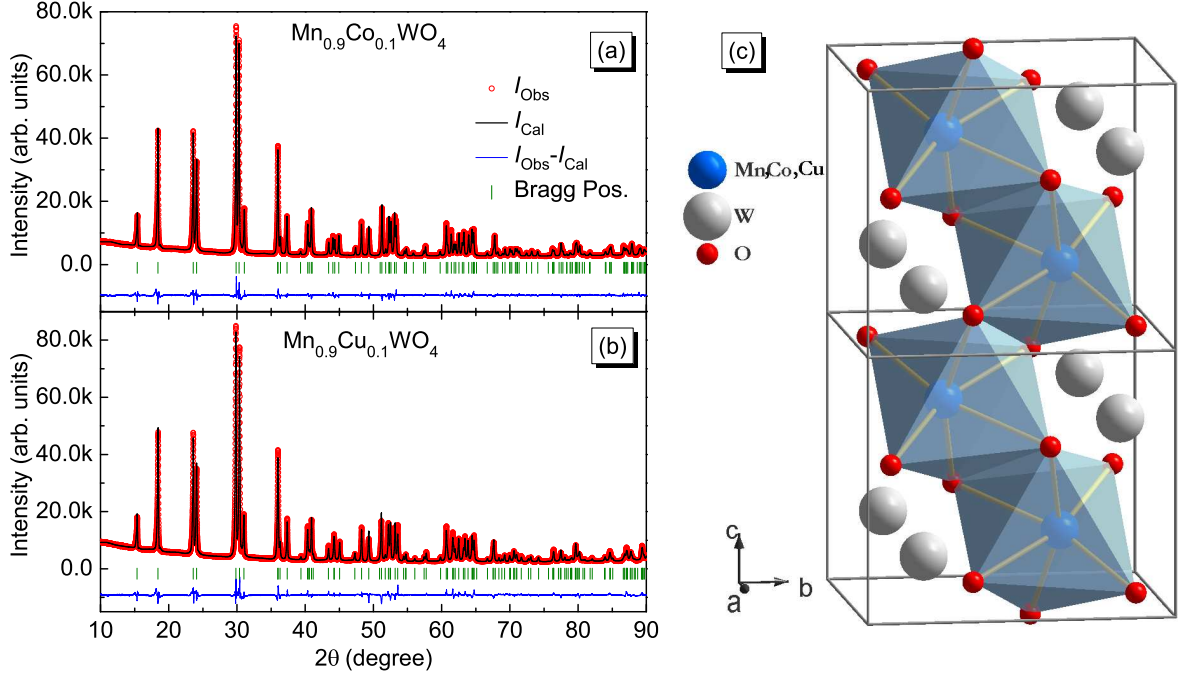


Figure 7.1: PXRD patterns collected at 300 K and Rietveld refinement results for (a) $Mn_{0.9}Co_{0.1}WO_4$ and (b) $Mn_{0.9}Cu_{0.1}WO_4$. (c) Clinographic view of the refined crystal structure, grey boxes indicate crystallographic unit cells.

MCoW the inverse susceptibility follows Curie-Weiss law down to ~ 30 K below which it deviates from the fitted curve, showing a marked deviation below ~ 13.5 K, which corresponds to long range magnetic ordering of Mn^{2+} spins, T_N . Inverse susceptibility of MCuW follows Curie-Weiss law down to ~ 80 K, below which it deviates from the fitted curve and shows a marked deviation below ~ 15 K which corresponds to T_N . The deviation of inverse susceptibility well above ordering temperatures in both compounds indicates the presence of short-range spin fluctuations above T_N which is more prominent in the case of MCuW. From Curie-Weiss fit of the susceptibility data for MCoW, the Curie-Weiss temperature (Θ_{CW}) and effective moment (μ_{eff}) were found to be $-79.6(1)$ K and $5.97(7) \mu_B$, respectively, and for MCuW, $\Theta_{CW} = -60.3(3)$ K and $\mu_{eff} = 5.4(1) \mu_B$. The frustration parameter calculated as $f = |\Theta_{CW}|/T_N$ for MCoW and MCuW are, ~ 5.9 and ~ 4 . In deed MWO has been known to be a moderately spin frustrated system with the frustration parameter, $f = |\Theta_{CW}|/T_N \approx 5$, where Θ_{CW} is approximately -75 K and the Néel temperature $T_N = 13.5$ K [203, 210]. Interestingly from our magnetization measurements we found that Co doping increases and Cu doping reduces the geometric spin frustration of MWO.

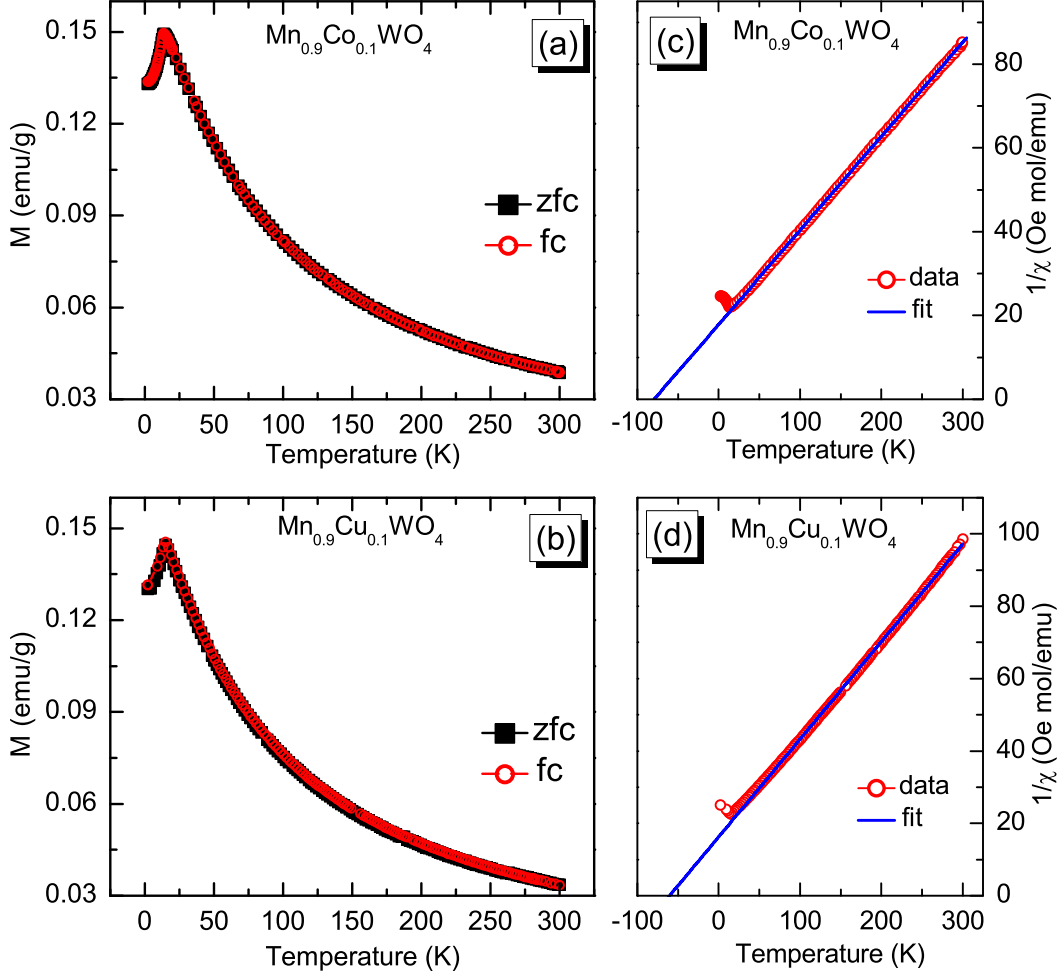


Figure 7.2: Zero-field-cooled (ZFC) and field-cooled (FC) magnetization curves of (a) $Mn_{0.9}Co_{0.1}WO_4$ and (b) $Mn_{0.9}Cu_{0.1}WO_4$, measured with an applied field of 1 kOe. (c) and (d) are the dc susceptibility and Curie-Weiss fits for, $Mn_{0.9}Co_{0.1}WO_4$ and $Mn_{0.9}Cu_{0.1}WO_4$ respectively.

The thermodynamic signature of transition between different phases is usually detected in distinct anomalies of the heat capacity, $C_p(T)$. Multiferroic materials with a sequence of subsequent transitions may show more or less pronounced sudden change of C_p . Specific heat measurements were performed on MCoW and MCuW pellets, using a physical property measurement system (Quantum Design) in the temperature range 3–300 K. The variation of specific heat (C_p) with temperature is presented in figure 7.3 (a) and (b) for MCoW and MCuW, respectively. The insets of figure 7.3 (a) and (b) clearly indicates two anomalies. The high temperature anomaly in MCoW is believed to be associated with T_N (≈ 14.5 K) where Mn(Co) orders, transforming from a paramagnetic (PM) state to a collinear spin sinusoidal state (AF3) as in the case of MWO. The second

anomaly in this case at T_2 (≈ 13.2 K) was attributed to transition from collinear AF3 state to incommensurate elliptical spiral phase (AF2') phase [211]. The nature of the phase transitions observed in the case of MCuW (≈ 14.6 K and ≈ 13.7 K) needs further studies and will be discussed in later section based on our NPD measurements.

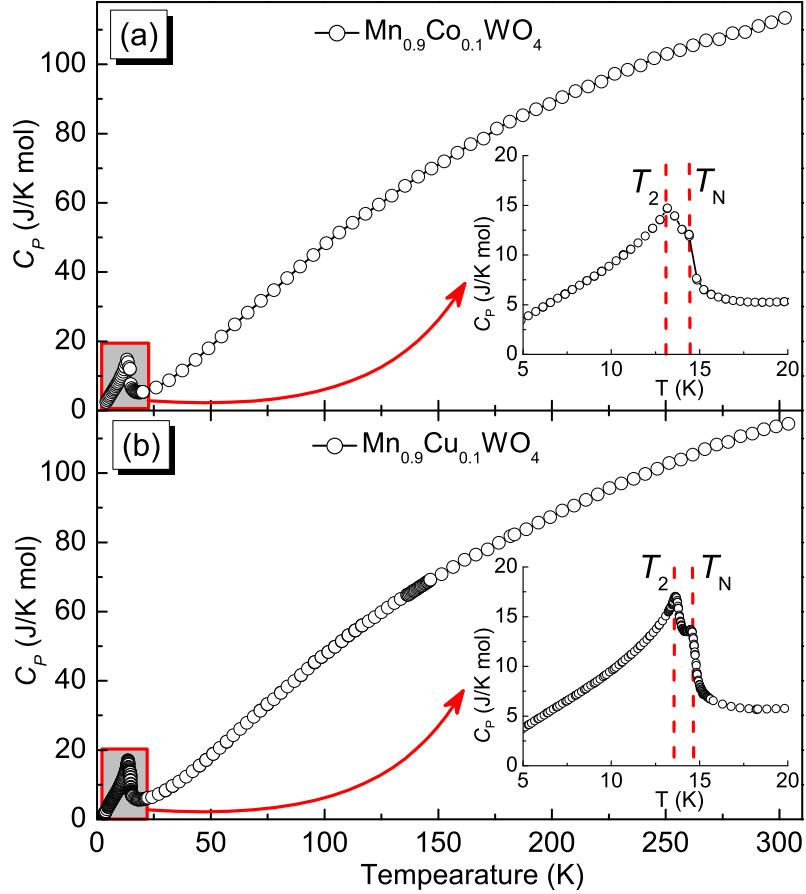


Figure 7.3: Specific heat C_p of (a) MCoW and (b) MCuW.

7.3 Magnetic ordering

7.3.1 Experimental

To determine the magnetic ordering of Mn in $\text{Mn}_{0.9}\text{M}_{0.1}\text{WO}_4$, several NPD patterns were acquired in the temperature range 3 – 150 K. About 5 g of polycrystalline powder samples were used in the measurements using the high-resolution powder diffractometer, SPODI, at the research reactor FRM II, Garching. The powder sample was held in a vanadium cylinder of diameter 5 mm with helium exchange gas. Vertical focussing

monochromator, consisting of 17 Ge(551) was used to achieve neutrons of wavelength 1.549Å. The magnetic structures were refined from the NPD data using the Rietveld refinement with *FullProf*. The input control files used for the refinement of all magnetic phases presented in the following sections of this chapter are presented in the appendix F.

7.3.2 Magnetic structure refinement

The starting models for the magnetic structure refinement analysis are adopted from the previous report by Lautenschläger *et al* [71]. The basis functions for the irreducible representations for Mn^{2+} spins in MWO were calculated for the propagation vector $\mathbf{k} = (k_x, \frac{1}{2}, k_z)$ from the group theory and summarized in table 7.2. It should be noted that same set of basis vectors shown in table 7.2 can be applied to all of the magnetic phases discussed in this chapter. For instance, one can obtain basis vectors for the commensurate AF1 phase by taking $k_z = 1/2$. In order to generate elliptical spiral with uniform pitches along the c axis, one should use a set of basis vectors from either $(\tau_1^1, \tau_2^2, \tau_1^3)$ or $(\tau_2^1, \tau_1^2, \tau_2^3)$. These two different sets of basis vectors produce spiral chains with opposite chirality from each other, which cannot be differentiated by unpolarized neutron scattering.

Table 7.2: Basis vectors for the irreducible representations for axial mode at the Mn sites in space-group $P2/c$ for the propagation vector $\mathbf{k} = (k_x, \frac{1}{2}, k_z)$ ($\psi = \exp^{\pi i k_z}$).

Position	$(\frac{1}{2}, y, \frac{1}{4})$	$(\frac{1}{2}, -y, \frac{3}{4})$
τ_1^1	$(1, 0, 0)$	$(\psi, 0, 0)$
τ_1^2	$(0, 1, 0)$	$(0, -\psi, 0)$
τ_1^3	$(0, 0, 1)$	$(0, 0, \psi)$
τ_2^1	$(1, 0, 0)$	$(-\psi, 0, 0)$
τ_2^2	$(0, 1, 0)$	$(0, \psi, 0)$
τ_2^3	$(0, 0, 1)$	$(0, 0, -\psi)$

7.3.2.1 $Mn_{0.9}Co_{0.1}WO_4$

In figure 7.6 we present the observed and the calculated NPD intensities of MCoW in two different phases: (a) PM, (b) AF2'. Due to temperature instability during the measurement of NPD, AF3 phase, which is expected to occur in a narrow temperature range of ~ 1 K, could not be determined. As expected MCoW orders with magnetic

state AF2' in the temperature range 3 – 13 K. In the case of MWO in the AF2 phase, the orientation of the spin vector at $\mathbf{r} = (x, y, z)$ can be expressed as,

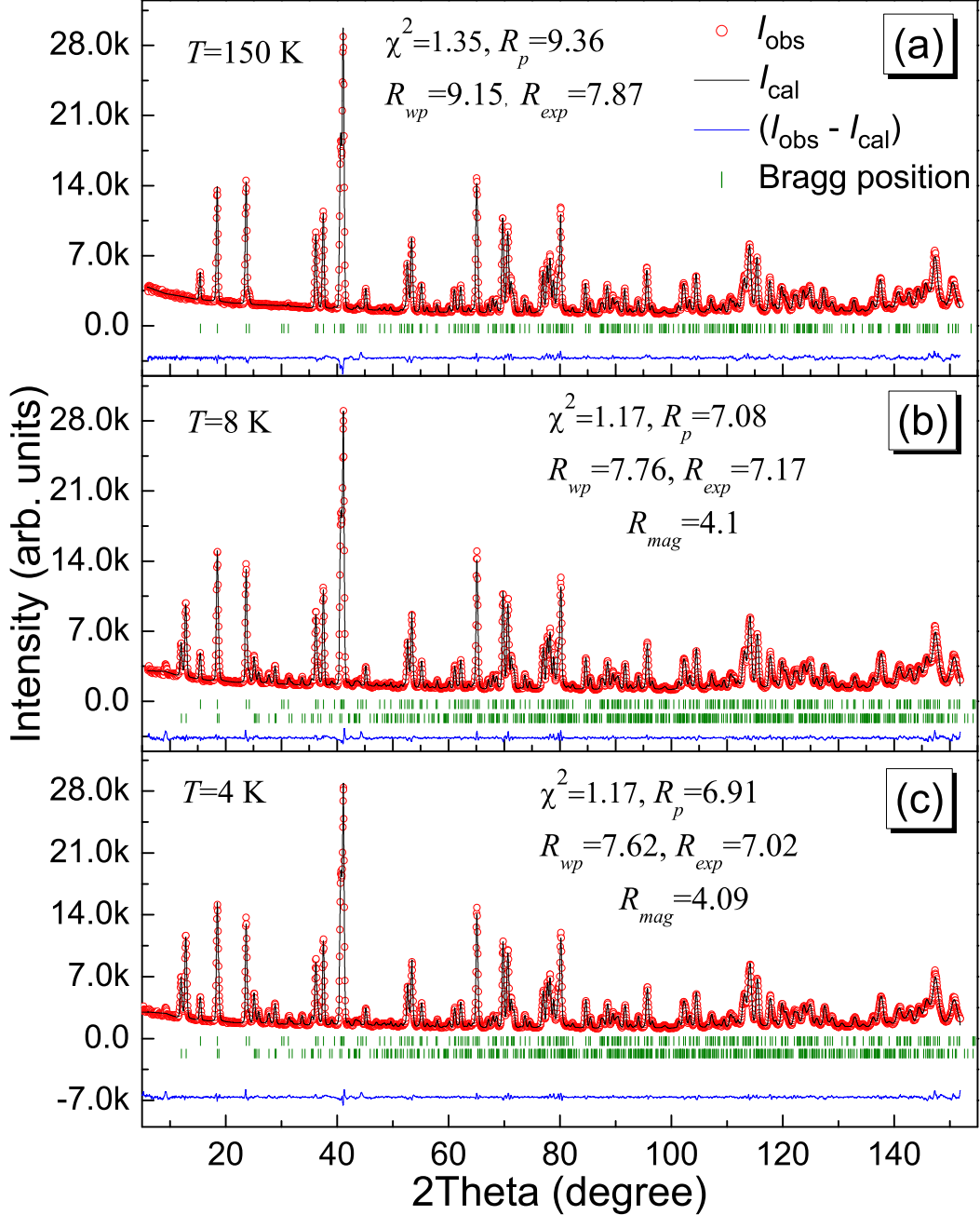


Figure 7.4: Observed (I_{obs}) and calculated (I_{cal}) NPD profiles of $Mn_{0.9}Co_{0.1}WO_4$ at, (a) paramagnetic, and (b), (c) AF2' phases, respectively. The discrepancy factors are also indicated. The blue line indicates the difference between observed and calculated patterns, the top and bottom vertical marks indicate nuclear and magnetic Bragg-peak positions.

$$\mathbf{m}(\mathbf{r}) = \mathbf{p} \cos(2\pi\mathbf{k}_2 \cdot \mathbf{r} + \phi) + \mathbf{q} \cos(2\pi\mathbf{k}_2 \cdot \mathbf{r} + \phi). \quad (7.2)$$

where, \mathbf{p} and \mathbf{q} are perpendicular to each other, and the spiral becomes elliptical when $|\mathbf{p}| \neq |\mathbf{q}|$.

The NPD patterns and Rietveld refinement results for temperatures, 150 K, 8 K and 4 K are plotted in figure 7.6(a), (b), (c), and (d) respectively along with discrepancy factors. The propagation vector is found to be $\mathbf{k}'_2 = (-0.220, \frac{1}{2}, 0.471)$ at both 8 K and 4 K which is in excellent agreement with the value reported based on single crystal neutron scattering measurements [212]. It was found that with increasing doping concentration the propagation vector is enlarged from the value $\mathbf{k}_2 = (-0.214, \frac{1}{2}, 0.457)$ in the case of MWO [211]. To compare our results we also measured NPD of parent MWO. In figure 7.5(a) and (b) we present the spin structures of MWO in AF1 and AF2 phases, respectively, and figure 7.5(c) indicates the spin structure of AF2' phase of MCoW. It can be noted that the spin spiral in AF2 phase of MWO is parallel to b axis. But in AF2' phase of MCoW the spin spiral is nearly perpendicular to b axis. This spin-flop transition is accompanied by a subsequent flop of the ferroelectric polarization from b to the a axis [212]. A careful inspection of 4 and 8 K data reveal the presence of a magnetic peak around $2\theta = 11^\circ$, it is attributed to the commensurate propagation vector $\mathbf{k}_4 = (\frac{1}{2}, 0, 0)$ as in the case of $CoWO_4$ [213] which is referred as AF4 in the rest of the paper.

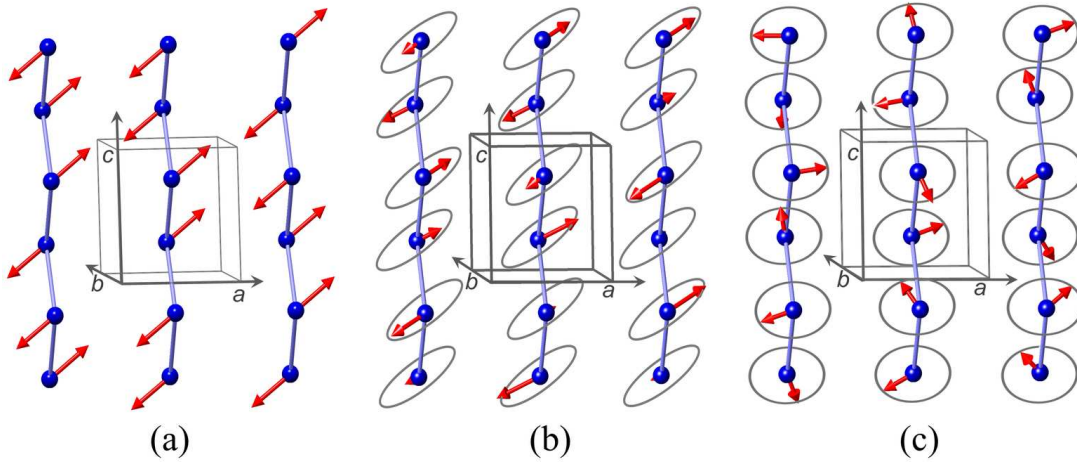


Figure 7.5: Spin structures of $MnWO_4$ obtained from Rietveld refinement of neutron diffraction data, (a) at 5 K (AF1) and (b) at 10 K (AF2) and (c) $Mn_{0.9}Co_{0.1}WO_4$ at 4 K (AF2') where spiral plane is parallel to a axis. The arrows represent the spins and the ellipse/circle indicate their plane of rotation.

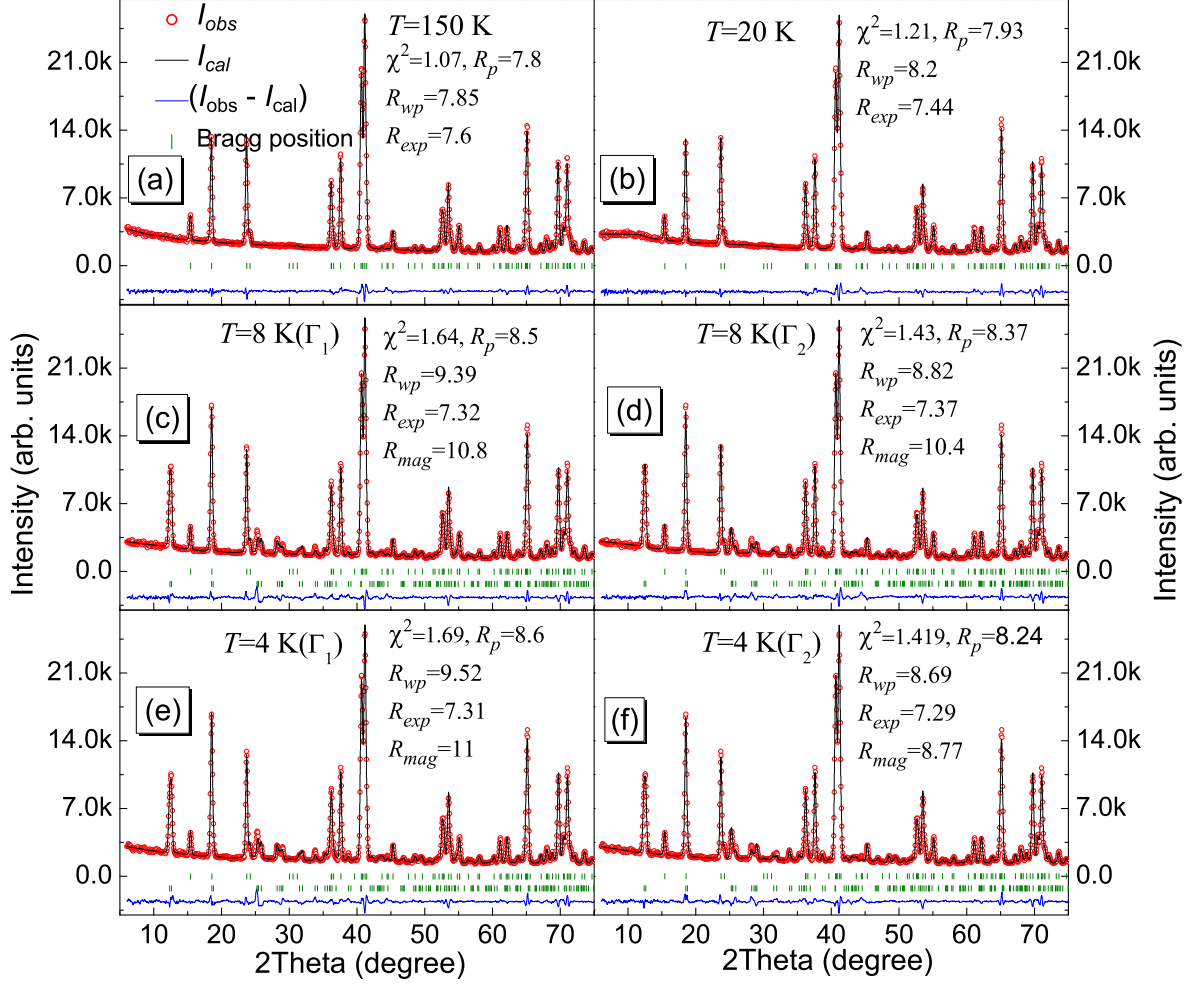
7.3.2.2 $\text{Mn}_{0.9}\text{Cu}_{0.1}\text{WO}_4$ 

Figure 7.6: Observed (I_{obs}) and calculated (I_{cal}) NPD profiles of $\text{Mn}_{0.9}\text{Cu}_{0.1}\text{WO}_4$ at, (a)–(b) paramagnetic, (c)–(f) AF3 phases, respectively. The discrepancy factors are also indicated. The blue line indicates the difference between observed and calculated patterns, the top and bottom vertical marks indicate nuclear and magnetic Bragg-peak positions. In (c) and (e) the NPD profiles correspond to magnetic structure calculated according to magnetic representation Γ_1 and, (d) and (f) according to Γ_2 .

In figure 7.6(a)–(f) we present the observed and the calculated NPD intensities of MCuW in two different phases: (a)–(b) PM and (c)–(f) AF3. Due to temperature instability during the measurement of NPD, AF3 phase, which is expected to occur in a narrow temperature range of ~ 1 K, was not conclusive. In contrast to MCoW the propagation vector in the case of MCuW in the temperature range 4 – 13 K is found to be $\mathbf{k}_3 = (-0.221, \frac{1}{2}, 0.495)$. The magnetic structure was refined in both possible representations Γ_1 and Γ_2 . The goodness of fit in the refinement (indicated as insets

in figure 7.6(a)-(f)), with Γ_2 representation is slightly better than the refinement with Γ_1 representation. Though it is tempting to conclude that the Γ_2 representation is the best model which represent the magnetic ordering in $MCuW$, we still need further single crystal measurements for a conclusive result. The refined spin structures are presented in figure 7.7, which shows a sinusoidal modulation along a axis. It should be noted that the helical magnetic order is suppressed by replacing Mn^{2+} ion by Cu^{2+} . This result is similar to that of $Mn_{0.9}Fe_{0.1}WO_4$ for which AF3 phase has a modulation vector $k_3 = (-0.235, \frac{1}{2}, 0.49)$. In $Mn_{0.9}Fe_{0.1}WO_4$ ferroelectric and helical magnetic orders were suppressed which could be restored by the application of external magnetic fields [204]. The lack of ferroelectricity at zero magnetic field was explained by the increase of the uniaxial anisotropy K . In contrast to $Mn_{0.9}Fe_{0.1}WO_4$ where a transition from paraelectric (PE) AF3 to AF1, that occurs around 12 K, $MnCuW$ remains in AF3 phase down to 4 K. Due to the suppression of helical magnetic order we can rule out the existence of ferroelectric phase in this compound in the temperature range 4 – 13 K under zero applied magnetic fields. The modification of magnetic structures and recovery of ferroelectric-helical phase needs to be scrutinized.

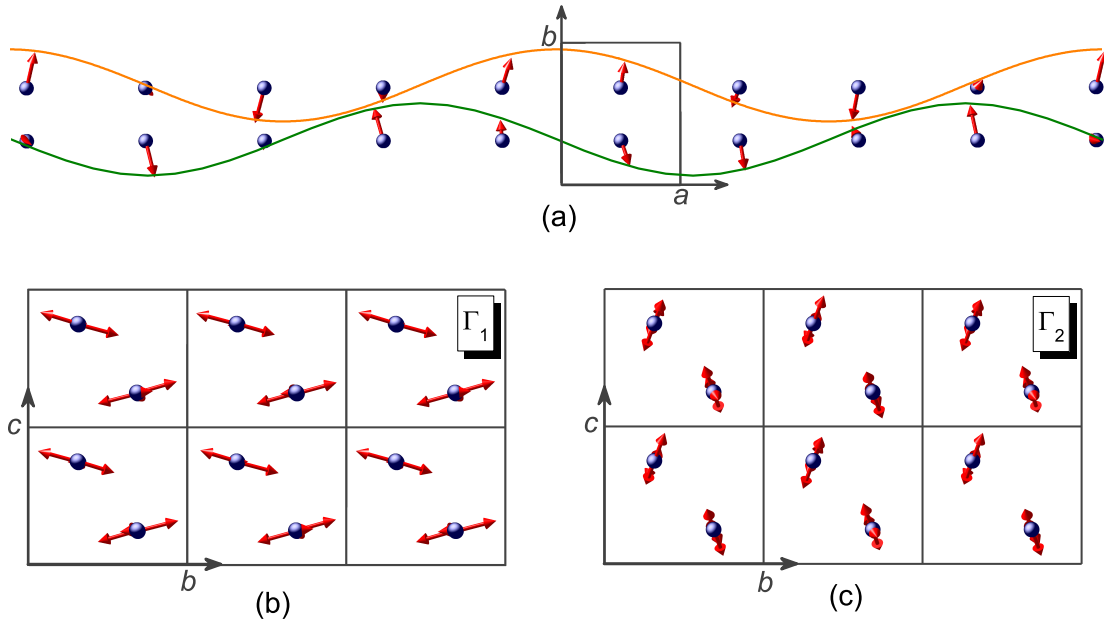


Figure 7.7: (a) Sinusoidal modulation of magnetic moments of $Mn_{0.9}Cu_{0.1}WO_4$ seen through c -direction obtained from Rietveld refinement of neutron diffraction data, for $z = \frac{1}{4}$ (orange line) and for $z = \frac{3}{4}$ (olive line) atoms. Grey box indicates the crystallographic unit cell. (b) and (c) shows the orientation of the magnetic moments as seen through c -direction in Γ_1 and Γ_2 magnetic symmetries, respectively.

7.4 Summary and Conclusions

In summary we have synthesized and studied the magnetic ordering in $\text{Mn}_{0.9}\text{Co}_{0.1}\text{WO}_4$ and $\text{Mn}_{0.9}\text{Cu}_{0.1}\text{WO}_4$. Rietveld refinement of room temperature PXR patterns showed that both compounds crystallize in monoclinic symmetry with space group $P2/c$. Curie-Weiss temperatures calculated from dc magnetic susceptibility measurements for MCoW and MCuW are $-79.6(1)$ K and $-60.3(3)$ K, respectively, indicating antiferromagnetic correlations. The frustration parameter is ~ 5.9 and ~ 4 for MCoW and MCuW, respectively. Specific heat measurements reveals two anomalies below ≈ 15 K in both compounds. The two anomalies in case of MCoW are at ≈ 14.5 K and ≈ 13.2 K and in case of MCuW the anomalies are at ≈ 14.6 K and ≈ 13.7 K. The NPD results of our studies on MCoW is in excellent agreement with earlier reports on the same compound based on powder and single crystal neutron diffraction studies. The spin flop transition of the elliptical spin plane from being parallel to b axis to nearly perpendicular to b axis in MCoW is confirmed. This spin-flop transition due to doping of Co, in the case of MCoW induces flop of the ferroelectric polarization from b to the a axis. This result is a good example in which the direction of ferroelectric polarization of a magnetic material can be controlled via chemical doping. The higher degree of distortion in the crystal structure of MCuW can be understood by considering the crystal structure of CuWO_4 [214]. CuWO_4 crystallizes in highly distorted triclinic structure. By doping Cu on Mn sites in case of MWO the distortion is increased. On the other end, both MWO and CoWO_4 , are iso-structural and hence Co doping on Mn site has least effect on the structural distortions. Our studies on the doping effects clearly demonstrate that doping on the Mn site acts like chemical pressure which changes the magnetic phase diagram, analogous to observed field induced magnetic phase transitions in the parent compound, MnWO_4 . Further detailed study of the nature of doping of Mn sites with various amount of Cu, and also the effect of applied magnetic field on the magnetic ordering, would be very interesting. We expect that such studies could lead to a better understanding of the nature of interaction leading to complex magnetic ordering and ferroelectricity in this class of multiferroics.

Chapter 8

Summary and outlook

Multiferroics are materials that display spontaneous ferroelectric and magnetic ordering at the same time. Multiferroics are very promising candidate materials to be used in high density data storage devices. A better understanding of crystal and magnetic structure is a key to understand the underlying physics in multiferroics, which could help to design efficient materials for application. In this thesis we present synthesis, structural and magnetic investigations on two kinds of multiferroic materials. We present our findings of geometrically frustrated multiferroics, polycrystalline orthorhombic HoCrO_3 (HCO) and hexagonal DyMnO_3 (*h*DMO) single crystals in chapters–(3, 4, 5) and chapter–6, respectively. We also presented our investigations on spin frustrated system, $\text{Mn}_{0.9}\text{M}_{0.1}\text{WO}_4$ (M=Co, Cu) in chapter–7. In the following sections we summarize our main results and outlook of the of the present work.

8.1 Orthorhombic HoCrO_3

One of the most important factors that influence materials investigation is the necessity of high quality samples. In this chapter we present synthesis and macroscopic characterization of multiferroic, orthorhombic HOCrO_3 (HCO). Polycrystalline samples were prepared by standard solid state reaction route. The quality of polycrystalline samples (phase purity) was monitored by powder x-ray diffraction (PXR) studies. Phase pure samples were then subjected to thermal, magnetic and temperature dependent x-ray diffraction studies. From the Rietveld refinement of PXR we refined the crystal structure in $Pbnm$ symmetry. From the temperature dependence of lattice parameters, it was found that HCO exhibits magneto-elastic (ME) effect. From magnetization measurements we found the ordering temperature $T_N = 142$ K. It was also shown that HCO undergoes magnetic field induced phase transitions. From a detailed analysis of specific heat data in the temperature 0.1 – 300 K we could separate contributions from nuclear, electronic, lattice and magnetic specific heat. The nuclear contribution is due to hyperfine interactions and was modeled using a 8–level nuclear Schottky term. The hyperfine splitting energy and effective field (H_{eff}) were determined as ~ 20.68 K and 600 T, respectively. The electronic Schottky anomaly due to crystal field interactions was modeled using a 5–level Schottky term. The calculated crystal field energy levels are in good agreement with reported values. The lattice specific heat was modeled with

one Debye term and two Einstein terms. By subtracting all the above contributions we determined the magnetic specific heat in HCO. The nuclear and magnetic entropies calculated are in good agreement with the theoretical values.

Further high resolution inelastic measurements can be performed to confirm the hyperfine energy levels as determined from the low temperature heat capacity measurements. Also single crystal magnetization and neutron scattering measurement in the presence of magnetic field can be performed to understand the nature of field induced phase transitions as indicated by magnetization measurements.

High resolution neutron powder diffraction (NPD) experiments were performed on HCO. Several NPD patterns were acquired in the temperature range 3 – 300 K. From symmetry analysis and observed magnetic reflections we found that the magnetic symmetry of Ho and Cr sublattices is $Pbn'm'$. From the Rietveld analysis of NPD patterns the temperature dependence of magnetic order parameters were determined. It was found that Cr orders antiferromagnetically with a small canting angle with respect to c -direction below $T_N 142.3(8)$ K. From the temperature dependent order parameter one can see that the Ho ordering is induced. Ho was ordered canted antiferromagnetically in ab plane with a ferromagnetic component along a . We modeled Cr and Ho ordered moments using molecular field theory. From the least squares fit of Ho ordered moment it was found that a small moment persists up to ≈ 142 K. The molecular field constants obtained from the fit are, $\lambda_0 \approx 37.1 \text{ T}/\mu_B$ and $\lambda_1 \approx 9.5 \text{ T}/\mu_B$, associated with Cr–Cr and Ho–Cr exchange interactions, respectively. Clearly Cr–Cr exchange is relatively stronger. From the fitting the lowest crystal field splitting energy was found to be $\Delta = 1.8(3) \text{ meV}$ which is comparable with the value obtained from specific heat measurements. Our measurements also indicate presence of spin fluctuations well below magnetic ordering temperature seen as a broad peak around magnetic reflection $(1\ 0\ 1)$, $Q \approx 1.46 \text{ \AA}^{-1}$.

From thermal variation of lattice parameters we show that HCO exhibit magnetoelastic effect. Lattice parameters show an anomalous change around magnetic ordering temperature. The temperature variation of unit cell volume in paramagnetic region was modeled using Grüneisen approximation for the zero pressure equation of state. The excess change in unit cell volume ΔV due to ME effect displays a linear relation with ordered magnetic moment of Cr ion. This confirms spin-phonon coupling in this material, which is commonly observed in geometrically frustrated materials.

Further inelastic neutron scattering measurements such as magnon-dispersion, on single crystals of HCO can give a better description of exchange interactions. It is

also worth studying the effect of external magnetic field on the the magnetic ordering. In light of multiferroicity a detailed quantitative study of dielectric measurements are needed. In this chapter we present our inelastic neutron scattering (INS) on polycrystalline HCO were collected at several temperatures with incident energies $E_i = 19.61, 10.25,$ and, 3.55 meV. Three well resolved crystal field transitions are visible at $1.41, 10.1,$ and, 15.5 meV. The crystal field levels at 1.5 K were modeled using point charge model. The crystal field levels obtained are in good agreement with those obtained from specific heat measurements. Due to the low point symmetry of Ho site (m or C_{1h}) in HCO and limited energy range measured, we could not model high temperature INS spectra.

Spin fluctuations are observed as a broad peak around $Q \approx 1.4\text{\AA}^{-1}$. The temperature dependence of full-width-half-maximum (FWHM) of this peak follows Cr ordered moment indicating the origin of fluctuations to be Cr. We calculated correlation lengths from FWHM as function of temperature using Selyakov-Scherrer formula. It was found that well above the magnetic ordering temperature the correlation length ξ is $\approx 10\text{\AA}$ which is close to next-nearest-neighbor distance in HCO. Around magnetic ordering temperature a sharp increase in correlations length was observed due to long range magnetic ordering of Cr.

Further, effect of applied magnetic field on the crystal field levels and magnetic fluctuations can be measured in this compound.

8.2 Hexagonal DyMnO₃

Single crystal of h DMO were synthesized by optical floating zone technique. Rietveld refinement of PXRD patterns of pulverized single crystals confirmed a pure hexagonal DMO with space group $P6_3cm$. Oriented and cut single crystals were characterized by specific heat and magnetization measurements, which confirmed two high temperature ($\sim 69(1)$ K, $\sim 65(1)$ K,) and two low temperature transitions ($\sim 8(1)$ K, ~ 5 K,). Isothermal magnetization measurements indicate a field induced transition from antiferromagnetic to ferrimagnetic phase. From the temperature dependence of PXRD patterns, anomalous changes in lattice parameters is found around magnetic ordering temperature (≈ 65 K), indicating the presence of ME effect. From single crystal neutron scattering measurements we determined magnetic ordering temperature of Mn ≈ 66 K. Our measurements also confirm that Dy orders below ≈ 7 K with magnetic symmetry $P6_3c'm'$. From our

specific heat, magnetization and single crystal neutron scattering measurements along with reports based on x-ray resonant magnetic scattering (XRMS) and second harmonic generation (SHG) measurements we show an unconventional magnetic ordering in h DMO. In the high temperature region Dy orders with magnetic symmetry $P6'_3cm'$ and Mn with magnetic symmetry $P6'_3c'm'$. This is in sharp contrast to other hexagonal manganites where both rare earth and Mn order with same magnetic symmetry. The present observation in case of h DMO indicates a weak $4f - 3d$ interactions in this compound. From the specific heat and neutron scattering data the ordering temperature of Mn is found to be $\sim 65(1)$ K. We suggest that the anomaly at $\sim 69(1)$ K in the specific heat data is due to magnetic ordering of Dy. This is a very unconventional type of magnetic ordering. Further at low temperature Dy and Mn order with same magnetic symmetry $P6_3c'm'$.

Detailed dielectric measurements are still need for this compound. Further inelastic neutron scattering studies are due. Inelastic neutron scattering measurements will be a challenging task due to large neutron absorption cross section of Dy. One should try isotope enrichment for a better experimental statistics.

8.3 Wolframite $Mn_{0.9}Co_{0.1}WO_4$ and $Mn_{0.9}Cu_{0.1}WO_4$

Spin frustrated multiferroic $Mn_{0.9}Co_{0.1}WO_4$ (MCoW) and $Mn_{0.9}Cu_{0.1}WO_4$ (MCuW) were prepared by standard solid state synthesis method. From magnetization and heat capacity measurements the compounds are found to order below ≈ 15 K. Heat capacity measurements show two anomalies below 15 K. From our NPD data measured at several temperatures we have determined two different magnetic phases in case of MCoW with same incommensurate propagation vector $\mathbf{k}'_2 = (-0.220, \frac{1}{2}, 0.457)$. Our measurements are in excellent agreement with the reported magnetic structure of $Mn_{0.9}Co_{0.1}WO_4$. From the Rietveld refinement of NPD data of MCuW, it was found that below 12 K in whole temperature range MCuW is in same magnetic phase in contrast to other doped and parent $MnWO_4$ compounds. The incommensurate wave vector is found to be $\mathbf{k}_3 = (-0.235, \frac{1}{2}, 0.49)$.

Lately single crystals of $Mn_{0.9}Co_{0.1}WO_4$ were studied extensively. But this is the first report on the magnetic structure of $Mn_{0.9}Cu_{0.1}WO_4$. In the present study we have very limited amount of temperature points. The study should be performed with better temperature resolution, to clearly investigate the temperature evolution of magnetic

ordering in this compound. Since the observed magnetic ordering in MCuW is very different compared to the parent and other doped compounds in this family one should study the implications of this magnetic ordering on dielectric properties. Two approaches would be: (i) to study the effect of chemical pressure by varying Cu doping concentration and (ii) to study the variation of magnetic ordering with the application of magnetic fields on the magnetic ordering.

In conclusion, we have shown on three different candidates for multiferroic compounds –two geometrical multiferroics and one with spiral spin mechanism– how crystal and spin structure determined with scattering techniques are related to physical properties like magnetization and specific heat. In this way, our study helps to elucidate the mechanisms of multiferroicity in transition metal oxides.

Appendices

Appendix A

List of acronyms

- AFM – Antiferromagnetic
- BF – Basis function
- CEF – Crystal-electric field
- CF – Crystal field
- CFT – Crystal field theory
- FE – Ferroelectric
- FC – Field-cooled
- FIM – Ferrimagnetic
- FM – Ferromagnetic
- FWHM – Full-width-half-maximum
- HCO – HoCrO_3
- hDMO – Hexagonal DyMnO_3
- INS – Inelastic neutron scattering
- IR – Irreducible representation
- ME – Magnetoelectric
- MCoW – $\text{Mn}_{0.9}\text{Co}_{0.1}\text{WO}_4$
- MCuW – $\text{Mn}_{0.9}\text{Cu}_{0.1}\text{WO}_4$
- MWO – MnWO_4
- OFZ – Optical Floating Zone
- NPD – Neutron powder diffraction
- SHG – Second harmonic generation
- PXRD – Powder x-ray diffraction
- RA – Representation analysis
- RE – Rare-earth
- SR – Spin reorientation
- XRMS – X-ray resonant magnetic spectroscopy
- ZFC – Zero field-cooled

Appendix B

The Rietveld Method

In the Rietveld method, least-squares refinements are carried out until a best fit is obtained between the observed powder diffraction pattern (integrated intensities in the case of single crystal diffraction) and the calculated pattern based on the simultaneously refined models for the crystal and/or magnetic structure(s), diffraction optics effects, instrumental factors, and other specimen characteristics like lattice parameters as can be modeled. A key factor of the method is the feature of feedback between improving knowledge of structure and the allocation of observed intensity to partially overlapping individual Bragg reflections. Earlier methods used just to follow a systematic procedure for decomposing the powder pattern into its component Bragg reflections without reference to a structural model—called *pattern decomposition*.

Mathematical background

For the refinement using the Rietveld method the data must be obtained in digitized form, i.e., intensity values y_i at equal increments i in case of powder diffraction or integrated intensities maximum possible Bragg reflections for the case of single diffraction experiments. The increment is normally in 2θ (in case of powder diffraction). It can also be in other variables like velocity or wavelength. Typical step sizes vary from 0.01 to $0.05^\circ 2\theta$. The best fit is sought for all the thousands of y_i s simultaneously. The quantity minimized in the least-squares refinement is the residual, S_y

$$S_y = \sum_i w_i (y_i - y_{ci})^2$$

where $w_i = 1/y_i$ for Gaussian statistics, y_i is the observed intensity at i th step and y_{ci} is the calculated intensity at the i th step. The calculated intensities are determined from

the \mathbf{F}_K values calculated from a structural model:

$$y_{ci} = s \sum_K L_K \mathbf{F}_K \phi(2\theta_i - 2\theta_k) P_K A + y_{bi}$$

where s is the scale factor, K represents the Miller indices, $h k l$, for a Bragg reflection, L_K contains the Lorenz, polarization, and multiplicity factors, ϕ is the reflection profile function, P_K is the preferred orientation function, A is an absorption factor, \mathbf{F}_K is the structure factor for the K^{th} Bragg reflection and y_{bi} is the background intensity at the i^{th} step.

The least squares minimization procedure leads to a set of *normal equations* involving derivatives of all of the calculated intensities y_{ci} with each of the adjustable parameters and are solvable by inversion of the *normal matrix* with elements M_{jk} formally given by

$$M_{jk} = - \sum_i 2w_i \left[(y_i - y_{ci}) \frac{\partial^2 y_{ci}}{\partial x_j \partial x_k} - \left(\frac{\partial y_{ci}}{\partial x_j} \right) \left(\frac{\partial y_{ci}}{\partial x_k} \right) \right]$$

where the parameters x_j, x_k are the same adjustable parameters.

Thus the procedure is one of creation and inversion of an $m \times m$ matrix, where m is the number of parameters to be refined. The solution is found by an iterative procedure in which the shifts Δx_k , are

$$\Delta x_k = \sum M_{jk}^{-1} \frac{\partial S_y}{\partial x_k}$$

The calculated shifts are then applied to the initial parameters to produce a improved model and the whole procedure is then repeated.

Various terms in y_{ci} :

a. Background intensity

The background intensity at the i th step, y_{bi} , can be obtained from (i) an operator-supplied table of background intensities or (ii) linear interpolation between operator-selected points in the pattern or (iii) a specified background function. The background is always refined. Several background functions are employed, and one of the simplest one is a fifth-order polynomial provided with an operator-specifiable origin to

help fitting the broad humps in the background curve.

$$y_{bi} = \sum_{m=0}^5 B_m [(2\theta_i/BKPOS) - 1]^m$$

where *BKPOS* is the origin that is to be user-specified in the input control file.

b. Reflection profile function

This function denoted as ϕ approximates the effects of both instrumental features and specimen features. Mostly used analytical profile functions are pseudo-Voigt functions, the Pearson VII function, Gaussian, Lorentzian and modified Lorentzian functions. For X ray data analysis the pseudo-Voigt function is mostly employed. It has the following functional form:

$$\begin{aligned} & \eta L + (1 - \eta)G; \\ G &= \frac{C_0^{1/2}}{H_K \pi^{1/2}} \exp \left[\frac{-C_0(2\theta_i - 2\theta_k)^2}{H_K^2} \right] \\ L &= \frac{C_1^{1/2}}{\pi H_K} \frac{1}{\left[1 + \frac{C_1(2\theta_i - 2\theta_k)^2}{H_K^2} \right]} \end{aligned}$$

c. Preferred orientation

Preferred orientation arises when there is a stronger tendency for the crystallites in a specimen to be oriented more one way than all others. This can occur, for example, in a material that has a strong cleavage or growth habit that is packed into a flat specimen holder. Preferred orientation mostly produces systematic distortions of the reflection intensities and the distortions can be modeled with preferred orientation functions such as,

$$\begin{aligned} P_K &= \exp(-G_1 \alpha_K^2) \\ \text{or} \\ P_K &= [G_2 + (1 - G_2) \exp(-G_1 \alpha_K^2)] \end{aligned}$$

where G_1 and G_2 are refinable parameters and α_K is an angle.

d. Structure factor

The structure factor in case of a simple cubic structure is given by

$$\mathbf{F}_K = \sum_j N_j f_j \exp [2\pi i (hx_j + ky_j + lz_j)] \exp (-M_j)$$

where, h , k and l are the Miller indices, x_j , y_j and z_j are the position parameters of the j th atom in the unit cell, $M_j = 8\pi^2 u_j^2 \sin^2 \theta / \lambda^2$, u_j^2 (isotropic atomic displacement parameter, for simplest case of purely harmonic thermal motion of equal magnitude in all directions) is the root-mean-square thermal displacement of the j th atom parallel to diffraction vector and N_j is the site occupancy multiplier for the j th atom site.

Agreement factors

The Rietveld refinement procedure will adjust the refinable parameters until the residual is minimized. The "best fit" will depend on the adequacy of the model employed and whether a *global minimum* is reached rather than a *local minimum*. Most programmes that use the Rietveld method have a set of R -values that are measure of quality of the agreement between observed and calculated profiles [215]. They are:

$$R - \text{Bragg factor}, R_B = \frac{\sum |I_K(\text{obs}) - I_K(\text{calc})|}{\sum I_K(\text{obs})}$$

$$R - \text{pattern}, R_p = \frac{\sum_i |y_i(\text{obs}) - y_i(\text{calc})|}{\sum_i y_i(\text{obs})}$$

$$R - \text{weighted pattern}, R_{wp} = \left[\frac{\sum_i w_i [y_i(\text{obs}) - y_i(\text{calc})]^2}{\sum_i w_i (y_i(\text{obs}))^2} \right]^{\frac{1}{2}}$$

In addition an expected profile R value R_{exp} can be calculated, which indicates the attainable limit for R_{wp} by considering only pure statistics on the nominator of the expression for R_{wp} . For n number of data points and m number of refined parameters, the expected profile value is,

$$R_{\text{exp}} = \left[\frac{(n - m)}{\sum_i w_i (y_i(\text{obs}))^2} \right]^{\frac{1}{2}}$$

One can also define a *Goodness of fit* as $\chi^2 = (R_{wp}/R_{\text{exp}})^2$. During the refinement process, χ^2 starts out large when the model is poor and decreases as the model produces better agreement with the data. Ideally, χ^2 should converge to 1 for a good fit.

Appendix C

Crystal and magnetic structure determination of HoCrO_3

For the symmetry analysis first one has to determine the crystal structure (space group) and lattice parameters near the magnetic transition temperature. Also with the knowledge of the magnetic peak position one has to determine the propagation vector (\vec{k}), which is straight forward with the use of program *k-search* (included in *FullProf* suit). Then the programs like *BasIreps* (included in *FullProf* suit) [216] or *SARAh* [153] can be used to deduce the allowed magnetic representations given the crystal symmetry and propagation vector. For the present case we used the program *BasIreps* .

C.1 Representation analysis of HoCrO_3 with *BasIreps*

The program *BasIreps* calculates the irreducible representations (irreps) of the so called "little groups" from which the full irreps of space group can be calculated using the induction formula. After calculating the irreps corresponding to a given space group and propagation vector the program calculates the basis function corresponding to vectorial properties (atom displacements or magnetic moments) of atoms in crystalline solids. This program calculates non-normalized basis functions of the irreps of the little group G_k for atom properties in a crystal. In particular the calculations can be performed for magnetic moments which are axial vectors. In general the magnetic moment of atom j in cell L

may be written as a Fourier series of the form:

$$\mathbf{m}_{jL} = \sum_{\mathbf{k}} \mathbf{S}_{\mathbf{k}j} \exp(-2\pi i \mathbf{k} \cdot \mathbf{R}_L) \quad (\text{C.1})$$

Here \mathbf{k} and \mathbf{R}_L are vectors referred to the reciprocal and direct crystallographic basis, respectively. The vectors \mathbf{m}_{jL} and $\mathbf{S}_{\mathbf{k}j}$ have the same units and are referred to a basis of unit vectors along the direct crystallographic cell basis. The $\mathbf{S}_{\mathbf{k}j}$ are the Fourier components of the magnetic moments \mathbf{m}_{jL} .

Taking in to account the symmetry, the vectors $\mathbf{S}_{\mathbf{k}j}$ can be written as linear combinations of the so-called basis functions of the irreducible representations of the propagation vector group G_k . The number of free parameters in a magnetic structure is less than $N = 3 \times n \times O\{\mathbf{k}\}$. The number 3 comes from the components of $\mathbf{S}_{\mathbf{k}j}$, n is the total number of atoms in a primitive cell and $O\{\mathbf{k}\}$ is the number of propagation vectors. The number of independent parameters (order parameters) can be calculated from the group theory. In general the vector $\mathbf{S}_{\mathbf{k}j}$ may be written as:

$$\mathbf{S}_{\mathbf{k}j} = \sum_{a,m} C_{a,m} \mathbf{V}_{a,m}(\mathbf{k}, \nu|j) \quad (\text{C.2})$$

Where $C_{a,m}$ are the coefficients (that may be real or purely imaginary) of the linear combination, and $\mathbf{V}_{a,m}(\mathbf{k}, \nu|j)$ are constant vectors referred to the basis of the direct cell. The labels are the following (\mathbf{k}, ν) is for the particular propagation vector and the representation called Γ_ν . The index a varies from 1 up to the dimension of the irreducible representation: $a = 1, 2, \dots, \dim(\Gamma_\nu)$. The index m varies from 1 to the number of times the irreducible representation Γ_ν is contained in the global magnetic representation constructed by working with the symmetry operators acting on atoms coordinates and components of axial vectors (dimension $3 \times n$) [84].

To calculate the allowed magnetic presentations (MRs) the program *BasIreps* requires the details (in the input file called **.smb*) of crystal symmetry, lattice parameters and \vec{k} . Once these are known it becomes rather simple straight forward to determine all the symmetry allowed magnetic representation. To makes things simple, *BasIreps* produces an output file **.fp* which contains symmetry operations corresponding to all possible MRs which can directly be used in refinement of magnetic structure using *FullProf*. The input file for *BasIreps* used for the case of HoCrO_3 is shown in figure C.1.

```

TITLE repre_HoCrO3
SPGR P B N M
KVEC 0.0000 0.0000 0.0000 X
BASIR AXIAL
ATOM Cr Cr 0.50000 0.00000 0.00000
ATOM Ho Ho -0.01795 0.06567 0.25000

```

Figure C.1: A snap-shot of the input file *.smb for the program *BasIreps*. Line one is the title, line-2 defines the space group (SPGR) *Pbnm*, line 3 defines the magnetic propagation vector (*KVEC*), $\vec{k} = (0\ 0\ 0)$ and lines 5 and 6 defines the atomic positions of *Cr* and *Ho* ion

The output of *BasIreps*, *.fp contains magnetic symmetry elements for eight MRs of *Cr* ions ($\Gamma_1 - \Gamma_8$) and four MRs of *Ho* ion ($\Gamma_1, \Gamma_3, \Gamma_5$ and Γ_7). Using these results one can simulate magnetic contribution to the neutron diffraction patterns (magnetic Bragg intensities) and also can refine the magnetic structure from experimental data from neutron, single crystal or powder diffraction measurements.

C.2 Magnetic structure refinement of HoCrO_3 using *FullProf*

For the present case only four MRs ($\Gamma_1, \Gamma_3, \Gamma_5$ and Γ_7) will be considered as allowed MRs as only these four are allowed for both *Cr* and *Ho* magnetic sublattices. The magnetic peak intensities were simulated for all four MRs mentioned above using the program *FullProf*. By comparing measured intensities and simulated intensities of few typical magnetic peaks we were able to determine unambiguously the magnetic representation to be Γ_5 for both *Cr* and *Ho* ions (see section 4.3.1.2 in chapter 4 for details). The magnetic structure was refined with the MR Γ_5 (space group *Pbn'm'*) simultaneously with the nuclear structure (space group *Pbnm*). The input control file (*.pcr) used for the simultaneous refinement of crystal and magnetic structures from the neutron powder diffraction data collected at 3 K is presented in the next page.

Input file (*.pcr) for the simultaneous refinement of crystal and magnetic structure of HoCrO₃:

```

COMM HoCrO3
! Current global Chi2 (Bragg contrib.) = 2.536
! Files => DAT-file: HCO_1, PCR-file: hocro3_3k
! Job Npr Nph Nba Nex Nsc Nor Dum Iwg Ilo Ias Res Ste Nre Cry Uni Cor Opt Aut
  1 7 2 60 2 0 0 1 0 2 1 0 1 0 0 0 0 0 1
!
!lpr Ppl loc Mat Pcr Ls1 Ls2 Ls3 NLI Prf Ins Rpa Sym Hkl Fou Sho Ana
  0 2 1 1 2 0 4 0 0 -3 10 -2 1 1 1 0 1
!
!lambda1 Lambda2 Ratio Bkpos Wdt Cthm muR AsyLim Rpolarz ->Patt# 1
  1.548100 1.548100 0.0000 14.000 7.0000 0.0000 0.3000 180.00 0.0000
!
!NCY Eps R_at R_an R_pr R_gl Thmin Step Thmax PSD Sent0
  99 0.32 0.98 0.98 0.98 0.98 1.0000 0.100065 153.8000 0.000 0.000
!
!2Theta/TOF/E(Kev) Background for Pattern# 1
  11.674 2297.190 261.000
  58 more background points in between
  151.705 1327.638 931.000
!
! Excluded regions (LowT HighT) for Pattern# 1
  0.00 10.00
  152.00 180.00
!
  94 !Number of refined parameters
!
! Zero Code SyCos Code SySin Code Lambda Code MORE ->Patt# 1
-0.00032 21.0 0.00000 0.0 0.00000 0.0 0.000000 0.00 0
!-----
! Data for PHASE number: 1 ==> Current R_Bragg for Pattern# 1: 2.26
!-----
HoCrO3 nuclear
!
!Nat Dis Ang Pr1 Pr2 Pr3 Jbt Irf Isy Str Furth ATZ Nvk Npr More
  4 0 0 1.0 1.0 2.0 0 0 0 0 0 1071.964 0 5 0
!
P b n m <--Space group symbol
!Atom Typ X Y Z Biso Occ In Fin N_t Spc /Codes
! beta11 beta22 beta33 beta12 beta13 beta23 /Codes
Cr Cr 0.50000 0.00000 0.00000 0.69980 0.50000 0 0 0 0
  0.00 0.00 0.00 61.00 0.00
Ho Ho -0.01795 0.06567 0.25000 0.68958 0.50000 0 0 0 0
  111.00 121.00 0.00 81.00 0.00
O1 O 0.10489 0.46432 0.25000 0.00000 0.50000 0 0 2 0
  131.00 141.00 0.00 0.00 0.00
  0.00705 0.00825 0.00314 -0.00200 0.00000 0.00000
  181.00 361.00 371.00 381.00 0.00 0.00
O2 O -0.30710 0.30293 0.05263 0.00000 1.00000 0 0 2 0
  151.00 161.00 171.00 0.00 0.00
  0.01018 0.00824 0.00373 -0.00134 -0.00042 -0.00046
  191.00 411.00 401.00 391.00 351.00 341.00
!-----> Profile Parameters for Pattern # 1
! Scale Shape1 Bov Str1 Str2 Str3 Strain-Model
  6.1897 0.22550 0.00000 0.00000 0.00000 0.00000 0
  51.00000 251.000 0.000 0.000 0.000 0.000

```

continued from previous page....

```

!   U   V   W   X   Y   GauSiz LorSiz Size-Model
0.072652 -0.038727 0.124308 0.000000 0.000000 0.000000 0.000000 0
211.000 221.000 231.000 0.000 0.000 0.000 0.000
!   a   b   c   alpha beta gamma #Cell Info
5.238771 5.513430 7.527004 90.000000 90.000000 90.000000
31.00000 41.00000 11.00000 0.00000 0.00000 0.00000
! Pref1 Pref2 Asy1 Asy2 Asy3 Asy4
0.00000 0.00000 0.10521 0.02096 0.00000 0.00000
0.00 0.00 241.00 201.00 0.00 0.00
!-----
! Data for PHASE number: 2 ==> Current R_Bragg for Pattern# 1: 2.24
!-----
HoCrO3 magnetic phase
!
!Nat Dis Mom Pr1 Pr2 Pr3 Jbt lrf lsy Str Furth ATZ Nvk Npr More
2 0 0 0.0 0.0 1.0 1 0 -1 0 0 0.000 0 5 0
!
P -1 <--Space group symbol for hkl generation
!Nsym Cen Laue MagMat
4 1 3 1
!
SYMM x,y,z
MSYM u,v,w,0.00
SYMM -x,-y,z+1/2
MSYM u,v,-w,0.00
SYMM x+1/2,-y+1/2,-z
MSYM u,-v,-w,0.00
SYMM -x+1/2,y+1/2,-z+1/2
MSYM u,-v,w,0.00
!
!Atom Typ Mag Vek X Y Z Biso Occ Rx Ry Rz
! lx ly lz beta11 beta22 beta33 MagPh
CR1 MCR3 1 0 0.50000 0.00000 0.00000 0.69196 1.0000 0.099 0.082 2.609
0.000 0.000 0.000 0.000 0.000 0.000 0.000
0.00 0.00 0.00 0.00 0.00 0.00 0.00
HO1 JHO3 1 0 -0.01798 0.06565 0.25000 0.68354 1.0000 3.644 7.010 0.000
111.00 121.00 0.00 81.00 0.00 91.00 101.00 0.00
0.000 0.000 0.000 0.000 0.000 0.000 0.000
0.00 0.00 0.00 0.00 0.00 0.00 0.00
!-----> Profile Parameters for Pattern # 1
! Scale Shape1 Bov Str1 Str2 Str3 Strain-Model
6.1930 0.22538 0.00000 0.00000 0.00000 0.00000 0
51.00000 251.000 0.000 0.000 0.000 0.000
!   U   V   W   X   Y   GauSiz LorSiz Size-Model
0.072516 -0.038507 0.124133 0.000000 0.000000 0.000000 0.000000 0
211.000 221.000 231.000 0.000 0.000 0.000 0.000
!   a   b   c   alpha beta gamma #Cell Info
5.238771 5.513427 7.527000 90.000000 90.000000 90.000000
31.00000 41.00000 11.00000 0.00000 0.00000 0.00000
! Pref1 Pref2 Asy1 Asy2 Asy3 Asy4
0.00000 0.00000 0.10510 0.02102 0.00000 0.00000
0.00 0.00 241.00 201.00 0.00 0.00
! 2Th1/TOF1 2Th2/TOF2 Pattern # 1
10.000 151.900 1

```

```

SYMM x,y,z
MSYM u,v,w,0.00
SYMM -x,-y,z+1/2
MSYM u,v,-w,0.00
SYMM x+1/2,-y+1/2,-z
MSYM u,-v,-w,0.00
SYMM -x+1/2,y+1/2,-z+1/2
MSYM u,-v,w,0.00

```

Magnetic symmetry elements corresponding to magnetic representation Γ_5 obtained from the output file of Baslreps as explained in the previous section

Appendix D

Refined structure parameters of HoCrO_3

Table D.1: Atomic positions (non-general positions only), Isothermal parameters (B_{iso}), selected bond lengths and bond angles of HCrO_3 obtained by Rietveld refinement of neutron powder diffraction (NPD) data collected at 300, 100, and 3 K. For comparison parameters obtained by refinement of powder x-ray diffraction (PXR) pattern collected at 300 K is also given.

		NPD			PXR
		3 K	100 K	300 K	300 K
Atomic positions					
Ho(4c)	x	-0.0178(3)	-0.0171(3)	-0.0163(2)	-0.0168(3)
	y	0.0658(2)	0.0657(2)	0.0650(2)	0.0655(5)
O1(4c)	x	0.1051(4)	0.1049(3)	0.1039(2)	0.1026(8)
	y	0.4645(4)	0.4647(3)	0.4647(2)	0.4664(8)
O2(8d)	x	-0.3073(3)	-0.3070(2)	-0.3066(1)	-0.3054(2)
	y	0.3032(3)	0.3031(2)	0.3027(1)	0.3055(2)
	z	0.0526(2)	0.0531(1)	0.0534(1)	0.0497(4)

Continued on next page

Table D.1 – continued from previous page

Temperature=	NPD			PXRD
	3 K	100 K	300 K	300 K
<hr/> <i>B</i> _{iso} (Å ²) <hr/>				
Ho(4c)	0.68(2)	0.69(4)	0.94(1)	0.69(4)
Cr(4b)	0.67(4)	0.62(2)	1.00(2)	0.62(2)
O1(4c)	0.83(3)	0.81(3)	1.16(2)	0.81(3)
O2(8d)	0.99(2)	0.94(2)	1.26(1)	0.94(2)
<hr/>				
Bond lengths (Å)				
Cr–O1(×2)	1.9704(6)	1.9705(5)	1.9715(3)	1.956(2)
Cr–O2(×2)	1.9814(16)	1.9815(11)	1.9836(7)	1.9587(6)
Cr–O2(×2)	1.9926(16)	1.9939(11)	1.9951(8)	2.0199(5)
< Cr – O >	1.9815(7)	1.9820(5)	1.9834(9)	1.978(3)
Cr–Cr(×2)	3.7635(1)	3.7644(1)	3.7693(0)	3.7774(5)
Cr–Cr(×4)	3.8027(1)	3.8032(1)	3.8066(0)	3.7998(1)
Ho–O1	2.2330(26)	2.2304(22)	2.2329(1)	2.2481(75)
Ho–O1	2.2907(25)	2.2910(2)	2.2938(2)	2.3392(67)
Ho–O2(×2)	2.2677(18)	2.2677(15)	2.2703(1)	2.2546(54)
Ho–O2(×2)	2.4941(19)	2.4934(16)	2.4970(12)	2.5112(53)
Ho–O2(×2)	2.6319(16)	2.6352(16)	2.6409(1)	2.6262(48)
< Ho – O >	2.4139(8)	2.4145(7)	2.4179(5)	2.4241(9)
<hr/>				
Bond angles (°)				
Cr–O1–Cr	145.497(1)	145.576(1)	145.855(0)	145.516(31)
Cr–O2–Cr	146.232(89)	146.142(59)	146.172(42)	148.226(1)

Appendix E

Refined structure parameters of $h\text{DyMnO}_3$

Table E.1: Atomic positions (non-general positions only), Isothermal parameters (B_{iso}), selected bond lengths and and bond angles of $h\text{DyMnO}_3$ obtained by Rietveld refinement of neutron powder diffraction (NPD) data collected at 300, 50, and 4 K. For comparison parameters obtained by refinement of powder x-ray diffraction (PXRD) pattern collected at 300 K is also given.

Temperature=		NPD			PXRD
		4 K	50 K	300 K	300 K
Atomic positions					
Dy1 (2a)	z	0.2947(8)	0.2948(8)	0.2939(8)	0.2746(7)
Dy2 (4b)	z	0.2532(7)	0.2533(7)	0.2543(7)	0.2367(7)
Mn (6c)	x	0.3435(17)	0.3391(21)	0.3303(21)	0.3602(7)
O1 (6c)	x	0.3140(14)	0.3140(14)	0.3153(17)	0.2838(16)
	z	0.1710(11)	0.1710(11)	0.1750(11)	0.1362(16)
O2 (6c)	x	0.6399(14)	0.6393(14)	0.6418(15)	0.6720(24)
	z	0.3463(1)	0.3461(9)	0.3473(11)	0.3455(16)

Continued on next page

Table E.1 – continued from previous page

	Temperature=	NPD			PXRD
		4 K	50 K	300 K	300 K
O3 (4b)	z	0.50042	0.50042	0.50042	0.4879(13)
O4 (2a)	z	-0.0241(3)	-0.0244(14)	-0.0200(16)	0.0368(29)

 B_{iso} (\AA^2)

Dy1 (2a)	0.08(4)	0.09(4)	0.30(4)	0.93(3)
Dy2 (4a)	0.08(4)	0.09(4)	0.30(4)	0.93(3)
Mn (6c)	0.13(4)	0.17(11)	0.45(11)	0.38(6)
O1 (6c)	0.47(7)	0.46(7)	0.75(7)	2.47(16)
O2 (6c)	0.47(7)	0.46(7)	0.75(7)	2.47(16)
O3 (4b)	0.20(6)	0.27(6)	0.51(6)	3.63(20)
O4 (2a)	0.20(6)	0.27(6)	0.51(6)	3.63(20)

Bond lengths (\AA)

Mn–O1	1.968(12)	1.969(12)	2.007(14)	1.630(21)
Mn–O2	1.767(11)	1.771(11)	1.759(13)	1.781(18)
Mn–O3	2.121(12)	2.090(12)	2.046(12)	2.232(4)
Mn–O4($\times 2$)	2.041(6)	2.057(63)	2.080(6)	2.028(4)
< Mn – O >	1.9815(7)	1.9820(5)	1.9834(9)	1.978(3)
Dy1–O1($\times 3$)	2.408(11)	2.401(10)	2.380(10)	2.365(16)
Dy1–O2($\times 3$)	2.297(6)	2.300(6)	2.298(6)	2.185(14)
Dy1–O3	2.360(9)	2.360(9)	2.366(9)	2.443(17)
Dy2–O1($\times 3$)	2.315(10)	2.318(10)	2.306(8)	2.5112(53)
Dy2–O2($\times 3$)	2.248(10)	2.245(10)	2.256(8)	2.423(11)
Dy2–O4	2.556(18)	2.551(18)	2.590(20)	2.288(35)
< Dy1 – O1, O2O3 >	2.4139(8)	2.4145(7)	2.4179(5)	2.4241(9)
< Dy2 – O1, O2, O4 >	2.4139(8)	2.4145(7)	2.4179(5)	2.4241(9)

Continued on next page

Table E.1 – continued from previous page

Temperature=	NPD			PXRD
	4 K	50 K	300 K	300 K
Bond angles (°)				
O1–Mn–O2	178.03(52)	179.84(52)	177.26(57)	156.69(95)
O1–Mn–O3	84.68(27)	85.38(25)	87.09(30)	76.69(35)
O4–Mn–O4	121.311(1)	119.826(1)	118.159(1)	123.357(1)
O2–Mn–O4	80.694(2)	80.084(2)	80.980(2)	104.798(1)
O3–Mn–O4	118.116(1)	118.868(1)	120.158(1)	115.980(2)
O2–Mn–O3	93.35(28)	94.46(28)	95.64(32)	80.00(40)
O1–Mn–O4	100.226(2)	99.992(2)	97.659(3)	85.620(1)
Mn–O3–Mn	119.999(1)	119.999(1)	119.999(1)	119.618(1)
Mn–O4–Mn	118.209(2)	118.177(1)	118.811(2)	115.74(1)
Dy1–O1–Mn	131.42(55)	130.76(54)	127.78(60)	148.96(31)
Dy2–O2–Mn	119.748(2)	120.127(2)	120.510(2)	117.506(1)

Appendix F

FullProf control (input) files used for the Rietveld refinement of the magnetic structures of $\text{Mn}_{1-x}\text{M}_x\text{WO}_4$

In the following sections we present the *FullProf* control files (*.pcr) used for the refinement of crystal and different magnetic phases of MnWO_4 , $\text{Mn}_{0.9}\text{Co}_{0.1}\text{WO}_4$ and $\text{Mn}_{0.9}\text{Cu}_{0.1}\text{WO}_4$.

Figure F.1: Magnetic part of the pcr file used for the Rietveld refinement of AF1 magnetic phase of $MnWO_4$ presented in figure 7.5(a)

```

-----
! Data for PHASE number: 2 ==> Current R_Bragg for Pattern# 1: 12.71
-----
MnWO4 magnetic phase
!
!Nat Dis Mom Pr1 Pr2 Pr3 Jbt lrf lsy Str Furth ATZ Nvk Npr More
  2 0 0.0 0.0 1.0 1 -1 -2 0 0 0.000 -1 5 0
!
P -1 <--Space group symbol for hkl generation
! Nsym Cen Laue lreps N_Bas
  2 1 1 -1 6
! Real(0)-Imaginary(1) indicator for Ci
  0 0 0 1 1 1
!
SYMM X, Y, Z
BASR 1 0 0 0 1 0 0 0 1 0 0 0 0 0 0 0
BASI 0 0 0 0 0 0 0 0 0 0 0 0 0 0 0 0
SYMM X, -Y+1, Z+1/2
BASR 0 0 0 0 0 0 0 0 0 0 0 0 0 0 0 0
BASI -1 0 0 0 1 0 0 0 -1 0 0 0 0 0 0 0
!
!Atom Typ Mag Vek X Y Z Biso Occ C1 C2 C3
! C4 C5 C6 C7 C8 C9 MagPh
MN1 MMN2 1 0 0.50000 0.68450 0.25000 0.00348 1.00000 3.919 -0.101 2.893
      0.00 161.00 0.00 0.00 0.00 141.00 131.00 121.00
      0.000 0.000 0.000 0.000 0.000 0.000 0.000000
      0.00 0.00 0.00 0.00 0.00 0.00 0.00
MN2 MMN2 1 0 0.50000 0.31592 0.75000 0.00348 1.00000 3.919 -0.101 2.893
      0.00 161.00 0.00 0.00 0.00 0.00 141.00 131.00 121.00
      0.000 0.000 0.000 0.000 0.000 0.000 0.000000
      0.00 0.00 0.00 0.00 0.00 0.00 0.00
!-----> Profile Parameters for Pattern # 1
! Scale Shape1 Bov Str1 Str2 Str3 Strain-Model
  61.533 0.22149 0.00000 0.00000 0.00000 0.00000 0
  11.00000 101.000 0.000 0.000 0.000 0.000
! U V W X Y GauSiz LorSiz Size-Model
  0.214768 -0.184468 0.146954 0.001110 0.001000 0.000000 0.000000 0
  261.000 271.000 281.000 291.000 0.000 0.000 0.000
! a b c alpha beta gamma #Cell Info
  4.821497 5.752274 4.991778 90.000000 91.069069 90.000000
  61.00000 51.00000 41.00000 0.00000 31.00000 0.00000
! Pref1 Pref2 Asy1 Asy2 Asy3 Asy4
  0.00026 0.00000 0.06005 0.01790 0.00000 0.00000
  241.00 0.00 251.00 151.00 0.00 0.00
! Propagation vectors:
  0.2500000 0.5000000 0.5000000 Propagation Vector 1
  0.0000000 0.0000000 0.0000000
! 2Th1/TOF1 2Th2/TOF2 Pattern # 1
  5.500 139.600 1

```

Figure F.2: Magnetic part of the pcr file used for the Rietveld refinement of AF2 magnetic phase of $MnWO_4$ presented in figure 7.5(b)

```

!-----
! Data for PHASE number: 2 ==> Current R_Bragg for Pattern# 1: 10.69
!-----
MnWO4
!
!Nat Dis Mom Pr1 Pr2 Pr3 Jbt lrf lsy Str Furth ATZ Nvk Npr More
  1 0 0 1.0 2.0 1.0 1 -1 -2 0 0 232.345 -1 5 0
!
P -1 <--Space group symbol for hkl generation
! Nsym Cen Laue lreps N_Bas
  2 1 1 -1 6
! Real(0)-Imaginary(1) indicator for Ci
  0 0 0 1 1 1
!
SYMM x,y,z
BASR 1 0 0 0 1 0 0 0 1 0 0 0 0 0 0 0 0 0 0 0
BASl 0 0 0 0 0 0 0 0 0 0 0 0 0 0 0 0 0 0 0 0
SYMM x,-y+1,z+1/2
BASR -0.1378 0.0000 0.0000 0.0000 0.1378 0.0000 0.0000 0.0000 -0.1378 0 0 0 0 0 0 0 0 0 0
BASl -0.9905 0.0000 0.0000 0.0000 0.9905 0.0000 0.0000 0.0000 -0.9905 0 0 0 0 0 0 0 0 0 0
!
!Atom Typ Mag Vek X Y Z Biso Occ C1 C2 C3
! C4 C5 C6 C7 C8 C9 MagPh
MN1 MMN2 1 0 0.50000 0.68436 0.25000 0.14777 1.00000 4.286 -1.156 2.234
      0.00 81.00 0.00 0.00 0.00 0.00 211.00 221.00 231.00
      0.00 0.000 0.000 0.000 0.000 0.000 0.00000
      0.00 0.00 0.00 0.00 0.00 0.00 0.00 0.00
!-----> Profile Parameters for Pattern # 1
! Scale Shape1 Bov Str1 Str2 Str3 Strain-Model
73.959 0.20221 0.00000 0.00000 0.00000 0.00000 0
11.00000 181.000 0.000 0.000 0.000 0.000
! U V W X Y GauSiz LorSiz Size-Model
0.165676 -0.193145 0.155862 0.005080 0.001000 0.000000 0.000000 0
1.000 1.000 0.000 0.000 0.000 0.000 0.000
! a b c alpha beta gamma #Cell Info
4.821724 5.751989 4.991212 90.000000 91.060455 90.000000
61.00000 51.00000 41.00000 0.0000 31.00000 0.00000
! Pref1 Pref2 Asy1 Asy2 Asy3 Asy4
-0.00089 0.00000 0.06310 0.01695 0.00000 0.00000
161.00 0.00 191.00 151.00 0.00 0.00
! Propagation vectors:
- 0.2155494 0.5000000 0.4562654 Propagation Vector 1
201.000000 0.000000 171.000000
! 2Th1/TOF1 2Th2/TOF2 Pattern # 1
6.100 140.000 1

```

Figure F.3: Magnetic part of the pcr file used for the Rietveld refinement of $AF2'$ magnetic phase of $Mn_{0.9}Co_{0.1}WO_4$ presented in figure 7.5(c)

```

!-----
! Data for PHASE number: 2 ==> Current R_Bragg for Pattern# 1: 4.10
!-----
Mn0.9Cu0.1WO4
!
!Nat Dis Mom Pr1 Pr2 Pr3 Jbt lrf lsy Str Furth ATZ Nvk Npr More
 2 0 0 0.0 0.0 1.0 1 -1 -2 0 0 0.000 -1 5 0
!
P -1 <--Space group symbol for hkl generation
!Nsym Cen Laue lreps N_Bas
 2 1 1 -1 6
! Real(0)-Imaginary(1) indicator for Ci
 0 0 0 1 1 1
!
SYMM X, Y, Z
BASR 1 0 0 0 1 0 0 0 1 1 0 0 0 1 0 0 0 1
BASl 0 0 0 0 0 0 0 0 0 0 0 0 0 0 0 0 0 0
SYMM X, -Y+1, Z+1/2
BASR 0 0 0 0 0 0 0 0 0 0 0 0 0 0 0 0 0 0
BASl -1 0 0 0 1 0 0 0 -1 -1 0 0 0 1 0 0 0 -1
!
!Atom Typ Mag Vek X Y Z Biso Occ C1 C2 C3
! C4 C5 C6 C7 C8 C9 MagPh
MN1 MMN2 1 0 0.50000 0.68536 0.25000 0.06796 0.90000 3.648 0.346 0.233
 0.00 81.00 0.00 151.00 0.00 271.00 261.00 251.00
 0.790 0.680 -3.313 0.000 0.000 0.000 0.00000
 281.00 291.00 301.00 0.00 0.00 0.00 0.00
Co1 MCO2 1 0 0.50000 0.68536 0.25000 0.06796 0.10000 3.648 0.346 0.233
 0.00 81.00 0.00 151.00 0.00 271.00 261.00 251.00
 0.790 0.680 -3.313 0.000 0.000 0.000 0.00000
 281.00 291.00 301.00 0.00 0.00 0.00 0.00
!-----> Profile Parameters for Pattern # 1
! Scale Shape1 Bov Str1 Str2 Str3 Strain-Model
33.373 0.25665 0.00000 0.00000 0.00000 0.00000 0
11.00000 0.000 0.000 0.000 0.000 0.000
! U V W X Y GauSiz LorSiz Size-Model
0.973787 -0.506189 0.217108 0.000000 0.000000 0.000000 0.000000 0
341.000 351.000 191.000 0.000 0.000 0.000 0.000
! a b c alpha beta gamma #Cell Info
4.808362 5.745683 4.987536 90.000000 90.985764 90.000000
61.00000 51.00000 41.00000 0.00000 31.00000 0.00000
! Pref1 Pref2 Asy1 Asy2 Asy3 Asy4
0.00000 0.00000 0.08588 0.00998 0.00000 0.00000
0.00 0.00 221.00 241.00 0.00 0.00
! Propagation vectors:
-0.2210499 0.5000000 0.4710944 Propagation Vector 1
311.000000 0.000000 211.000000
! 2Th1/TOF1 2Th2/TOF2 Pattern # 1
6.100 151.900 1

```

Figure F.4: Magnetic part of the pcr file used for the Rietveld refinement of $Mn_{0.9}Cu_{0.1}WO_4$, AF3 magnetic phase with Γ_1 representation, which is presented in figure 7.6(c) and figure 7.7(a)-(b)

```

!-----
! Data for PHASE number: 2 ==> Current R_Bragg for Pattern# 1: 10.83
!-----
Mn0.9Cu0.1WO4
!
!Nat Dis Mom Pr1 Pr2 Pr3 Jbt lrf lsy Str Furth ATZ Nvk Npr More
 2 0 0 0.0 0.0 1.0 1 -1 -2 0 0 0.000 -1 5 0
!
P -1 <--Space group symbol for hkl generation
! Nsym Cen Laue lreps N_Bas
 2 1 1 -1 6
! Real(0)-Imaginary(1) indicator for Ci
 0 0 0 1 1 1
!
SYMM X, Y, Z
BASR 1 0 0 0 1 0 0 0 1 1 0 0 0 1 0 0 0 1
BASl 0 0 0 0 0 0 0 0 0 0 0 0 0 0 0 0 0 0
SYMM X, -Y+1, Z+1/2
BASR 0 0 0 0 0 0 0 0 0 0 0 0 0 0 0 0 0 0
BASl 1 0 0 0 -1 0 0 0 1 1 0 0 0 -1 0 0 0 1
!
!Atom Typ Mag Vek X Y Z Biso Occ C1 C2 C3
! C4 C5 C6 C7 C8 C9 MagPh
MN1 MMN2 1 0 0.50000 0.68483 0.25000 0.36665 0.90000 0.941 4.611 0.759
 0.00 81.00 0.00 151.00 0.00 271.00 261.00 251.00
 -1.428 -1.498 -0.371 0.000 0.000 0.000 0.00000
 281.00 291.00 301.00 0.00 0.00 0.00 0.00
Cu1 MCU2 1 0 0.50000 0.68483 0.25000 0.36665 0.10000 0.941 4.611 0.759
 0.00 81.00 0.00 151.00 0.00 271.00 261.00 251.00
 -1.428 -1.498 -0.371 0.000 0.000 0.000 0.00000
 281.00 291.00 301.00 0.00 0.00 0.00 0.00
!-----> Profile Parameters for Pattern # 1
! Scale Shape1 Bov Str1 Str2 Str3 Strain-Model
 34.135 0.23255 0.00000 0.00000 0.00000 0.00000 0
 11.00000 231.000 0.000 0.000 0.000 0.000
! U V W X Y GauSiz LorSiz Size-Model
 0.675342 -0.407156 0.153223 0.000000 0.000000 0.000000 0.000000 0
 351.000 361.000 381.000 0.000 0.000 0.000 0.000
! a b c alpha beta gamma #Cell Info
 4.803870 5.757205 4.977845 90.000000 91.308815 90.000000
 61.00000 51.00000 41.00000 0.00000 31.00000 0.00000
! Pref1 Pref2 Asy1 Asy2 Asy3 Asy4
 0.00000 0.00000 0.09026 0.01806 0.00000 0.00000
 0.00 0.00 221.00 241.00 0.00 0.00
! Propagation vectors:
 -0.2216804 0.5000000 0.4952928 Propagation Vector 1
 311.000000 0.000000 321.000000
! 2Th1/TOF1 2Th2/TOF2 Pattern # 1
 6.100 151.900 1

```

Figure F.5: Magnetic part of the *pcr* file used for the Rietveld refinement of $Mn_{0.9}Cu_{0.1}WO_4$, AF3 magnetic phase with Γ_2 representation, which is presented in figure 7.6(d) and figure 7.7(c)

```

!-----
! Data for PHASE number: 2 ==> Current R_Bragg for Pattern# 1: 10.38
!-----
Mn0.9Cu0.1WO4
!
!Nat Dis Mom Pr1 Pr2 Pr3 Jbt lrf lsy Str Furth ATZ Nvk Npr More
  2 0 0 0.0 0.0 1.0 1 -1 -2 0 0 0.000 -1 5 0
!
P -1 <--Space group symbol for hkl generation
! Nsym Cen Laue lreps N_Bas
  2 1 1 -1 6
! Real(0)-Imaginary(1) indicator for Ci
  0 0 0 1 1 1
!
SYMM X, Y, Z
BASR 1 0 0 0 1 0 0 0 1 1 0 0 0 1 0 0 0 1
BASI 0 0 0 0 0 0 0 0 0 0 0 0 0 0 0 0 0 0
SYMM X, -Y+1, Z+1/2
BASR 0 0 0 0 0 0 0 0 0 0 0 0 0 0 0 0 0 0
BASI -1 0 0 0 1 0 0 0 -1 -1 0 0 0 1 0 0 0 -1
!
!Atom Typ Mag Vek X Y Z Biso Occ C1 C2 C3
! C4 C5 C6 C7 C8 C9 MagPh
MN1 MMN2 1 0 0.50000 0.68479 0.25000 0.20782 0.90000 -3.123 -1.110 -2.638
      0.00 81.00 0.00 151.00 0.00 211.00 201.00 191.00
      1.697 -1.338 -1.036 0.000 0.000 0.000 0.000000
      281.00 291.00 301.00 0.00 0.00 0.00 0.00
Co1 MCO2 1 0 0.50000 0.68479 0.25000 0.20782 0.10000 -3.123 -1.110 -2.638
      0.00 81.00 0.00 151.00 0.00 211.00 201.00 191.00
      1.697 -1.338 -1.036 0.000 0.000 0.000 0.000000
      281.00 291.00 301.00 0.00 0.00 0.00 0.00
!-----> Profile Parameters for Pattern # 1
! Scale Shape1 Bov Str1 Str2 Str3 Strain-Model
33.151 0.01800 0.00000 0.00000 0.00000 0.00000 0
11.00000 251.000 0.000 0.000 0.000 0.000
! U V W X Y GauSiz LorSiz Size-Model
0.629853 -0.457726 0.195723 0.000000 0.000000 0.000000 0.000000 0
351.000 361.000 381.000 0.000 0.000 0.000 0.000
! a b c alpha beta gamma #Cell Info
4.804053 5.757355 4.978009 90.000000 91.308327 90.000000
61.00000 51.00000 41.00000 0.00000 31.00000 0.00000
! Pref1 Pref2 Asy1 Asy2 Asy3 Asy4
0.00000 0.00000 0.11078 0.01533 0.00000 0.00000
0.00 0.00 261.00 241.00 0.00 0.00
! Propagation vectors:
-0.2230622 0.5000000 0.4953777 Propagation Vector 1
311.000000 0.000000 321.000000
! 2Th1/TOF1 2Th2/TOF2 Pattern # 1
6.100 151.900 1

```

Bibliography

- [1] G. A. Smolenskii *et al.*, Segnetoelectrics and antisegetoelectrics, 1971 (in Russian).
- [2] G. A. Smolenskii and I. E. Chupis, Sov. Phy. Uspekhi **25**, 475 (1982).
- [3] Y. N. Venevtsev and V. V. Gagulin, Ferroelectrics **162**, 23 (1994).
- [4] K. Aizu, Phys. Rev. B **2**, 754 (1970).
- [5] H. Schmid, Ferroelectrics **162**, 317 (1994).
- [6] N. A. Spaldin and M. Fiebig, Science **309**, 391 (2005).
- [7] M. Fiebig, J. Phys. D: Appl. Phys. **38**, R123 (2005).
- [8] W. Eerenstein, N. D. Mathur and J. F. Scott, NATURE **442**, 759 (2006).
- [9] D. I. Khomskii, J. Magn. Magn. Mater. **306**, 1 (2006).
- [10] S. W. Cheong and M. Mostovoy, Nat. Mater. **6**, 13 (2007).
- [11] Y. Tokura, Science **312**, 1481 (2006).
- [12] R. Ramesh and N. A. Spaldin, Nat. Mater. **6**, 21 (2007).
- [13] N. A. Spaldin and M. Fiebig, Science **309**, 391 (2005).
- [14] Y. Tokura, SCIENCE **312**, 1481 (2006).
- [15] T. Kimura, T. Goto, H. Shintani, K. Ishizaka, T. Arima and Y. Tokura, Nature **426**, 55 (2003).
- [16] N. Hur, S. Park, P. A. Sharma, J. S. Ahn, S. Guha and S. Cheong, Nature **429**, 392 (2004).

- [17] G. Lawes, A. B. Harris, T. Kimura, N. Rogado, R. J. Cava, A. Aharony, O. Entin-Wohlman, T. Yildirim, M. Kenzelmann, C. Broholm *et al.*, Phys. Rev. Lett. **95**, 87205 (2005).
- [18] O. Heyer, N. Hollmann, I. Klassen, S. Jodlauk, L. Bohatý, P. Becker, J. A. Mydosh, T. Lorenz and D. Khomskii, J. Phys. Condens. Matter **18**, L471 (2006).
- [19] S. Park, Y. J. Choi, C. L. Zhang and S.-W. Cheong, Phys. Rev. Lett. **98**, 057601 (2007).
- [20] T. Kimura, G. Lawes and A. P. Ramirez, Phys. Rev. Lett. **94**, 137201 (2005).
- [21] J. Baier, D. Meier, K. Berggold, J. Hemberger, A. Balbashov, J. A. Mydosh and T. Lorenz, Phys. Rev. B **73**, 100402 (2006).
- [22] T. Kimura, J. C. Lashley and A. P. Ramirez, Phys. Rev. B **73**, 220401 (2006).
- [23] E. K. Salje, *Phase transitions in ferroelastic and co-elastic crystals Vol-1* (Cambridge University Press, Cambridge, 1993).
- [24] Y. Tokura, J. Magn. Magn. Mater. **310**, 1145 (2007).
- [25] I. E. Dzyaloshinskii, Sov. Phys.–JETP **10**, 628 (1960).
- [26] D. N. Asrov, Sov. Phys.–JETP **11**, 708 (1960).
- [27] M. Fiebig, J. Phys. D: Appl. Phys. **38**, R123 (2005).
- [28] C. W. Nan, M. I. Bichurin, S. Dong, D. Viehland and G. Srinivasan, J. Appl. Phys. **103**, 031101 (2008).
- [29] M. Zeng, J. G. Wan, Y. Wang, H. Yu, J. M. Liu, X. P. Jiang and C. W. Nan, J. Appl. Phys. **95**, 8069 (2004).
- [30] S. Dong, J. Cheng, J. Li and D. Viehland, Appl. Phys. Lett. **83**, 4812 (2003).
- [31] N. Cai, C. W. Nan, J. Zhai and Y. Lin, Appl. Phys. Lett. **84**, 3516 (2004).
- [32] C. Nan, G. Liu, Y. Lin and H. Chen, Phys. Rev. Lett. **94**, 197203 (2005).
- [33] H. Zheng, J. Wang, S. Loffland, Z. Ma, L. Mohaddes-Ardabili, T. Zhao, L. Salamanca-Riba, S. Shinde, S. Ogale, F. Bai *et al.*, Science **303**, 661 (2004).

BIBLIOGRAPHY

- [34] D. Khomskii, *Physics* **2**, 1 (2009).
- [35] K. F. Wang, J. M. Liu and Z. F. Ren, *Adv. Phys.* **58**, 321 (2009).
- [36] A. G. Gavriliuk, S. A. Kharlamova, I. S. Lyubutin, I. A. Troyan, S. G. Ovchinnikov, A. M. Potseluiiko, M. I. Eremets and R. Boehler, *JETP Lett.* **80**, 426 (2004).
- [37] H. Mo, C. S. Nelson, L. N. Bezmaternykh and V. T. Temerov, *Phys. Rev. B* **78**, 214407 (2008).
- [38] E. Ascher, H. Rieder, H. Schmid and H. Stössel, *J. Appl. Phys.* **37**, 1404 (1966).
- [39] E. Ascher, H. Schmid and D. Tar, *Solid State Commun.* **2**, 45 (1964).
- [40] Y. N. Venevtsev, V. V. Gagulin and I. D. Zhitomirsky, *Ferroelectrics* **73**, 221 (1987).
- [41] R. Wongmaneerung, X. Tan, R. W. McCallum, S. Ananta and R. Yimnirun, *Appl. Phys. Lett.* **90**, 242905 (2007).
- [42] A. Moreira dos Santos, A. K. Cheetham, T. Atou, Y. Syono, Y. Yamaguchi, K. Ohoyama, H. Chiba and C. N. R. Rao, *Phys. Rev. B* **66**, 064425 (2002).
- [43] R. Seshadri and N. A. Hill, *Chem. Mater.* **13**, 2892 (2001).
- [44] I. Sosnowska, T. P. Neumaier and E. Steichele, *J. Phys. C: Solid State Phys.* **15**, 4835 (1982).
- [45] J. Bucci, B. Robertson and W. James, *J. Appl. Crystallogr.* **5**, 187 (1972).
- [46] D. Lebeugle, D. Colson, A. Forget and M. Viret, *Appl. Phys. Lett.* **91**, 022907 (2007).
- [47] V. V. Shvartsman, W. Kleemann, R. Haumont and J. Kreisel, *Appl. Phys. Lett.* **90**, 172115 (2007).
- [48] D. J. Singh, *Phys. Rev. B* **73**, 094102 (2006).
- [49] G. Meunier and M. Bertaud, *J. Appl. Crystallogr.* **9**, 364 (1976).
- [50] J. W. G. Bos, C. V. Colin and T. T. M. Palstra, *Phys. Rev. B* **78**, 094416 (2008).
- [51] G. Lawes, A. P. Ramirez, C. M. Varma and M. A. Subramanian, *Phys. Rev. Lett.* **91**, 257208 (2003).

- [52] B. B. Van Aken, T. T. M. Palstra, A. Filippetti and N. A. Spaldin, *Nature Mater.* **3**, 164 (2004).
- [53] B. Lorenz, A. P. Litvinchuk, M. M. Gospodinov and C. W. Chu, *Phys. Rev. Lett.* **92**, 087204 (2004).
- [54] B. Lorenz, F. Yen, M. M. Gospodinov and C. W. Chu, *Phys. Rev. B* **71**, 014438 (2005).
- [55] H. D. Zhou, J. A. Janik, B. W. Vogt, Y. J. Jo, L. Balicas, M. J. Case, C. R. Wiebe, J. C. Denyszyn, J. B. Goodenough and J. G. Cheng, *Phys. Rev. B* **74**, 094426 (2006).
- [56] T. Lottermoser, T. Lonkai, U. Amann, D. Hohlwein, J. Ihringer and M. Fiebig, *Nature* **430**, 541 (2004).
- [57] H. Salama, C. Voyer, D. Ryan and G. Stewart, *J. Appl. Phys.* **105**, 07E110 (2009).
- [58] C. Serrao, S. Krupanidhi, J. Bhattacharjee, U. Waghmare, A. Kundu and C. Rao, *J. Appl. Phys.* **100**, 076104 (2006).
- [59] A. Belik, S. Kamba, M. Savinov, D. Nuzhnyy, M. Tachibana, E. Takayama-Muromachi and V. Goian, *Phys. Rev. B* **79**, 054411 (2009).
- [60] K. Ramesha, A. Llobet, T. Proffen, C. R. Serrao and C. N. R. Rao, *J. Phys. Condens. Matter* **19**, 102202 (2007).
- [61] N. Ray and U. V. Waghmare, *Phys. Rev. B* **77**, 134112 (2008).
- [62] J. R. Sahu, C. R. Serrao, N. Ray, U. V. Waghmare and C. N. R. Rao, *J. Mater. Chem.* **17**, 42 (2007).
- [63] M. Mostovoy, *Phys. Rev. Lett.* **96**, 067601 (2006).
- [64] J. J. Betouras, G. Giovannetti and J. van den Brink, *Phys. Rev. Lett.* **98**, 257602 (2007).
- [65] I. A. Sergienko and E. Dagotto, *Phys. Rev. B* **73**, 094434 (2006).
- [66] Q. Li, S. Dong and J.-M. Liu, *Phys. Rev. B* **77**, 054442 (2008).
- [67] H. Katsura, N. Nagaosa and A. V. Balatsky, *Phys. Rev. Lett.* **95**, 057205 (2005).

BIBLIOGRAPHY

- [68] J. Hu, Phys. Rev. Lett. **100**, 077202 (2008).
- [69] M. Kenzelmann, A. B. Harris, S. Jonas, C. Broholm, J. Schefer, S. B. Kim, C. L. Zhang, S. W. Cheong, O. P. Vajk and J. W. Lynn, Phys. Rev. Lett. **95**, 087206 (2005).
- [70] O. Prokhnenko, R. Feyerherm, E. Dudzik, S. Landsgesell, N. Aliouane, L. C. Chapon and D. N. Argyriou, Phys. Rev. Lett. **98**, 057206 (2007).
- [71] G. Lautenschläger, H. Weitzel, T. Vogt, R. Hock, A. Böhm, M. Bonnet and H. Fuess, Phys. Rev. B **48**, 6087 (1993).
- [72] K. Taniguchi, N. Abe, T. Takenobu, Y. Iwasa and T. Arima, Phys. Rev. Lett. **97**, 97203 (2006).
- [73] H. Sagayama, K. Taniguchi, N. Abe, T. Arima, M. Soda, M. Matsuura and K. Hirota, Phys. Rev. B **77**, 220407 (2008).
- [74] K. Taniguchi, N. Abe, H. Umetsu, H. A. Katori and T. Arima, Phys. Rev. Lett. **101**, 207205 (2008).
- [75] P. S. Savchenko, Russ. J. Inorg. Chem. **4**, 186 (1959).
- [76] S. M. Koochpayeh, D. Fort and J. S. Abell, Prog. Cryst. Growth Charact. Mater. **54**, 121 (2008).
- [77] H. A. Dabkowska and A. B. Dabkowski, Springer Handbook of Crystal Growth , 367 (2010).
- [78] A. Guinier, *X-ray diffraction in crystals, imperfect crystals, and amorphous bodies* (Dover Publications, New York, 1994).
- [79] A. Guinier, *X-ray crystallographic technology* (Hilger and Watts, London, 1952 (p. 166)).
- [80] H. M. Rietveld, J. Appl. Crystallogr. **2**, 65 (1969).
- [81] J. Rodríguez-Carvajal, Physica B **192**, 55 (1993).
- [82] W. Marshall and S. W. Lovesey, *Theory of thermal neutron scattering: the use of neutrons for the investigation of condensed matter* (Clarendon Press, Oxford, 1971).

- [83] G. E. Bacon, *Neutron Diffraction* (Clarendon Press, Oxford, 1975).
- [84] Y. A. Izyumov, V. E. Naish and R. P. Ozerov, *Neutron Diffraction of Magnetic Materials* (Springer, New York, 1991).
- [85] G. L. Squires, *Introduction to the theory of thermal neutron scattering* (Dover Publications, New York, 1996).
- [86] L. Van Hove, Phys. Rev. **95**, 249 (1954).
- [87] O. Halpern and M. H. Johnson, Phys. Rev. **55**, 898 (1939).
- [88] P. G. de Gennes, In: G. T. Rado and H. Suhl, Editors, *Magnetism* Vol. III (Academic Press, New York, 1963).
- [89] R. M. Moon, T. Riste and W. C. Koehler, Phys. Rev. **181**, 920 (1969).
- [90] S. W. Lovesey, *Theory of Neutron Scattering from Condensed Matter*. (Clarendon Press, Oxford, 1984).
- [91] P. J. Brown in: E. Prince (Editor), *International tables for crystallography, Volume C: Mathematical, Physical and Chemical Tables* (Kluwer Academic Publishers, London, 2004).
- [92] F. Elf, R. Gilles, G. R. J. Artus and S. Roth, Appl. Phys. A **74**, s1477 (2002).
- [93] Institut Laue-Langevin web page for the instrument neutron powder diffractometer D2B, <http://www.ill.eu/instruments-support/instruments-groups/instruments/d2b/>.
- [94] Institut Laue-Langevin web page for the hot neutron four-circle diffractometer D9, <http://www.ill.eu/instruments-support/instruments-groups/instruments/d9/>.
- [95] Institut Laue-Langevin web page for the hot neutron four-circle diffractometer D23, <http://www.ill.eu/instruments-support/instruments-groups/instruments/d23/>.
- [96] J. Mesot, S. Janssen, L. Holitzner and R. Hempelmann, J. Neutron Res. **3**, 293 (1996).

BIBLIOGRAPHY

- [97] S. Janssen, J. Mesot, L. Holitzner, A. Furrer and R. Hempelmann, *Physica B* **234**, 1174 (1997).
- [98] Paul Scherrer Institut web page for the time of flight spectrometer FOCUS, http://spectroscopy.web.psi.ch/focus/focus_description.
- [99] S. Geller and E. A. Wood, *Acta Crystallogr.* **9**, 563 (1956).
- [100] S. Geller, *J. Chem. Phys.* **24**, 1236 (1956).
- [101] E. F. Bertaut and F. Forrat, *J. Phys. (Paris)* **17**, 129 (1956).
- [102] E. Bertaut, J. Mareschal, G. De Vries, R. Aleonard, R. Pauthenet, J. Rebouillat and V. Zarubicka, *IEEE Trans. Magn.* **2**, 453 (1966).
- [103] P. Pataud and J. Sivardière, *J. de Phys.* **31**, 803 (1970).
- [104] R. M. Hornreich, B. M. Wanklyn and I. Yaeger, *Int. J. Magn.* **2**, 77 (1972).
- [105] G. V. Subba Rao, G. V. Chandrashekhar and C. N. R. Rao, *Solid State Commun.* **6**, 177 (1968).
- [106] C. R. Serrao, A. K. Kundu, S. B. Krupanidhi, U. V. Waghmare and C. N. R. Rao, *Phys. Rev. B* **72**, 220101 (2005).
- [107] J. M. D. Coey, M. Viret and S. Von Molnar, *Adv. Phys.* **48**, 167 (1999).
- [108] R. I. Hines, *Atomistic Simulation and Ab Initio Studies of Polar Solids* (PhD thesis, University of Bristol, 1997).
- [109] R. D. Shannon, *Acta Crystallogr., Sect. A: Found. Crystallogr.* **32**, 751 (1976).
- [110] S. Quezel-Ambrunaz and J. Mareschal, *Bull. Soc. Fr. Mineral. Crystallogr.* **36**, 204 (1963).
- [111] A. J. Freeman, R. E. Watson, in: G.T. Rado, H. Suhl and (Editors), *Magnetism Vol. IIA* (Academic Press, New York, 1965).
- [112] W. Marshall, *Phys. Rev.* **110**, 1280 (1958).
- [113] J. Kondo, *J. Phys. Soc. Jpn.* **16**, 1690 (1961).
- [114] O. V. Lounasmaa, *Phys. Rev.* **128**, 1136 (1962).

- [115] B. Bleaney and R. W. Hill, Proc. Phys. Soc. London **78**, 313 (1961).
- [116] J. Rossat-Mignod, G. Quezel, A. Berton and J. Chaussy, Phys. Status Solidi B **63**, 105 (1974).
- [117] A. Tari, *The specific heat of matter at low temperatures* (Imperial College Press, London, 2003).
- [118] E. S. R. Gopal, *Specific heats at low temperatures* (Heywood books London, 1966).
- [119] J. Hemberger, M. Brando, R. Wehn, V. Y. Ivanov, A. A. Mukhin, A. M. Balbashov and A. Loidl, Phys. Rev. B **69**, 064418 (2004).
- [120] F. Mayr, C. Hartinger, M. Paraskevopoulos, A. Pimenov, J. Hemberger, A. Loidl, A. A. Mukhin and A. M. Balbashov, Phys. Rev. B **62**, 15673 (2000).
- [121] R. Courths and S. Hübner, Zeitschrift für Physik B Condensed Matter **24**, 193 (1976).
- [122] P. Pataud and J. Sivardière, J. de Phys. **31**, 1017 (1970).
- [123] N. Shamir, H. Shaked and S. Shtrikman, Physica B+ C **90**, 211 (1977).
- [124] N. Shamir, H. Melamud *et al.*, Physica B+C **90**, 217 (1977).
- [125] L. Ghivelder, I. Abrego Castillo, N. Alford, G. J. Tomka, P. Riedi, J. MacManus-Driscoll, A. Akther Hossain and L. Cohen, J. Magn. Magn. Mater. **189**, 274 (1998).
- [126] J. J. Hamilton, E. L. Keatley, H. L. Ju, A. K. Raychaudhuri, V. N. Smolyaninova and R. L. Greene, Phys. Rev. B **54**, 14926 (1996).
- [127] J. M. D. Coey, M. Viret, L. Ranno and K. Ounadjela, Phys. Rev. Lett. **75**, 3910 (1995).
- [128] B. F. Woodfield, M. L. Wilson and J. M. Byers, Phys. Rev. Lett. **78**, 3201 (1997).
- [129] L. Ghivelder, I. Abrego Castillo, M. A. Gusmao, J. A. Alonso and L. F. Cohen, Phys. Rev. B **60**, 12184 (1999).
- [130] H. Imai, H. Wada and M. Shiga, J. Phys. Soc. Jpn. **65**, 3460 (1996).

BIBLIOGRAPHY

- [131] P. Raychaudhuri, C. Mitra, A. Paramekanti, R. Pinto, A. K. Nigam and S. K. Dhar, *J. Phys. Condens. Matter* **10**, L191 (1998).
- [132] D. Meschede, F. Steglich, W. Felsch, H. Maletta and W. Zinn, *Phys. Rev. Lett.* **44**, 102 (1980).
- [133] M. Kaneko, S. Kurita and K. Tsushima, *J. Phys. C: Solid State Phys.* **10**, 1979 (1977).
- [134] K. Toyokawa, S. Kurita and K. Tsushima, *Phys. Rev. B* **19**, 274 (1979).
- [135] J. E. Gordon, C. W. Dempsy and T. Soller, *Phys. Rev.* **124**, 724 (1961).
- [136] H. Van Kempen, A. R. Miedema and W. J. Huiskamp, *Physica* **30**, 229 (1964).
- [137] D. Bloch, A. Voiron, A. Berton and J. Chaussy, *Solid State Commun.* **12**, 685 (1973).
- [138] Y. M. Jana and D. Ghosh, *Phys. Rev. B* **61**, 9657 (2000).
- [139] G. Ehlers, E. Mamontov, M. Zamponi, K. C. Kam and J. S. Gardner, *Phys. Rev. Lett.* **102**, 016405 (2009).
- [140] H. D. Zhou, J. Lu, R. Vasic, B. W. Vogt, J. A. Janik, J. S. Brooks and C. R. Wiebe, *Phys. Rev. B* **75**, 132406 (2007).
- [141] K. Tsushima, K. Aoyagi and S. Sugano, *J. Appl. Phys.* **41**, 1238 (1970).
- [142] R. M. Hornreich, *J. Magn. Magn. Mater.* **7**, 280 (1978).
- [143] N. Shamir, H. Shaked and S. Shtrikman, *Phys. Rev. B* **24**, 6642 (1981).
- [144] E. F. Bertaut, In: G. T. Rado and H. Suhl, Editors, *Magnetism* Vol. III (Academic Press, New York, 1963).
- [145] R. L. White, *J. Appl. Phys.* **40**, 1061 (1969).
- [146] H. Horner and C. M. Varma, *Phys. Rev. Lett.* **20**, 845 (1968).
- [147] E. O. Wollan and W. C. Koehler, *Phys. Rev.* **100**, 545 (1955).

- [148] H. Wondratschek and U. Müller, *International Tables for Crystallography Volume A1: Symmetry Relations Between Space Groups* (International Union of Crystallography, 2004).
- [149] E. F. Bertaut, *Acta Crysta.* **A24**, 217 (1968).
- [150] E. F. Bertaut, *J. Appl. Phys.* **33**, 1138 (1962).
- [151] C. J. Bradley and A. P. Cracknell, *The mathematical theory of symmetry in solids* (Clarendon Press, Oxford, 1972).
- [152] Y. A. Izyumov and V. E. Naish, *J. Magn. Magn. Matter* **12**, 239 (1979).
- [153] A. S. Wills, *Physica B.* **276**, 680 (2000).
- [154] X. Fabrèges, I. Mirebeau, P. Bonville, S. Petit, G. Lebras-Jasmin, A. Forget, G. André and S. Pailhès, *Phys. Rev. B* **78**, 214422 (2008).
- [155] M. N. Popova, S. A. Klimin, E. P. Chukalina, E. A. Romanov, B. Z. Malkin, E. Antic-Fidancev, B. V. Mill and G. Dhalenne, *Phys. Rev. B* **71**, 024414 (2005).
- [156] R. Sachidanandam, T. Yildirim, A. B. Harris, A. Aharony and O. Entin-Wohlman, *Phys. Rev. B* **56**, 260 (1997).
- [157] N. Shamir and U. Atzmony, *Physica B+ C* **94**, 85 (1978).
- [158] U. Ranon and K. Lee, *Phys. Rev.* **188**, 539 (1969).
- [159] V. Hardy, C. Martin, G. Martinet and G. André, *Phys. Rev. B* **74**, 064413 (2006).
- [160] K. H. J. Buschow, *Handbook of Magnetic Materials, Volume 17* (Elsevier Science, Amsterdam, 2007).
- [161] T. Chatterji, B. Ouladdiaf and D. Bhattacharya, *J. Phys. Condens. Matter* **21**, 306001 (2009).
- [162] D. C. Wallace, *Thermodynamics of crystals* (Dover Publications, New York, 1998).
- [163] B. Morosin, *Phys. Rev. B* **1**, 236 (1970).
- [164] P. Fulde and M. Loewenhaupt, *Adv. Phys.* **34**, 589 (1985).
- [165] K. Stevens, *Rep. Prog. Phys.* **30**, 189 (1967).

BIBLIOGRAPHY

- [166] M. T. Hutchings, In: Frederick Seitz and David Turnbull, Editors, *Point-Charge Calculations of Energy Levels of Magnetic Ions in Crystalline Electric Fields, Volume 16* (Academic Press, New York and London, 1964).
- [167] K. W. H. Stevens, Proc. Phys. Soc. London, Sect. A **65**, 209 (1952).
- [168] Mcphase: a software package for the calculation of phase diagrams and magnetic properties of magnetic systems, M. Rotter *et al.*, (2002–2010), available at <http://www.mcphase.de>.
- [169] V. Sechovský, L. Havela and K. H. J. Buschow, *Handbook of Magnetic Materials, Volume 11* (Elsevier Science, Amsterdam, 1998).
- [170] P. Fulde and M. Loewenhaupt, *Spin waves and magnetic excitations* edited by Borovik-Romanov, A. S. and Sinha, S. K (Elsevier Science Pub. Co. Inc., New York, NY, 1988).
- [171] R. T. Azuah, L. R. Kneller, Y. Qiu, P. L. W. Tregenna-Piggott, C. M. Brown, J. R. D. Copley and R. M. Dimeo, J. Res. Natl. Inst. Stand. Technol. **114**, 341 (2009).
- [172] L. I. Mirkin and H. M. Otte, *Handbook of X-Ray Analysis of Polycrystalline Materials* (Physics-Mathematics Literature, Moscow, 1961).
- [173] M. Gajek, M. Bibes, S. Fusil, K. Bouzehouane, J. Fontcuberta, A. Barthelemy and A. Fert, Nat. Mater. **6**, 296 (2007).
- [174] W. Eerenstein, N. D. Mathur and J. F. Scott, Nature **442**, 759 (2006).
- [175] W. Prellier, M. P. Singh and P. Murugavel, J. Phys.: Condens. Matter. **17**, R803 (2005).
- [176] S. Harikrishnan, S. Rößler, C. M. N. Kumar, H. L. Bhat, U. K. Rößler, S. Wirth, F. Steglich and S. Elizabeth, J. Phys. Condens. Matter **21**, 096002 (2009).
- [177] T. J. Sato, S. H. Lee, T. Katsufuji, M. Masaki, S. Park, J. R. D. Copley and H. Takagi, Phys. Rev. B **68**, 014432 (2003).
- [178] J. Park, J. G. Park, G. S. Jeon, H. Y. Choi, C. Lee, W. Jo, R. Bewley, K. A. McEwen and T. G. Perring, Phys. Rev. B **68**, 104426 (2003).

- [179] B. Lorenz, A. P. Litvinchuck, M. M. Gospodinov and C. W. Chu, Phys. Rev. Lett. **92**, 087204 (2004).
- [180] C. Wehrenfennig, D. Meier, T. Lottermoser, T. Lonkai, J. U. Hoffmann, N. Aliouane, D. N. Argyriou and M. Fiebig, Phys. Rev. B **82**, 100414 (2010).
- [181] B. Lorenz, F. Yen, M. M. Gospodinov and C. W. Chu, Phys. Rev. B **71**, 014438 (2005).
- [182] S. Lee, A. Pirogov, M. Kang, K. H. Jang, M. Yonemura, T. Kamiyama, S. W. Cheong, F. Gozzo, N. Shin, H. Kimura *et al.*, Nature **451**, 805 (2008).
- [183] S. Nandi, A. Kreyssig, J. Q. Yan, M. D. Vannette, J. C. Lang, L. Tan, J. W. Kim, R. Prozorov, T. A. Lograsso, R. J. McQueeney and A. I. Goldman, Phys. Rev. B **78**, 075118 (2008).
- [184] T. Lonkai, D. G. Tomuta, U. Amann, J. Ihringer, R. W. A. Hendrikx, D. M. Többens and J. A. Mydosh, Phys. Rev. B **69**, 134108 (2004).
- [185] S. Lee, A. Pirogov, J. H. Han, J. G. Park, A. Hoshikawa and T. Kamiyama, Phys. Rev. B **71**, 180413 (2005).
- [186] N. Kamegashira, H. Sato and S. Ashizuka, Mater. Sci. Forum **449**, 1045 (2004).
- [187] D. P. Kozlenko, S. E. Kichanov, S. Lee, J. G. Park, V. P. Glazkov and B. N. Savenko, JETP letters **82**, 193 (2005).
- [188] D. P. Kozlenko, S. E. Kichanov, S. Lee, J. G. Park, V. P. Glazkov and B. N. Savenko, JETP letters **83**, 346 (2006).
- [189] V. Y. Ivanov, A. A. Mukhin, A. S. Prokhorov, A. M. Balbashov and L. D. Iskhakova, Phys. Solid State **48**, 1726 (2006).
- [190] T. Kyömen, M. Morita, M. Itoh, K. Kohn and N. Kamegashira, Ferroelectrics **264**, 223 (2001).
- [191] M. Tachibana, J. Yamazaki, H. Kawaji and T. Atake, Phys. Rev. B **72**, 064434 (2005).
- [192] H. S. Nair, C. M. N. Kumar, H. L. Bhat, S. Elizabeth and T. Brückel, Phys. Rev. B **83**, 104424 (2011).

BIBLIOGRAPHY

- [193] J. C. Lashley, R. Stevens, M. K. Crawford, J. Boerio-Goates, B. F. Woodfield, Y. Qiu, J. W. Lynn, P. A. Goddard and R. A. Fisher, *Phys. Rev. B* **78**, 104406 (2008).
- [194] B. G. Wybourne and W. F. Meggers, *Spectroscopic properties of rare earths* (Interscience, New York, 1965).
- [195] D. Bravo, A. Kaminskii and F. López, *J. Phys. Condens. Matter* **10**, 3261 (1998).
- [196] O. V. Kovalev, H. T. Stokes and D. M. Hatch, *Representations of the crystallographic space groups: irreducible representations, induced representations, and corepresentations* (CRC, 1993).
- [197] A. Wills, *Physica B* **276**, 680 (2000).
- [198] P. J. Brown and T. Chatterji, *J. Phys. Condens. Matter* **18**, 10085 (2006).
- [199] M. Fiebig, T. Lottermoser and R. V. Pisarev, *J. Appl. Phys.* **93**, 8194 (2003).
- [200] S. Nandi, A. Kreyssig, L. Tan, J. W. Kim, J. Q. Yan, J. C. Lang, D. Haskel, R. J. McQueeney and A. I. Goldman, *Phys. Rev. Lett.* **100**, 217201 (2008).
- [201] T. Kimura, T. Goto, H. Shintani, K. Ishizaka, T. Arima and Y. Tokura, *Nature* **426**, 55 (2003).
- [202] J. Stremper, B. Bohnenbuck, M. Mostovoy, N. Aliouane, D. N. Argyriou, F. Schrettle, J. Hemberger, A. Krimmel and M. Zimmermann, *Phys. Rev. B* **75**, 212402 (2007).
- [203] A. H. Arkenbout, T. T. M. Palstra, T. Siegrist and T. Kimura, *Phys. Rev. B* **74**, 184431 (2006).
- [204] R. P. Chaudhury, B. Lorenz, Y. Q. Wang, Y. Y. Sun and C. W. Chu, *Physical Review B* **77**, 104406 (2008).
- [205] E. García-Matres, N. Stüßer, M. Hofmann and M. Reehuis, *Eur. Phys. J. B* **32**, 35 (2003).
- [206] H. Katsura, A. Balatsky and N. Nagaosa, *Phys. Rev. Lett.* **98**, 27203 (2007).

- [207] T. Kimura, G. Lawes, T. Goto, Y. Tokura and A. P. Ramirez, Phys. Rev. B **71**, 224425 (2005).
- [208] T. Goto, T. Kimura, G. Lawes, A. P. Ramirez and Y. Tokura, Phys. Rev. Lett. **92**, 257201 (2004).
- [209] T. Finger, D. Senff, K. Schmalzl, W. Schmidt, L. P. Regnault, P. Becker, L. Bohatý and M. Braden, Phys. Rev. B **81**, 054430 (2010).
- [210] H. Dachs, Solid State Commun. **7**, 1015 (1969).
- [211] Y.-S. Song, J.-H. Chung, J. M. S. Park and Y.-N. Choi, Phys. Rev. B **79**, 224415 (2009).
- [212] Y. S. Song, L. Q. Yan, B. Lee, S. H. Chun, K. H. Kim, S. B. Kim, A. Nogami, T. Katsufuji, J. Schefer and J. H. Chung, Phys. Rev. B **82**, 214418 (2010).
- [213] J. B. Forsyth and C. Wilkinson, J. Phys. Condens. Matter **6**, 3073 (1994).
- [214] L. Kihlborg and E. Gebert, Acta Crystallogr., Sect. B: Struct. Sci **26**, 1020 (1970).
- [215] E. Jansen, W. Schafer and G. Will, J. Appl. Crystallogr. **27**, 492 (1994).
- [216] J. Rodrigues-Carvajal, Basireps, program available from, <http://www.ccp14.ac.uk/ccp/ccp14/ftp-mirror/fullprof/pub/divers>.

Acknowledgements

It is a great pleasure for me to express my sincere gratitude to my promotor Prof. Dr. Thomas Brückel for giving me the opportunity to pursue my PhD within his group. I also thank him for giving me a lot of freedom in my work. I am indebted to him for his support, advice and endless patience he showed in my work and in improving my writing. I have deep feelings of gratitude towards Dr. Yinguo Xiao for his consistent support throughout my thesis work. The energy and time he has put into this work has been amazing.

I would like to thank Dr. Tapan Chatterji and Dr. Yixi Su for their help during neutron scattering experiments and also for their genuine concern about my work. My special thanks to Dr. Shibabrata Nandi for his extensive help in my research, whose computational skills, I always admire. I extend my sincere thanks to Prof. Jane Brown (ILL) and Dr. Anatoliy Senyshyn (FRM II), for their help in neutron scattering measurements and data analysis.

I really appreciate the efforts of DP Jörg Perßon in keeping the preparation labs in the best conditions for the use, and his help in orientation of single crystals. My special thanks go to Mr. Berthold Schmitz. I also would like to thank Dr. Emmanuel Kentzinger for his great efforts in the maintenance and scheduling of the measurements at MPMS, PPMS and x-ray diffraction instruments. Thanks to Dr. Andreas Houben for his help in x-ray diffraction measurements and structure refinement. Thanks to Dimitrios for his assistance during measurements on CCMS. Many thanks to DI Peter Hiller for his help in designing a sample holder. Thanks to Dr. Jörg Voigt for his help during neutron scattering experiment at PSI. All the group members and colleagues at Forschungszentrum Jülich will have my gratitude for their impartial and consistent cooperation through out my career in the institute. A special thanks to Zhendong Fu, it was pleasure to be your office-mate throughout my PhD life. I would like to thank, Prof. Raphaël Hermann, Prof. Manuel Angst and Dr. Werner Schweika for fruitful discussions. I also would like

to extend my thanks to all my colleagues at JCNS-2, PGI-4, Forschungszentrum Jülich GmbH.

My great appreciations and thanks to secretary, Frau. Barbara Köppchen, for she is conscientious.

I would like to thank all the instrument responsible personnel at FRM II-Garching, ILL-Grenoble and PSI-Villigen for their support, in neutron scattering measurements.

I would like to thank the four examiners Prof. Dr. Thomas Brückel, Prof. Dr. Uwe Klemradt, Prof. Dr. Carsten Honerkamp and Prof. Dr. Markus Morgenstern.

Hari – you are right, we brothers don't thank each other ☺.

Shilpa, I am very grateful to you for what you are for me. You might never know how much I value your friendship. Uday, my heartfelt thanks to you for being there for me in some of the toughest times of my life. A special thanks to Dev, who is more than my brother to me. Thanks to Gabbar aka Rohit for his motivational words about research-life.

I would like to thank all my V6 pals, MVK, MBA, NBN, BAE and CLR. Many thanks to my friends, Nicky, Bhavi, Chachu, Ravi, DTH, Vinod, Sunil, Joby, Shimjith, Ullas, Yashodhar, Vinayak, Kokke, Vanishri, Babu Reddy, Ganesan, Padmanabhan, Poori, Junior, Shivu, Anu, Prem, Sanmati, Subhash, Sayee, RK, Suma and many more I might not have mentioned by name here. You all have special place in my heart throughout my life. A special thanks to my new-friend Shari. A thanks to Bharathiya Janatha in Jülich who, once in a while simulated comforting homely feeling, thanks to Jaydeepda ☺.

I would like to thank all my teachers and past supervisors. To name few who influenced my academic career a lot are, Ananthaprakash, Nanjundappa, Nijalingappa, Dr. Kunjomana, Dr. Suja Elizabeth and Emeritus Prof. H. L. Bhat.

I am grateful to my uncle Narayan and aunt Pavithra Narayan, for their incredible love and support at difficult times. Heartily thanks to my lovely sister Savitha and her family for their love. Also bunch of thanks to aunt, Manjula and her family for the help when it was most needed. My sincere thanks to Jagannath and Dr. Srinivas for their help at some point of time in my academic career. I also would remember the support and love of my uncles and aunts Srinivas, Ramadevi, Ravikumar, Anasuya and their family and also Grandpa and Grandma. Love you and thank you all.

To Amma and Appa who are always proud of me

– I owe you everything.